APPLIED PHYSICS REVIEWS

GaN: Processing, defects, and devices

S. J. Pearton[a)]
Department of Materials Science and Engineering, University of Florida, Gainesville, Florida 32611

J. C. Zolper
Office of Naval Research, Arlington, Virginia 22217

R. J. Shul
Sandia National Laboratories, Albuquerque, New Mexico 87185

F. Ren
Department of Chemical Engineering, University of Florida, Gainesville, Florida 32611

(Received 16 October 1998; accepted for publication 3 March 1999)

The role of extended and point defects, and key impurities such as C, O, and H, on the electrical and optical properties of GaN is reviewed. Recent progress in the development of high reliability contacts, thermal processing, dry and wet etching techniques, implantation doping and isolation, and gate insulator technology is detailed. Finally, the performance of GaN-based electronic and photonic devices such as field effect transistors, UV detectors, laser diodes, and light-emitting diodes is covered, along with the influence of process-induced or grown-in defects and impurities on the device physics. [S0021-8979(99)00613-1]

TABLE OF CONTENTS

I. INTRODUCTION

Current GaN-based device technologies include light-emitting diodes (LEDs), laser diodes, and UV detectors on the photonic side and microwave power and ultrahigh power switches on the electronics side.[1] The LED technology is by now relatively mature, with lifetimes of blue and green emitters apparently determined mostly by light-induced degradation of the polymer package that encapsulates the devices.[2] The main trends in this technology appear to be optimization of optical output efficiency and solving the polymer package degradation issue. For the laser diodes one of the main lifetime limiters is *p*-ohmic contact metal migration along dislocations which short out the GaN *p*-contact layer by spiking all the way to the *n* side of the junction.[3,4] This is exacerbated by the generally high specific contact resistance (R_C) of the *p*-ohmic contact and the associated heating of this area during device operation. The advent of lower threshold devices and dislocation-free GaN overgrowth of SiO_2-masked regions has allowed achievement of laser lifetimes over 10 000 h.[5] Facet formation on the laser has been achieved by dry etching, cleaving, polishing, and selective/crystallographic growth. In structures grown on Al_2O_3 both contacts must be made on the top of the device and hence dry etching is necessary to expose the *n* side of the junction. Fabrication of UV detectors is relatively straightforward and the main issue seems to be one of improving material purity and quality.

With respect to electronic devices for microwave power applications, the main process improvements needed are in the areas of low R_C *n*-ohmic contacts (the requirements are more stringent than for photonic devices, with $R_C \leqslant 10^{-7}\ \Omega\ \mathrm{cm}^{-2}$ being desirable), stable and reproducible Schottky contacts, and low damage dry etching that maintains surface stoichiometry. For the proposed high power switches (capable of 25 kA with 3 kV-voltage standoff) there are a number of possible device structures, including thyris-

a)Electronic mail: spear@mse.ufl.edu

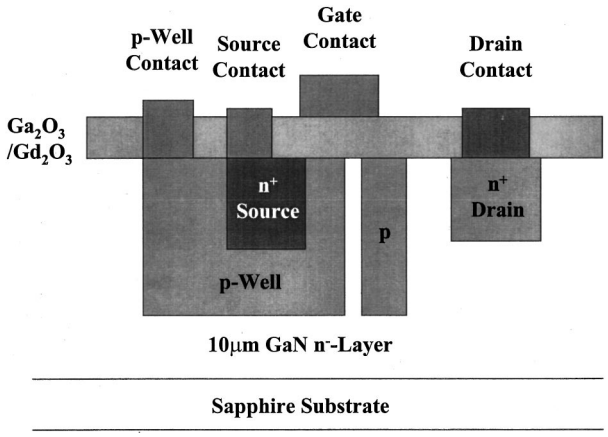

FIG. 1. Schematic of an ultra high breakdown voltage GaN power MOSFET.

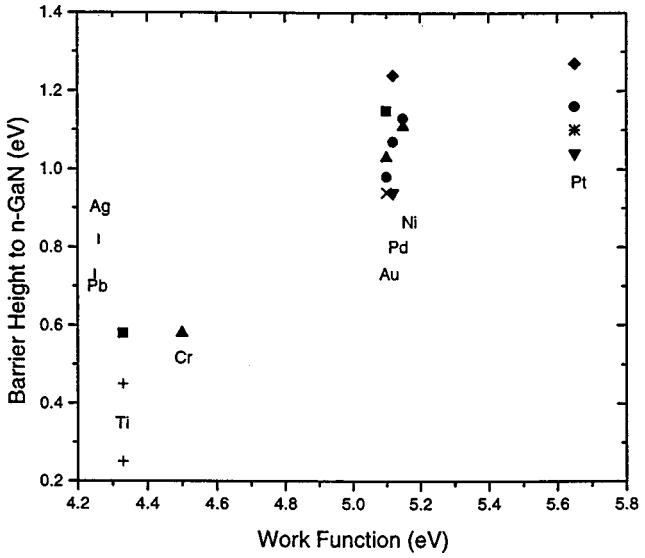

FIG. 2. Compilation of published results for Schottky barrier heights on GaN (after Refs. 18, 28, and 68).

tors and several types of power metal-oxide-semiconductor field-effect transistor (MOSFET). A schematic of a lateral GaN MOSFET is shown in Fig. 1. In this case, critical technologies include high implant activation efficiency, gate insulator, trench etching for capacitor formation, and stable high temperature/high current stable ohmic contacts.

Recent progress in the development of dry and wet etching techniques, implant doping and isolation, thermal processing, gate insulator technology, and high reliability contacts is first reviewed. Etch selectivities up to 10 for InN over AlN are possible in inductively coupled plasmas using a Cl_2/Ar chemistry, but in general selectivities for each binary nitride relative to each other are low ($\leqslant 2$) because of the high ion energies required to initiate etching. Improved *n*-type ohmic contact resistances are obtained by selective area Si^+ implantation followed by very high temperature ($>1300\,°C$) anneals to minimize the thermal budget and AlN encapsulation which prevents GaN surface decomposition. Implant isolation is effective in GaN, AlGaN, and AlInN, but marginal in InGaN. Candidate gate insulators for GaN include AlN, AlON, and $Ga(Gd)O_x$, but interface state densities must still be decreased to realize state-of-the-art metal-insulator-semiconductor (MIS) devices.

Many outstanding reviews on GaN materials and devices have appeared previously,[6–14] so we will focus on processing and the influence of defects and impurities on devices.

II. PROCESSING

A. Ohmic and Schottky contacts

1. Schottky contacts

There are still large variations in barrier heights reported by different workers for standard metals on GaN. Pt appears to produce the highest consistent values (~1.0–1.1 eV) with Ti producing the lowest (0.1–0.6 eV). The variability appears to result from the presence of several transport mechanisms, and to materials and process factors such as defects present in these films, the effectiveness of surface cleans prior to metal deposition, local stoichiometry variations, and variations in surface roughness which could affect uniformity of the results. New work on silicides shows promise.[15,16] For Schottky contacts Pt appeared to be stable to approximately 400 °C for 1 h, while PtSi is somewhat more stable (500 °C, 1 h), and also has barrier heights of ~0.8 eV.

Recent reviews and studies of Schottky contact properties on GaN have appeared.[15–28] The measured barrier heights in most cases are a function of the difference between the metal work function and the electron affinity of GaN. Some typical values for barrier height for different metals are 1.1 eV for Pt,[19] 0.91–1.15 eV for Au,[20,21] 0.6 eV for Ti,[22] and 0.94 eV for Pd.[23] For Ni there is a fairly large discrepancy in reported values, ranging from 0.66[24] to 0.99 eV.[25] For deposition onto *n*-GaN ($\sim 10^{17}\,cm^{-3}$), rectifying behavior was observed for Pt, Ni, Pd, Au, Co, Cu, Ag, ohmic behavior for So, Hf, Zn, Al, and V, while intermediate behavior (slightly rectifying) was obtained for Nb, Ti, Cr, W, and Mo.[16] Schmitz *et al.*[16] calculated from their data that the density of surface states on GaN was $\sim 1.8 \times 10^{13}\,cm^{-2}\,eV^{-1}$, suggesting the degree of pinning of the barrier height is less than GaAs where the surface state density is roughly an order of magnitude higher.

A comparison of barrier height data from various sources is shown in Fig. 2.[16,29–33] In the early days of forming rectifying contacts on GaN it was often believed the Fermi level at the surface and at the metal–nitrides interface was unpinned. The data of Fig. 2 shows that indeed the barrier height does vary with metal work function. The strategy is then to use a metal with a large work function on GaN (such as Pt) to form a Schottky barrier, while a metal with a low work function (such as Ti) should be selected for ohmic contacts.

The influence of the surface cleanliness is obviously most important in determining the quality of the Schottky contact. *In situ* deposition of Ga, followed by thermal desorption under ultrahigh vacuum conditions is found to produce clean GaN surfaces,[34,35] while *in situ* N_2^+ ion sputtering can also remove native oxides.[36,37] Liu and Lau[15],

Liu *et al.*,[38] and Mohney and Lau[18] have reviewed surface cleaning processes for GaN. A number of different acid solutions, including HNO_3/HCl, HCl/H_2O, and HF/H_2O, have been examined for removing the native oxide,[39] and superior current–voltage characteristics are observed for the resultant rectifying contacts.[40] As with other III–V compound semiconductors, HCl and HF can significantly reduce the oxide on GaN,[41,42] while the bases NH_4OH and NaOH can also dissolve the oxide.[43] To this point, there has been no clear demonstration of the effect of the polarity of the epilayer on the barrier height.

Mohney and Lau[18] have also commented on the fact that there can be significant spatial differences in the quality of Schottky barrier contacts on a *n*-GaN, with diodes showing ideality factors ranging from <1.1 to $\geqslant 1.3$ on the same wafer. While thermionic emission is clearly the dominant current transport mechanism in most diodes, tunneling and generation recombination may also be present. In many cases the high dislocation density in material used to date are probably responsible for most of the spatial variations.

The thermal stability of Schottky contacts on GaN is critically important for practical device operation. The thermal limits of most of the metal/GaN combinations are between 300 and 600 °C, specifically 300 °C for Pd,[44] 400 °C for Pt,[45] 575 °C for Au,[46] and 600 °C for Ni.[18] As mentioned earlier, the silicides of Pt and Ni display greater thermal stability than the pure metals.[45] These contacts however may not be in thermodynamic equilibrium with the GaN, leading to the formation of metal gallides and silicon nitride upon prolonged annealing.

There is little information on barrier heights on *p*-GaN due to the general difficulty in growing high quality *p*-type material and the low hole mobility. A barrier height of 2.38 eV was reported for Au on *p*-GaN.[47]

2. n-ohmic contacts

The commonly accepted ohmic contact to *n*-GaN is Ti/Al, which is generally annealed to produce oxide reduction on the GaN surface. Multilevel Au/Ni/Al/Ti structures appear to give wider process windows, by reducing oxidation of the Ti layer.[48] R_C values of $\leqslant 10^{-5}\,\Omega\,\mathrm{cm}^2$ have been produced on heterostructure field-effect transistor (HFET) devices using Ti/Al annealed at 900 °C for 20 s.[15]

Both W and WSi_x on n^+ epi-GaN layers ($n \sim 10^{19}\,\mathrm{cm}^{-3}$) produce reasonable contacts ($R_C \sim 8 \times 10^{-5}\,\Omega\,\mathrm{cm}^2$), but extremely stable behavior[49]—annealing at 1000 °C led to shallow reacted regions of $\leqslant 100$ Å, and in junction field-effect transistor structures these contacts can withstand implant activation anneals at 1100 °C.[50] Reaction with the GaN is relatively limited, although β-W_2N interfacial phases are found after 800 °C anneals, and this appears to be a barrier to Ga out-diffusion.[49]

By contrast to the *n*-metal systems, the standard *p*-ohmic contact to GaN is Ni–Au, with R_C values $\geqslant 10^{-2}\,\Omega\,\mathrm{cm}^2$. Efforts to find a superior alternative have proved fruitless to date,[51] even though strong efforts have been made on multicomponent alloyed contacts where one attempts to extract one of the lattice elements, replace it with an acceptor dopant, and simultaneously reduce the ''balling-up'' of the metallization during this reaction. The model system for this type of contact is AuGeNi/*n*-GaAs. A promising approach is to reduce the band gap through use of *p*-type InGaN on the top of the GaN. To date there have been reports of achieving *p*-doping ($\sim 10^{17}\,\mathrm{cm}^{-3}$) in compositions up to ~15% In.

The III nitrides pose a problem however, in the development of low resistance ohmic contacts because of their wide band gaps. Most of the work done in the area has been focused on *n*-type GaN. Au and Al single metal contacts to n^+GaN and nonalloyed Au/Ti and Al/Ti were found to have contact resistances of $\sim 10^{-3}$ to $10^{-4}\,\Omega\,\mathrm{cm}^2$.[46,52–58] Al-containing contacts perform best when oxidation is minimized. Lin *et al.*[59] reported the lowest contact resistance to n^+GaN, with Ti/Al contacts after annealing at 900 °C for 30 s in a rapid thermal annealer ($R_C = 8 \times 10^{-6}\,\Omega\,\mathrm{cm}^2$). They suggested the formation of a TiN interface as important in the formation of the low resistance contact. Most of the transition metal elements, including Ti, V, and Sc react with GaN to form nitrides, gallides, and metal–Ga–N ternary phases.[18] Thermodynamic calculation indicate that the metals themselves are not in equilibrium with GaN under normal processing conditions, with the consequent probability of interfacial reactions occurring.[60] Both Ti and TiN have been shown to produce ohmic contacts on *n*-GaN,[61,62] with Ti consuming GaN during reaction (a few hundred angstroms at ~1000 °C for 30 s) to form TiN.[63] Three phase equilibria for the Ti–Ga–N (and V–Ga–N and Cr–Ga–N) systems at 800 °C have been reported by several groups.[64–66] The annealing ambient plays a strong role, since if the N_2 partial pressure is greater than that in equilibrium with a metal/GaN contact during reaction, there is a driving force to incorporate nitrogen from the gas phase.[18] Moreover, there is quite different behavior observed for deposited TiN/GaN contacts relative to those formed by reaction of Ti with GaN in a N_2 ambient. In the former case, thermionic emission appears to be the dominant conduction mechanism whereas in the latter tunneling seems to be most important.[18]

Modification of the GaN surface by high temperature annealing[67] or reactive ion etching[48,68] to produce preferential loss of N_2 can improve *n*-type ohmic contact resistance by increasing electron concentration in the near-surface region.

Many other metals can be employed to form bilayer Al/metal/GaN *n*-ohmic contacts, including Pd,[69,70] Ta,[71] Nd,[72] Sc,[18] and Hf.[18] All of these form good ohmic contacts, with specific contact resistances in the $10^{-5}\,\Omega\,\mathrm{cm}^2$ range.

A particularly attractive method for reducing R_C on device structures is self-aligned implantation of Si^+ to heavily dope source/drain ohmic contact regions. This approach has been employed to achieve high quality contacts on heterostructure field-effect transistor (HFET) structures.[73] W was found to produce low resistance ohmic contacts to n^+GaN ($R_C = 8 \times 10^{-6}\,\Omega\,\mathrm{cm}^2$) with little interaction between the semiconductor and the metal up to 800 °C.[49] WSi_x on n^+GaN was found to be stable to 800 °C as well, with a contact resistance of $\sim 10^{-5}\,\Omega\,\mathrm{cm}^2$. Graded contact layers to GaN have been formed with both InN[74] and InGaN using WSi_x metallization. Nonalloyed Ti/Pt/Au on InN produced specific contact resistance $R_C = 1.8 \times 10^{-7}\,\Omega\,\mathrm{cm}^2$.[74] Graded

$In_xGa_{1-x}As/InN$ contacts have been employed on GaAs/AlGaAs heterojunction bipolar transistors, with R_C as low as $5\times10^{-7}\,\Omega\,cm^2$.[75]

For high temperature electronics applications, or for high reliability, it would be preferable to employ refractory metal contacts such as W and WSi_x. Moreover, the contact resistance could be reduced if lower band gap In-containing alloys (or InN) were used as contact layers on GaN, much as in the case of InGaAs on GaAs. However, the In-based nitrides are less thermally stable than GaN, and we need to establish the trade off between contact resistance and poorer temperature stability.

Recent experiments on formation of W, $WSi_{0.44}$ and Ti/Al contacts deposited on $n^+In_{0.65}Ga_{0.35}N$ ($n\sim10^{20}\,cm^{-3}$), n^+InN ($n\sim10^{20}\,cm^{-3}$), and $n^-In_{0.75}Al_{0.25}N$ ($n\sim10^{18}\,cm^{-3}$) have been reported.[74,75] The electrical, structural, and chemical stability of these contacts were examined after anneals up to 900 °C. It was found that InGaN allows achievement of excellent contact resistance ($<10^{-6}\,\Omega\,cm^2$), with stability up to ~ 600 °C for W metallization.

The 2000-Å-thick InGaN, InN, and InAlN samples were grown using metal organic molecular beam epitaxy (MOMBE) on semi-insulating, (100) GaAs substrates in an Intevac Gen II system as described previously.[76,77] The InN, $In_{0.65}Ga_{0.35}N$, and $In_{0.75}Al_{0.25}N$ were highly autodoped *n* type ($\sim10^{20}$, $\sim10^{19}$, and $8\times10^{18}\,cm^{-3}$, respectively) due to the presence of native defects.

The samples were rinsed in $H_2O:NH_4OH$ (20:1) for 1 min just prior to deposition of the metal to remove native oxides. The metal contacts were sputter deposited to a thickness of 1000 Å in the case of W and $WSi_{0.44}$ (film composition), and then etched in SF_6/Ar in a plasma-therm reactive ion etcher (RIE) to create transmission line method (TLM) patterns. For the Ti/Al contacts, 200 Å of Ti and then 1000 Å of Al was deposited and the TLM pattern formed by lift-off of the resist mask. The nitride samples were subsequently etched in $Cl_2/CH_4/H_2/Ar$ in an electron cyclotron resonance (ECR) etcher to produce the mesas for the TLM patterns.[78] The samples were annealed at temperatures from 300 to 900 °C for 15 s under a nitrogen ambient in a rapid thermal annealing (RTA) system (AG-410).

The contact resistance for W, WSi_x, and Ti/Al ohmic contacts to InGaN as a function of annealing temperature is shown in Fig. 3. All contacts had similar contact resistance as deposited, $2-4\times10^{-7}\,\Omega\,cm^{-2}$. Above 600 °C, the Ti/Al contacts degraded rapidly, and the WSi_x continued to degrade, while R_C for both samples increased up to $\sim10^{-5}\,\Omega\,cm^2$ at 900 °C. The error in these measurements was estimated to be ±10% due mainly to geometrical contact size effects. The widths of the TLM pattern spacings varied slightly due to processing (maximum of ±5%) as determined by scanning electron microscopy (SEM) measurements, which were taken into account when calculating the contact resistances.

SEM micrographs of W and Ti/Al contacts on InGaN as grown and annealed showed the W was still quite smooth even after 900 °C anneal, while the Ti/Al had significant pitting at the lowest anneal of 500 °C even though the contact resistance did not degrade until ⩾600 °C. Auger electron spectroscopy (AES) showed that the degradation was due to out-diffusion of In and N.

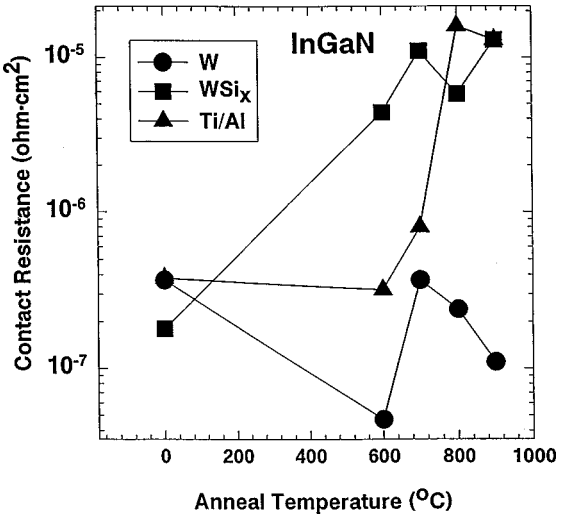

FIG. 3. Contact resistance for W, $WSi_{0.44}$, and Ti/Al ohmic contacts to InGaN as a function of annealing temperature.

The contact resistance for ohmic contacts of W, WSi_x, and Ti/Al to InN as a function of annealing temperature is shown in Fig. 4. As-deposited samples had similar contact resistances to InGaN, indicating a similar conduction mechanism. WSi_x contacts showed the most degradation at low temperature, with the resistance rising a factor of 5 after 300 °C annealing and then remaining constant. Ti/Al deviated little from initial values, although there was severe pitting on samples annealed at 500 °C while W resistance began to degrade at 500 °C.

In Fig. 5 the contact resistance is shown for W, WSi_x, and Ti/Al ohmic contacts to InAlN as a function of annealing temperature. As-deposited Ti/Al had the lowest contact resistance on this material, $R_C\sim10^{-4}\,\Omega\,cm^2$. Tungsten had the

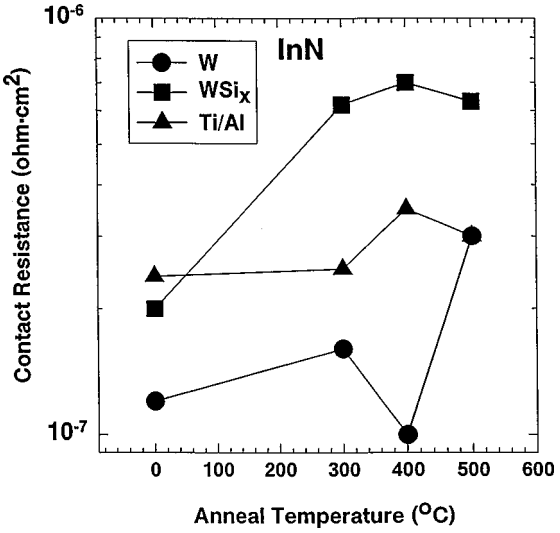

FIG. 4. Contact resistance for ohmic contacts of W, WSi_x, and Ti/Al to InN as a function of annealing temperature.

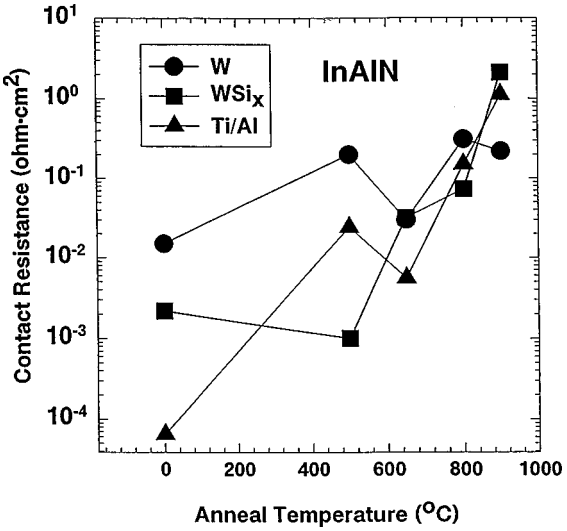

FIG. 5. Contact resistance for W, WSi_x, and Ti/Al ohmic contacts to InAlN as a function of annealing temperature.

highest initial contact resistance, $R_C \sim 10^{-2}\,\Omega\,\mathrm{cm}^2$. The contacts showed morphological stability up to 400 °C (Ti/Al) and to 800 °C (W).

SEM micrographs of InAlN contacted with W, WSi_x, and Ti/Al as-grown and annealed at 800, 700, and 400 °C, respectively, were examined. The W on InAlN remained smooth until 800 °C, and then began to form hillocks, as did the WSi_x contact at 700 °C. The Ti/Al began pitting at 400 °C. The pitting in the Ti/Al contacts was due to diffusion of the Al through the Ti into the sample. Hillocks appear to be formed from diffusion of In from the nitride sample into the contact layer.

In summary, W, WSi_x, and Ti/Al were found to produce low resistance ohmic contacts on n^+ InGaN and InN. *W* contacts proved to be the most stable, and also gave the lowest resistance to InGaN and InN, $R_C < 10^{-7}\,\Omega\,\mathrm{cm}^2$ after 600 °C anneal, and $1\times10^{-7}\,\Omega\,\mathrm{cm}^2$ after 300 °C anneal, respectively. Significant interdiffusion of In, N, and Al, as well as Ti and W, were found after annealing. The contact resistance stability varies for each material and degraded at temperatures >400 °C on InN, ≥500 °C on InAlN, and ≥600 °C on InGaN. Only W contacts remained smooth at the highest anneal temperature.

3. p-ohmic contacts

One of the life-limiting factors in GaN laser diodes to date has been the *p*-ohmic contact.[79] Due to the relatively poor specific contact resistance (R_C) achievable, the metallization will heat-up as current flows across the *p-n* junction, leading to metal migration down threading dislocations and eventual shorting of the junction.[79] Removal of the dislocations, such as in epitaxial lateral overgrowth structures, will greatly extend the device lifetime.[79] There are a number of contributing factors to the high R_C values for contacts on *p*-GaN, including:

(i) The absence of a metal with a sufficiently high work function (the band gap of GaN is 3.4 eV, and the electron affinity is 4.1 eV, but metal work functions are typically ≤5 eV).

(ii) The relatively low hole concentrations in *p*-GaN due to the deep ionization level of the Mg acceptor (~170 meV).

(iii) The tendency for the preferential loss of nitrogen from the GaN surface during processing, which may produce surface conversion to *n*-type conductivity.

In the search for improved contact characteristics, a wide variety of metallizations have been investigated on *p*-GaN besides the standard Ni/Au,[80–85] including Ni,[82,83,86] Au,[82,85,87,88] Pd,[82] Pd/Au,[88,89] Pt/Au,[84] Au/Mg/Au,[61,87] Au/C/Ni,[90] Ni/Cr/Au,[88,91] and Pd/Pt/Au.[84] Typically Ni, Pd, or Pt is the metal in direct contact with the GaN, and the structure is annealed at 400–750 °C. This produces contact resistances in the 10^{-1}–$10^{-3}\,\Omega\,\mathrm{cm}^2$ range. For higher temperatures severe degradation in contact morphology is observed, usually resulting from the formation of the metal gallides.

To examine thermal stability of contacts, *p*-type ($N_A = 10^{18}\,\mathrm{cm}^{-3}$), Mg-doped GaN layers 1 μm thick were grown on Al_2O_3 substrates by molecular beam epitaxy (MBE) using solid Ga and radio-frequency (rf) plasma-activated N_2.[92] Strong cathodoluminescent was observed at ~385 nm, with very little deep level emission, indicative of high quality material. Undoped GaN layers ~3 μm thick were grown on Al_2O_3 by metal organic chemical vapor deposition, with similar cathodoluminescent properties to the MBE material. These samples were implanted with 100 keV Si^+ ions at a dose of $5\times10^{15}\,\mathrm{cm}^{-2}$, and annealed with AlN caps in place to 1400 °C for 10 s.[93] This produced a peak *n*-type doping concentration of $\sim5\times10^{20}\,\mathrm{cm}^{-3}$. W or $WSi_{0.45}$ layers ~1000 Å thick were deposited using an MRC501 sputtering system. The sample position was biased at 90 V with respect to the Ar discharge. Prior to sputtering, the native oxide was removed in a 201 H_2O:NH_4OH solution. Transmission line patterns were defined by dry etching the exposed metal with SF_6/Ar, and forming mesas around the contact pads using BCl_3/N_2 dry etching to confine the current flow. For comparison, on the *p*-GaN, Au (1000 Å)/Ni (500 Å) was deposited by *e*-beam evaporation, defined by lift-off and mesas formed by dry etching. Both *n*- and *p*-type samples were annealed for 60 s (in some experiments this was varied for 30–300 s) at 300–1000 °C under flowing N_2.

From Fermi–Dirac statistics we can calculate the Fermi level position E_F for *p*-GaN containing 10^{18} acceptors cm^{-3} as a function of absolute temperature T, from

$$N_A \frac{1}{1+2\exp[(E_a-E_F)/kT]} = N_V \exp[-(E_F-E_V)/kT],$$

where N_A is the acceptor concentration, $E_a = 171$ meV for Mg in GaN, and N_v is the valence band density of states. Using this relation, we calculated the ionization efficiency for Mg as a function of sample temperature, as shown in Fig. 6. Since the hole concentration in the *p*-GaN will increase rapidly with temperature, we would expect better ohmic contact properties at high temperatures.

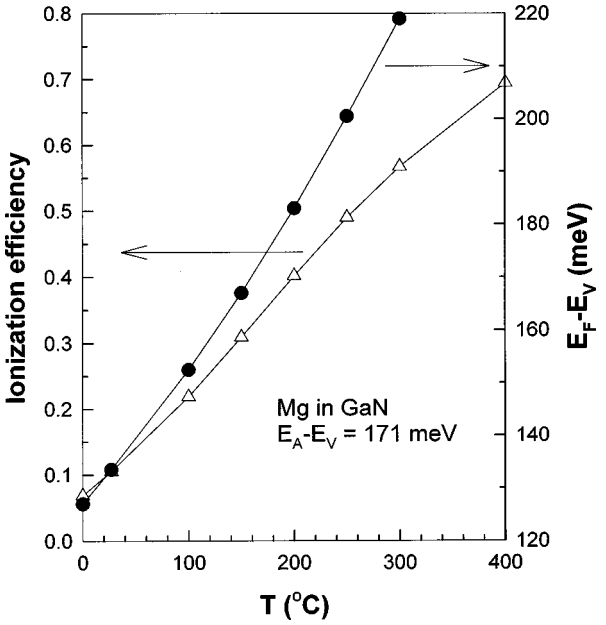

FIG. 6. Ionization efficiency of Mg acceptors in GaN and Fermi level position for GaN containing 10^{18} cm^{-3}Mg acceptors, as a function of temperature.

Figure 7 shows annealing temperature dependence of the current–voltage ($I-V$) characteristics of the Ni/Au, W, and WSi on *p*-GaN, with the measurements made at 25 °C in all cases. Note that for the optimum anneal temperatures (700 °C for Ni/Au and W, and 800 °C for WSi_x), the contacts are not ohmic, but are more accurately described as leaky Schottky diodes. In the case of W and WSi, we assume that annealing above the optimum temperature produces loss of N_2 and poorer contact properties.

The contact morphology on the W and WSi metallization remained featureless to the highest temperature we investigated. This is in sharp contrast to the case of Ni/Au, as shown in Fig. 8. For the latter metallization, islanding is quite severe after 700 °C annealing due to reaction of the Ni with the GaN.[94,95]

From the earlier discussion, we would expect the contact properties to improve at elevated temperatures because of the increased hole density and more efficient thermionic hole emission across the metal–GaN interface. Figure 9 shows the $I-V$ characteristics for the 700 (Ni/Au and W) or 800 °C (WSi) annealed samples, as a function of the measurement temperature (25–300 °C). For the Ni/Au, the contacts become ohmic at $\geqslant$200 °C, while for W and WSi_x this occurs at 300 °C. Table I shows the R_C values at 300 °C are 9.2×10^{-2} (Ni/Au), 6.8×10^{-2} (W), and 2.6×10^{-2} Ω cm^2 (WSi). The TLM measurements showed that the substrate sheet resistance is reduced from 1.39×10^4 $\Omega/\square$ at 200 °C, to 8470$\Omega/\square$ at 250 °C, and 4600$\Omega/\square$ at 300 °C, indicating that the increased hole concentration plays a major role in decreasing R_C.

There was not a strong dependence of the room temperature $I-V$ characteristics on annealing time. An example is shown in Fig. 10 for W/*p*-GaN, annealed at 700 °C. There is little change in the characteristics for 30–120 s, but the contacts become more rectifying for longer times, probably due to the onset of metal-semiconductor reactions.

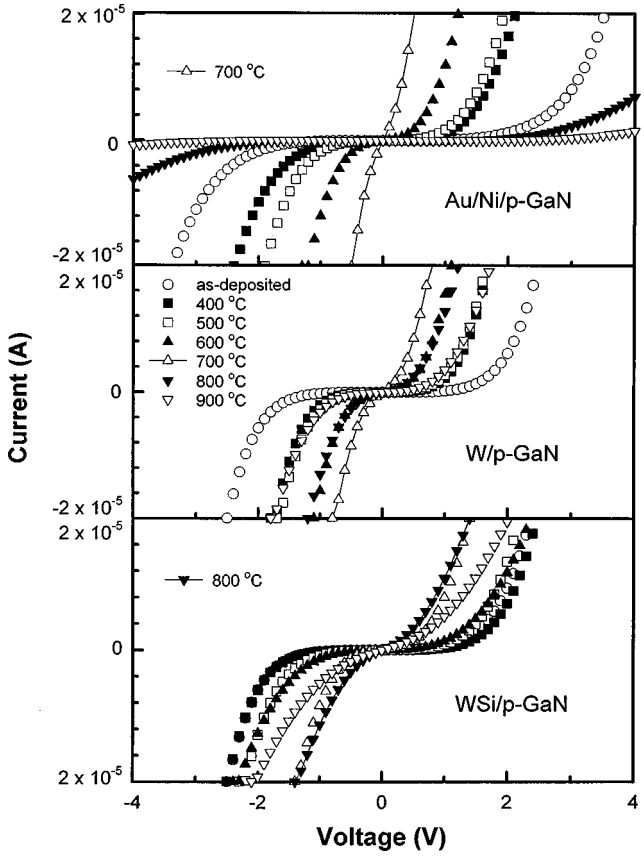

FIG. 7. Annealing temperature dependence of $I-V$ characteristics of WSi, W, and Ni/Au contacts on *p*-GaN (60 s anneal times).

As a comparison to *n*-type GaN, Fig. 11 shows the annealing temperature dependence of R_C for W contacts on Si-implanted (*n* type) GaN. The specific contact resistance improves with annealing up to ~950 °C, which appears to correspond to the region where the β-W_2N interfacial phase is formed. Cole *et al.*[49] reported that W and WSi contacts on GaN annealed in the range of 750–850 °C showed the minimum degree of metal protrusion in the interfacial regions containing the β-W_2N phase, whereas at lower annealing temperatures the horizontal spatial extent of this phase was smaller and allowed more protrusions to develop. Excellent structural stability of the W on GaN was shown in SEM micrographs, where a sharp interface was retained after 750 °C annealing.

In summary, one of the emerging applications for GaN is in ultrahigh power electronic switches, where thermal stability of the contact metallization will be of paramount importance. Tungsten-based contacts on both *n*- and *p*-type GaN offer superior thermal stability to the standard metallization used in photonic devices, TiAl and Ni/Au, respectively.

B. Rapid thermal processing

1. Surface protection

The usual environment for high-temperature annealing of III nitrides is NH_3,[79] but this is inconvenient for processes such as rapid thermal annealing for implant activation, contact annealing for implant isolation. In those situations we

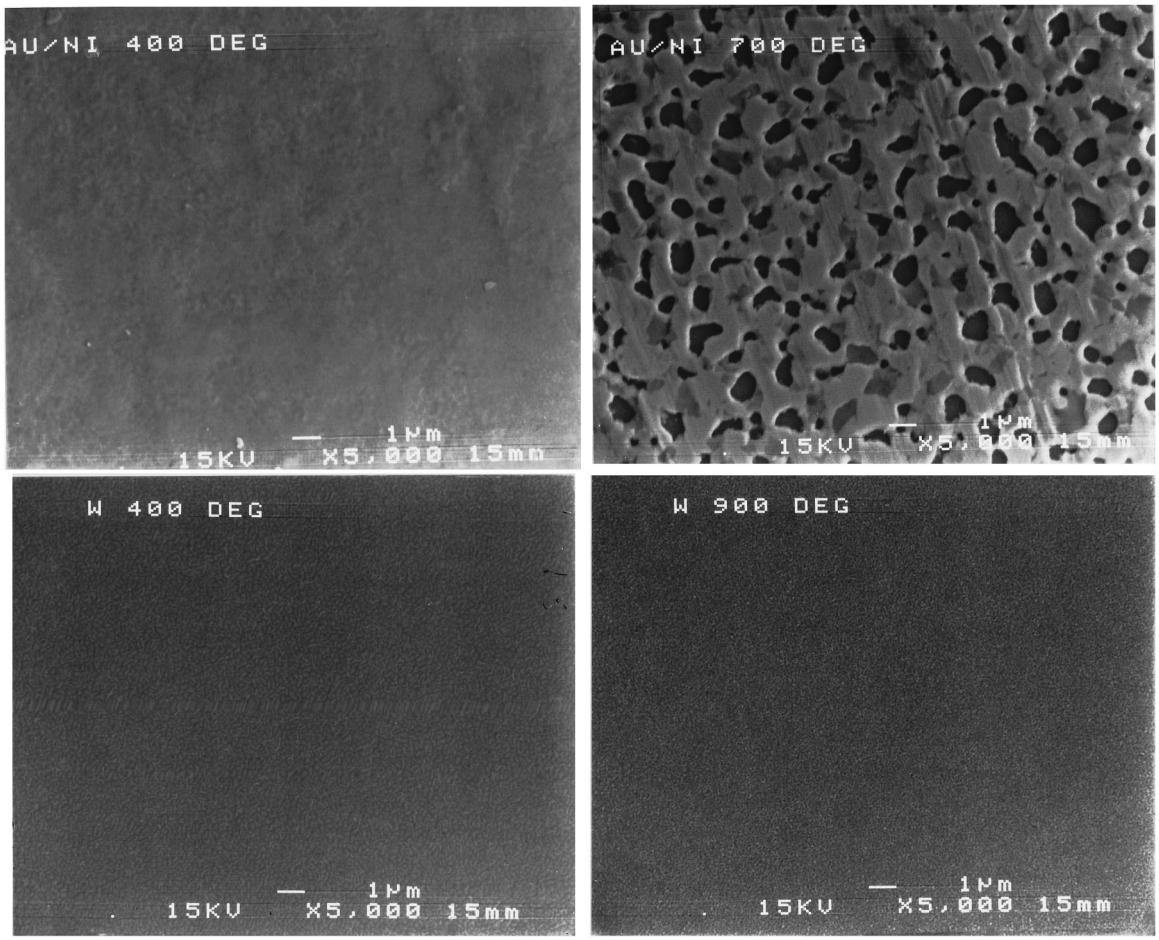

FIG. 8. SEM micrographs of Ni/Au contacts on *p*-GaN after 60 s anneals at either 400 (top left) or 700 °C (top right), or W contacts after similar annealing at 400 (bottom left) or 900 °C (bottom right).

would like to provide some form of N_2 overpressure to minimize loss of nitrogen from the semiconductor surface at high temperature.[96] With conventional III–V materials such as GaAs and InP this is achieved in several ways,[97–110] namely by two methods: (i) placing the sample of interest face down on a substrate of the same type,[101,107] so that the onset of preferential As or P loss quickly suppresses further loss. The disadvantages of this method include the fact that some group V atoms are lost from the near surface. There is always a possibility of mechanical abrasion of the face of the sample of interest, and contamination can easily be transferred from the dummy wafer to the one of interest. The second method involves: (ii) placing the wafer in a SiC-coated graphite susceptor,[109,110] which either has had its internal surfaces coated with As or P by heating a sacrificial wafer within it, or in which granulated or powdered GaAs or InP is placed in reservoirs connected to the region in which the wafer is contained. In both cases subsequent heating of the susceptor produces an As or P vapor pressure above the surface of the process wafer, suppressing loss of the group V element.

The former approach is widely used in III–V research and is known as the proximity geometry. The latter approach is widely used in industry for anneal processes for GaAs and to a lesser extent InP.

It would be convenient for GaN device processing if development of a similar process for rapid thermal processing of III nitrides occurred, in which an overpressure of N_2 is supplied to a susceptor. In this section we compare use of powdered AlN or InN as materials for use in the susceptor reservoirs, and compare the results with those obtained by simple proximity annealing.

The GaN, AlN, InN, InGaN, and InAlN samples were grown using metal organic molecular beam epitaxy on semi-insulating, (100) GaAs substrates or Al_2O_3 *c*-plane substrates in an Intevac Gen II system as described previously.[76,77] The group-III sources were triethylgallium, trimethylamine alane, and trimethylindium, respectively, and the atomic nitrogen was derived from an electron cyclotron resonance Wavemat source operating at 200 W forward power. The layers were single crystal with a high density ($10^{11}-10^{12}\,cm^{-2}$) of stacking faults and microtwins. The GaN and AlN were resistive as-grown, and the InN was highly autodoped *n* type ($>10^{20}\,cm^{-3}$) due to the presence of native defects. InAlN and InGaN were found to contain both hexagonal and cubic forms. The $In_{0.75}Al_{0.25}N$ and $In_{0.5}Ga_{0.5}N$ were conducting *n* type as grown ($\sim 10^{20}\,cm^{-3}$) due to residual autodoping by native defects.

The samples were annealed either (i) face down on samples of the same type, i.e., GaN when annealing GaN,

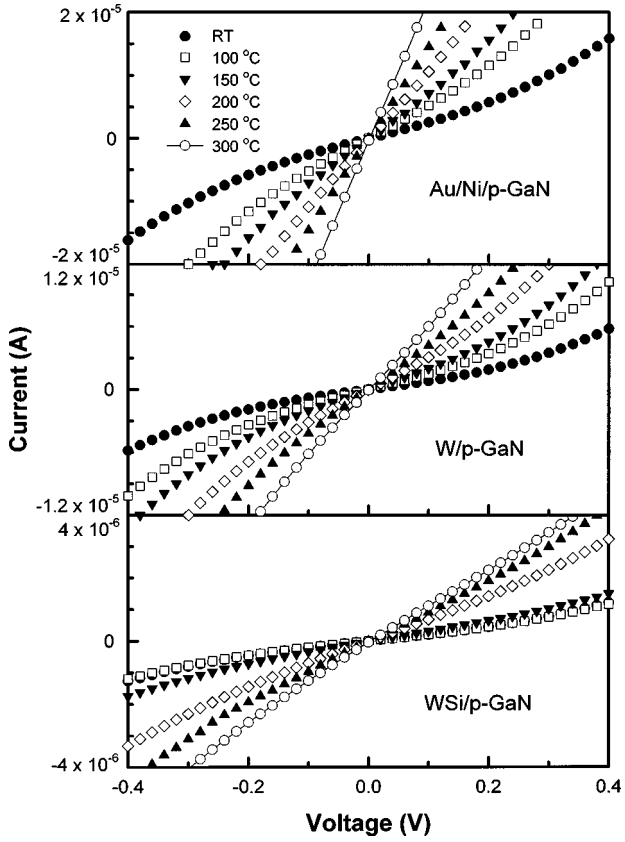

FIG. 9. Measurement temperature dependence of $I-V$ characteristics of Ni/Au, W, or WSi_x contacts on p-GaN.

InN for InN, etc., or (ii) within a SiC-coated graphite susceptor in which the reservoirs were filled with either powdered AlN or InN (average particle size ~10 μm).[111] Annealing was performed for 10 s at peak temperatures between 650 and 1100 °C in flowing N_2 gas. The sheet resistance was measured at room temperature on a van der Pauw Hall system with 1:1 InHg alloyed contacts (400 °C, 3 min) on the corners. An atomic force microscope (AFM), operated in tapping mode with Si tips, was used to measure the root-mean-square (rms) roughness of the samples. The surface morphology was examined with a scanning electron microscope (SEM). Energy dispersive x-ray spectroscopy (EDAX) was used to analyze the surface composition of some samples. Auger electron spectroscopy (AES) was used to investigate near-surface stoichiometry before and after anneal.

The rms surface roughness of binary nitrides measured by AFM after annealing face down in the proximity geometry is shown at the top of Fig. 12. The InN begins to degrade above 500 °C, while AlN roughness at 1000 °C at the surface is as smooth as the as-grown material. The GaN remains smooth across the entire annealing range investigated. Similar results are shown for the ternaries at the bottom of Fig. 12. The InAlN morphology degrades above 800 °C, and In droplets are visible on the surface by 900 °C. At 1000 °C, however, the In droplets also evaporate, leading to an apparently better morphology as measured by AFM. The InGaN had fairly similar behavior.

A comparison of the annealing temperature dependence of nitride rms surface roughness for sample processed in the graphite susceptor with either AlN or InN powder in the reservoirs is shown in Fig. 13. One would expect the InN powder to provide higher vapor pressure of N_2 at equivalent temperatures than AlN[112,113] and this appears to be evident in the rms data for InN, where the surface roughens dramati-

TABLE I. Temperature-dependent contact data for p-GaN.

Contact	Measurement temperature (°C)	Specific contact resistance (Ω cm^2)	Contact resistivity (Ω mm)
Ni/Au	200	0.125	415.7
Ni/Au	250	0.121	319.5
Ni/Au	300	0.092	205.9
W	300	0.682	758.4
WSi	300	0.026	1728.3

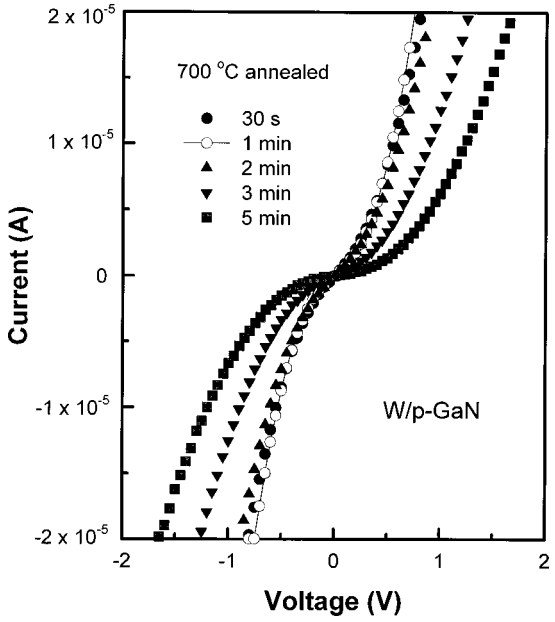

FIG. 10. Annealing time dependence at 700 °C of $I-V$ characteristics from W contacts on p-GaN.

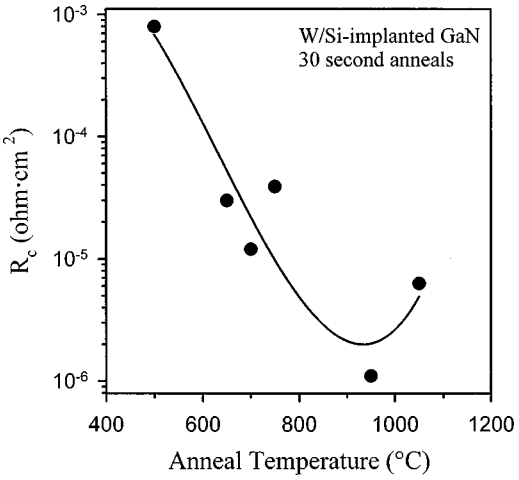

FIG. 11. Annealing temperature dependence of R_C for W contacts on Si-implanted GaN.

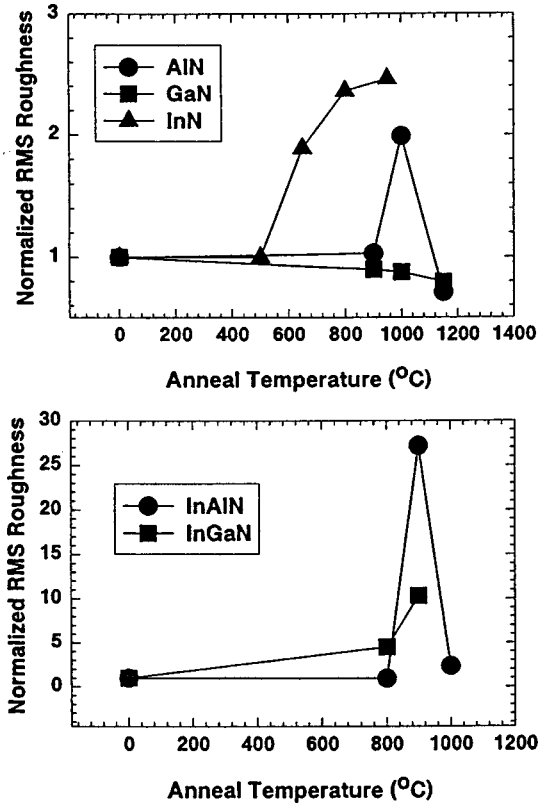

FIG. 12. Root-mean-square surface roughness normalized to the as-grown value, as a function of anneal temperature for AlN, GaN, and InN (top) and InAlN and InGaN (bottom) annealed in the proximity geometry.

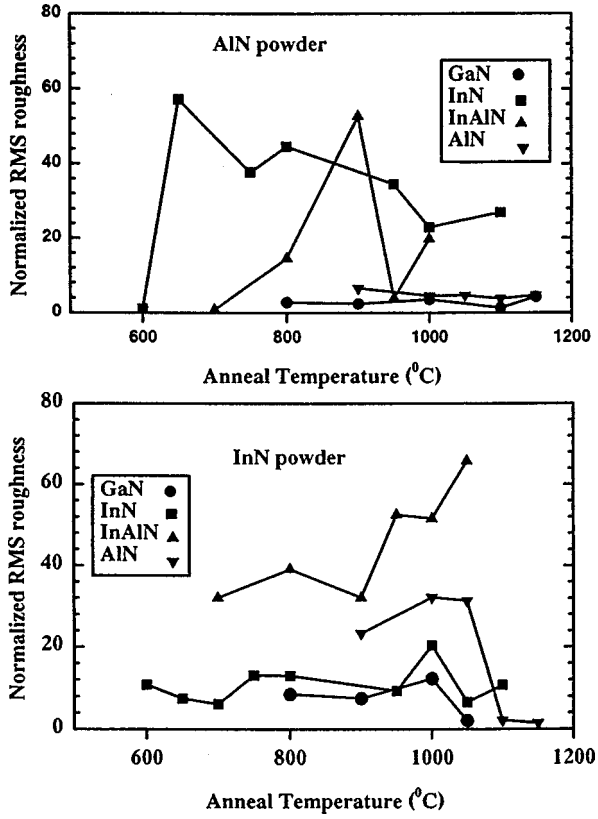

FIG. 13. Root-mean-square surface roughness of nitrides normalized to the as-grown value, as a function of anneal temperature using either AlN powder (top) or InN powder (bottom) in the susceptor reservoirs.

cally above 600 °C with AlN powder while the roughening is less obvious with InN powder. The data in Fig. 13 need to be considered in the light of the results from the other materials. For example, the GaN and AlN rms values are consistently higher for the InN powder annealing. These results clearly indicate large-scale ($\sim$1 μm) roughness evident on the samples annealed with the InN powder. Similar results were evident for the AlN and InAlN samples, with large-scale roughness detectable by AFM on the ones annealed with the InN powder.

SEM examination of all the samples revealed the cause of this roughening. After 1000 °C annealing with AlN powder there is no change in morphology from the control samples. By sharp contrast, metallic droplets are visible on samples annealed with InN powder even at 800 °C. Similar droplets were observed in all materials after annealing with InN powder at $\geqslant$750 °C. EDAX measurements identified these droplets as In in each case. Therefore, it is clear that the InN powder initially provides good surface protection for annealing temperatures $\geqslant$750 °C through incongruent evaporation of N_2. Above this temperature, however, evaporation of In from the powder leads to condensation of droplets on the samples contained within the reservoir. At temperatures approaching 1100 °C, these droplets evaporate from the surface of GaN or AlN, leading to an apparent surface smoothing when measured by AFM.

Some other features of the annealing are salient with respect to implant activation processes. First, if we employed 90%N_2:10%H_2 as the purge gas in the rapid thermal annealing (RTA) system instead of pure N_2, we noticed that the temperature at which surface dissociation was evident by either AFM or SEM was lowered by 100–200 °C for each of the nitrides. A similar effect was observed if O_2 was present in the annealing ambient, and thus, it is critical to avoid residual O_2 or H_2 in RTA systems during annealing of the nitrides. Second, under optimized ambient conditions (pure N_2 purge gas, and use of either the proximity geometry or powdered AlN in the susceptor reservoirs), AES was able to detect N_2 loss from the surface of GaN even after 1000 °C anneals, and from InAlN and InGaN after 800 °C anneals.[114] However, N_2 loss from AlN was detectable only after anneals at 1150 °C, emphasizing the extremely good thermal stability of this material. Indeed Zolper *et al.*[115] have recently reported use of sputtered AlN as an encapsulant for annealing GaN at temperatures up to 1100 °C for Si^+ or Mg^+ ion implant activation. The AlN could be selectively removed with KOH solutions after the annealing process.[116]

The loss of N_2 from binary nitride surfaces during annealing produced thin ($<$0.5 μm as determined by subsequent dry etching and remeasurement) highly conducting n^+ regions. These were evident for annealing temperatures above $\sim$600 °C in InN and at $\sim$1125 °C in GaN. For example, the sheet resistance increased by 2–4 orders of magnitude in both materials. This agrees with the theoretical prediction of Maruska and Tietjen[117] that N vacancies create a shallow donor state in binary nitrides, and the temperatures to which the materials are stable are in general agreement

with the published vapor pressure and melting point data for the binary nitrides.[112,114,118–120] In the ternary materials, however, the sheet resistance of the epitaxial layers increased with annealing temperature, suggesting that simple nitrogen vacancies are not the only cause of the residual *n*-type conductivity in these samples, since at the highest temperatures there is clear loss of nitrogen. The annealing, in this case, appears to create compensating acceptors, or else annealing of the native donors is occurring. The nature of the defects present in as-grown and annealed nitrides is currently under investigation with IR absorption and variable temperature Hall measurements.

In summary, several approaches to rapid thermal processing of binary and ternary nitrides have been investigated. In the proximity geometry AlN and GaN retain smooth stoichiometric surfaces to $\geqslant$1000 °C, InAlN and InGaN to 800 °C and InN up to 600 °C. Similar thermal stabilities were obtained for face-up annealing in graphite susceptors in which AlN powder provides a N_2 overpressure. An attempt to increase this overpressure through use of InN powder was unsuccessful because of In droplet condensation on all samples at temperatures $\geqslant$750 °C. This could only be rectified if one could design a two-zone rapid thermal processing chamber in which a reservoir of InN powder was maintained at $\geqslant$750 °C, while the samples to be annealed were separately heated to their required temperatures.

2. Ultrahigh temperature annealing

Recent interest in developing advanced electronic devices that operate at high temperature and/or high power has brought into focus many new challenges for semiconductor materials and the related processing technology. Compound semiconductors such as SiC and GaN have significant advantages for such device applications because of their wider band gaps (higher operating temperature), larger breakdown fields (higher operating voltage), higher electron saturated drift velocity (higher operating current and faster switching), and better thermal conductivity (higher power density).[119,120] Some of the examples of SiC- and GaN-based electronic devices are the SiC power MOSFET[121] and the GaN junction field effect transistor (JFET).[122] In the development of advanced electronic devices, the technology of rapid thermal processing (RTP) plays a critical role at numerous points such as implant activation of dopant species, implantation-induced damage removal, alloying of ohmic contacts, maximization of sheet resistance in implant isolation regions, etc. High annealing temperature and short processing time have been identified as two key requirements in RTP annealing of compound semiconductors such as GaN and SiC, especially for implant activation and damage removal.[123] It has been found in high dose Si-implanted GaN that, although Si donors can be efficiently activated at 1100 °C, complete removal of ion implantation-induced damage requires even higher annealing temperatures.[124] A more recent study has shown that implantation-induced damage in GaN can only be significantly reduced by using annealing temperatures up to 1400 °C.[125]

The existing commercial RTP equipment typically relies on a series of tungsten-halogen lamps as heat sources to rapidly heat up the semiconductor wafers.[126] However, this type of lamp-based RTP system suffers from many problems such as their point heat source nature, fluctuating lamp temperature during processing and only modest temperature capacity ($<$1100 °C). Recent interest in developing wide band gap compound semiconductors has pushed the processing temperature requirements to much higher values (up to 1500 °C). Presently, there are no specific RTP systems that can operate at such high temperatures. In the study of annealing of GaN up to 1400 °C,[127] a custom system (based on MOCVD system) that employed rf heating was built and utilized. There is an urgent need in GaN and SiC technology to develop new RTP systems which can provide uniform heating to very high temperatures ($>$1500 °C).

There has recently been development of a unique high temperature RTP unit called Zapper™. This novel RTP unit has been specifically designed to achieve very high temperatures ($>$1500 °C) with excellent uniformity for high temperature thermal processing of semiconductor materials. In this section, we first give a brief introduction about the Zapper™ unit. We then report the implant activation annealing studies of Si^+-implanted GaN thin films (with and without an AlN encapsulation layer) using the Zapper™ unit at temperatures up to 1500 °C. The electrical analysis and characterization results of such annealed samples are presented and discussed. Based on these experiments, the significant potential of the MHI Zapper™ unit in the development of advanced electronics is summarized.

Most existing RTP equipment utilized either an array of ten or more tungsten-halogen lamps, or a single arc lamp as heat sources.[125] These lamp-based RTP equipment can achieve only modest processing temperatures ($<$1100 °C), primarily because of the point-like nature of the sources and large thermal mass of the systems. To realize higher temperature capacity, new types of heat sources have to be employed. In the past few years, there has been development of novel molybdenum intermetallic composite heaters that may be used in air at temperatures up to 1900 °C.[127,128] These heaters have high emissivity (up to 0.9) and allow heat-up time of the order of seconds and heat fluxes up to 100 W/cm^2. This novel RTP unit is capable of achieving much higher temperatures than the lamp-based RTP equipment. Figure 14 shows some typical time-temperature fluctuation to rapidly heat up and cool down the wafer, the Zapper™ unit relies on wafer movement (in/out of furnace horizontally) to achieve rapid ramp-up and ramp-down rates similar to those of conventional RTP systems.

A variety of undoped GaN layers $\sim$3 μm thick were grown at $\sim$1050 °C by metal organic chemical vapor deposition using trimethylgallium and ammonia. Growth was preceded by deposition of thin ($\sim$200 Å) GaN or AlN buffers (growth temperature 530 °C) on the Al_2O_3 substrates. Capacitance–voltage measurements on the GaN showed typical *n*-type background carrier concentrations of $\leqslant 3\times10^{16}\,cm^{-3}$. Si^+ was implanted to a dose of $5\times10^{15}\,cm^{-2}$, 100 keV, producing a maximum Si concentration of $\sim 6\times10^{20}\,cm^{-3}$ at a depth of $\sim$800 Å. Some of the samples were encapsulated with 1000–1500 Å of AlN deposited in one of two ways. In the first, AlN was deposited

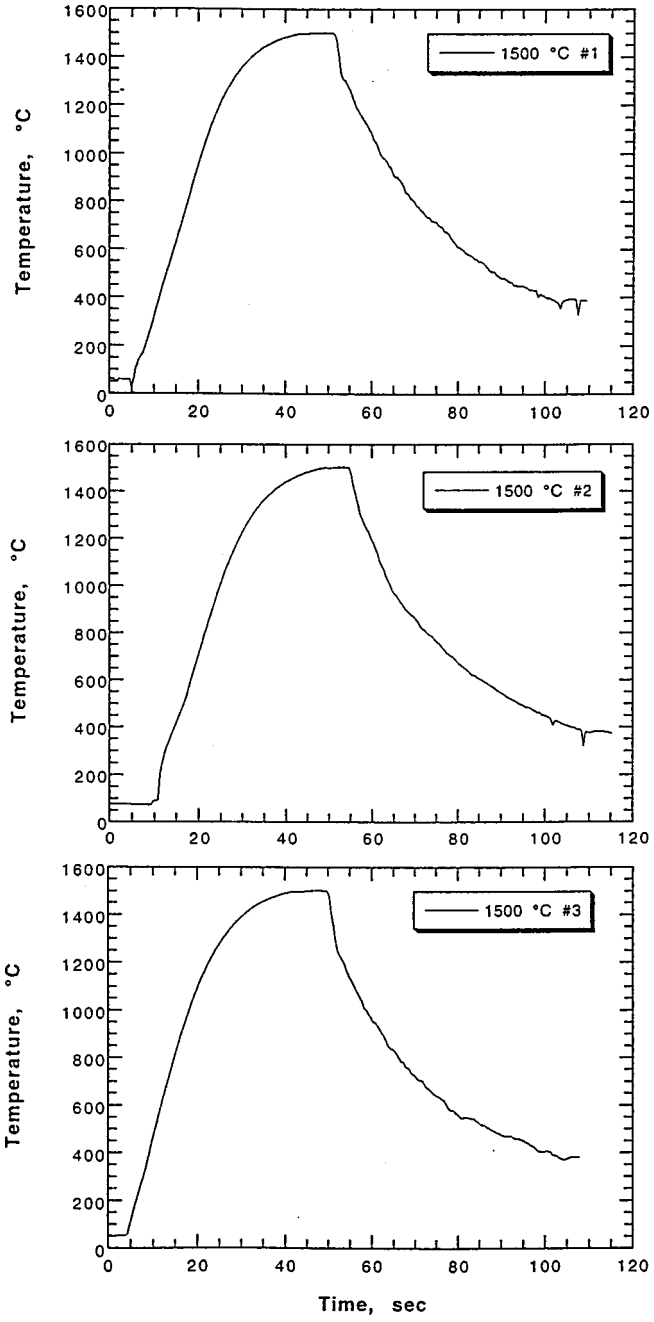

FIG. 14. Time-temperature profiles for RTP annealing of GaN at 1500 °C.

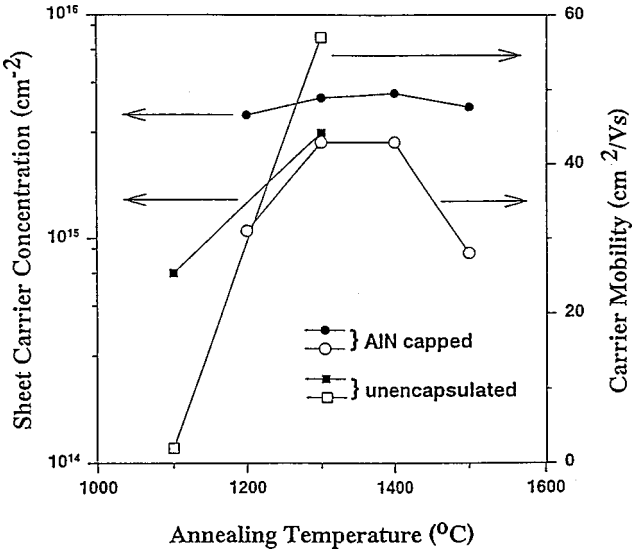

FIG. 15. Sheet carrier density and electron mobility in capped and uncapped Si-implanted GaN, as a function of annealing temperature.

by reactive sputtering of pure AlN targets in 300 mTorr of 20% N_2Ar. The deposition temperature was 400 °C. In the second method, AlN was grown by metal organic molecular beam epitaxy (MOMBE) at 750 °C using dimethylamine alane and plasma dissociated nitrogen.[77]

The samples were sealed in quartz ampoules under N_2 gas. To ensure good purity of this ambient the quartz tube (with sample inside and one end predoped) was subjected to an evacuation/N_2 purge cycle for three repetitions before the other end of the tube was closed, producing a final N_2 pressure of ~15 psi. This negative pressure was necessary to prevent blowout of the ampoule at elevated annealing temperatures. The samples were then annealed at 1100–1500 °C, for a dwell time of ~ 10 s (Fig. 14). The time difference for reaching the annealing temperature was between 4 and 6 s. To compensate for this heating time lag inside the ampoule, the dwell time was purposely extended to ~ 15 s. Ramp rates were 80 °C s^{-1} from 25–1000 °C and 30 °C s^{-1} from 1000–1500 °C, producing an average ramp-up rate over the entire cycle of ~50 °C s^{-1}. The typical ramp-down rate was ~25 °C s^{-1}. Thermocouple measurements of temperature uniformity over a typical wafer size (4 in. diameter) were ±8 °C at both 1400 and 1500 °C. After removal of the samples from the ampoules they were examined by scanning electron microscopy (SEM), atomic force microscopy (AFM), and van der Pauw geometry Hall measurements obtained with alloyed HgIn eutectic contacts.

SEM micrographs of unencapsulated GaN surfaces annealed at 1200, 1300, 1400, or 1500 °C showed that the 1200 °C annealing does not degrade the surface, and the samples retain the same appearance as the as-grown material. After 1300 °C annealing, there is a high density (~10^8 cm^{-2}) of small hexagonal pits which we believe is due to incongruent evaporation from the surface. The 1400 °C annealing produces complete dissociation of the GaN, and only the underlying AlN buffer survives. Annealing at 1500 °C also causes loss of this buffer layer, and a smooth exposed Al_2O_3 surface is evident.

By sharp contrast to the results for GaN, both the sputtered and MOMBE AlN were found to survive annealing above 1300 °C.[129] For the sputtered material we often observed localized failure of the film, perhaps due to residual gas agglomeration. For the MOMBE films this phenomenon was absent. Also in the sputtered material the root-mean-square (rms) surface roughness tended to go through a maximum, due to some initial localized bubbling, followed by the film densification.

The clear result from all this data is that the implanted GaN needs to be encapsulated with AlN in order to preserve the surface quality. We have previously shown that AlN is selectively removable from GaN using KOH-based solution.[115,130] Figure 15 shows the sheet carrier concentra-

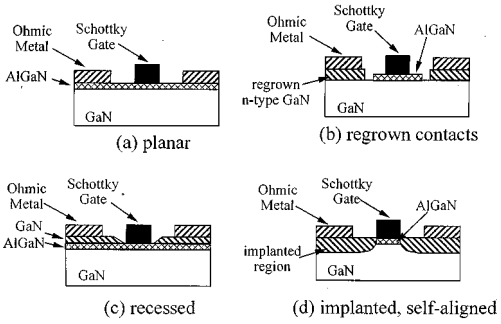

FIG. 16. Comparison of GaN-based HFET structures: (a) planar, (b) recessed gate, (c) regrown n^+ ohmic regions, and (d) self-aligned, implanted. Implantation is the most practical means to achieve the selective area doping required to reduce the transistor access resistance.

tion and electron mobility in the Si^+-implanted GaN, for both unencapsulated and AlN-encapsulated material, as a function of annealing temperature. For unencapsulated annealing we see an initial increase in electron concentration, but above 1300 °C the GaN layer disintegrates. By contrast, for AlN-encapsulated samples the Si^+ implant activation percentage is higher (~90%) and peaks around 1400 °C. This corresponds to a peak carrier concentration of $\geqslant 5 \times 10^{20}\,cm^{-3}$. For 1500 °C annealing both carrier concentration and mobility decrease, and this is consistent with Si-site switching as observed in Si^+-implanted GaAs at much lower temperatures.[129] The results in Fig. 15 are compelling evidence of the need for high annealing temperatures and the concurrent requirement for effective surface protection of the GaN.

There is clear evidence from both ion channeling and TEM measurements that temperatures above 1300 °C are required to completely remove implantation damage in GaN. Since the residual damage tends to produce *n*-type conductivity, it is even more imperative in acceptor-implanted material to completely remove its influence. However a premium is placed on prevention of surface dissociation, because loss of nitrogen also leads to residual *n*-type conductivity in GaN. The combination of RTP annealing in the Zapper™ unit at 1400–1500 °C and high quality AlN encapsulants produce metallic doping levels ($\sim 5 \times 10^{20}\,cm^{-3}$) in Si^+-implanted GaN.

3. Implanted dopant activation

a. Background. The best example of how ion implantation can directly impact the performance of group III-nitride transistors is illustrated in Fig. 16. The figure shows four device structures that could be employed to fabricate AlGaN/GaN high electron mobility transistors (HEMTs). To date, the majority of the AlGaN/GaN HEMTs transistors have been fabricated in a planar structure as shown in Fig. 16(a), where the ohmic source and drain contacts are placed directly on the wide band gap AlGaN layer without any increased local doping to reduce the contact or access resistance.[131] This leads to a high access resistance, reduced current capability, and a high transistor knee voltage. This in turn reduces the transistors power gain, power added efficiency, and linearity.[132] Figures 16(b) and 16(c) show two approaches that have been taken to reduce the access resistance. One is to selectively etch away the wide band gap material in the contact regions and then regrow highly doped GaN to improved access resistance; however, the manufacturability of this approach as, with any regrowth process, is questionable.[133] The recess gate approach of Fig. 16(c) has been widely used in other mature compound semiconductors such as GaAs and InP. Although this type of structure has been demonstrated in GaN-based devices, the unavailability of controlled wet etching of GaN requires the use of a plasma recess etch.[134] Use of a plasma etch introduces surface damage in the semiconductor in the region under Schottky gate that degrades the rectifying properties of the gate. Finally, the self-aligned ion implanted structure of Fig. 16(d) is used to create selective areas of highly doped regions for the source and drain contacts in a highly manufacturable fashion without any plasma etching of the gate region. To date, ion implantation has been used to realize a GaN junction field effect transistor (JFET) but has not been applied to AlGaN/GaN HEMTs.[135] As will be discussed later, one of the key challenges to applying ion implantation to AlGaN/GaN HEMTs is the avoidance of surface degradation that will negatively impact the Schottky gate formation during the high temperature implant activation anneal.

The first work on implantation in GaN was performed by Pankove and co-workers in the earlier 1970s.[136,137] They reported primarily on the photoluminescence properties of a large array of implanted impurities in GaN. The work was successful in identifying Mg as the shallowest acceptor found to date for GaN.

In 1995 Pearton *et al.*, reported the first successful use of ion implantation to realize electrically active *n*- and *p*-type dopants in GaN.[138] In that work, Si was used as the *n*-type dopant and Mg, with a coimplantation of P, was used to achieve *p*-type doping. Rapid thermal annealing (RTA) at 1100 °C was employed for the activation anneal. Subsequently, implanted O was shown to also be a donor and implanted Ca an acceptor in GaN.[139] While Mg demonstrated some degree of diffusion during these annealing conditions, all other impurities (Be, C, Zn, Ca, Si, and O) showed no measurable diffusion.[140]

Details of ion implanted isolation using either H, He, or N have also been established. The damage created by H implantation was shown to anneal out near 400 °C while He and N isolation damage remained intact to ~800 °C.[141] From this work followed the fabrication and performance of the first ion implanted JFET fabricated in GaN.[134]

To fully apply ion implantation technology to GaN-based electronics, both Schottky and ohmic contacts must be readily fabricated on the semiconductor following the implantation and activation process. For example, for an all ion implanted GaN metal-semiconductor field effect transistor (MESFET) to be achieved, a Schottky gate contact must be formed on the implanted channel regions after the activation anneal. When performing the implant activation anneal, the GaN surface can dissociate by the loss of N. Some of the work on the equilibrium pressure of N over GaN has been

reviewed by Ambacher *et al.*[142] and Porowski and Grzegory.[112]

b. Annealing. Since the activation anneal for GaN was initially done in the range of 1100 °C,[138,139] the formation of a Pt/Au Schottky contact on *n*-type GaN was studied after such a high temperature anneal with and without a AlN encapsulation layer.[114] Since AlN has a higher dissociation temperature it should act to suppress the dissociation of the GaN. One set of samples was *n*-type as-grown with a background donor concentration of $\sim 5-10\times 10^{16}\,\mathrm{cm}^{-3}$ (samples A1, A2). The second set of samples (B1, B2) was semi-insulating as-grown and was implanted with ^{28}Si (100 keV, $5\times 10^{13}\,\mathrm{cm}^{-2}$) to simulate a MESFET channel implant ($n \sim 3\times 10^{17}\,\mathrm{cm}^{-3}$). One sample from each set had 120 nm of AlN deposited in an Ar plasma at 300 W using an Al target and a 10 sccm flow of N_2. The film had an index of refraction of 2.1 ± 0.05 corresponding to stoichiometric AlN. All samples were annealed together in a SiC coated graphite crucible at 1100 °C for 15 s in flowing N_2. Following annealing, the AlN was removed in a selective KOH-based etch (AZ400K developer) at 60–70 °C.[115] This etch has been shown to etch AlN at rates of 60–10 000 Å/min, depending on the film quality, while under the same conditions no measurable etching of GaN was observed.[130] Ti/Al ohmic contacts were deposited and defined by conventional lift-off techniques on all samples and annealed at 500 °C for 15 s. Pt/Au Schottky contacts were deposited and defined by lift-off within a circular opening in the ohmic metal. Electrical characterization was performed on a HP4145 at room temperature on 48 μm diameter diodes. Samples prepared in the same way, except without any metallization, were analyzed with Auger electron spectrometry (AES) surface and depth profiles. The surface morphology was also characterized by atomic force microscopy (AFM) before and after annealing.

Figure 17 shows three dimensional AFM images of the surface of samples A1 (uncapped) and A2 (AlN cap) after annealing at 1100 °C. While both of the annealed samples displayed some increase in their root-mean-square (rms) surface roughness (A1:4.02 nm, A2: 2.51 nm) over the as-grown sample (1.4 nm) the sample annealed without the AlN cap (A1) was markedly rougher with a dramatically different surface morphology. These differences were attributed to more N loss in the uncapped sample as will be discussed later.

Figure 18 shows the reverse current–voltage characteristics of the Pt/Au Schottky diodes for the four samples studied. Samples A1 and B1, annealed without the AlN cap, demonstrated very leaky reverse characteristics with roughly a 3 to 4 order-of-magnitude increase in leakage current over the samples annealed with the AlN cap. In fact, sample A1 approached ohmic behavior. Samples A2 and B2, on the other hand, demonstrated very good rectification with reverse breakdown voltages in excess of 40 V where the breakdown voltage is taken at 1 μA/μm of diode perimeter current. Figure 19 shows the current–voltage characteristics for adjacent Ti/Al ohmic contacts for the two unintentionally doped samples A1 and A2. In this case, the samples annealed without the AlN cap demonstrated improved ohmic behavior as compared to the samples annealed with the AlN cap. This

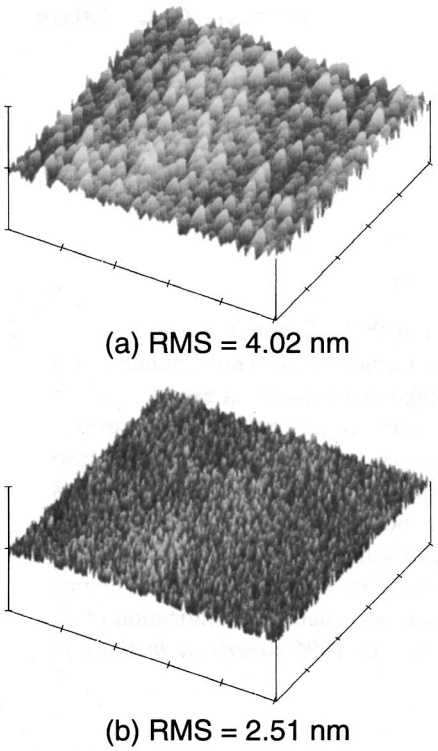

FIG. 17. Atomic force microscope images of GaN after an 1100 °C, 15 s anneal either (a) uncapped or (b) capped with reactively sputtered AlN. The AlN film was removed in a selective KOH-based etch (AZ400K developer) at 60–70 °C. On both images, the vertical scale is 50 nm per division and the horizontal scale is 2 μm per division.

is consistent with the Schottky characteristics and suggests a change in the near surface stoichiometry of the GaN resulting from the uncapped anneal as will be discussed below.

In an attempt to quantify the change in the GaN surface resulting from annealing with and without the AlN cap, AES surface and depth profiles were performed. When comparing the Ga/N ratio for each case an increase was seen for the sample annealed without the AlN cap (Ga/N ration = 2.34) as compared to the as-grown sample (Ga/N ratio = 1.73). This was explained by N loss from the GaN during the annealing process.[143] The AlN cap prevented this loss. AES depth profiles of the uncapped and annealed sample suggests that the N loss occurred in the very near surface region (~50 Å).

N loss and the formation of N vacancies was proposed as the key mechanism involved in changing the electrical properties of the Schottky diodes and ohmic contacts. Since N vacancies are thought to contribute to the background *n*-type conductivity in GaN, an excess of N vacancies at the surface should result in an n^+ region (possibly a degenerate region) at the surface.[116] This region would then contribute to tunneling under reverse bias for the Schottky diodes and explain the increase in the reverse leakage in the uncapped samples. Similarly, a n^+ region at the surface would improve the ohmic contact behavior as seen for the uncapped samples.[144] The effectiveness of the AlN cap during the anneal to suppress N loss is readily understood by the inert nature of AlN and its extreme thermal stability thereby acting as an effective diffusion barrier for N from the GaN substrate.

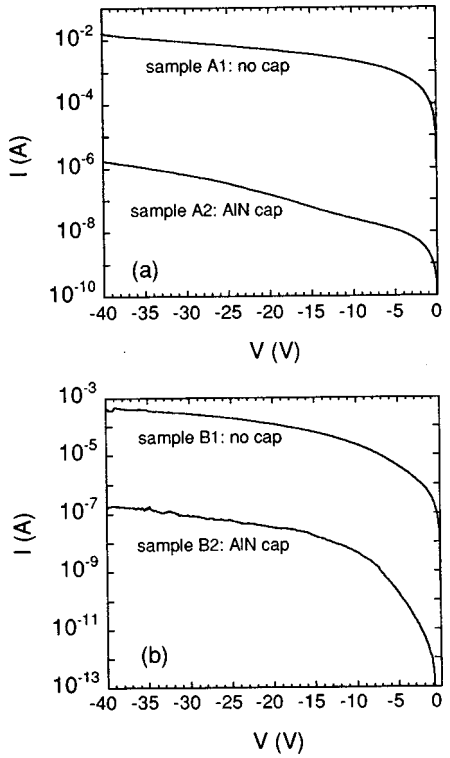

FIG. 18. Reverse current–voltage characteristics for Pt/Au Schottky contacts on GaN annealed at 1100 °C, 15 s either uncapped (samples A1, B1) or capped with AlN (samples A2, B2). (a) is for unintentionally doped GaN with an as-grown donor concentration of $5-10\times10^{16}\,\mathrm{cm}^{-3}$ and (b) is for initially semi-insulating GaN implanted with ^{28}Si (100 keV, $5\times10^{13}\,\mathrm{cm}^{-2}$) to simulate a MESFET channel implant.

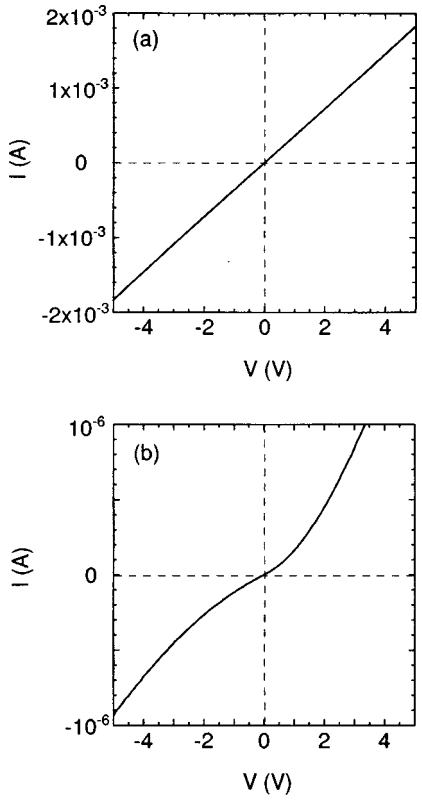

FIG. 19. Current–voltage characteristics for Ti/Al ohmic contacts on GaN after an 1100 °C, 15 s anneal either (a) uncapped or (b) capped with reactively sputtered AlN. The as-grown GaN was *n* type with a background concentration of $5-10\times10^{16}\,\mathrm{cm}^{-3}$. Note the change in scale for the current axis between the two plots.

In summary, the viability of using reactively sputtered AlN films as an encapsulating layer for GaN during 1100 °C annealing was demonstrated. The AlN cap was selectively removed in a KOH-based etch. By employing an AlN cap, Pt/Au Schottky barriers with reverse breakdown voltages in excess of 40 V were realized on samples annealed at 1100 °C. Samples annealed uncapped under the same conditions have 3 to 4 orders-of-magnitude higher reverse leakage than the capped samples while also displaying improved ohmic contact performance. These results are explained by the formation of a n^+ layer at the surface created by N-loss and N-vacancy formation in the uncapped samples. The AlN encapsulation, on the other hand, effectively suppressed N loss from the GaN substrate. The use of AlN capping should allow the realization of all ion implanted GaN MESFETs.

c. Damage accumulation. Previous work on damage accumulation during implantation had been limited to Si-implanted GaN at 77 K or room temperature.[145,146] That work demonstrated that the amorphization dose for ~100 keV Si implantation was $\sim2\times10^{16}\,\mathrm{cm}^{-2}$. Recent work has addressed the damage accumulating during Ca, Ar, and In implants in GaN at 77 K (Ca and Ar) and room temperature (In).[147,148] Additional work has also been reported from the damage annealing characteristics for high dose Si implantation.[149] Figure 20 shows the change in the Rutherford backscattering (RBS) minimum channeling yield (χ_{mm}) versus dose for Ca and Ar implanted GaN at 77 K.[147] The amorphization dose ($\chi_{mm}=100\%$) is $6\times10^{15}\,\mathrm{cm}^{-2}$ for both elements. As expected, this dose is lower than that reported for Si-implanted GaN of $2\times10^{16}\,\mathrm{cm}^{-2}$ due to the higher mass of Ca and Ar as compared to Si.[147] In the same study, it was determined that for a Ca dose as low as $3\times10^{14}\,\mathrm{cm}^{-2}$ an amorphous component to the x-ray diffraction spectra is created (see Fig. 21). This suggests that local pockets of amorphous material (peak A) are formed prior to the complete amorphization of the implanted region. Further study of the removal of such an amorphous material during

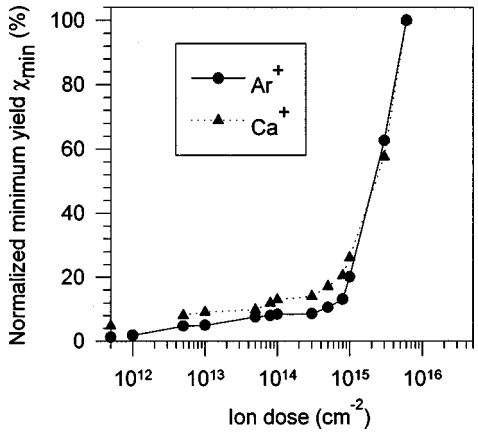

FIG. 20. Change in the RBS minimum channeling yield ($\chi_{\min}$) vs implant dose for 180 keV Ca and Ar implanted GaN at 77 K.

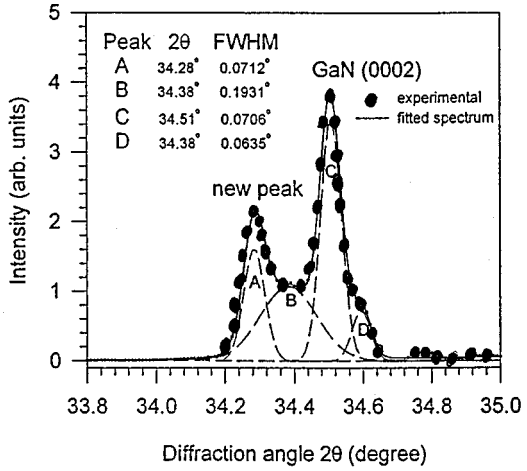

FIG. 21. X-ray diffraction spectrum and its fitting results for GaN implanted with Ca (180 keV, $3\times10^{14}\,\mathrm{cm}^{-2}$). The inset table shows the fitting results: the position (2θ) and the FWHM of each peak. Peak A, expanded GaN (0002); peak B, amorphous component; peak C, undamaged GaN (0002) after implantation; and peak D the cubic GaN (111) peak.

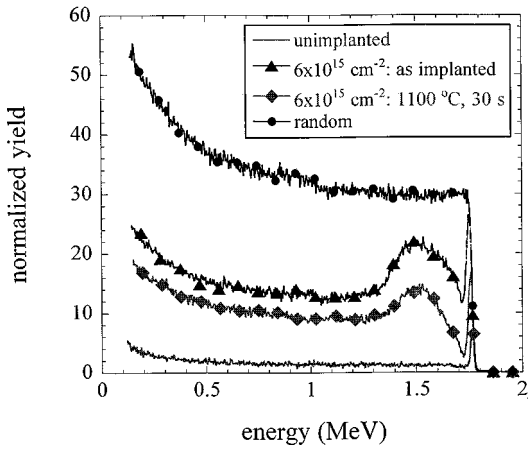

FIG. 22. Channeling Rutherford backscattering (C-RBS) spectra for as-grown (random and aligned, unimplanted) and Si-implanted (90 keV, $6\times10^{15}\,\mathrm{cm}^{-2}$) GaN (as-implanted and after a 1100 °C, 30 s anneal). The implants were performed at room temperature.

annealing will be important to optimizing the annealing process.

The In-implantation study examined the local lattice environment after implantation and subsequent annealing using the emission channeling technique and perturbed-$\gamma\gamma$-angular correlation.[148] Ronning and co-workers[148] found that the majority of the In atoms were substitutional as-implanted but within a heavily defective lattice. A gradual recovery of the damage was seen between 600 and 900 °C with about 50% of the In atoms occupying substitutional lattice sites with defect free surroundings after to 900 °C anneal. Results for higher temperature annealing were not reported. It remains to be determined at what point complete lattice recovery is achieved as determined by this technique.

Additional work on Si implantation had demonstrated significant implantation-induced damage remains in GaN even after a 1100 °C activation anneal that produces electrically active donors.[149,150] This is shown in the RBS spectra of Fig. 22 and the cross sectional transmission electron microscopy (XTEM) images of Fig. 23. The RBS spectra shows that even after a 1100 °C anneal the high channeling yield is evidence of significant damage in the crystal. This is confirmed by the XTEM images before and after annealing of Fig. 23 where, despite some coarsening of the damage, no significant reduction in the damage concentration has occurred. In the following section, work on complete removal of the implantation damage by annealing up to 1500 °C is presented.

As discussed in the previous section, an annealing temperature well above 1100 °C is needed to remove the implantation-induced damage in GaN. However, since GaN will readily dissociate at these temperatures, special precautions must be taken. The approaches used to maintain the GaN stoichiometry at up to 1500 °C were either to use an encapsulating overlayer such as the AlN described above or to perform the anneal under a high N overpressure. Results from both approaches are presented below. Both electrical and structural data are presented to correlate the effect of the removal of implantation-induced damage to electrical activation of implanted Si donors.

To better understand the removal of implantation-induced damage, annealing experiments were performed in an MOCVD growth reactor capable for reaching 1400 °C. While the anneal was performed in flowing ammonia to help stabilize the surface against decomposition, AlN encapsula-

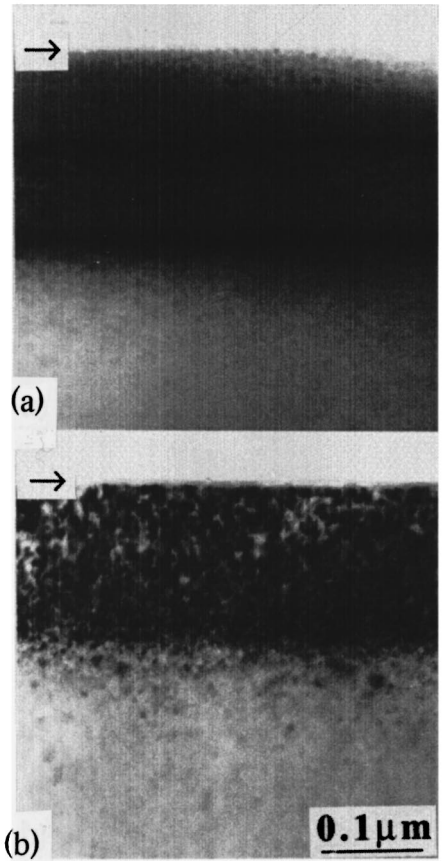

FIG. 23. Cross-sectional transmission electron micrograph (XTEM) of Si-implanted GaN (90 keV, $6\times10^{15}\,\mathrm{cm}^{-2}$): (a) as-implanted and (b) after a 1100 °C, 30 s anneal. The implants were performed at room temperature.

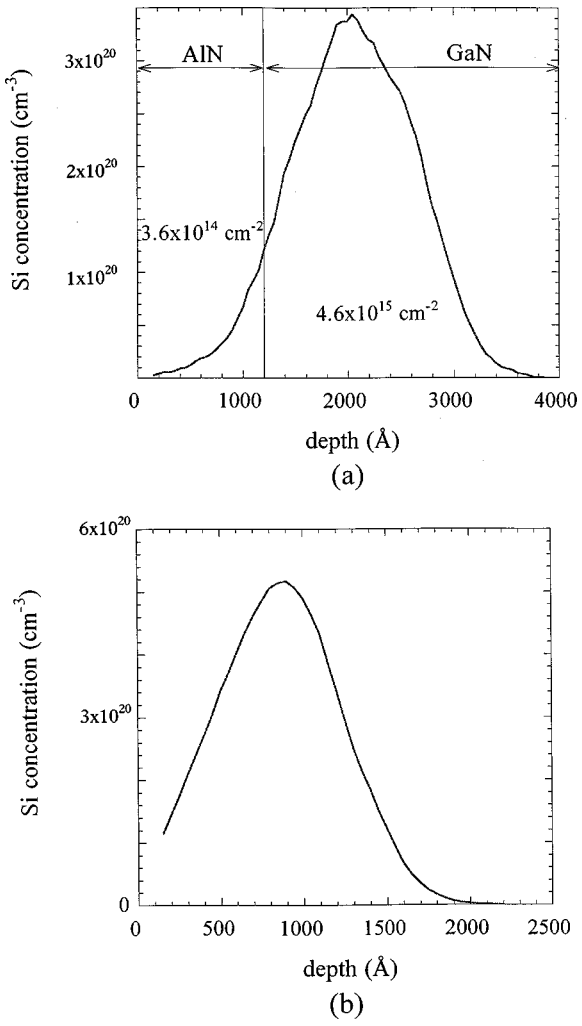

FIG. 24. Calculated Si-implantation profiles using TRIM92 code (a) 210 keV, $5\times10^{15}\,cm^{-2}$ Si in AlN/GaN and (b) 100 keV, $5\times10^{15}\,cm^{-2}$ Si in GaN.

tion was also studied to further suppress N loss.[149,151] The first set of samples was encapsulated with 120 nm of sputter deposited AlN. Si implantation was performed through the AlN at an energy of 210 keV and a dose of $5\times10^{15}\,cm^{-2}$. The results of Monte Carlo TRIM calculations, shown in Fig. 24(a), predict that ~7% of the Si ions come to rest in the AlN film with a dose of $4.6\times10^{15}\,cm^{-2}$ being placed in the GaN.[152,153] The Si peak range from the GaN surface is estimated to be approximately 80 nm. The second set of samples was unencapsulated and implanted with Si at an energy of 100 keV and dose of $5\times10^{15}\,cm^{-2}$. This also gives a range from the GaN surface of 80 nm as shown in Fig. 24(b). A sample from each set was annealed under one of four conditions as shown in Table II. One pair of samples was annealed in a rapid thermal annealer (RTA) inside a SiC coated graphite susceptor and processed in flowing N_2 since this procedure was used previously to activate implanted Si in GaN.[140] The remaining samples were annealed in a custom built metal organic chemical vapor deposition (MOCVD) system that employed rf heating with the samples placed on a molybdenum holder on a SiC coated graphite susceptor. The stated temperatures were measured with a Accufiber Model-10 or a Minolta Cyclota-52 pyrometer which were

TABLE II. Summary of annealing conditions.

Samples	Anneal temperature (°C)/time(s)	Reactor	Ambient
4, 8	1100/15	RTA	N_2
3, 7	1100/30	MOCVD	N_2/NH_3
2, 6	1300/30	MOCVD	N_2/NH_3
1, 5	1400/30	MOCVD	N_2/NH_3

calibrated by the melting point of Ge at 934 °C. The pressure in the MOCVD reactor was 630 mTorr with gas flows of 4 slm of N_2 and 3 slm of NH_3. The encapsulated and unencapsulated sample for a given temperature were annealed together.

Figures 25(a) and 25(b) shows the sheet electron concentration and electron Hall mobility versus the annealing con-

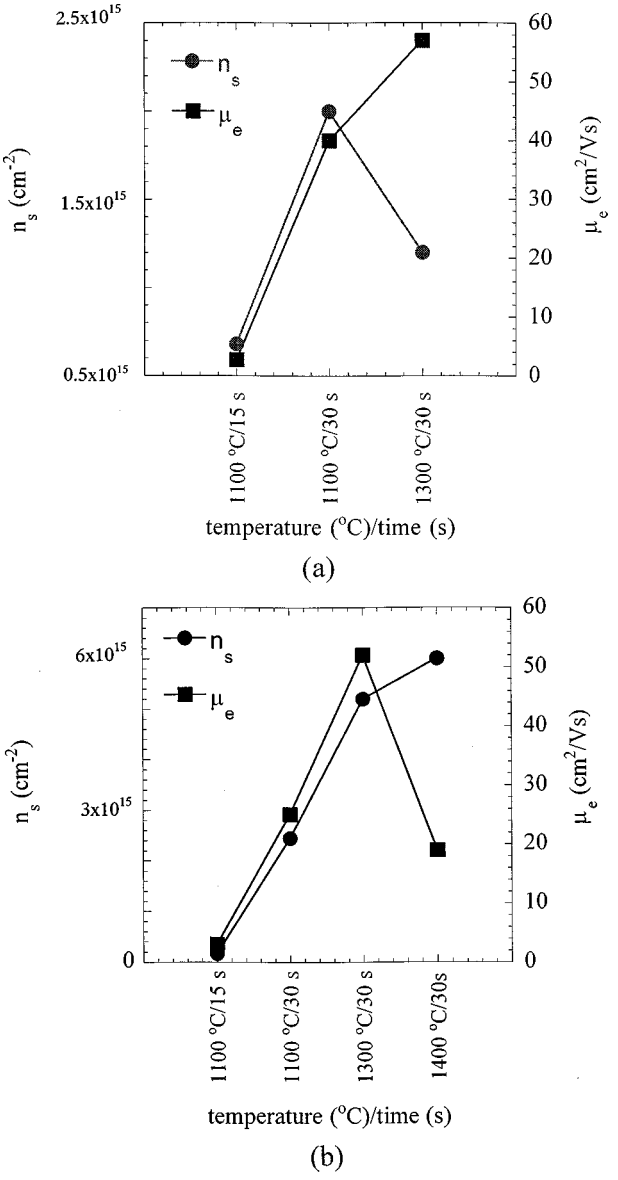

FIG. 25. Sheet electron concentration and electron Hall mobility vs annealing treatment for (a) unencapsulated and (b) AlN encapsulated Si-implanted GaN.

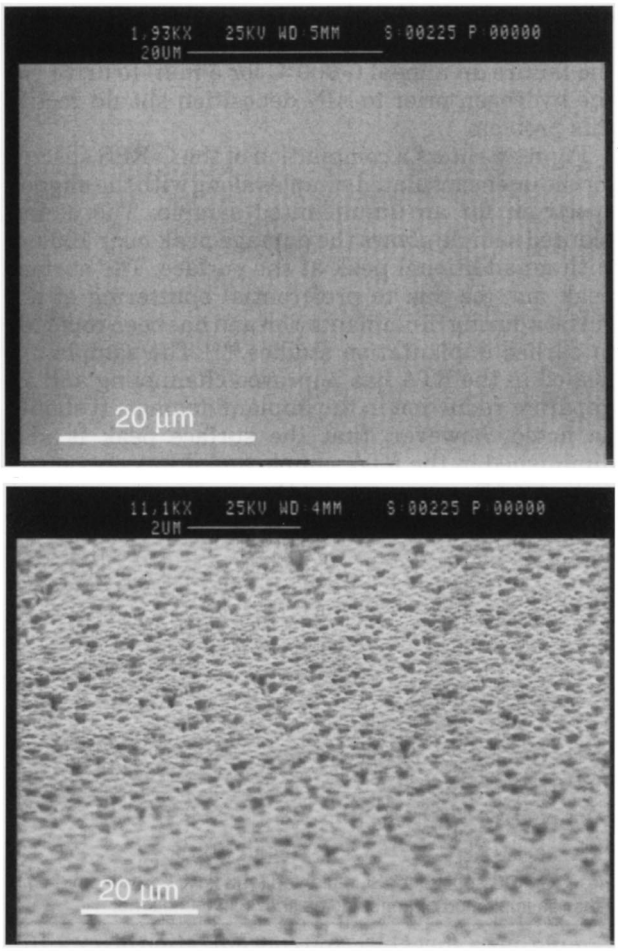

FIG. 26. SEM micrograph of (top) 1100 and (bottom) 1300 °C annealed unencapsulated sample showing degradation of the surface after the 1300 °C anneal.

ditions for the unencapsulated and AlN encapsulated samples, respectively.[151] An unimplanted sample annealed at 1100 °C for 15 s in the RTA remained highly resistive with $n \ll 1\times10^{15}\,\mathrm{cm}^{-2}$ after annealing. The mobility of this undoped film could not be reliably measured with the Hall effect due to the low carrier concentration.

First looking at the data for the unencapsulated samples [Fig. 25(a)], the sample annealed at 1100 °C for 15 s in the RTA has a sheet electron concentration of $6.8\times10^{14}\,\mathrm{cm}^{-2}$ or 13.6% of the implanted dose. This activation percentage is in the range reported for earlier Si-implanted GaN samples annealed in this way.[138,148] After the 1100 °C, 30 s MOCVD anneal the number of free electrons goes up to 40% of the implanted dose before decreasing to 24% for the 1300 °C anneal. The decrease for the 1300 °C sample was accompanied by a degradation of the surface of the sample as determined by observation under an electron microscope as shown in the SEM micrographs of Fig. 26. This point will be revisited when discussing the channeling Rutherford backscattering (C-RBS) spectra later, but it is believed that the GaN layer has started to decompose during this anneal. Therefore, the reduction in the electron concentration may be due to loss of material. The Hall mobility increased with increasing thermal treatment and is suggestive of improved crystalline quality. No data is given in Fig. 25(a) for the unencapsulated sample annealed at 1400 °C since the GaN film completely sublimed or evaporated during this anneal. This was confirmed by C-RBS data for this sample that showed only the substrate Al and O peaks with a slight Ga surface peak.

Now turning to the data for the AlN encapsulated samples [Fig. 25(b)]. There is increasing sheet electron density with increasing thermal treatments for the encapsulated samples including the highest temperature anneal. The RTA sample has a lower activity than the comparable unencapsulated sample (3.6% vs 13.6%), however, all the other AlN encapsulated samples have higher electron concentrations than the comparable unencapsulated sample. The 1300 °C sample has a sheet electron concentration of $5.2\times10^{15}\,\mathrm{cm}^{-2}$ that is 113% of the Si dose that should have been retained in the GaN layer ($4.6\times10^{15}\,\mathrm{cm}^{-2}$). The excess electron concentration may be due to small uncertainties in the Hall measurement due to the nonideal contact geometry (i.e., ideal point contacts were not used). The error in the Hall measurement is estimated to be ~10%. The apparent excess electron concentration may also be due to indiffusion of the Si from the AlN encapsulant into the GaN substrate or to the activation of other native donor defects in the GaN layer such as N vacancies. The sample annealed at 1400 °C has a still higher free electron concentration ($6\times10^{15}\,\mathrm{cm}^{-2}$) that may also be partly due to measurement errors or to activation of native defects. This sample had visible failures in the AlN layer (cracks and voids) that allowed some degree of decomposition of the GaN layer. This was confirmed by the scanning electron microscope (SEM) micrographs in Fig. 27 that show regions of GaN loss (confirmed by AES). Therefore, the formation of N vacancies in this sample is very likely and may contribute to the electron concentration. This would also contribute to the observed reduction in the electron mobility. The failure of the AlN film may be due to nonoptimum deposition conditions resulting in nonstoichiometric AlN or to evolution of hydrogen from the GaN epitaxial layer that ruptures the AlN during escape. If the failure is due to nonoptimum AlN properties, this can be rectified by examining the AlN deposition parameters. If hydrogen evolution is the cause of the failure an anneal (~900 °C for 5 min) to drive out the hydrogen prior to AlN deposition should rectify this problem.

Figure 28 shows a compilation of the C-RBS spectra for the unencapsulated samples along with the aligned spectrum for an unimplanted sample. The as-implanted sample shows the damage peak near 100 nm with an additional peak at the surface. The surface peak may be due to preferential sputtering of the surface during Si implantation and has been reported in earlier implantation studies.[146,154] The sample annealed in the RTA has improved channeling and an apparent reduction in the implant damage. It should be noted, however, that the surface peak is also diminished in the RTA sample and it has previously been reported that the change in the surface peak can account for the apparent reduction in the implantation damage peak.[154] Upon annealing at higher temperatures or longer times in the MOCVD reactor, the channeling continues to improve and approaches, but does not

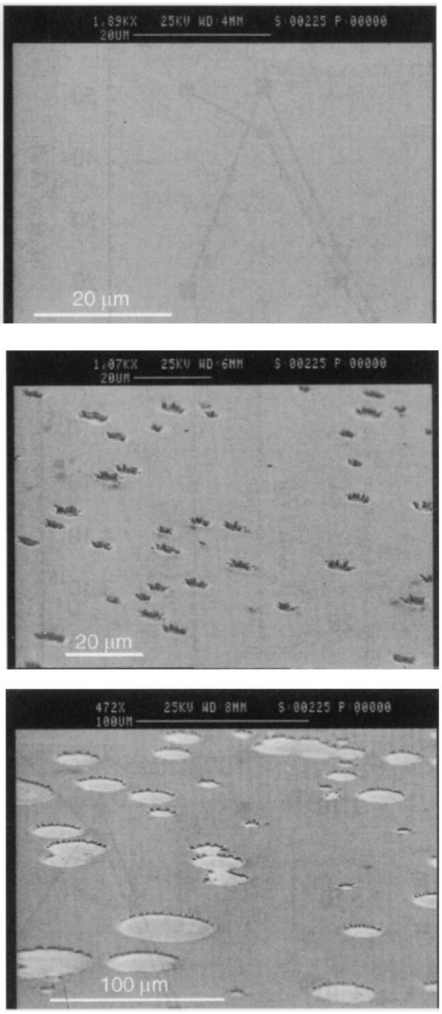

FIG. 27. SEM micrographs of Si-implanted and annealed (top) 1100, (bottom) 1300, and (bottom) 1400 °C AlN-encapsulated GaN. The anneals were performed in flow N_2/NH_3. Craters have started to form on the 1300 °C sample and enlarged on the 1400 °C sample in regions where the AlN encapsulant failed.

reach, the unimplanted aligned spectra. The 1300 °C sample, however, appeared to show evidence of material loss as demonstrated by the change in position and abruptness of the substrate signal as well as the observation of surface roughing. Therefore, the reduction in the implantation damage peak in this sample may be due to sublimation or evaporation of the implanted region and not recovery of the original crystal structure. The loss of at least part of the Si-implanted region is consistent with the reduction in the free electron concentration in this sample shown in Fig. 25(a).

Figure 29 shows a compilation of the C-RBS spectra for the AlN encapsulated sample. The as-implanted sample has a damage peak at ~80 nm with no additional surface peak as seen in the unencapsulated sample. The lack of surface peak in this samples supports the hypothesis that this peak on the unencapsulated sample is due to preferential sputtering since the GaN surface of the encapsulated sample is protected from sputter loss during implantation. A significant reduction in the implantation-induced damage peak occurs after the

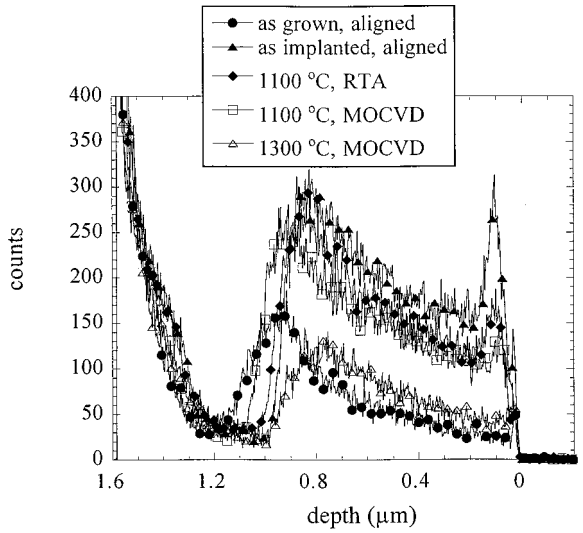

FIG. 28. Channeling Rutherford backscattering (C-RBS) spectra for Si-implanted (100 keV, 5×10^{15} cm^{-2}) GaN either as-implanted or annealed as shown in the legend.

RTA anneal with a further reduction with increasing thermal processing.

Table III summarizes the values for the minimum channeling yield (χ_{min}) of the GaN layer for the sample studied. The dechanneling for an unimplanted sample was estimated to be 2.5% and is close to the theoretical limit.[155] For the AlN encapsulated samples the value of χ_{min} has had the effect of the AlN overlayer subtracted out based on spectra of unimplanted, unannealed AlN on GaN. The unencapsulated samples show a continuous reduction in χ_{min} with increasing annealing temperature. This reduction is at least partly due to removal of a surface damage peak as previously discussed.[154] The χ_{min} value at 1300 °C of 6.7% may be anomalously low due to sublimation of the damaged region in this sample (see Fig. 26). The 1400 °C annealed encapsulated sample shows a significant reduction in χ_{min} from the as-implanted value of 38.6% to 12.6%. Since the RBS analysis was performed on regions of the sample with the lowest

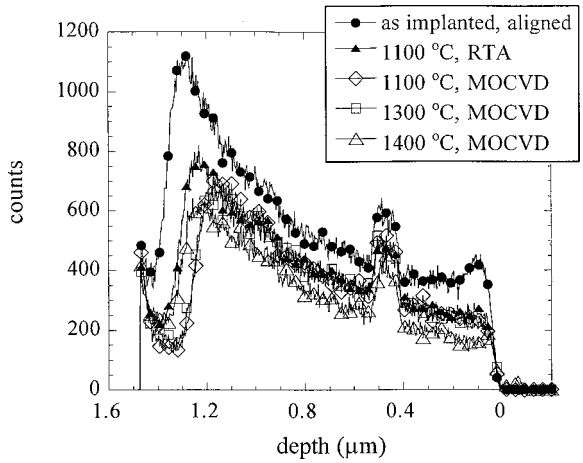

FIG. 29. Channeling Rutherford backscattering (C-RBS) spectra for Si-implanted (210 keV, 5×10^{15} cm^{-2}), GaN encapsulated with 120 nm of AlN either as-implanted or annealed as shown in the legend.

TABLE III. Summary of C-RBS results for Si-implanted AlN-encapsulated and unencapsulated GaN annealed under the conditions shown. All 30 s anneals were done in an MOCVD reactor under flowing N_2/NH_3 and the 15 s anneals were done in a RTA under flowing N_2.

Sample	Anneal (temperature/time) (°C)	χ_{min} for GaN (%)	GaN thickness (μm)
GaN as-grown	none	2.5	1.12
AlN/GaN as-implanted	None	38.6	1.36
1	1400, 30	17.2	1.23
3	1100, 30	20.2	1.23
4	1100, 15	23.6	1.29
GaN as-implanted	None	34.1	0.90
5	1400, 30	[a]	···
6	1300, 30	6.7	0.90
7	1100, 30	17.2	0.98
8	1100, 15	20.8	0.94

[a]The GaN layer completely evaporated during the anneal.

density of craters, this χ_{min} value should be characteristic of the GaN that has not decomposed during the anneal. While the reduction in χ_{min} demonstrated partial recovery of the crystal lattice, the original channeling properties were not realized. This suggests still higher temperature anneals may be required. This would be consistent with a 2/3 rule for relating the melting point (T_{mp}) of a semiconductor to the implantation activation temperature (T_{act}) since for GaN $T_{mp} \sim 2500\,°C$ and therefore T_{act} should be $\sim 1650\,°C$.[135] To reach this temperature in a controllable manner will require development of new annealing furnaces. Preferably, such a furnace should operate in a rapid thermal processing mode (i.e., with rapid heating and cooling) to minimize the thermal budget of the anneal process. This will require new equipment designs such as has been reported in the previous section. The following section presents results for annealing up to 1500 °C in high N pressure that supports the need for a much higher temperature anneal to restore the crystal lattice.

d. Extreme annealing conditions. High pressure, high-temperature annealing was used to study the fundamental limits of implantation induced damage removal in GaN.[156] By employing high N-overpressures (up to 15 kbar) sample decomposition is suppressed and the damage removal can be uncompromisingly examined.[157,158] Figure 30 shows aligned C-RBS spectra for GaN implanted with 100 keV Si at dose of $5\times10^{15}\,cm^{-2}$ and annealed under the conditions shown in the legend. Included in the legend in parentheses is the minimum channeling yield (χ_{min}) for each sample. An as-implanted sample (spectra not shown) had a χ_{min} of ~34%, therefore significant damage removal has occurred for the 1250 °C ($\chi_{min}=14.28\%$) sample with continuing improvement with increased temperature. The 1500 °C sample has a channeling yield equivalent to an unimplanted sample and demonstrated no macroscopic surface decomposition. This result suggests that implantation damage can in fact be removed in GaN given a high enough annealing temperature.[156] The next step will be to find alternative ways, besides the extremely high N overpressure, to maintain the sample stoichiometry.

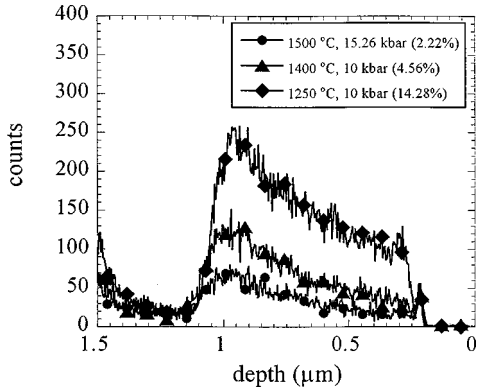

FIG. 30. Aligned C-RBS spectra for Si-implanted (100 keV, $5\times10^{15}\,cm^{-2}$) GaN annealed for 15 min under the conditions show. In parenthesis is the minimum channeling yield (χ_{min}) for each sample.

The samples of Fig. 30 were also characterized by the Hall technique, by photoluminescence, and by secondary ion mass spectroscopy (SIMS). Hall data suggest 46% electric activity of the implanted Si at 1250 °C with increasing activity to 88% at 1500 °C. However, the SIMS data show high levels of oxygen in the samples, therefore, the free donor concentration may also have a component due to O which is known to act as donor in GaN.[139,159] The source of the O is unclear, however, it may have diffused out from the sapphire substrate or in from the annealing ambient. The Hall mobility of the 1250 °C was ~100 $cm^2/V\,s$ and is very respectable for such a high donor level (on the order of $10^{20}\,cm^{-3}$). The mobility was roughly constant for the higher annealing temperatures.

The photoluminescence spectra of samples as-grown and after implantation and annealing is shown in Fig. 31. The as-implanted samples (not shown) had no appreciable luminescence while the annealed samples had both near band edge and donor/acceptor-like emission peaks. The 1500 °C annealed sample has a stronger band edge luminescence in-

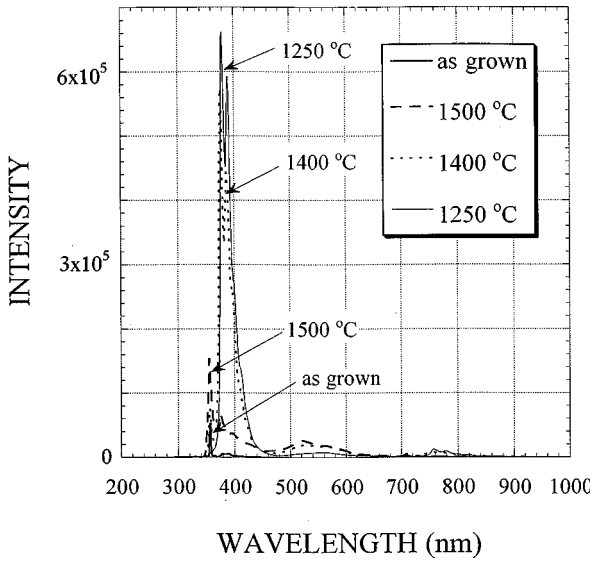

FIG. 31. The photoluminescence spectra of samples as-grown and after implantation (Si: 100 keV, $5\times10^{15}\,cm^{-2}$) and annealing as listed in the legend.

tensity than the as-grown material by a factor of three, but was worse than the 1250 and 1400 °C samples. This may result from indiffusion of contaminants. The exact nature of this enhancement is under study, but an enhanced donor/acceptor recombination associated with the Si doping along with removal of nonradiative centers during the annealing process was postulated.

Additional work on Zn implantation in GaN by Strite and co-workers has also demonstrated the benefits of annealing the implanted samples near 1500 °C at high N pressures to recover, and even enhance, the overall luminescence.[160] Suski *et al.* also showed that annealing unimplanted (i.e., as-grown) samples at such a high temperature and pressure can improve the luminescence efficiency of the material.[161] At this point the details of the improvement in luminescence after such annealing is not understood by it may be due to stress relief or to defect annihilation.

e. Dose dependence. While *n*- and *p*-type implantation doping of GaN was previously reported with the use of Si and O or *n* type and Mg and Ca for *p* type, further work was needed to optimize the implantation and annealing process.[138,139] In particular, the limits on achievable doping levels via ion implantation are of interest. Along these lines, the dose dependence of damage formation in Si-implanted GaN at 90 keV and 77 K has been reported as discussed above.[146,154] In that study, GaN was shown to have a Si-dose threshold for amorphization at 77 K of $\sim 2\times10^{16}\,\mathrm{cm}^{-2}$ that is much larger than the amorphization dose for GaAs ($4\times10^{13}\,\mathrm{cm}^{-2}$) but closer to the level for AlAs ($\sim 8\times10^{15}\,\mathrm{cm}^{-2}$) at this temperature. Since for other compound semiconductors the upper limit on the practical implantation dose is generally determined by the onset of amorphization and the impurity solubility level, this result suggested that very high implantation doses, and therefore high doping levels, may be possible via implantation in GaN.

The electrical properties of Si-implanted GaN up to doses of $1\times10^{16}\,\mathrm{cm}^{-2}$ were investigated to ascertain the dose dependence of electrical activation on implantation dose. Implantation of Ar which should be a neutral impurity in GaN, was also studied to better understand the electrical nature of the implantation-induced damage.[149]

Si ions were implanted at 100 keV at doses from 5×10^{13} to $1\times10^{16}\,\mathrm{cm}^{-2}$. Ar ions were implanted at 140 keV and over the same dose range to place its peak range at the equivalent position as the Si. All samples were annealed at 1100 °C for 15 s in flowing N_2 with the samples in a SiC-coated graphite susceptor. This annealing sequence has previously been shown to activate implanted dopants in GaN,[138,139] although it was found not to completely restore the crystal lattice.[149] Following annealing the samples were electrically characterized at room temperature by the Hall technique with evaporated Ti/Au ohmic contacts at the corners of each sample.

Figure 32 shows the room temperature sheet carrier concentrations versus implant dose for the Si- and Ar-implanted samples after the 1100 °C anneal. For the Si-implanted samples, there appears to be no significant donor activation until a dose of $5\times10^{15}\,\mathrm{cm}^{-2}$ is achieved. This is in contrast to earlier results at a dose of $5\times10^{14}\,\mathrm{cm}^{-2}$ where roughly

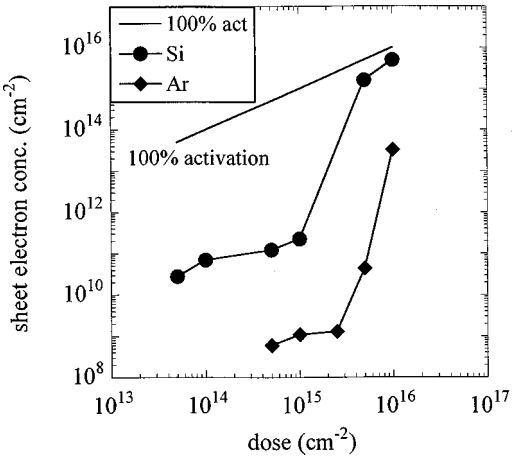

FIG. 32. Sheet electron density vs implantation dose of each ion for Si- and Ar-implanted GaN annealed at 1100 °C for 15 s. The top line represents 100% activation of the implanted dose assuming full ionization.

10% of the implanted Si ions were ionized at room temperature, corresponding to 94% of the implanted Si forming active donors on the Ga sublattice assuming a Si-donor ionization energy of 62 meV.[138] The absence of free electrons for the lower dose Si-implanted samples in this study may have been due to compensation by background carbon in the as-grown GaN, as was postulated to exist based on the photoluminescence spectra. For the two highest dose Si-implanted samples (5 and $10\times10^{15}\,\mathrm{cm}^{-2}$) 35% and 50%, respectively, of the implanted Si ions created ionized donors at room temperature. The possibility that implant damage alone was generating the free electrons can be ruled out by comparing the Ar-implanted samples at the same dose with the Si-implanted samples which had over a factor of 100 times more free electrons. If the implantation damage was responsible for the carrier generation or for enhanced conduction by a hopping mechanism then the Ar-implanted samples, which would have more damage than the Si-implanted samples as a result of Ar's heavier mass, would have demonstrated at least as high a concentration of free electrons as the Si-implanted samples. Since this is not the case, implant damage cannot be the cause of the enhanced conduction and the implanted Si must be activated as donors. The significant activation of the implanted Si in the high-dose samples and not the lower-dose samples is explained by the need for the Si concentration to exceed the background carbon concentration ($\sim 5\times10^{18}\,\mathrm{cm}^{-3}$) that was thought to be compensating the lower-dose Si samples.

Recent work has shown that implanted Si is almost 100% substitutional on the Ga site for doses up to at least $7\times10^{14}\,\mathrm{cm}^{-2}$ and annealing at 1100 °C.[162] The lattice location was determined by a combination of ion channeling, particle-induced x-ray emission, and nuclear reaction analysis. This directly ties the observed *n*-type conductivity to incorporation of Si donors in the GaN lattice.

In summary, although low dose samples do not show Si activation, possibly due to a background carbon level in the sample, a Si dose of $1\times10^{16}\,\mathrm{cm}^{-2}$ demonstrated 50% activation. The possibility that implantation damage alone is responsible for the enhanced conductivity was discounted by

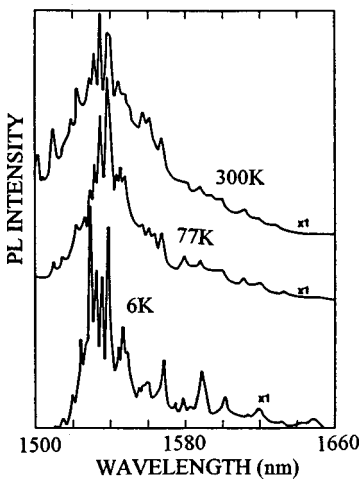

FIG. 33. Photoluminescence spectra from Er-implanted GaN coimplanted with O and annealed at 700 °C.

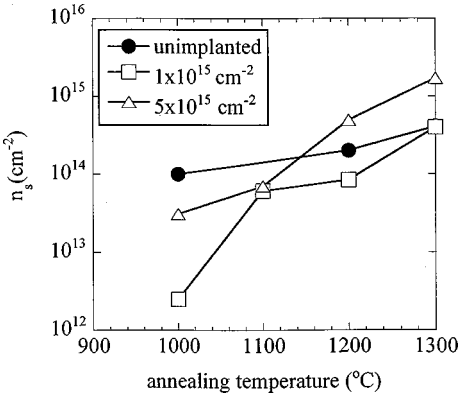

FIG. 34. Sheet electron concentration for unimplanted and Si-implanted (100 keV) AlGaN (15% AlN) at the doses shown vs annealing temperature.

comparing the Si-implanted samples to Ar-implanted samples.

f. Rare-earth implantation. Er implantation is an additional area of research related to GaN. The introduction of Er into a host III–V semiconductor is of interest as a potential source of optical emission at 1.54 μm for use in telecommunications via optical fiber links.[163] The optical emission is a result of the Er^{3+} atomic transition, in the presence of the local semiconductor field, that has the required energy level. This is the transition presently used in Er-doped fiber amplifiers (EDFA).[164–166] If this transition can be efficiently activated within a semiconductor laser cavity, this would produce an effective source for optical fiber communications at 1.54 μm.[163]

One of the first reports of the luminescence properties of Er-implanted GaN was by Wilson *et al.*,[167] with subsequent confirmation of the results by Qiu *et al.*[168] The Er was implanted along with O which has been shown to enhance the Er luminescence intensity in other semiconductors. The enhancement by O (or F) codoping has been attributed to the impurity atoms forming ligands with the Er atoms and converting the local bonds into a more ionic state.[169–171] The Er-implanted GaN was annealed between 650 and 700 °C and the luminescence spectrum shown in Fig. 33 with many of the characteristic Er-emission lines was achieved under optical excitation using an Ar-ion laser at a wavelength of 457.9 nm.[167] In addition, the luminescence intensity was nearly as strong at room temperature as at 77 K. This in contrast to reports of thermal quenching of the Er emission at room temperature in narrower band gap semiconductors. It is this suppression of the temperature dependence of the Er^{3+} luminescence in GaN that makes a wide band gap host so attractive for this application.[163]

The work by Qiu *et al.* compared Er/O implanted GaN to similarly implanted sapphire and found only a 5% reduction in the Er-related emission between 6 and 380 K compared to an 18% reduction for the sapphire. In that study the samples were implanted at Er dose of 1 or $10\times10^{14}\,cm^{-2}$ (O dose of $1\times10^{16}\,cm^{-2}$) and annealed at 900 °C for 30–60 min in flowing NH_8.[168] The work confirmed the results of Wilson that Er-doped GaN maintained most of its low temperature luminescence at room temperature.[167,168]

Since both of these studies used implant activation annealing temperatures of $\leqslant$900 °C, significant implantation-induced damage will still exist in the samples and degrade the luminescence efficiency. When more optimum, higher temperature annealing is applied to this technology, significant improvement in the 1.54 μm luminescence should result.

g. Activation in alloys. AlGaN layers will be employed in heterostructure transistors to realize a two dimensional electron gas (2-DEG) and to increase the transistor breakdown voltage. As discussed in the introduction, implantation can be used to reduce the transistor access resistance of the AlGaN barrier. One would anticipate that the addition of Al to the GaN matrix will increase the damage threshold as is the case for AlGaAs as compared to GaAs,[172] but little work has been reported in this area. Recently the first implantation doping studies have been reported for AlGaN.[156,173]

For the work by Zolper *et al.*,[115] the AlGaN layer used for the Si implantation was nominally 1.0 μm-thick grown on a *c*-plane sapphire substrate. The Al composition was estimated to be 15% based on x-ray and photoluminescence measurements. The as-grown minimum backscattering yield measured by channeling Rutherford backscattering was 2.0% and is comparable to a high quality GaN layer.

The AlGaN samples were implanted with Si at room temperature at an energy of 100 keV at one of two doses, 1 or $5\times10^{15}\,cm^{-2}$. The higher Si dose has previously been shown not to amorphize GaN and produce an as-implanted channeling yield of 34% in GaN.[29]

Samples were characterized by channeling Rutherford backscattering (C-RBS) with a 2 MeV beam with a spot size of 1 mm^2 at an incident angle of 155°. Aligned spectra are taken with the beam parallel to the *c* axis of the GaN film. Random spectra are the average of five off-axis, off-planar orientations. Electrical characterization was performed using the Hall technique at room temperature.

Figure 34 shows the sheet electron concentration and versus the annealing temperature for the Si-implanted AlGaN sample. Data for an unimplanted sample is included as a control. First of all, it is clear that the unimplanted samples

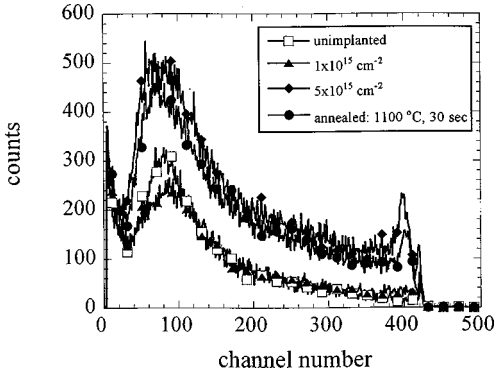

FIG. 35. Channeling Rutherford backscattering (C-RBS) spectra for as-grown, unimplanted, Si-implanted (100 keV, 1 or $5\times10^{15}\,\mathrm{cm}^{-2}$), and implanted (100 keV, $5\times10^{15}\,\mathrm{cm}^{-2}$) annealed at AlGaN.

have significant donors produced by the annealing process alone. This may be due to the activation of unintentional impurities, such as Si or O, in the film. O may be a particular suspect due to the tendency of O to incorporate in Al-containing material. At the highest temperature, the high dose Si-implanted sample has four times higher free electron concentration ($1.7\times10^{15}\,\mathrm{cm}^{-2}$) than the unimplanted sample. This corresponds to 34% activation of the implanted Si.

Figure 35 shows aligned C-RBS spectra for 15% Al in AlGaN either as-grown (unimplanted), after Si implantation at a dose of 1 or $5\times10^{15}\,\mathrm{cm}^{-2}$, and for the higher dose samples after annealing.[156] As was the case for GaN, the $1\times10^{15}\,\mathrm{cm}^{-2}$ sample shows limited dechanneling while the higher dose sample shows a marked damage peak. The minimum channeling yield for the high dose sample was 26.67% which is lower than that seen for GaN which showed $\chi_{\min}$ between 34% and 38% implanted under the same conditions. This means the addition of 15% aluminum to the GaN matrix increases its damage threshold as is the case for Al additions to GaAs to form AlGaAs.[172] The spectra for the annealed sample shows limited damage removal, again consistent with that seen for GaN at this temperature.[149] There is evidence, however, of improvement in the near surface as seen by the reduction in the first surface peak. This peak has been suggested to be due to preferential sputtering of nitrogen from the film surface.[154] The reduction of this peak via annealing suggests the surface stoichiometry is restored during the anneal. Further study is needed to better understand this effect.

The redistribution of implanted Si, Mg, and C in $Al_{0.12}Ga_{0.88}N$ was studied by Polyakov and co-workers.[173] While Si and C demonstrated no measurable diffusion by SIMS after at 1140 °C, 1 h anneal, Mg did show appreciable profile broadening and indiffusion under these conditions. Activation of a modest Si dose ($5\times10^{14}\,\mathrm{cm}^{-2}$) was also achieved by annealing at 1140 °C with a resulting peak electron concentration of $1.2\times10^{18}\,\mathrm{cm}^{-3}$. More work is needed on the affect of Al composition on the implantation properties of AlGaN.

Although significant progress has been reported for ion implantation doping and annealing of GaN and AlGaN, there are still many areas for further research. For example, further work is needed to develop a manufacturable annealing process between 1300 and 1500 °C at reproducible N pressures. The role of native defects, particularly dislocations, on the activation of implanted dopants can now be addressed with the demonstration of nearly dislocation free GaN formed by lateral epitaxial overgrowth (LEO).[174–176] This defect free material is likely to make the study of *p*-type implantation more reproducible. Areas of interest for implant isolation include demonstration of truly thermally stable isolation, understanding the nature of hydrogen implant isolation, determination of the behavior of deeps levels such as Cr and Fe, and the effect of implant isolation on the properties of waveguide losses.

TABLE IV. Comparison of Ga_2O_3 and SiO_2.

Oxide	Ga_2O_3	SiO_2
Melting point (°C)	1850	1600
Dielectric constant	10.2–14.2	3.9
Energy gap (eV)	4.4	9
Dielectric strength (V/cm)	3.5×10^6	10^7

The possibilities are extensive for the application of ion implantation to group III-nitride semiconductor devices. A few examples would be the use of selective area implantation doping to improve the contact resistance of III–N laser or FET structures or using ion implantation isolation to realize an electrically injected vertical cavity surface emitting laser or to produce light-emitting device (LED) arrays.

With continued improvements in the quality of group III–N materials, ion implantation doping and isolation can be expected to play an enabling role in the realization of many advanced device structures. As reviewed in this section, significant progress has been made in proof-of-principle demonstration. However, significantly more effort is needed on the starting material and the process technology to make implantation of group III-nitride semiconductors the same workhorse technology it is in an other, more mature semiconductor material systems.

C. Gate dielectrics

Work in this area for power MOSFETs and gate turn-off thyristors is just commencing and some preliminary results are becoming available for AlN, AlON, and $Ga(Gd)O_x$, the latter producing excellent characteristics on GaAs and InGaAs and now being applied to GaN. Channel modulation has been demonstrated for AlN and $Ga(Gd)O_x$, but interface state densities appear well above $10^{11}\,\mathrm{cm}^{-2}$ at this point and much future effort is required to reduce this level. Table IV shows a comparison of the properties of Ga_2O_3 (which is the major component of the dielectric) and SiO_2.[129] While the latter is superior in terms of breakdown strength, Ga_2O_3 is an attractive option.

A number of GaN field effect transistors (FETs) and AlGaN/GaN heterostructure FETs have been reported, showing excellent device breakdown characteristics.[177,178] However, the conventional low resistance n^+-cap layer structure for the GaAs technology cannot be applied in the nitride based material system to reduce the parasitic resistance, ow-

ing to no adequate gate recess technology being available. The III nitrides are chemically very stable and few wet etching recipes exist. GaN may be etched by molten KOH of NaOH at $\geqslant 400\,^{\circ}\mathrm{C}$, while laser enhanced HCl or KOH solutions produce etch rates of a few hundred angstroms per minute at room temperature.[179] Virtually all of the nitride devices reported to data have employed dry etching for pattern transfer and ion bombardment induced low gate breakdown voltages were observed.[180,181] Both of these problems (gate recess and surface degradation) may be overcome by using a MOSFET approach.

Recently, interface properties of $Ga_2O_3(Gd_2O_4)$/GaAs structures fabricated using *in situ* multiple-chamber molecular beam epitaxy have been investigated. The oxide films were deposited on clean, atomically ordered (100) GaAs surfaces at $\sim 550\,^{\circ}\mathrm{C}$ by electron-beam evaporation using a $Gd_3Ga_5O_{12}$ single crystal source. A midgap surface state density of $2\times 10^{10}\,\mathrm{cm}^{-2}\,\mathrm{eV}^{-1}$ was obtained, several orders of magnitude lower than with most other dielectrics.[182] Both *n*- and *p*-GaAs based enhancement-mode MOSFETs were also demonstrated.[183–185]

Aluminum nitride has been proposed as a potential replacement for silicon dioxide in high temperature MIS based silicon carbide device applications. AlN is a wide band gap semiconductor (6.2 eV) but if made undoped, its properties are most like those of an insulator. A high relative dielectric constant (8–9) alleviates the problem of high fields in the dielectric in high voltage application. The breakdown electric field, however, is not yet well determined. Moreover, the thermal conductivity of AlN is high, making this material a potential high temperature stable gate dielectric. One difficulty associated with this material may be its tendency to deposit as a polycrystalline layer rather than an amorphous one. This allows more rapid diffusion of impurities and is highly undesirable.

$Ga_2O_3(Gd_3O_3)$ has recently been applied to make GaN diodes and MOSFETs. We also used a MOMBE system to grow the aluminum nitride for the alternative diode insulator. The MIS diodes using these two insulators were then fabricated and characterized with $I-V$ and capacitance–voltage ($C-V$) measurements. The dielectric thickness and interface roughness were measured with x-ray reflectivity.[186,187]

The GaN layer structure was grown on c-Al_2O_3 substrates prepared initially by $HCl/HNO_3/H_2O$ cleaning and an *in situ* H_2 bake at 1070 °C. A GaN buffer <300 Å thick was grown at 500 °C using trimethylgallium and ammonia, and crystallized by ramping the temperature to 1040 °C within 2 min. The same precursors were again used to grow $\sim 3\ \mu$m of undoped GaN ($n<1\times 10^{16}\,\mathrm{cm}^{-3}$) and a 2000 Å Si-doped ($n=2\times 10^{17}\,\mathrm{cm}^{-3}$) active layer.[188]

The diode fabrication started with ohmic contact formation by depositing In on the edge of the GaN samples by using shadow mask and heat up to 500 °C. Then, the samples were transferred to growth chamber for insulator growth. For the $Ga_2O_3(Ga_2O_3)$ growth, the sample was loaded into a solid source MBE chamber and the native oxides of GaN were thermally desorbed at a substrate temperature of 700 °C. After oxide desorption, the wafer was transferred under vacuum (10^{-10} Torr) into a second chamber and the

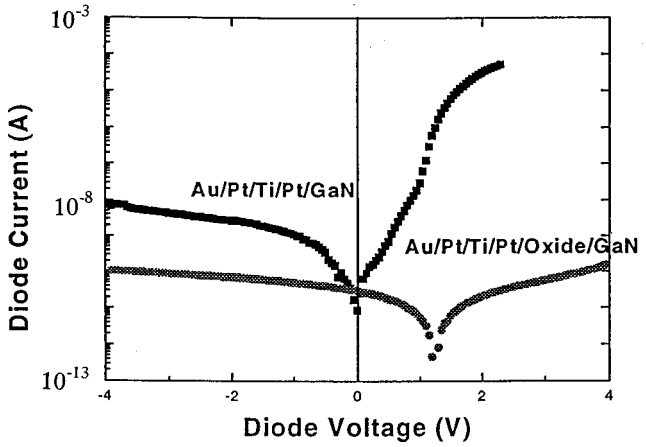

FIG. 36. Comparison of the $I-V$ characteristics of Schottky gate and $Ga_2O_3(Gd_2O_3)$/GaN diode.

$Ga_2O_3(Gd_2O_3)$ was deposited on the GaN using e-beam evaporation at a substrate temperature of 550 °C.[189]

For the AlN growth, a MOMBE system was used. The GaN oxides were thermally desorbed at 700 °C under N_2 plasma, and AlN was grown with trimethylamine alane and nitrogen generated from a Wavemat ECR N_2 plasma at $\sim 400\,^{\circ}\mathrm{C}$.

After the AlN or $Ga_2O_3(Gd_2O_3)$ deposition, a metallization of Pt/Ti/Pt/Au (50 Å/50 Å/200 Å/2000 Å) was directly deposited on the insulator layer again through the shadow mask with different diameters to complete the diode formation.

The development of a suitable insulator for GaN MOSFET structures is a critical step. Conventional dielectrics such as SiO_2 and Si_3N_4 have generally failed on III–V materials because of high interface state densities. We believe that AlN or $Ga_2O_3(Gd_2O_3)$ layers offer the best opportunities for sustaining high fields at low defect densities. $Ga_2O_3(Gd_2O_3)$ had recently been developed as an excellent insulator on GaAs.[190] The same approach can be extended to GaN.

As shown in Fig. 36, the $I-V$ characteristics of a $Ga_2O_3(Gd_2O_3)$/GaN diode shows a very low leakage current on both forward and reverse bias. The forward breakdown voltage (defined at 10 μA of diode current) is 6 V. The charge modulation of the MOS diode was clearly demonstrated from the change from accumulation mode (positive bias) to depletion mode (negative bias) at different frequencies. The typical inversion phenomena exhibited in SiO_2/Si diode is not observed, which might be due to the nature of ionic bonding of nitride-based materials which have long minority carrier lifetime.

From x-ray reflectivity measurements, the thickness of the $Ga_2O_3(Gd_2O_3)$ and the root-mean-square roughness of the $Ga_2O_3(Gd_2O_3)$/GaN interface were estimated to be 195 and 3 Å, respectively. The slope of the x-ray reflectivity is a function of the oxide thickness and the roughness of the $Ga_2O_3(Gd_2O_3)$/GaN interface as well as the air/$Ga_2O_3(Gd_2O_3)$ interface will determine the widths of oscillation periods. With the 195-Å-thick $Ga_2O_3(Gd_2O_3)$ and the 6 V forward breakdown, the breakdown field of the oxide is

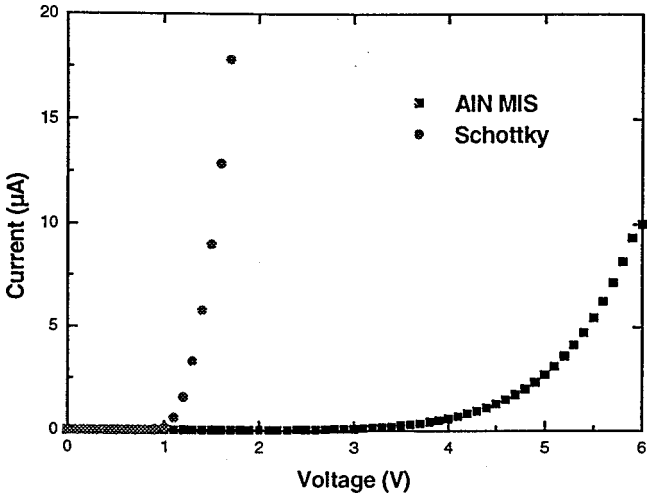

FIG. 37. Comparison of the $I-V$ characteristics of a Schottky gate and AlN/GaN diode.

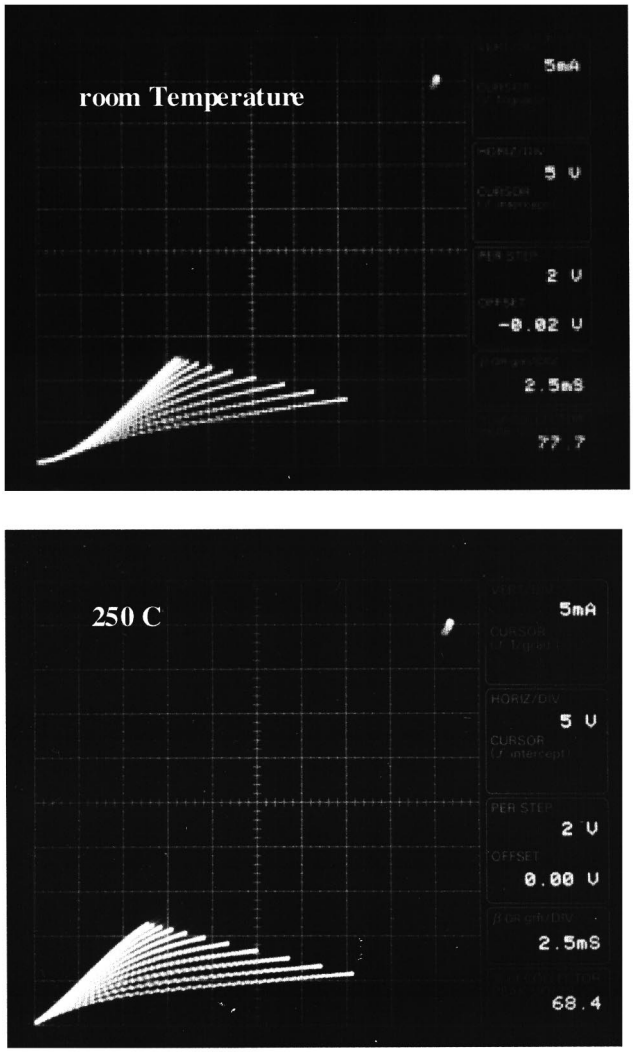

FIG. 38. GaN D-MOSFET $I-V$ characteristics measured at different temperatures.

>12 MV/cm. The atomic level (3 Å) smoothness for the $Ga_2O_3(Gd_2O_3)$/GaN interface can provide a higher carrier mobility in the channel for a MOSFET.

For the AlN/GaN material system, the diode $I-V$ characteristics also show a very low leakage current on both forward and reverse bias. A forward breakdown of 5 V was obtained, as shown in Fig. 37. From $C-V$ data the charge modulation of the MIS diode was also clearly demonstrated from accumulation mode to depletion mode at different frequencies.

The thickness of the AlN and the root-mean-square roughness of the AlN/GaN interface were determined to be 345 and 20 Å, respectively. The 20 Å roughness of the AlN/GaN interface may be due to the interdiffusion between Al and Ga, however, more detailed study is needed to confirm this. With the 345 Å-thick AlN and the 5 V forward breakdown, the breakdown field of the oxide is around 1.4 MV/cm. The lower breakdown field may be caused by the rough AlN/GaN interface or the crystallinity of the AlN.

In summary, GaN MIS diodes were demonstrated using MOMBE grown AlN and MBE evaporated $Ga_2O_3(Gd_2O_3)$ as the insulators. The breakdown fields of AlN and $Ga_2O_3(Gd_2O_3)$ diodes are 1.4 and 12 MV/cm, respectively. From the $C-V$ measurement, both kinds of diodes show good charge modulation from accumulation to depletion at different frequencies (100 kHz–10 MHz). Extremely smooth $Ga_2O_3(Gd_2O_3)$/GaN interfaces are achieved and the rms of the interface roughness is 3 Å which is the atomic range. However, the rms roughness AlN/GaN interface is around 20 Å which may be caused by interdiffusion by Al and Ga, more detailed study is needed to confirm this. For future studies, the surface cleaning (*in situ* or *ex situ*) wet/dry processes, including thermal oxide desorption, ozone cleaning of HF vapor, and thermal stability of the diodes are the key to the realization of the GaN based MISFET technology.

The advantages of MOSFETs relative to MESFETs are well established, but due to the absence of a suitable dielectric for compound semiconductors, GaAs-based integrated circuits use MESFETs. This means that the circuits require two supply voltages, with relatively high power consumption. In particular it is desirable to have available enhancement-mode MOSFETs to reduce circuit complexity and power consumption.

Using the $Ga(Gd)O_x$, we have recently fabricated depletion mode GaN MOSFETs on *n*-type ($\sim 3\times 10^{17}\,cm^{-3}$) epilayers grown on Al_2O_3. Figure 38 shows $I-V$ characteristics at 25 and 250 °C. The characteristics are affected by the relatively high source/drain contact resistance, but improve at higher temperatures (Fig. 39). We have tested these devices to >400 °C where the characteristics continue to improve.

While $Ga(Gd)O_x$ (where Ga is predominantly in the +3 oxidation state, Gd is the electropositive stabilizer element for stabilizing Ga in the 3+ oxidation state, and x is high enough to satisfy the requirement that Ga and Gd are essentially fully oxidized) has been the oxide that has worked best on compound semiconductors to date, there are many other possible dielectrics that might have a low enough interface state density (i.e., $\leqslant 10^{11}\,cm^{-2}\,eV^{-1}$ to successfully produce MOSFETs on GaN.

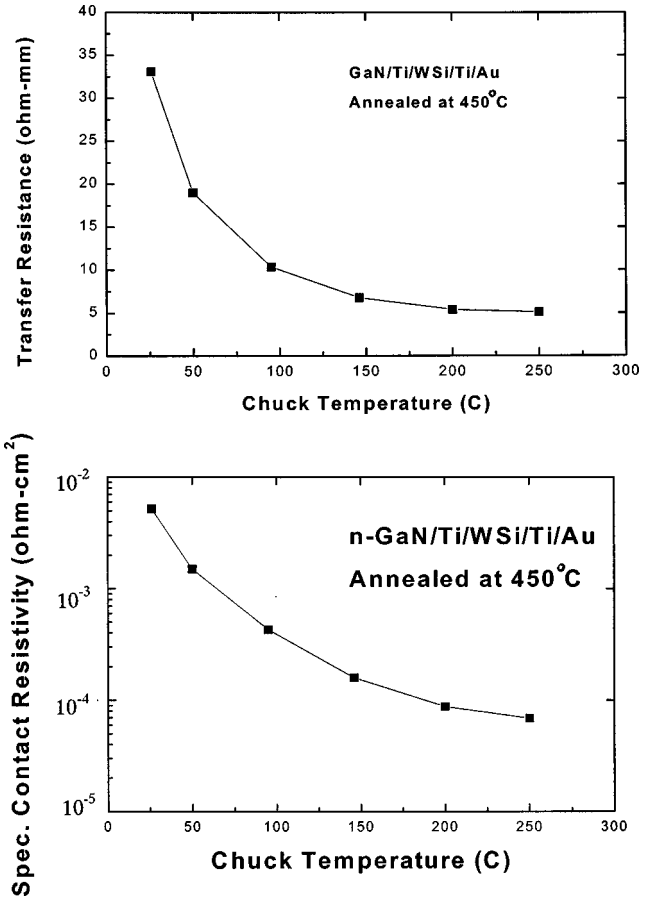

FIG. 39. Temperature dependence of contact properties for $Ti/WSi_x/Ti/Au$ on *n*-GaN.

D. Wet etching

Under normal conditions, only molten salts such as KOH or NaOH at temperatures above ~250 °C have been found to etch GaN at practical rates, and the difficulty of handling these mixtures and the inability to find masks that will hold up to them has limited the application of wet etching in GaN device technology. We have found that AlN and Al-rich alloys can be wet etched in KOH at temperatures of 50–100 °C.[191] The Adesida group has recently published several reports on photochemical etching of *n*-GaN using 365 nm illumination of KOH solutions near room temperature,[192] following on the work of Minsky *et al.*[179] Rates of 3000 Å min^{-1} were obtained for light intensities of 50 mW/cm^2, and the etch reaction was assumed to be

$$2GaN + 6h + \rightarrow 2Ga^{3+} + N_2\uparrow.$$

The etching was generally diffusion limited, with somewhat rough surfaces. Intrinsic and *p*-GaN do not etch under these conditions, and undercut encroachment occurred in some small-scale features due to light scattering and hole diffusion in the GaN itself. This process looks very promising and may be useful for several different fabrication steps in both electronic and photonic devices, as well as for defect counting.

A compilation of etch results for binary and ternary nitrides is shown in Table V. These results are for nonlight-assisted conditions. For single crystal AlN we find that KOH-based solutions, such as AZ400K developer, produce reaction-limited etching with an activation energy of ~15.5 kCal mol^{-1} (Fig. 40). The rates are a strong function of material quality, with higher quality AlN etching at a slower rate.

In this section, we report on an examination of the wet etching of AlN and $In_xAl_{1-x}N$ in KOH solutions as a function of crystal quality, etch temperature, and composition. AlN sample prepared by reactive sputtering on Si substrates at ~200 °C were annealed at temperatures from 400 to 1100 °C and as expected, the etch rate decreased with anneal temperature, indicating improved crystal quality. We found that InAlN on Si substrates had higher wet etch rates compared to the same material on Al_2O_3. Both AlN and InAlN samples had an increase in etch rate with etch temperature. The etch rate for the InAlN increased as the In composition increased from 0% to 36%, and then decreased to zero for InN. Finally, the effect of doping concentration in InAlN samples of similar In concentration (~3%) was examined and much higher etch rates were observed for the heavily doped material at solution temperatures above 60 °C, due to the Fermi-level dependent etch mechanism.

The AlN was reactively sputter deposited on a Si substrate to a thickness of ~1200 Å using a N_2 discharge and a pure Al target. This type of AlN film has been shown to be an effective annealing cap for GaN at a temperature of 1100 °C. The InAlN samples were grown using metal organic molecular beam epitaxy (MOMBE) on semi-insulating, (100) GaAs substrates or *p*-type (1 Ω cm) Si substrates in an Intevac Gen II system. The group III sources were triethylgallium, trimethylamine alane, and trimethylindium, respectively, and the atomic nitrogen was derived from an ECR Wavemat source operating a 200 W forward power. Both AlN and InAlN layers were single crystal with a high density (10^{11} to 10^{12} cm^{-2}) of stacking faults and microtwins. InAlN samples were found to contain both hexagonal and cubic forms. The $In_xAl_{1-x}N$ films were either conducting *n*-type as-grown (~10^{18} cm^{-3}) for $x \geq 0.03$ due to residual autodoping by native defects or fully depleted for $x < 0.03$. The compositions examined were 100%, 75%, 36%, 29%, 19%, 3.1%, 2.6%, and 0% In.

The AlN samples were annealed in a RTA system (AG410T) face down on a GaAs substrate for 10 s at temperatures between 500 and 1150 °C in a N_2 atmosphere. For wet etching studies, all samples were masked with Apiezon wax patterns. Etch depths were obtained by Dektak stylus profilometry after the removal of mask with an approximate 5% error. Scanning electron microscopy (SEM) was used to examine the undercutting on the etched sample. AZ400K developer solution, with an active ingredient KOH, was used for the etch, and etch temperatures were between 20 and 80 °C.

Figure 41 shows the etch rate of the sputtered AlN as a function of etch temperature for samples as grown or annealed at 500, 700, 900, 1000, and 1100 °C. The etch rates of both the as-deposited and 500 °C annealed sample increase sharply as the etch temperature increases from 20 to 50 °C, and then level off; the rate drops by approximately 10% with a 500 °C anneal. The samples annealed at 700, 900, and

TABLE V. Compilation of etching results in acid and base solutions, performed at room temperature (25 °C) unless otherwise noted.

	GaN	InN	AlN	InAlN	InGaN
Citric acid (75 °C)	0	0	0	0	0
Succinic acid (75 °C)	0	0	0	0	0
Oxalic acid (75 °C)	0	Lifts off	Lifts off	Lifts off	Lifts off
Nitric acid (75 °C)	0	Lifts off	Lifts off	Lifts off	Lifts off
Phosphoric acid (75 °C)	0	0	Oxide removed	Oxide removed	0
Hydrofluoric acid	0	Lifts off	0	0	Lifts off
Hydriodic acid	0	0	0	0	0
Sulfuric acid (75 °C)	0	Lifts off	0	0	0
Hydrogen peroxide	0	0	0	0	0
Potassium iodide	0	0	0	0	0
2% Bromine-methanol	0	0	0	0	0
n-Methyl-2-pyrrolidone	0	0	0	0	0
Sodium hydroxide	0	Lifts off	Lifts off	Lifts off	Lifts off
Potassium hydroxide	0	Lifts off	22,650 Å min^{-1}	0	0
AZ400K Photoresist developer (75 °C)	0	Lifts off	~60–10,000 Å min^{-1}	Composition dependent	0
Hydriodic acid/hydrogen peroxide	0	0	0	0	0
Hydrochloric acid/hydrogen peroxide	0	0	0	0	0
Potassium triphosphate (75 °C)	0	0	0	0	0
Nitric acid/potassium triphosphate (75 °C)	0	Lifts off	0	0	0
Hydrochloric acid/potassium triphosphate (75 °C)	0	0	0	0	0
Boric acid (75 °C)	0	0	0	0	0
Nitric/boric acid (75 °C)	0	Lifts off	0	0	Lifts off
Nitric/boric/hydrogen peroxide	0	Lifts off	0	0	Removes oxide
$HCl/H_2O_2/HNO_3$	0	Lifts off	0	Lifts off	Lifts off
Potassium tetraborate (75 °C)	0	Oxide removal	Oxide removal	Oxide removal	Oxide removal
Sodium tetraborate (75 °C)	0	0	0	0	0
Sodium tetraborate/hydrogen peroxide	0	0	0	0	0
Potassium triphosphate (75 °C)	0	0	0	0	0
Potassium triphosphate/hydrogen peroxide	0	0	0	0	0

1000 °C also show similar trends, with a monotonic decrease in rate for higher anneal temperatures. The crystal quality appears to improve significantly with anneal temperature as indicated by the drop in the etch rate. The etch rate continues to drop by ~10% with each successive anneal, to 1000 °C. After 1100 °C the etch rate drops and is less temperature dependent. Overall there is an ~90% reduction in etch rate from the as-deposited AlN film to those annealed at 1100 °C for etching at 80 °C.

The activation energy for an etch solution can be determined from an Arrhenius plot, and is shown in Fig. 42. The activation energies for all samples was the same within experimental error, 2.0 ± 0.5 kcal mol^{-1}. This is indicative of a diffusion-limited reaction.[116] This is much lower than the activation energy of 15.45 kcal mol^{-1} reported by Mileham *et al.*[116] for AlN grown by metal organic molecular beam

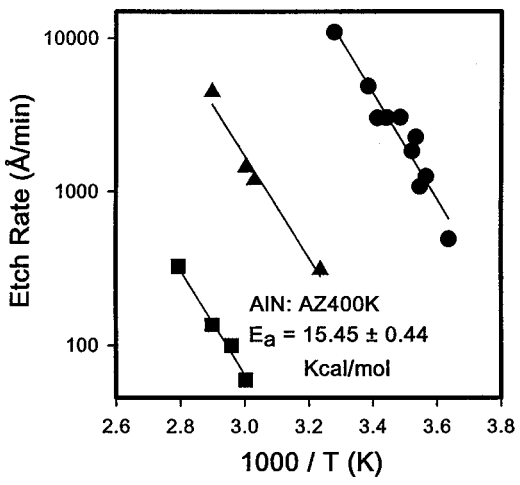

FIG. 40. Arrhenius plot of etch rate of three different AlN samples in AZ400K developer solution. The higher the AlN quality, as measured by XRD, the slower the etch rate.

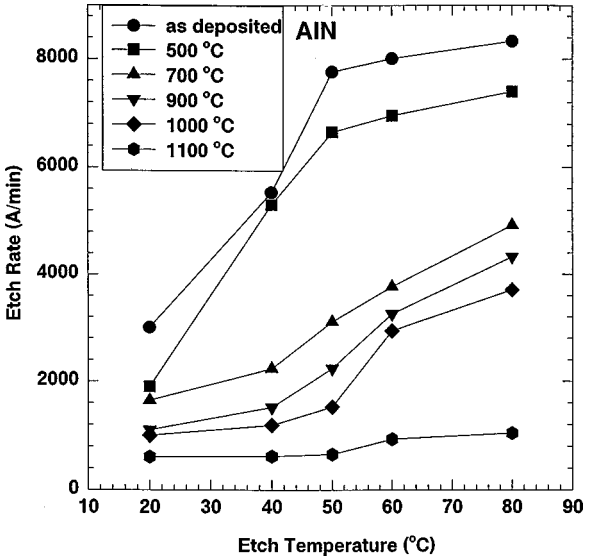

FIG. 41. Etch rate of AlN as a function of etch temperature for samples as-deposited or annealed at 500, 700, 900, 1000, and 1100 °C.

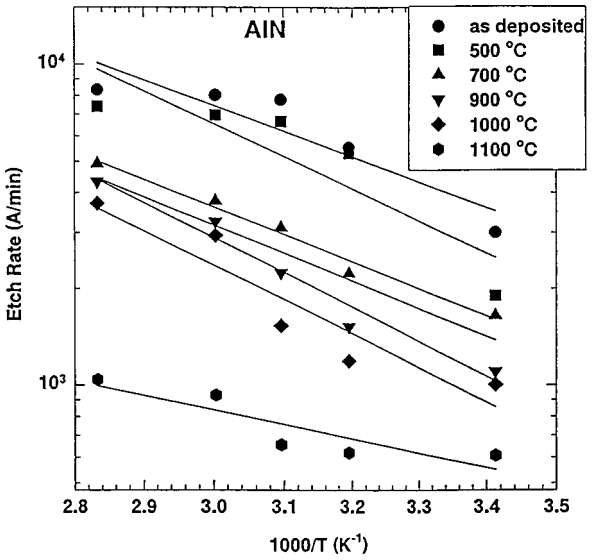

FIG. 42. Arrhenius plots of etch rates for as-deposited or annealed AlN as a function of reciprocal etch temperature.

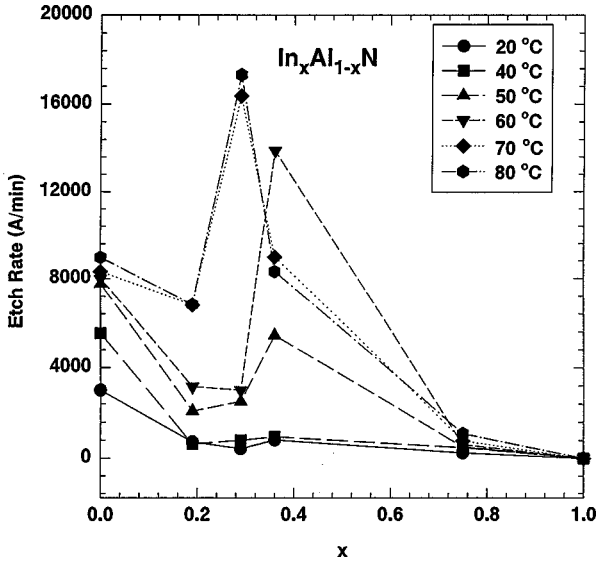

FIG. 44. Etch rate for $In_xAl_{1-x}N$ for $0 \leqslant x \leqslant 1$ at solution temperatures between 20 and 80 °C.

epitaxy. The quality of the material in the current experiment is much lower though, and the etch may be proceeding at such a rapid rate that the solution is becoming depleted of reactants near the materials surface.

The etch rates as a function of solution temperature for $In_xAl_{1-x}N$ ($x=0.19$) grown on either GaAs or Si is shown in Fig. 43. At 20 °C etch temperature there is no difference in etch rate. The etch rates for both materials increase with etch temperature, with the differential in etch rates also increasing with temperature. As was mentioned previously, the InAlN grown on Si has a greater concentration of crystalline defects as evident from x-ray diffraction and absorption measurements. At 80 °C the etch rate for the film on the Si substrate is approximately three times faster than for film grown on GaAs. This is another clear indication of the dependence of wet etch rate on material quality and emphasizes why it has proven very difficult to find etch solutions for high quality single-crystal nitrides.

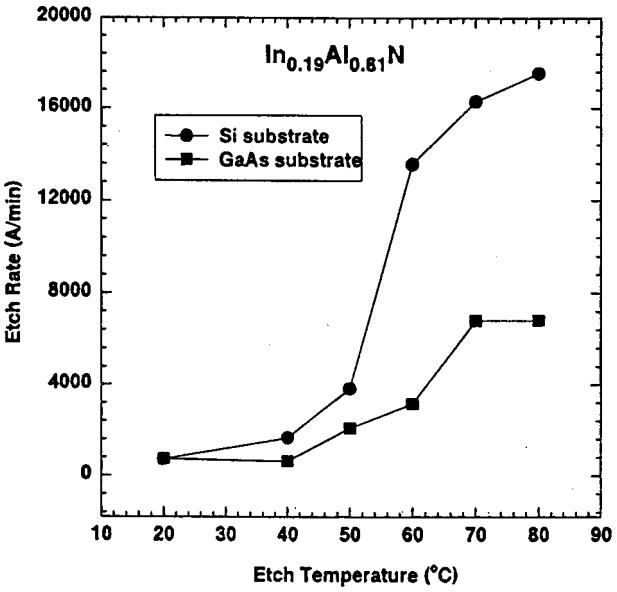

FIG. 43. Etch rates as a function of etch temperature for $In_xAl_{1-x}N$ grown on GaAs and Si for 19% In.

Etch rates for $In_xAl_{1-x}N$ grown on GaAs for $0 \leqslant x \leqslant 1$ are shown in Fig. 44, for etch temperatures between 20 and 80 °C. Up to 40 °C the etch rates are very low and show little dependence on In composition. The AlN etches much faster at these temperatures than any composition of the ternary alloy InAlN. As the etch temperature increases to 60 °C, the etch rates increase, showing a peak for 36% In. This is presumably due to a tradeoff between the reduction in average bond strength for InAlN relative to the pure binary AlN, and the fact that the chemical sensitivity falls off at higher In concentrations. Thus the etch rates initially increase for increasing In, but then decrease at higher concentrations because there is no chemical driving force for etching to occur. InN did not etch in this solution at any temperature but was occasionally lifted off during long etches because of the defective interfacial region between InN and GaAs being attached by the KOH.

Arrhenius plots of etch rates for $In_xAl_{1-x}N$ for $0 \leqslant x \leqslant 1$ giving activation energies for the etches are shown in Fig. 45. There is substantial scatter in the data, but the activation energies are all in the range of 2–6 kcal mol^{-1}, which again is consistent with diffusion-controlled etching.[116] This is not desirable for device fabrication processes because the rates are then dependent on solution agitation and the etched surface morphology are generally rougher than for reaction-controlled solutions.

Apart from material quality or composition, another factor which often plays a role in determining etch rates is sample conductivity. Figure 46 shows a plot of InAlN etch versus etch rate temperature for samples with 2.6% and 3.1% In, which were depleted ($n < 10^{16}\,cm^{-3}$) and doped at $n \sim 5 \times 10^{18}\,cm^{-3}$, respectively. Since the autodoping changes rapidly around this composition, but there is little change in In concentration, these samples represent a good test of any

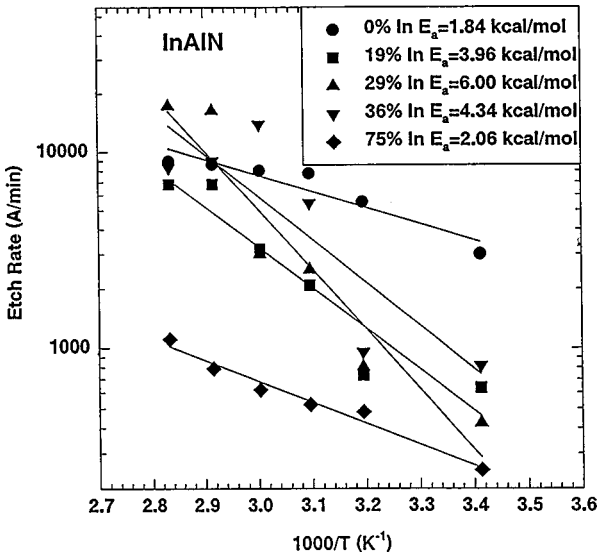

FIG. 45. Arrhenius plots of etch rates for $In_xAl_{1-x}N$ for $0 \leqslant x \leqslant 1$ as function of reciprocal etch temperature, giving activation energy for etch.

effects related to conductivity. The samples have similar etch rates at low solution temperatures. Above 60 °C, however, the *n*-type sample etch rate increases more rapidly, approximately two times faster than the depleted sample. These results imply that at temperatures where fast etch rates occur, the electrons in the *n*-type sample are part of the chemical reaction between the OH^- ions and the Al in the InAlN film. They may enhance formation of these ions initially and thus the etch rate is enhanced.

Etching with KOH-based solution is completely selective for InAlN over GaN or InN. We have discussed that annealing of sputtered AlN improved the crystal quality of the film and decreased the chemical etch rate in KOH solutions. InAlN etch rates are also seen to increase with decreasing crystalline quality. Both AlN and InAlN samples had activation energies for etching in KOH $\leqslant 6$ kcal mol^{-1}, values

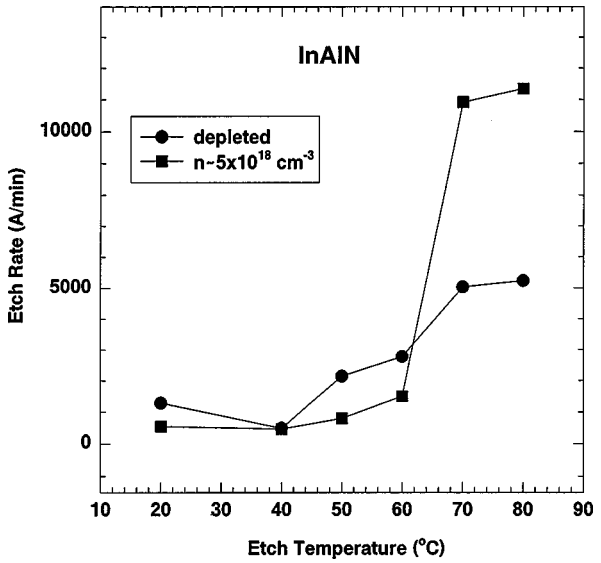

FIG. 46. Etch rate for *n* type (3.1% In) and depleted InAlN (2.6% In) as a function of solution temperature.

that are typical of a diffusion-controlled etch mechanism. The etch rate for the InAlN initially increased as the In composition increased from 0% to 36%, and then decreased to zero for pure InN. The *n*-type InAlN etched approximately two times faster than the undoped material above 60 °C, indicating that electrons play a role in the etch mechanism.

Kim *et al.*[193] reported that H_3PO_4, NaOH, and KOH solutions were able to remove N_2-deficient layers in GaN created by processes such as high temperature annealing or dry etching. The onset of etching occurred at ~160 °C, with rates of ~45 Å s^{-1} at 180 °C for defective GaN surface layers.

Stocker *et al.*[194] found they could obtain effective crystallographic etching of wurtzite GaN in similar solutions at ~170 °C. Use of ethylene glycol rather than H_2O as the dilutent enabled them to carry out the etching at temperatures up to ~190 °C. Phosphoric acid was able to etch the $\{10\bar{1}2\}$ and $\{10\bar{1}3\}$ planes, molten KOH the $\{10\bar{1}0\}$ and $\{10\bar{1}1\}$ planes, and KOH in ethylene glycol the $\{10\bar{1}0\}$ plane. Molten KOH has been shown previously to reveal dislocations in GaN.[195,196]

Lee *et al.*[197] found that the lowest contact resistivity for Pd/Au on *p*-GaN was achieved using KOH rinsing prior to metal deposition. For example, without this treatment, R_C was $2.9\times10^{-1}\,\Omega\,\mathrm{cm}^2$ for a *p*-doping level of $3\times10^{16}\,\mathrm{cm}^{-3}$, whereas the KOH treatment reduced this to $7.1\times10^{-3}\,\Omega\,\mathrm{cm}^2$. Surface analysis showed that the KOH removed the native oxide, which apparently inhibits hole transport from metal-to-GaN.

E. Dry etching

Due to limited wet chemical etch results for the group-III nitrides, a significant amount of effort has been devoted to the development of dry etch processing.[198–202] Dry etch development was initially focused on mesa structures where high etch rates, anisotropic profiles, smooth sidewalls, and equirate etching of dissimilar materials were required. For example, commercially available LEDs and laser facets for GaN-based laser diodes were patterned using reactive ion etch (RIE). However, as interest in high power, high temperature electronics[203–206] increased, etch requirements expanded to include smooth surface morphology, low plasma-induced damage, and selective etching of one layer over another occurred. Dry etch development is further complicated by the inert chemical nature and strong bond energies of the group-III nitrides as compared to other compound semiconductors. GaN has a bond energy of 8.92 eV/atom, InN 7.72 eV/atom, and AlN 11.52 eV/atom as compared to GaAs which has a bond energy of 6.52 eV/atom.[207] In this section we will review dry etch processes for the group-III nitrides.

1. Etch techniques

a. Plasma etching. Dry plasma etching has become the dominant patterning technique for the group-III nitrides due to the shortcomings in wet chemical etching. Plasma etching proceeds by either physical sputtering, chemical reaction, or a combination of the two often referred to as ion-assisted plasma etching. Physical sputtering is dominated by the ac-

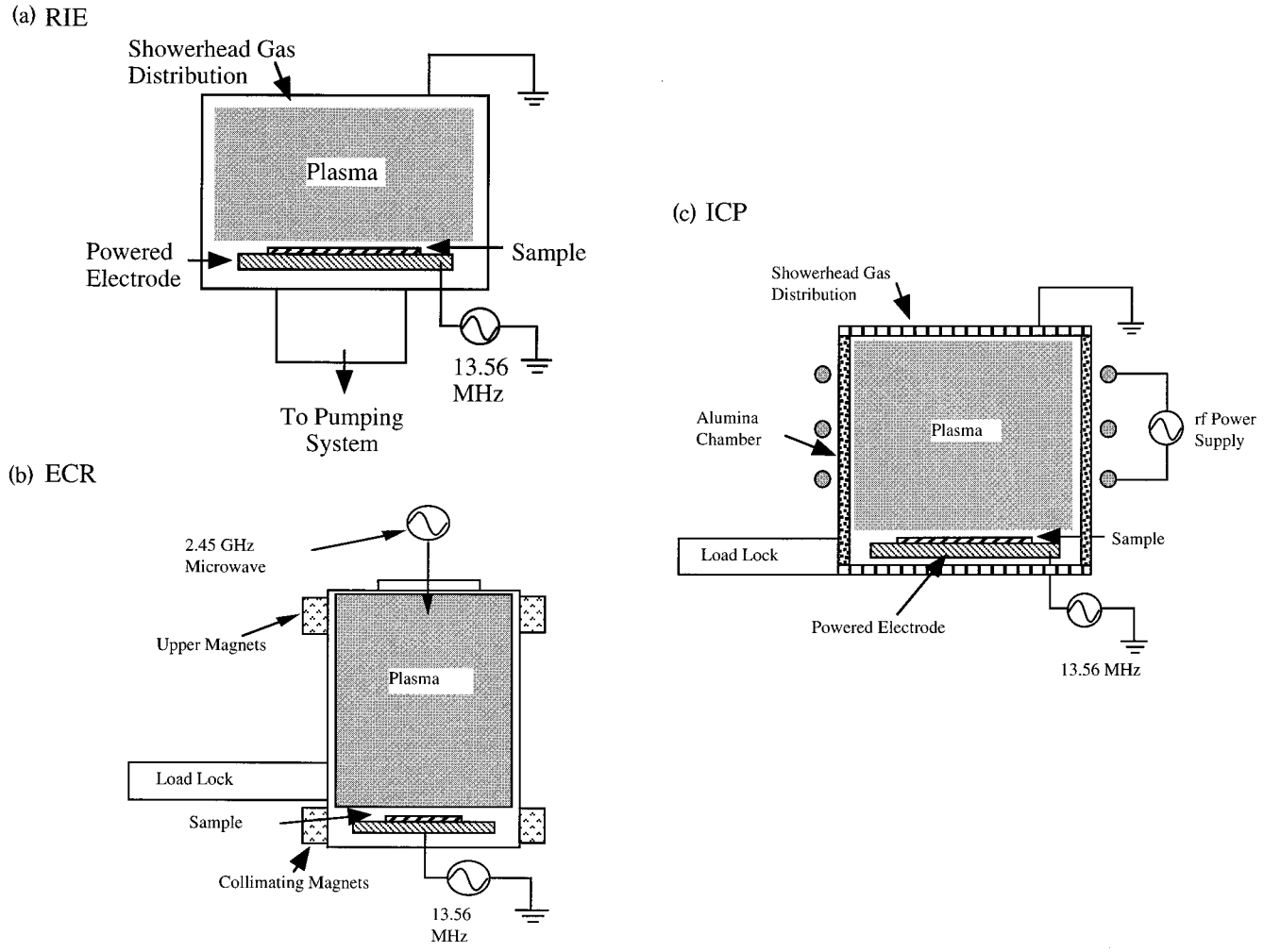

FIG. 47. Schematic diagram of (a) RIE, (b) ECR, and (c) ICP etch platforms.

celeration of energetic ions formed in the plasma to the substrate surface at relatively high energies, typically >200 eV. Due to the transfer of energy and momentum to the substrate, material is ejected from the surface. This sputter mechanism tends to yield anisotropic profiles; however, it can result in significant damage, rough surface morphology, trenching, poor selectivity, and nonstoichiometric surfaces thus minimizing device performance. Pearton and co-workers measured sputter rates for GaN, InN, AlN, and InGaN as a function of Ar^+ ion energy.[208] The sputter rates increased with ion energy but were quite slow, <600 Å/min, due to the high bond energies of the group III–N bond.

Chemically dominated etch mechanisms rely on the formation of reactive species in the plasma which adsorb to the surface, form volatile etch products, and then desorb from the surface. Since ion energies are relatively low, etch rates in the vertical and lateral direction are often similar thus resulting in isotropic etch profiles and loss of critical dimensions. However, due to the low ion energies used plasma-induced damage is minimized. Alternatively, ion-assisted plasma etching relies on both chemical reactions and physical sputtering to yield anisotropic profiles at reasonably high etch rates. Provided the chemical and physical components of the etch mechanism are balanced, high resolution features with minimal damage can be realized and optimum device performance can be obtained.

b. Reactive ion etching. RIE utilizes both the chemical and physical components of an etch mechanism to achieve anisotropic profiles, fast etch rates, and dimensional control. RIE plasmas are typically generated by applying radio frequency (rf) power of 13.56 MHz between two parallel electrodes in a reactive gas [see Fig. 47(a)]. The substrate is placed on the powered electrode where a potential is induced and ion energies, defined as they cross the plasma sheath, are typically a few hundred eV. RIE is operated at low pressures, ranging from a few mTorr up to 200 mTorr, which promotes anisotropic etching due to increased mean free paths and reduced collisional scattering of ions during acceleration in the sheath.

Adesida *et al.* were the first to report RIE of GaN in $SiCl_4$-based plasmas.[201] Etch rates increased with increasing dc bias, and were >500 Å/min at −400 V. Lin *et al.* reported similar results for GaN in BCl_3 and $SiCl_4$ plasmas with etch rates of 1050 Å/min in BCl_3 at 150 W cathode (area 250 $in.^2$) rf power.[209] Additional RIE results have been reported for HBr-,[210] CHF_3-, and CCl_2F_2-based[211] plasmas with etch rates typically <600 Å/min. The best RIE results for the group-III nitrides have been obtained in chlorine-

based plasmas under high ion energy conditions where the III–N bond breaking and the sputter desorption of etch products from the surface are most efficient. Under these conditions, plasma damage can occur and degrade both electrical and optical device performance. Lowering the ion energy or increasing the chemical activity in the plasma to minimize the damage often results in slower etch rates or less anisotropic profiles which significantly limits critical dimensions. Therefore, it is necessary to pursue alternative etch platforms which combine high quality etch characteristics with low damage.

c. High-density plasma etching. The use of high-density plasma etch systems including electron cyclotron resonance (ECR), inductively coupled plasma (ICP), and magnetron RIE (MRIE), has resulted in improved etch characteristics for the group-III nitrides as compared to RIE. This observation is attributed to plasma densities which are 2 to 4 orders of magnitude higher than RIE thus improving the III–N bond breaking efficiency and the sputter desorption of etch products formed on the surface. Additionally, since ion energy and ion density can be more effectively decoupled as compared to RIE, plasma-induced damage is more readily controlled. Figure 47(b) shows a schematic diagram of a typical low profile ECR etch system. High-density ECR plasmas are formed at low pressures with low plasma potentials and ion energies due to magnetic confinement of electrons in the source region. The sample is located downstream from the source to minimize exposure to the plasma and to reduce the physical component of the etch mechanism. Anisotropic etching can be achieved by superimposing an rf bias (13.56 MHz) on the sample and operating at low pressure (<5 mTorr) to minimize ion scattering and lateral etching. However, as the rf biasing is increased the potential for damage to the surface increases.

Pearton and co-workers were the first to report ECR etching of group-III nitride films.[212,213] Etch rates for GaN, InN, and AlN increased as either the ion energy (dc bias) or ion flux (ECR source power) increased. Etch rates of 1100 Å/min for AlN and 700 Å/min for GaN at -150 V dc bias in a Cl_2/H_2 plasma and 350 Å/min for InN in a $CH_4/H_2/Ar$ plasma at -250 V dc bias were reported. The etched features were anisotropic and the surface remained stoichiometric over a wide range of plasma conditions. GaN ECR etch data has been reported by several authors with etch rates as high as 1.3 μm/min.[214–225]

ICP offers another high-density plasma etch platform to pattern group-III nitrides. ICP plasmas are formed in a dielectric vessel encircled by an inductive coil into which rf power is applied [see Fig. 47(c)]. The alternating electric field between the coils induces as strong alternating magnetic field trapping electrons in the center of the chamber and generating a high-density plasma. Since ion energy and plasma density can be effectively decoupled, uniform density and energy distributions are transferred to the sample while keeping ion and electron energy low. Thus, ICP etching can produce low damage while maintaining fast etch rates. Anisotropy is achieved by superimposing a rf bias on the sample. ICP etching is generally believed to have several advantages over ECR including easier scale-up for production, improved plasma uniformity over a wider area, and lower cost-of-operation. The first ICP etch results for GaN were reported in a $Cl_2/H_2/Ar$ ICP-generated plasma with etch rates as high as $\sim$6875 Å/min.[226,227] Etch rates increased with increasing dc bias and etch profiles were highly anisotropic with smooth etch morphologies over a wide range of plasma conditions. GaN etching has also been reported in a variety of halogen- and methane-based ICP plasmas.[228–237]

MRIE is another high-density etch platform which is comparable to RIE. In MRIE, a magnetic field is used to confine electrons close to the sample and minimize electron loss to the wall.[238–240] Under these conditions, ionization efficiencies are increased and high plasma densities and fast etch rates are achieved at much lower dc biases (less damage) as compared to RIE. GaN etch rates of $\sim$3500 Å/min were reported in BCl_3-based plasmas at dc biases <-100 V.[240] The etch was fairly smooth and anisotropic.

d. Additional plasma etch platforms. Chemically assisted ion beam etching (CAIBE) and reactive ion beam etching (RIBE) have also been used to etch group-III nitride films.[202,241–245] In these processes, ions are generated in a high-density plasma source and accelerated by one or more grids to the substrate. In CAIBE, reactive gases are added to the plasma downstream of the acceleration grids thus enhancing the chemical component of the etch mechanism, whereas in RIBE, reactive gases are introduced in the ion source. Both etch platforms rely on relatively energetic ions (200–2000 eV) and low chamber pressures (<5 mTorr) to achieve anisotropic etch profiles. However, with such high ion energies, the potential for plasma-induced damage exists. Adesida and co-workers reported CAIBE etch rates for GaN as high as 2100 Å/min with 500 eV Ar^+ ions and Cl_2 or HCl ambients.[201,241–243] Rates increased with beam current, reactive gas flow rate, and substrate temperature. Anisotropic profiles with smooth etch morphologies were observed. GaN etch rates of $\sim$500 Å/min have been obtained in a RIBE-generated Cl_2/Ar plasma at beam voltages of 600 V.[245] RIBE etch profiles were anisotropic with slight trenching at the base of the feature.

Low energy electron enhanced etching (LE4) of GaN has been reported by Gillis and co-workers.[199,246–248] LE4 is an etch technique which depends on the interaction of low energy electrons (<15 eV) and reactive species at the substrate surface. The etch process results in minimal surface damage since there is negligible momentum transferred from the electrons to the substrate. GaN etch rates of $\sim$500 Å/min in a H_2-based LE4 plasma and $\sim$2500 Å/min in a pure Cl_2 LE4 plasma have been reported.[199,248] GaN has also been etched using photoassisted dry etch processes where the substrate is exposed to a reactive gas and ultraviolet laser radiation simultaneously. Vibrational and electronic excitations lead to improved bond breaking and desorption of reactant products. Leonard and Bedair reported GaN etch rates <80 Å/min in HCl using 193 nm ArF excimer laser. [249]

GaN etch rates are compared in Fig. 48 for RIE, ECR, and ICP $Cl_2/H_2/CH_4/Ar$ plasmas as well as a RIBE Cl_2/Ar plasma. CH_4 and H_2 were removed from the plasma chemistry to eliminate polymer deposition in the RIBE chamber. Etch rates increased as a function of dc bias independent of

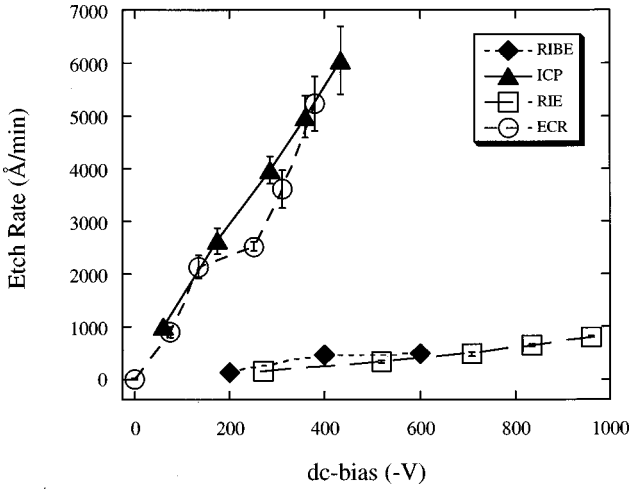

FIG. 48. GaN etch rates in RIE, ECR, ICP, and RIBE Cl_2-based plasmas as a function of dc bias.

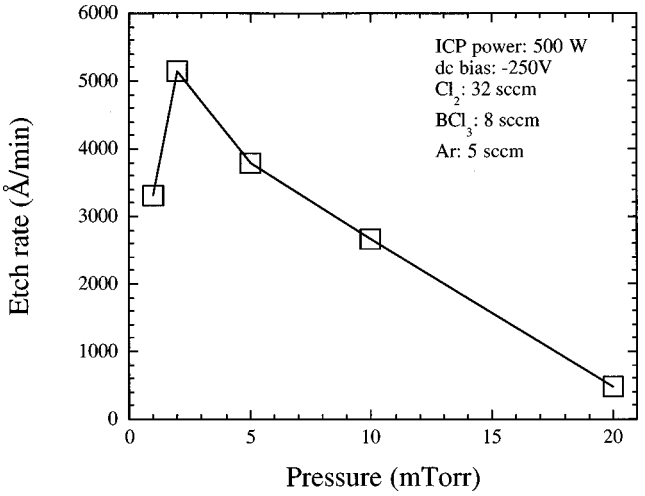

FIG. 49. GaN etch rates as a function of pressure in an ICP-generated $BCl_3/Cl_2/Ar$ plasma at 32 sccm Cl_2, 8 sccm BCl_5, 5 sccm Ar, 500 W ICP source power, dc-bias −250 V, and 10 °C electrode temperature.

etch technique. GaN etch rates obtained in the ICP and ECR plasmas were much faster than those obtained in RIE and RIBE. This was attributed to higher plasma densities (1–4 orders of magnitude higher) which resulted in more efficient breaking of the III–N bond and sputter desorption of the etch products. Slower rates observed in the RIBE may also be due to lower operational pressures (0.3 mTorr compared to 2 mTorr for the ICP and ECR) and/or lower ion and reactive neutral flux at the GaN surface due to the high source-to-sample separation.

2. Dry etch plasma parameters: Pressure, ion energy, and plasma density

Etch characteristics are often dependent upon plasma parameters including pressure, ion energy, and plasma density. As a function of pressure, plasma conditions including the mean free path and the collisional frequency can change resulting in changes in both ion energy and plasma density. GaN etch rates are shown as a function of pressure for an ICP-generated BCl_3/Cl_2 plasma in Fig. 49. Etch rates increased as the pressure was increased from 1 to 2 mTorr and then decreased at higher pressures. The initial increase in etch rate suggested a reactant limited regime at low pressure, however at higher pressures the etch rates decreased due either to lower plasma densities (ions or radical neutrals), redeposition, or polymer formation on the substrate surface. At pressures <10 mTorr, GaN etches were anisotropic and smooth, while at pressure >10 mTorr the etch profile was undercut and poorly defined due to a lower mean free path, collisional scattering of the ions, and increased lateral etching of the GaN.

GaN etch rates are plotted as a function of dc bias (which correlates to ion energy) for an ICP-generated BCl_3/Cl_2 plasma in Fig. 50. The GaN etch rates increased monotonically as the dc bias or ion energy increased. Etch rates increased due to improved sputter desorption of etch products from the surface as well as more efficient breaking of the Ga–N bonds. Etch rates have also been observed to decrease under high ion bombardment energies due to sputter desorption of reactive species from the surface before the reactions occur. This is often referred to as an adsorption limited etch regime. In Fig. 51, SEM micrographs are shown for (a) −50, (b) −150, and (c) −300 V dc bias. The etch profile became more anisotropic as the dc bias increased from −50 to −150 V dc bias due to the perpendicular path of the ions relative to the substrate surface which maintained straight wall profiles. However, as the dc bias was increased to −300 V, a tiered etch profile with vertical striations in the sidewall was observed due to erosion of the resist mask edge. The GaN may become rougher at these conditions due to mask redeposition and preferential loss of N_2.

In Fig. 52, GaN etch rates are shown as a function of ICP-source power while the dc bias was held constant at −250 V. GaN etch rates increased as the ICP source power increased due to higher concentrations of reactive species which increases the chemical component of the etch mechanism and/or higher ion flux which increases the bond breaking and sputter desorption efficiency of the etch. Etch rates

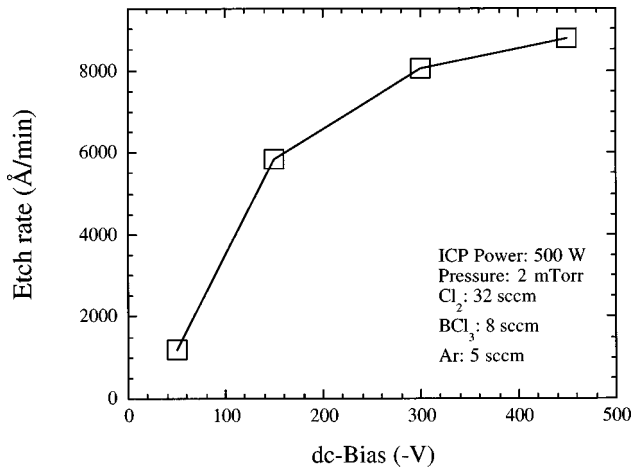

FIG. 50. GaN etch rates as a function of dc bias in an ICP-generated $BCl_3/Cl_2/Ar$ plasma at 32 sccm Cl_2, 8 sccm BCl_3, 5 sccm Ar, 500 W ICP source power, 2 mTorr pressure, and 10 °C electrode temperature.

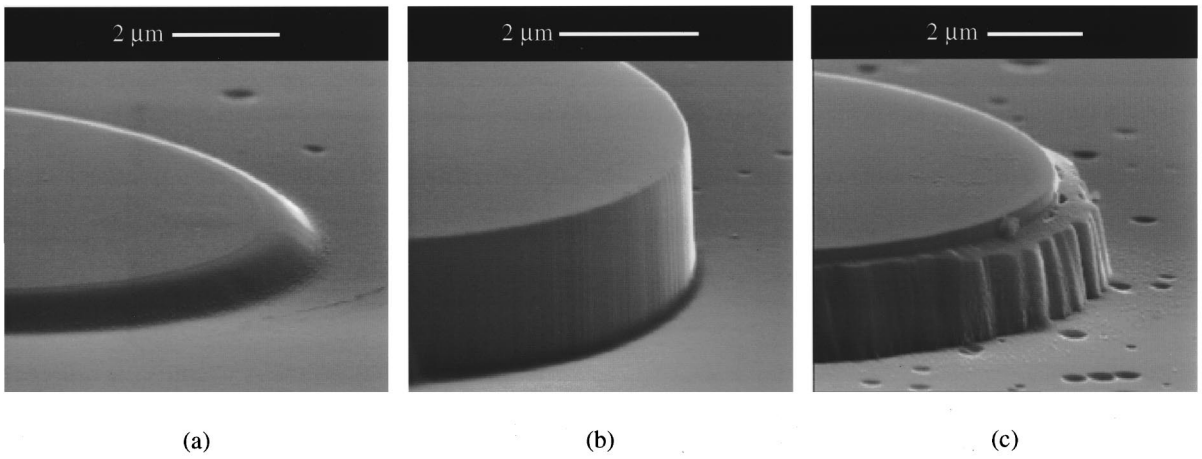

FIG. 51. SEM micrographs for GaN etched at (a) −50, (b) −150, and (c) −300 V dc bias. ICP etch conditions were 32 sccm Cl_2, 8 sccm BCl_3, 5 sccm Ar, 500 W ICP source power, 2 mTorr pressure, and 10 °C electrode temperature.

have also been observed to stabilize or decrease under high plasma flux conditions due either to saturation of reactive species at the surface or sputter desorption of reactive species from the surface before the reactions occur. The etch profile was anisotropic and smooth up to 1000 W ICP power where the feature dimensions were lost and sidewall morphology was rough due to erosion of the mask edge under high plasma flux conditions.

In addition to etch rates, etch selectivity or the ability to etch one film at higher rates than another can be very important in device fabrication. For example, optimization of etch selectivity is critical to control threshold voltage uniformity for high electron mobility transistors (HEMTs), to accurately stop on either the emitter or collector regions for metal contacts for heterojunction bipolar transistors (HBTs), and for low resistivity *n*-ohmic contacts on InN layers. Several studies have recently reported etch selectivity for the group-III nitrides.[233,236,250–254] For example, Fig. 53 shows GaN, InN, and AlN etch rates and etch selectivities as a function of cathode rf power in an ICP-generated Cl_2/Ar plasma. Etch rates for all three films increased with increasing cathode rf power or dc bias due to improved breaking of the III–N bonds and more efficient sputter desorption of the etch products. Increasing InN etch rates were especially significant since $InCl_3$, the primary In etch product in a Cl-based

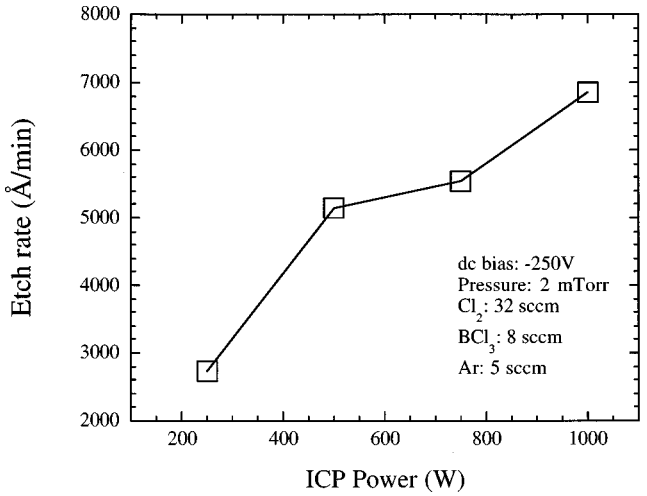

FIG. 52. GaN etch rates as a function of ICP source power in an ICP-generated BCl_3/Cl_2/Ar plasma at 32 sccm Cl_2, 8 sccm BCl_3, 5 sccm Ar, −250 V dc bias, 2 mTorr pressure, and 10 °C electrode temperature.

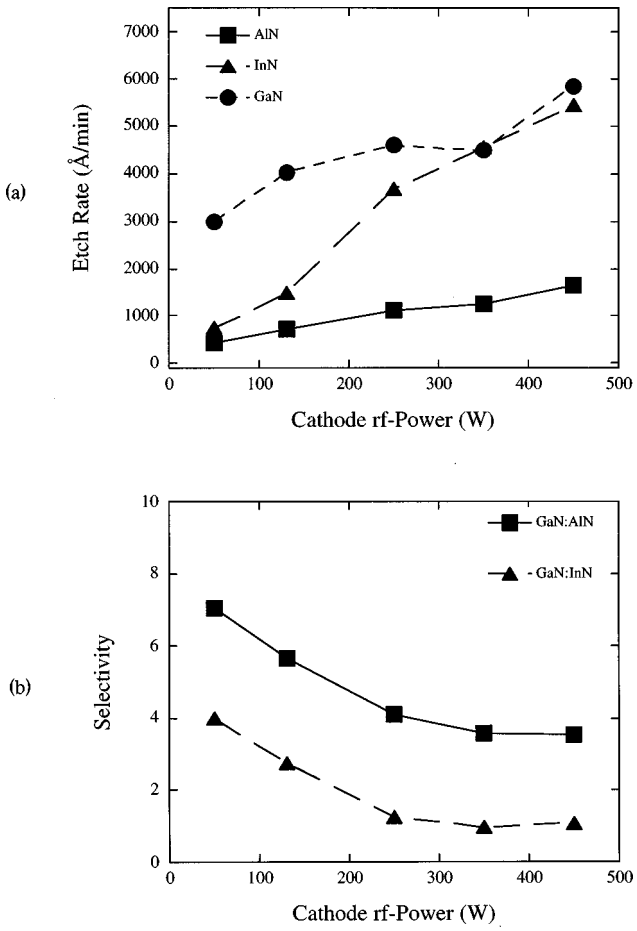

FIG. 53. GaN, InN, and AlN (a) etch rates and (b) GaN:AlN and GaN:InN etch selectivities as a function of dc bias in a Cl_2/Ar ICP plasma. Plasma conditions were: 25 sccm Cl_2, 5 sccm Ar, 2 mTorr chamber pressure, 500 W ICP-source power, and 25 °C cathode temperature.

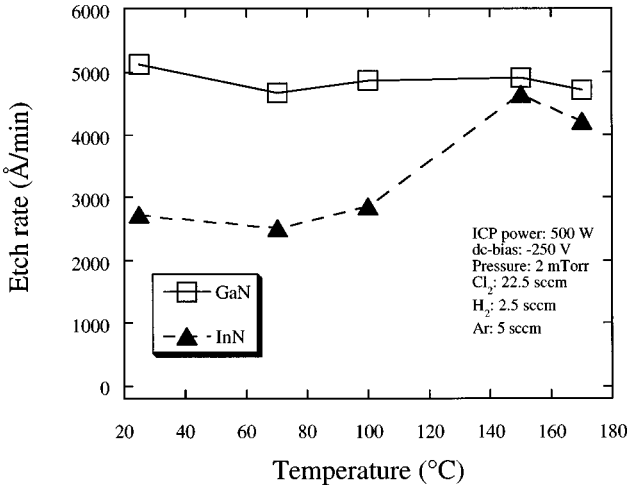

FIG. 54. GaN and InN etch rates as a function of temperature for an ICP-generated $Cl_2/H_2/Ar$ plasmas. ICP etch conditions were 22.5 sccm Cl_2, 2.5 sccm H_2, 5 sccm Ar, 500 W ICP source power, −250 V dc bias, and 2 mTorr pressure.

plasma, has a relatively low volatility. However, under high dc-bias conditions, desorption of the $InCl_3$ etch products occurred prior to coverage of the etch surface.[251] The GaN:InN and GaN:AlN etch selectivities were <8:1 and decreased as the cathode rf power or ion energy increased. Smith and co-workers reported similar results in a Cl_2/Ar ICP plasma where GaN:AlN and GaN:AlGaN selectivities decreased as dc bias increased.[236] At −20 V dc bias, etch selectivities of ~38:1 were reported for GaN:AlN and ~10:1 for GaN:AlGaN.

3. Temperature dependent etching

Temperature dependent etching of the group-III nitrides have been reported in ECR and ICP etch systems.[215,225,237] Etch rates are often influenced by the substrate temperature which can effect the desorption rate of etch products, the gas-surface reaction kinetics, and the surface mobility of reactants. Substrate temperature can be controlled and maintained during the etch process by a variety of clamping and backside heating or cooling procedures. GaN and InN etch rates are shown in Fig. 54 as a function of temperature in a $Cl_2/H_2/Ar$ ICP plasma. GaN etch rates were much faster than InN due to higher volatility of the $GaCl_3$ etch products as compared to $InCl_3$ and showed little dependence on temperature. However, the InN etch rates showed a considerable temperature dependence increasing at 150 °C due to higher volatilities of the $InCl_3$ etch products at higher substrate temperatures.

4. Plasma chemistry

Several different plasma chemistries have been used to etch the group-III nitrides. As established above, etch rates and profiles can be strongly affected by the volatility of the etch products formed. Table VI shows the boiling points of possible etch products for the group-III nitrides exposed to halogen- and hydrocarbon-based plasmas. For halogen-based plasmas, etch rates are often limited by the volatility of the

TABLE VI. Boiling points for possible etch products of group-III nitride films etched in halogen- or CH_4/H_2-based plasmas.

Etch products	Boiling points (°C)
$AlCl_3$	183
AlF_3	na
AlI_3	360
$AlBr_3$	263
$(CH_3)_3Al$	126
$GaCl_3$	201
GaF_3	1000
GaI_3	sublimes 345
$GaBr_3$	279
$(CH_3)_3Ga$	55.7
$InCl_3$	600
InF_3	>1200
InI_3	na
$InBr_3$	sublimes
$(CH_3)_3In$	134
NCl_3	<71
NF_3	−129
NBr_3	na
NI_3	explodes
NH_3	−33
N_2	−196
$(CH_3)_3N$	−33

group-III halogen etch product. For Ga- and Al-containing films, chlorine-based plasmas typically yield fast rates with anisotropic, smooth etch profiles. CH_4/H_2-based plasma chemistries have also yielded smooth, anisotropic profiles for Ga-containing films, however at much slower rates. Based only on a comparison of etch product volatility, slower etch rates in CH_4-based plasmas is unexpected since the $(CH_3)_3Ga$ etch product has a much lower boiling point than $GaCl_3$. This observation demonstrates the complexity of the etch process where redeposition, polymer formation, and gas-phase kinetics can influence the results. As shown above, etch rates for In-containing films obtained in room temperature chlorine-based plasmas tend to be slow with rough surface morphology and overcut profiles due to the low volatility of the $InCl_3$ and preferential loss of the group-V etch products. However, at elevated temperatures (>130 °C), the $InCl_3$ volatility increases and the etch rates and surface morphology improve.[215,225,237,255–257] Significantly better room temperature etch results are obtained in CH_4/H_2-based plasmas due to the formation of more volatile $(CH_3)_3In$ etch products.[213,258]

The source of reactive plasma species and the addition of secondary gases to the plasma can vary etch rates, anisotropy, selectivity, and morphology. The fragmentation pattern and gas-phase kinetics associated with the source gas can have a significant effect on the concentration of reactive neutrals and ions generated in the plasma thus affecting the etch characteristics. Secondary gas additions and variations in gas ratios can change the chemical: physical ratio of the etch mechanism. The effect of Ar, SF_6, N_2, and H_2 additions to Cl_2- and BCl_3-based ICP and ECR plasmas for GaN etching has been reported.[259] In general, GaN etch rates were faster in Cl_2-based plasmas as compared to BCl_3 due to higher concentrations of reactive Cl. The addition of H_2, N_2, or SF_6

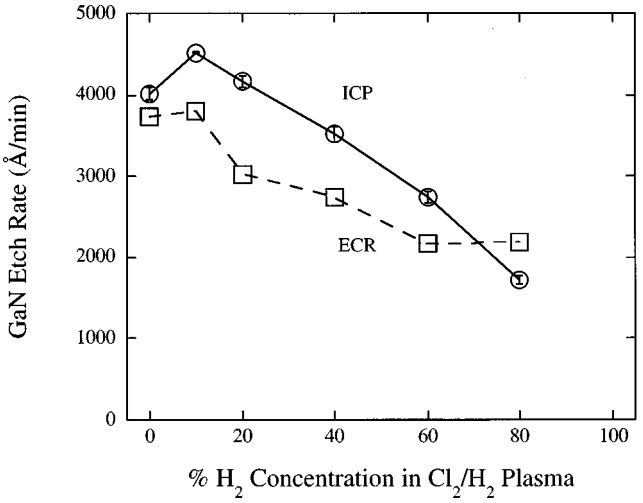

FIG. 55. GaN etch rates in an ICP and ECR Cl_2H_2/Ar plasma as a function of $\%H_2$.

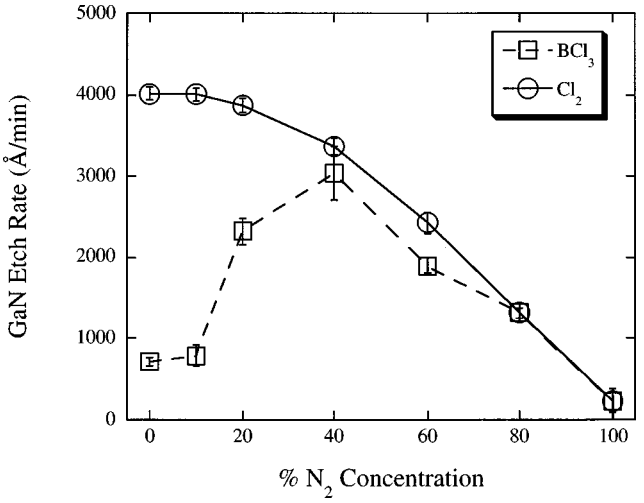

FIG. 57. GaN etch rates as a function of $\%N_2$ for ICP-generated Cl_2- and BCl_3-based plasmas.

to either Cl_2- or BCl_3-based plasmas changed the relative concentration of reactive Cl in the plasma which directly correlated to the GaN etch rate. For example, in Fig. 55, GaN etch rates are shown as a function of % H_2 concentration for ECR- and ICP-generated $Cl_2/H_2/Ar$ plasmas. GaN etch rates in the ECR and ICP increased slightly as H_2 was initially added to the Cl_2/Ar plasma indicating a reactant limited regime. Monitoring the ECR plasma with a quadrupole mass spectrometry (QMS) showed that the Cl concentration (indicated by $m/e=35$) remained relatively constant at 10% H_2. As the H_2 concentration was increased above 10%, the Cl concentration decreased and a peak corresponding to HCl increased. GaN etch rates decreased at H_2 concentrations $>10\%$ in both the ECR and ICP, presumably due to the consumption of reactive Cl by hydrogen. In Fig. 56, H_2 was added to BCl_3-based ECR and ICP plasmas. In the ECR plasma, the GaN etch rate increased at 10% H_2 corresponding with an increase in the reactive Cl concentration as observed by QMS. As the H_2 concentration was increased further, GaN etch rates decreased, the Cl concentration decreased, and the HCl concentration increased presumably due to the consumption of reactive Cl by hydrogen. In the ICP reactor, GaN etch rates were slow and decreased as hydrogen was added to the plasma up to 80% H_2 where a slight increase was observed.

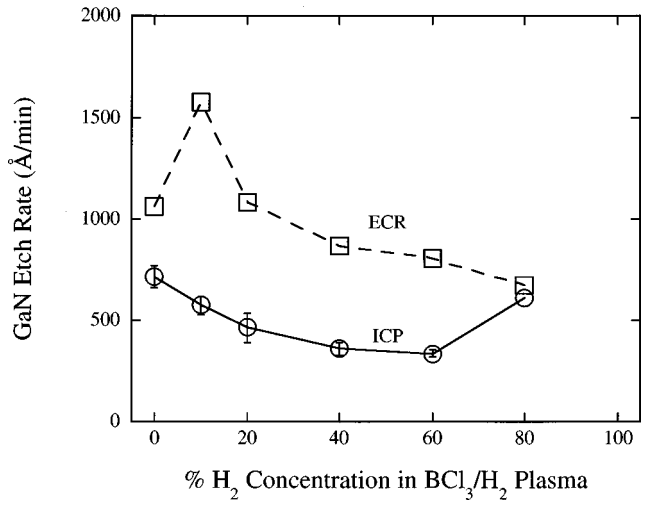

FIG. 56. GaN etch rates in an ICP and ECR $BCl_3/H_2/Ar$ plasma as a function of $\%H_2$.

Another example of plasma chemistry dependent etching of GaN is shown in Fig. 57 for $Cl_2/N_2/Ar$ and $BCl_3/N_2/Ar$ ICP-generated plasmas. In the Cl_2-based plasma, GaN etch rates decreased as the % N_2 increased, presumable due to a reduction in reactive Cl. In the BCl-based plasma GaN etch rates increased up to 40% N_2 and then decreased at higher N_2 concentrations. This observation has also been reported for ECR and ICP etching of GaAs, GaP, and In-containing films.[260–262] Ren and co-workers first observed maximum etch rates for In-containing films (InGaN and InGaP) in an ECR discharge at a gas ratio of 75/25 for BCl_3/N_2.[260] Using optical emission spectroscopy (OES), Ren reported maximum emission intensity for atomic and molecular Cl at 75% BCl_3 as well as a decrease in the BCl_3 intensity and the appearance of a BN emission line. The authors speculated that N_2 enhanced the dissociation of BCl_3 resulting in higher concentrations of reactive Cl and Cl ions and thus higher etch rates. Additionally, the observation of BN emission suggested that less B was available to recombine with reactive Cl. This explanation may also be applied to the peak GaN etch rates observed at 40% N_2 in the ICP $BCl_3/N_2/Ar$ plasmas. However, OES of the $BCl_3/N_2/Ar$ ICP discharge did not reveal higher concentrations of reactive Cl nor a BN peak emission. In Fig. 58, OES spectra are shown for (a) 100% BCl_3, (b) 75% BCl_3–25% N_2, (c) 25% BCl_3–75% N_2, and (d) 100% N_2 ICP plasmas. As N_2 was added to the BCl_3 plasma, the BCl_3 emission (2710 Å) and Cl emission (5443 and 5560 Å) decreased while the BN emission (3856Å) was not obvious.

BCl_3/Cl_2 plasmas have shown encouraging results in the etching of GaN films.[228,235] The addition of BCl_3 to a Cl_2 plasma can improve sputter desorption due to higher mass ions and reduce surface oxidation by gettering H_2O from the

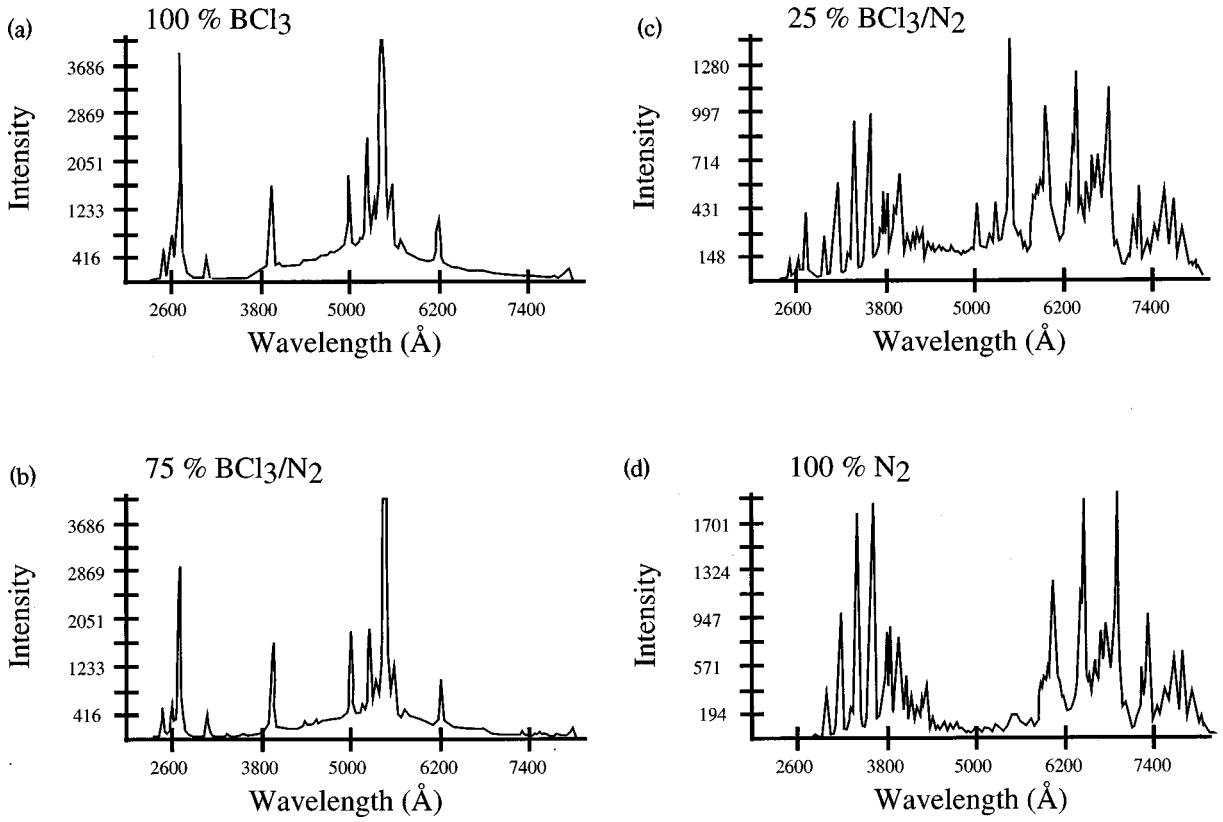

FIG. 58. Optical emission spectra (OES) for an ICP-generated BCl_3/N_2 plasma as a function of BCl_3 percentage.

chamber. In Fig. 59, GaN etch rates are shown as a function of % Cl_2 in a $BCl_3/Cl_2/Ar$ ICP plasma. As the % Cl_2 increased, GaN etch rates increased up to 80% due to higher concentrations of reactive Cl. OES showed the Cl emission intensity increased and the BCl emission intensity decreased as the % Cl_2 increased. Slower GaN etch rates in a pure Cl_2 plasma were attributed to less efficient sputter desorption of etch products in the absence of BCl_3. Similar results were reported by Lee *et al.*[228] The fastest GaN etch rates were observed at 10% BCl_3 where the ion current density and Cl radical density were the greatest as measured by OES and a Langmuir probe.

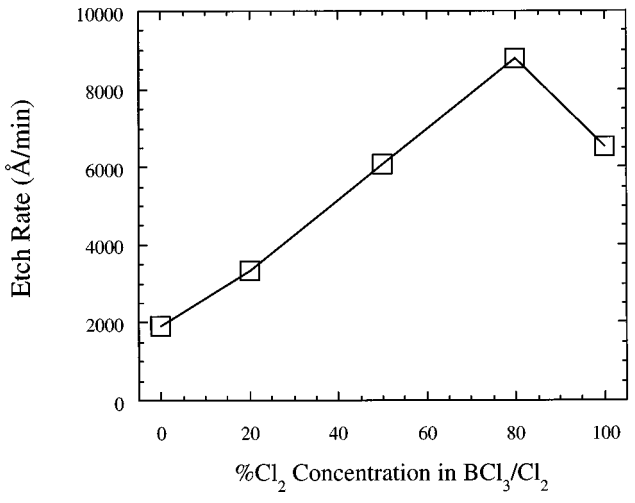

FIG. 59. GaN etch rates in an ICP BCl_3/Cl_2 plasmas as a function of $\%Cl_2$.

In general, GaN:AlN and GaN:InN etch selectivities are $<10:1$ as a function of plasma chemistry for Cl_2- or BCl_3-based plasmas. GaN:AlN and GaN:InN etch selectivities were higher for Cl_2-based ICP plasmas as compared to BCl_3-based ICP plasmas due to higher concentrations of reactive Cl produced in the Cl_2-based plasmas thus resulting in faster GaN etch rates.[254] Alternatively, InN and AlN etch rates showed much less dependence on plasma chemistry and were fairly comparable in Cl_2 and BCl_3-based plasmas. An example of etch selectivity dependence on plasma chemistry is shown in Fig. 60. GaN, AlN, and InN etch rates and etch selectivities are plotted as a function of % SF_6 for an ICP $Cl_2/SF_6/Ar$ plasma. GaN and InN etch rates decreased as SF_6 was added to the plasma due to the consumption of Cl by S and therefore lower concentrations of reactive Cl. The AlN etch rates increased with the addition of SF_6 and reached a maximum at 20% SF_6. As SF_6 was added to the Cl_2 plasma, slower AlN etch rates were expected due to the formation of low volatility AlF_3 etch products. However, due to the high ion flux in the ICP, the sputter desorption of the AlF_3 may occur prior to passivation of the surface.[251] Therefore, the GaN:AlN selectivity decreased rapidly from ~6:1 to $<1:1$ with the addition of SF_6. The GaN:InN selectivity reached a maximum of 4:1 at 20% SF_6.

Other halogen-containing plasmas including ICl/Ar, IBr/Ar, BBr_3/Ar, and BI_3/Ar have been used to etch GaN with promising results.[221,250,263–265] Vartuli and co-workers re-

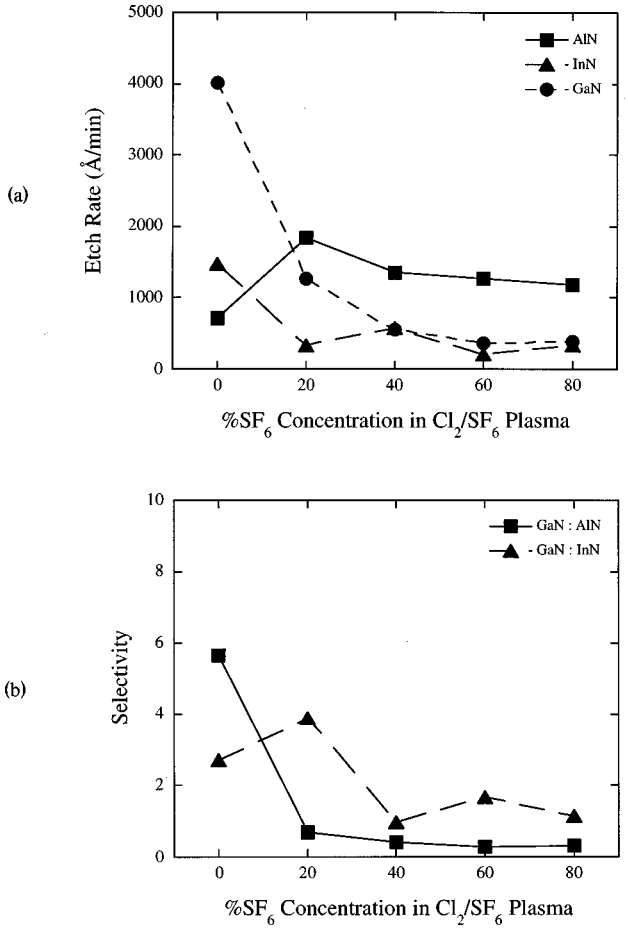

FIG. 60. GaN, InN and AlN (a) etch rates and (b) GaN:AlN and GaN:InN etch selectivities as a function of $\%SF_6$ in a $Cl_2/SF_6/Ar$ ICP plasma.

ported GaN, InN, AlN, InN, InAlN, and InGaN etch rates and selectivities in ECR ICl/Ar and IBr/Ar plasmas.[250] In general, etch rates increased for all films as a function of dc bias due to improved III–N bond breaking and sputter desorption of etch products form the surface. GaN etch rates >1.3 μm/min were obtained in the ICl/Ar plasma at a rf power of 250 W[221] (bias of -200 V) while GaN etch rates were typically <4000 Å/min in IBr/Ar.[264] Cho *et al.* reported GaN etch rates typically <2000 Å/min in ICP-generated BI_3/Ar and BBr_3/Ar plasmas.[265] ICl/Ar and IBr/Ar ECR plasmas yielded GaN:InN, GaN:AlN, GaN:InGaN, and GaN:InAlN selectivities $<6:1$, however, etch selectivities $>100:1$ were obtained for InN:GaN and InN:AlN in BI_3/Ar plasmas.[250,251,263–265] Fast etch rates obtained for InN were attributed to the high volatility of the InI_3 etch products as compared to the GaI_3 and AlI_3 etch products which can form passivation layers on the surface. Maximum selectivities of $\sim 100:1$ for InN:AlN and ~ 7.5 for InN:GaN were reported in the BBr_3/Ar plasma.[265]

Pearton and co-workers were the first to etch group-III nitride films in an ECR-generated $CH_4/H_2/Ar$ plasmas.[213] Etch rates for GaN, InN, and AlN were <400 Å/ min at ~ -250 V dc bias. Vartuli *et al.* reported ICP GaN, InN, and AlN etch rates approaching 2500 Å/min in $CH_4/H_2/Ar$ and $CH_4/H_2/N_2$ plasmas.[266] Etch rates increased with increasing dc bias or ion flux and were higher in $CH_4/H_2/Ar$ plasmas. Anisotropy and surface morphology were good over a wide range of conditions. As compared to Cl-based plasmas, etch rates were consistently slower which may make the CH_4/H_2-based processes applicable for devices where etch depths are relatively shallow and etch control is extremely important.

Vartuli and co-workers compared etch selectivities in $CH_4/H_2/Ar$ and Cl_2/Ar plasmas in both RIE- and ECR-generated plasmas.[251] For $CH_4/H_2/Ar$ plasmas, InN:GaN and InGaN:GaN etch selectivities ranged from $\sim 1:1$ to 6:1 whereas etch selectivities of 1:1 or favoring GaN over the In-containing films was reported for Cl_2/Ar plasmas.

5. Etch profile and etched surface morphology

Etch profile and etched surface morphology can be critical to postetch processing steps including the formation of metal contacts, deposition of interlevel dielectric or passivation films, or epitaxial regrowth. Figure 61 shows SEM micrographs of GaN, AlN, and InN etched in Cl_2-based plasmas. The GaN [Fig. 61(a)] was etched at 5 mTorr chamber pressure, 500 W ICP power, 22.5 sccm Cl_2, 2.5 sccm H_2, 5 sccm Ar, 25 °C temperature, and a dc bias of -280 ± 10 V. Under these conditions, the GaN etch rate was ~ 6880 Å/min with highly anisotropic, smooth sidewalls. The sapphire substrate was exposed during a 15% overetch. Pitting of the sapphire surface was attributed to defects in the substrate or growth process. The AlN [Fig. 61(b)] and InN [Fig. 61(c)] features were etched at 2 mTorr chamber pressure, 500 W

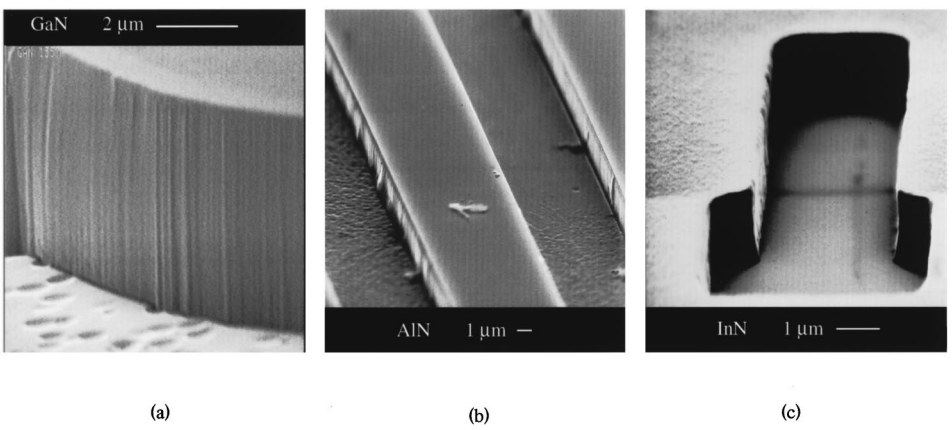

FIG. 61. SEM micrographs of (a) GaN, (b) AlN, and (c) InN etched in Cl_2-based ICP plasmas.

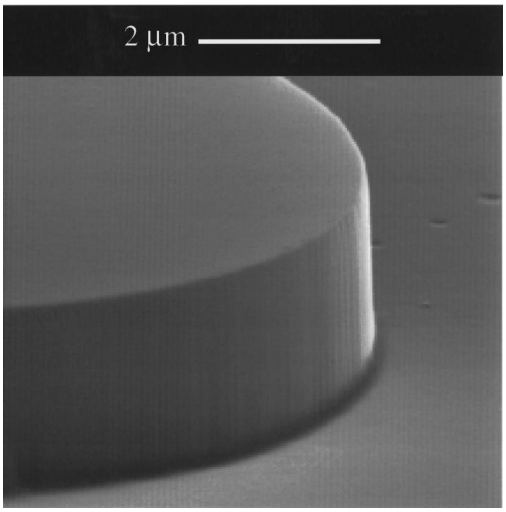

FIG. 62. SEM micrographs of GaN etched in a BCl_3/Cl_2-based ICP plasmas.

ICP power, 25 sccm Cl_2, 5 sccm Ar, 25 °C temperature, and a cathode rf power of 250 W. Under these conditions, the AlN etch rate was ~980 Å/min and the InN etch rate was ~1300 Å/min. Anisotropic profiles were obtained over a wide range of plasma chemistries and conditions, with sidewall striations present.

Sidewall morphology is especially critical in the formation of laser mesas for ridge waveguide emitters or for buried planar devices. The vertical striations observed in the GaN sidewall in Fig. 61(a) were due to striations in the photoresist mask which were transferred into the GaN feature during the etch. The sidewall morphology and in particular the vertical striations were improved in an ICP Cl_2/BCl_3 plasma at −150 V dc bias. In Fig. 62, a SEM micrograph of GaN etched in an ICP Cl_2/BCl_3 plasma shows highly anisotropic profiles and smooth sidewall morphology. The etch conditions were at 2 mTorr chamber pressure, 500 W ICP power, 32 sccm Cl_2, 8 sccm BCl_3, 5 sccm Ar, 25 °C temperature, and a dc bias of -150 ± 10 V. Ren *et al.* have demonstrated improved GaN sidewall morphology etched in an ECR using a SiO_2 mask.[267] Vertical striations in the SiO_2 mask were reduced by optimizing the lithography process used to pattern the SiO_2. The SiO_2 was then patterned in a SF_6/Ar plasma in which a low temperature dielectric overcoat was used to protect the resist sidewall during the etch.

In several studies atomic force microscopy (AFM) has been used to quantify the etched surface morphology as root-mean-square (rms) roughness. Rough etch morphology often indicates a nonstoichiometric surface due to preferential removal of either the group-III or group-V species. For example, in Fig. 63, GaN and InN rms roughnesses are shown for as-grown samples and for samples exposed to an ECR $Cl_2/H_2/CH_4$/Ar plasma as a function of cathode rf power. The rms roughnesses for as-grown GaN and InN was 3.21 ± 0.56 and 8.35 ± 0.50 nm, respectively. The GaN rms roughness increased as the cathode rf power was increased reaching a maximum of ~85 nm at 275 W. The rms roughness for InN was greatest at 65 W cathode rf power implying that the ion-bombardment energy is critical to balance the chemical and sputtering effect of this plasma chemistry to maintain smooth surface morphologies.

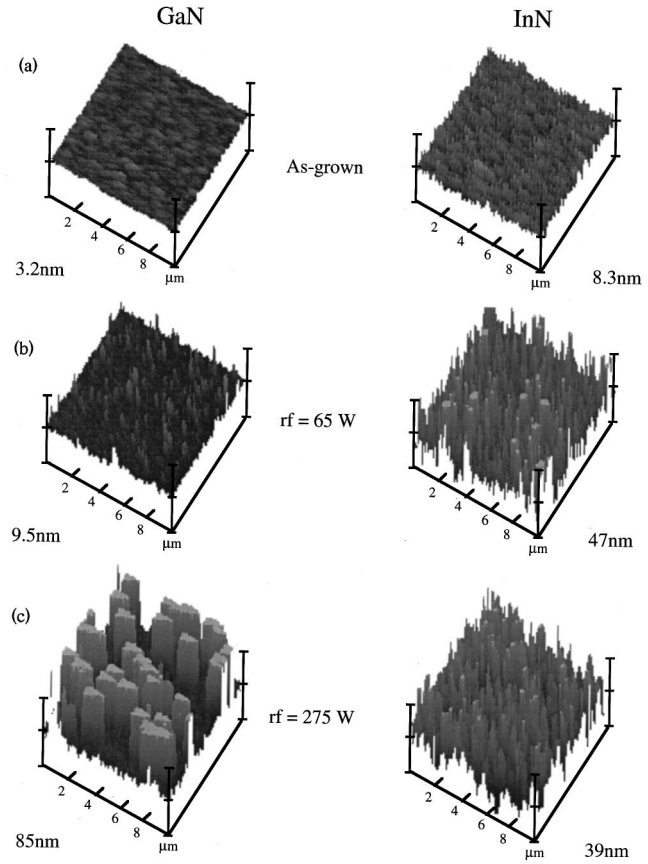

FIG. 63. AFM micrographs for (a) GaN and InN as-grown, (b) GaN and InN etched at a rf-cathode power of 65 W, and (c) GaN and InN etched at a rf-cathode power of 275 W in an ECR-generated $Cl_2/H_2/CH_4$/Ar plasma. The *Z* scale is 100 nm/division.

6. Plasma–induced damage

Plasma-induced damage often degrades the electrical and optical properties of compound semiconductor devices. Since GaN is more chemically inert than GaAs and has higher bonding energies, more aggressive etch conditions (higher ion energies and plasma flux) may be used with potentially less damage to the material. Limited data have been reported for plasma-induced damage of the group-III nitrides.[268–271] Pearton and co-workers reported increased plasma-induced damage as a function of ion flux and ion energy for InN, InGaN, and InAlN in an ECR.[268] The authors also reported; (a) more damage in InN films as compared to InGaN, (b) more damage in lower doped materials, and (c) more damage under high ion energy conditions due to formation of deep acceptor states which reduced the carrier mobility and increased resistivity. Postetch annealing processes removed the damage in the InGaN while the InN damage was not entirely removed.

Ren and co-workers measured electrical characteristics for InAlN and GaN FET structures to study plasma-induced damage for ECR BCl_3, BCl_3/N_2, and CH_4/H_2 plasmas.[269] They reported: (a) doping passivation in the channel layer in the presence of hydrogen; (b) high ion bombardment ener-

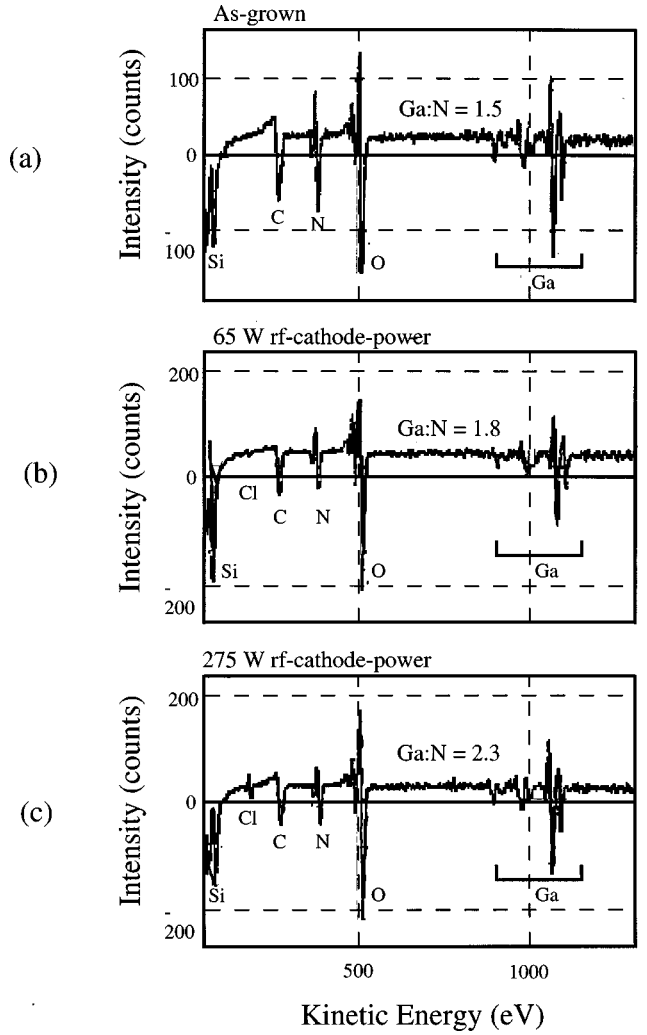

FIG. 64. AES surface scans of GaN (a) before exposure to the plasma, (b) at 65 W (−120 V bias), and (c) 275 W rf-cathode power (−325 V bias), 1 mTorr, 170 °C, and 850 W microwave power in an ECR-generated Cl_2/H_2 discharge.

gies can create deep acceptor states that compensate the material; and (c) preferential loss of N can produce rectifying gate characteristics. Ping and co-workers studied Schottky diodes for Ar and $SiCl_4$ RIE plasmas.[270] More damage was observed in pure Ar plasmas and under high dc-bias conditions. Plasma-induced damage of GaN was also evaluated in ICP and ECR Ar plasmas using photoluminescence (PL) measurements as a function of cathode rf power and source power.[271] The peak PL intensity decreased with increasing ion energy independent of etch technique. As a function of source power or plasma density the results were less consistent. The PL intensity showed virtually no change at low ICP source power and then decreased as the plasma density increased. In the ECR plasma, the PL intensity increased by ~115% at low ECR source power and improved at higher ECR source powers but at a lower rate. The effect of postetch annealing in Ar varied depending on initial film conditions, however, annealing at temperatures above 400 °C resulted in a reduction in the PL intensity.

Surface stoichiometry can also be used to evaluate plasma-induced damage. Nonstoichiometric surfaces can be

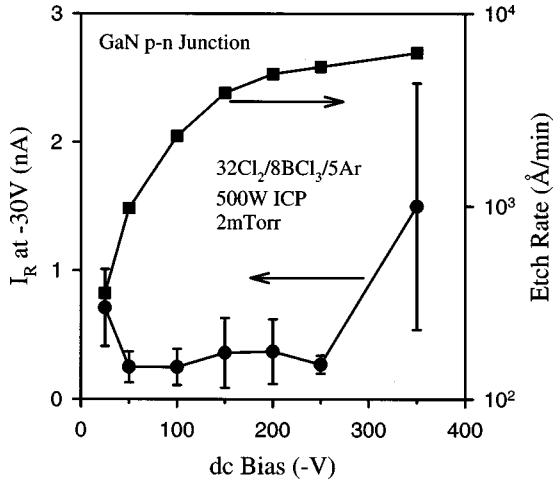

FIG. 65. Reverse leakage currents in GaN *p-i-n* diodes etched with different dc biases in $Cl_2/BCl_3/Ar$.

created by preferential loss of one of the lattice constituents. This may be attributed to higher volatility of the respective etch products, leading to enrichment of the less volatile species, or preferential sputtering of the lighter element. Auger electron spectroscopy (AES) can be used to measure surface stoichiometry. Figure 64 shows characteristic Auger spectra for (a) as-grown GaN samples and samples exposed to an ECR plasma at 850 W applied microwave power and cathode rf powers of (b) 65 and (c) 275 W. For the as-grown sample, the Auger spectrum showed a Ga:N ratio of 1.5 with normal amounts of adventitious carbon and native oxide on the GaN surface. Following plasma exposure, the Ga:N ratio increased as the cathode rf power increased with some residual atomic Cl from the plasma. Under high ion energy conditions, preferential removal of the lighter N atoms was observed resulting in Ga-rich surfaces.

Figures 65 and 66 show the influence of dc self-bias and ICP source power on the reverse leakage current of GaN *p-I-n* mesa diodes in which the mesas were created by dry etching. Clearly both ion energy and ion flux can influence the diode characteristics.

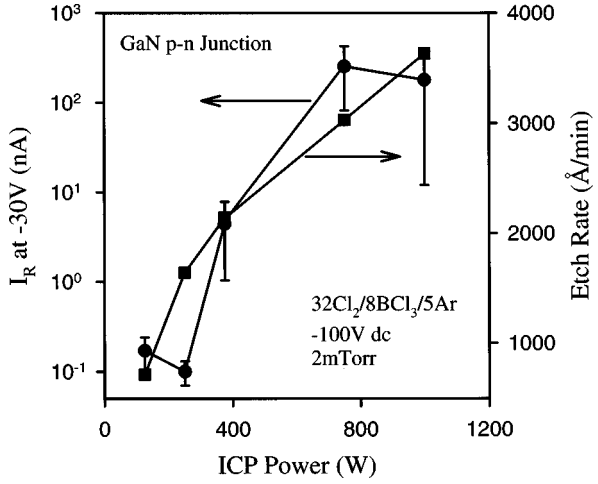

FIG. 66. Reverse leakage currents in GaN *p-i-n* diodes etched with different source powers in $Cl_2/BCl_3/Ar$.

7. Conclusions

Reliable, well-controlled patterning of the group-III nitrides can be achieved by a variety of dry etch platforms. In particular, high-density plasma ECR and ICP etch processes have yielded, smooth, highly anisotropic, etch characteristics with rates often exceeding 1.0 μm/min. These results are attributed to high ion and neutral flux which improves the III–N bond breaking efficiency and the sputter desorption of etch products formed on the surface. Halogen-based plasma chemistries, in particular Cl-, I-, and Br-based plasmas, yield high quality etch characteristics. The choice of source gas (Cl_2, BCl_3, ICl, IBr, BI_3, BBr_3, etc.) and secondary gases (H_2, N_2, SF_6, Ar, etc.) change the concentration of reactive neutrals and ions in the plasma which directly correlates to etch rate. Very smooth, ansiotropic pattern transfer was obtained over a wide range of plasma etch platforms, chemistries, and conditions. Fast etch rates, high resolution features, and low damage are obtained when the chemical and physical components of the etch mechanism are balanced.

F. Implant isolation

Implant isolation has been widely used in compound semiconductor devices for interdevice isolation such as in transistor circuits or to produce current channeling such as in lasers.[272–274] The implantation process can compensate the semiconductor layer either by a damage or chemical mechanism. For damage compensation, the resistance typically goes through a maximum with increased postimplantation annealing temperature as the damage is annealed out and hopping conduction is reduced. At higher temperatures the defect density is further reduced below that required to compensate the material and the resistivity decreases. For chemical compensation, the postimplantation resistance again increases with annealing temperature with a reduction in hopping conduction but it then stabilizes at higher temperatures as a thermally stable compensating deep level is formed. Typically there is a minimum dose (dependent on the doping level of the sample) required for the chemically active isolation species to achieve thermally stable compensation.[275] Thermally stable implant isolation has been reported for *n*- and *p*-type AlGaAs where an Al–O complex is thought to form[275,276] and for C-doped GaAs and AlGaAs where a C–N complex is postulated.[277] With this background, the implant isolation properties of the III–N materials are reviewed.

As shown in Fig. 67, N implantation (at doses of $10^{12}-10^{13}\,\mathrm{cm}^{-3}$) effectively compensates both *p*- and *n*-type GaN. For both doping types the resistance first increases with annealing temperature then reaches a maximum before demonstrating a significant reduction in resistance after a 850 °C anneal for *n*-type and a 950 °C anneal for *p*-type GaN. This behavior is typical of implant-damage compensation. The defect levels estimated from Arrhenius plots of the resistance/temperature product are 0.83 eV for initially *n*-type and 0.90 eV for initially *p*-type GaN. These levels are still not at midgap, but are sufficiently deep to realize a sheet resistance $>10^9\,\Omega/\square$. The implantation has also been reported to effectively isolate *n*-type GaN,[141] with the material remaining compensated to over 850 °C. Interestingly, H-implanted compensation of *n*-type GaN is reported to anneal out at ~400 °C[141] with an anomalous dependence on implant energy. The reason for this is presently not known. In light of this result, however, H implantation in GaN will require further study as H is often the ion of choice for photonic device isolation applications that require deep isolation schemes. Moreover, both the He and N isolation appear to rely solely on implantation damage without any chemical compensation effects analogous to those in the O/Al/GaAs case.[272,275,276] However, the implantation-induced defects in GaN are more thermally stable than other III–V semiconductor materials, such as GaAs or InP, where the damage levels begin to anneal out below 700 °C.[272] This may be a result of the higher band gap of GaN or the more polar nature of the lattice causing more stable defects. Further work is still required to understand the nature of the implantation damage in GaN.

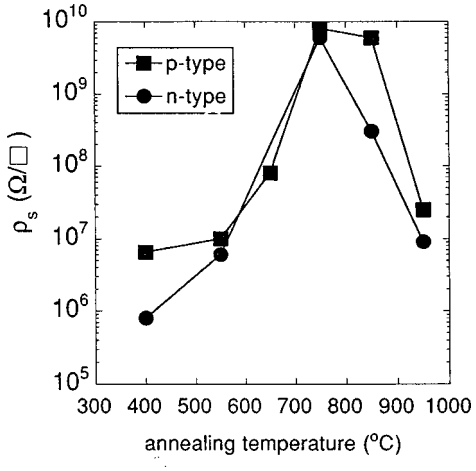

FIG. 67. Sheet resistance vs annealing temperature for N implanted initially *n*- and *p*-type GaN. The N was implanted at multiple energies to give an approximately uniform ion concentration of $4\times10^{18}\,\mathrm{cm}^{-3}$ across ~500 nm.

Implant isolation of the In-containing nitrides (InN, InGaN, and InAlN) was first reported using F implantation.[278] That work showed that InN did not demonstrate significant compensation while the ternaries increased in sheet resistance by roughly an order-of-magnitude after a 500 °C anneal. Data from a more extensive study of $In_xG_{1-x}N$ implant isolation for varying In composition using N and F implantation is summarized in Fig. 68.[279] The InGaN ternaries only realize a maximum of a 100 fold increase in sheet resistance independent of ion species after a 550 °C anneal. Pure InN shows a higher increase of 3 orders-of-magnitude but still only achieves a maximum sheet resistance of $10^4\,\Omega/\square$. This may be high enough for some photonic device current-guiding applications but is not sufficient for interdevice isolation in electronic circuits. The damage levels created by N implantation are estimated from an Arrhenius plot of the resistance/temperature product to be a maximum of 390 meV below the conduction band.[279] The defect level is high in the energy gap, not near midgap as is ideal for implant compensation. The position of the damage

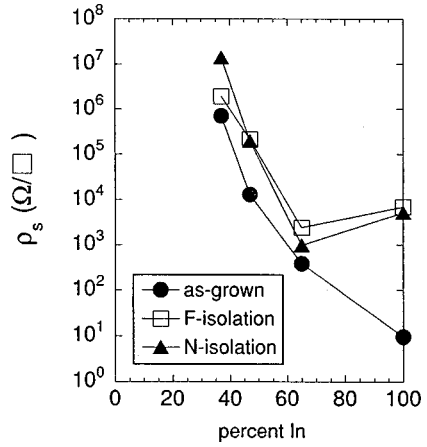

FIG. 68. Maximum sheet resistance vs percent In for InGaN either as-grown or implanted with F or N and annealed at the temperature for maximum compensation for each composition (ion concentration $\sim 5\times10^{19}\,\mathrm{cm}^{-3}$).

level is analogous to the defect position reported for implant compensated *n*-type InP and InGaAs[280] but different from the damage-associated, midgap states created in GaAs and AlGaAs.[274,275]

As shown in Fig. 69, $In_{0.75}Al_{0.25}N$, in contrast to InGaN, can be highly compensated with N or O implantation with over a 3 order-of-magnitude increase in sheet resistance after a 600–700 °C anneal while F implantation produces only 1 order-of-magnitude increase in sheet resistance.[278,281] The compensating level in InAlN is also high in the band gap with the deepest level estimated from Arrhenius plots as being 580 meV below the conduction band edge in high dose N-isolated material, however it is sufficiently deep to achieve highly compensated material.[281] The enhanced compensation for N and O implantation, as compared to F implantation, in InAlN suggests some chemical component to the compensation process. For N implantation a reduction in N vacancies, that are thought to play a role in the as-grown *n*-type conduction, may explain the enhance compensation. For O implantation, the enhanced compensation may be the result of

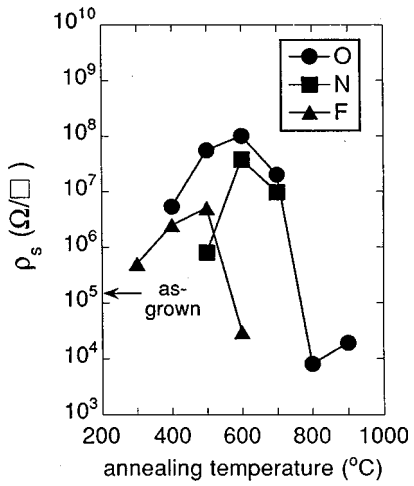

FIG. 69. Sheet resistance vs annealing temperature for O-, N-, or F-implanted $In_{0.75}Al_{0.25}N$ (ion concentration $\sim 5\times10^{18}\,\mathrm{cm}^{-3}$).

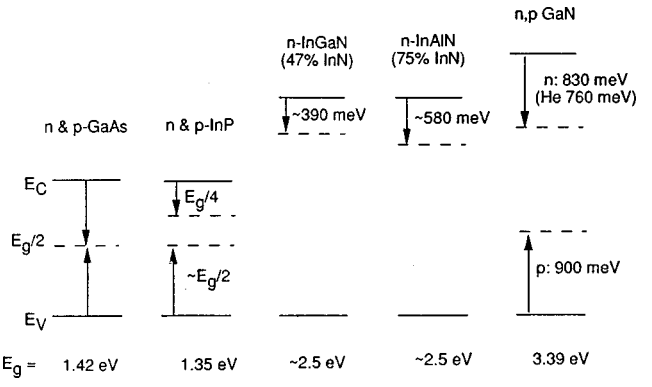

FIG. 70. Schematic representation of the position in the energy gap of compensating defect levels from implant isolation in GaAs, InP, $In_{0.47}Ga_{0.53}N$, $In_{0.75}Al_{0.25}N$, and GaN.

the formation of an O–Al complex as is thought to occur in O-implanted AlGaAs.[275,276]

Figure 70 schematically summarizes the present knowledge of the position in the band gap of the compensating implanted defect levels in III–N materials and compares these to those in GaAs and InP. Although the levels are not at midgap, as is ideal for optimum compensation as occurs in GaAs and *p*-type InP, with the exception of InGaN, the levels are sufficiently deep to produce high resistivity material.

Very effective isolation of AlGaN/GaN heterostructure field effect transistor (HFET) structures has been achieved using a combined P^+/He^+ implant process.[282] The groups of Asbeck and Lau at UCSD demonstrated that a dual energy (75/180 keV) P^+ implant (doses of 5×10^{11} and $2\times10^{12}\,\mathrm{cm}^{-2}$, respectively), followed by a 75 keV He^+ implant ($6\times10^{13}\,\mathrm{cm}^{-2}$) was able to produce sheet resistance of $\sim10^{12}\,\Omega/\square$ in AlGaN/GaN structures with 1-μm-thick undoped GaN buffers. The temperature dependence of the resistivity showed an activation energy of 0.71 eV, consistent with past measurements of deep states induced in GaN by implant damage.[138]

III. ROLE OF IMPURITIES

The properties of virtually all bulk and epitaxial GaN are still strongly influenced by residual impurities such as O, Si, C, and H and by point and extended defects such as nitrogen vacancies and threading dislocation. The role of these entities has been reviewed previously,[283–293] and in this section we will focus on H, O, C, and structural defects.

A. Hydrogen

Hydrogen is a component of most of the gases and liquids used in the growth, annealing, and processing of semiconductors and a great deal of attention has been focused on the effects of hydrogen incorporation in Si, GaAs, SiC, and other materials.[294–303] It is fairly well established that H_2 (or larger aggregates) are basically electrically and optically inactive in all semiconductors, and that the diatomic species has low diffusivity once formed inside the semiconductor. By contrast, atomic hydrogen (which may exist as H^0, H^+, or H^- depending on the position of the Fermi level) diffuses rapidly even at low temperatures (25–250 °C) and can attach

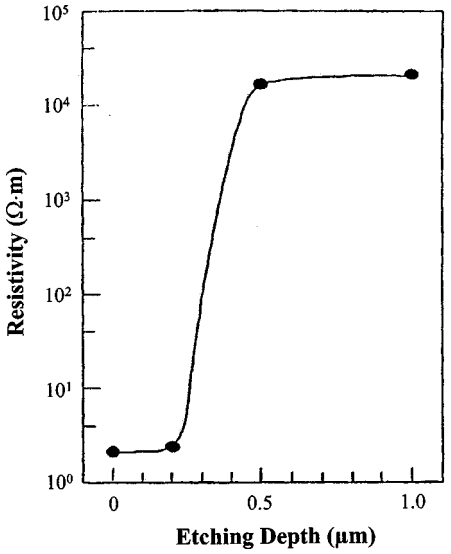

FIG. 71. Resistivity change of GaN(Mg) layer after low energy electron beam irradiation, as a function of depth from the surface (after Ref. 306).

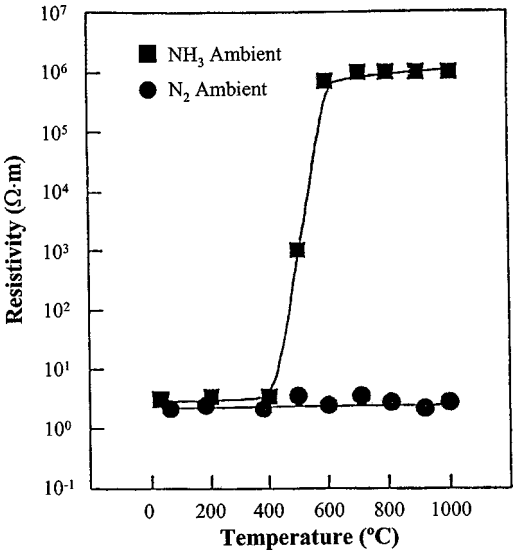

FIG. 72. Resistivity of GaN(Mg) layers as a function of annealing temperature in either NH_3 or NH_2 ambients (after Ref. 308).

to dangling or defective bonds associated with point or line defects, and can also form neutral complexes with dopants, i.e.,

$$D^+ + H^- \rightarrow (DH)^0$$

$$A^- + H^- \rightarrow (AH)^0$$

where D^+ and A^- are ionized shallow donor and acceptor dopants, respectively. These reactions manifest themselves as increases in resistivity of the semiconductor, and an increase in carrier mobility as ionized impurity scattering is reduced. A typical signature of an unintentional hydrogen passivation process is a reduction in doping density in the near-surface region ($\leqslant 1$ μm) due to in-diffusion of atomic hydrogen from the liquid or gas in which the sample is immersed.

In GaN and related materials (AlN, InN, InGaN, InAlN, AlGaN) it has been found that hydrogen is present in relatively high concentrations in as-grown samples, especially *p*-type GaN, and that hydrogen is readily incorporated during many device process steps such as plasma etching, plasma-enhanced chemical vapor deposition (PECVD), solvent boiling, and wet chemical etching.[304]

For many years it was not possible to achieve *p*-type doping in GaN, due partially to the often high residual *n*-type background (resulting from nitrogen vacancies or Si or O impurities) and the high ionization energy level of most acceptor dopants. However even in GaN(Mg) in which the Mg concentration was easily sufficient to produce *p*-type conductivity, the material was generally resistive.

Amano *et al.*[305] found that when the electron beam in a scanning electron microscope was focused on these samples, blue emission was evident, and the resistivity of the exposed area had dramatically decreased. Nakamura *et al.*[306–308] later found low *p*-type conductivity in as-grown GaN(Mg). Further treatment in a low-energy electron beam irradiation facility reduced the resistivity from 4×10^4 to ~ 3 Ω cm in the top 0.5 μ of the surface, as shown in Fig. 71. A maximum hole concentration of $7\times10^{18}\,\mathrm{cm}^{-3}$ and a mobility of 3 $\mathrm{cm}^2/\mathrm{V\,s}$ were obtained by this method.

Subsequently, Nakamura *et al.*[306–308] showed that low resistivity *p*-type GaN with uniform carrier densities throughout their entire thickness could be obtained by post-growth thermal annealing in N_2 at temperatures $\geqslant$700 °C. Once again the resistivity was observed to drop from $\sim 10^6$ to 2 Ω cm. Deep level emission at $\sim$750 nm sharply decreased with annealing, while the blue (450 nm) emission was maximized at 700 °C. To elucidate the mechanism responsible for these changes, Nakamura *et al.*[306–308] annealed *p*-type GaN(Mg) in either N_2 or NH_3. As shown in Fig. 72, while there was no change in the resistivity with N_2 annealing, above $\sim$500 °C the GaN returned to high resistivity when NH_3 was the annealing ambient. Subsequent annealing in N_2 returned these films to their low-resistivity condition, and these changes correlated well with changes in the photoluminescence spectrum from the samples (Fig. 73). NH_3 decomposes above $\sim$200 °C from N_2 and H_2 (99.9% disso-

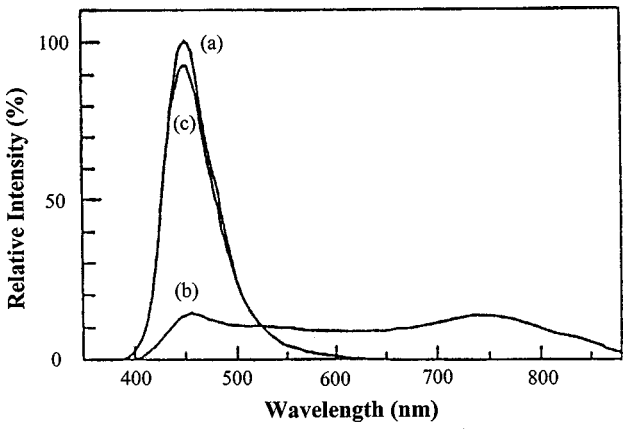

FIG. 73. PL spectra of GaN(Mg) layers after sequential (a) N_2 ambient annealing at 800 °C, (b) subsequent NH_3 ambient annealing at 800 °C, (c) subsequent N_2 ambient annealing at 800 °C (after Ref. 308).

ciation at 800 °C),[309] and dissociation of the hydrogen can be catalyzed by the presence of the GaN surface. Thus there is a sizable flux of atomic hydrogen available for indiffusion into the GaN film, where it can form neutral complexes with the Mg acceptors through the reactions

$$Mg^- + H^+ \rightarrow (Mg-H)^0.$$

This produces compensation of the holes from the acceptors and leads to high resistivity. The reaction can be driven in the reverse direction by either annealing or injection of minority carrier (electrons) through the low energy electron beam irradiation or by shining above band gap light onto the sample, or by forward biasing of a *p-n* junction structure. One usually observes a decrease in blue emission from samples annealed above ~700 °C, unless special precautions are taken, because of the onset of surface dissociation.[308] Amano *et al.*[310] reported that the intensity of Zn-related blue emissions in GaN(Zn) was enhanced by electron injection, suggesting that $(Zn-H)^0$ complexes also form in this material.

In as-grown GaN there are numerous potential sources of hydrogen, since the growth reaction by metal organic chemical vapor deposition (MOCVD) proceeds as

$$(CH_3)_3Ga + NH_3 \rightarrow GaN + CH_4\uparrow + H_2\uparrow.$$

In some cases H_2 is also employed as a carrier gas for the trimethylgallium. Previous work in other semiconductor systems grown with metal-organic precursors has shown that all three of the components of the growth chemistry, i.e., group III source, group V source, and carrier gas, can contribute to dopant passivation. Even the dopant sources (Cp_2Mg and Si_2H_6 are the most common for GaN) are potential supplies of hydrogen in the GaN films. There is a direct correlation of H and Mg concentrations in MOCVD GaN, suggesting that there is trapping of hydrogen at the acceptors.[311–313] Further implication of hydrogen passivation as the hole reduction mechanism comes from the fact that *p*-GaN has been achieved by Mg doping in molecular beam epitaxy material without postgrowth annealing.[314] In this case N_2 is derived from as plasma source and solid Ga is the group III source, hence no hydrogen is present in the growth environment.

In most III–V semiconductors it is found that atomic hydrogen diffuses more rapidly in *p*-type material where it is likely in a positive charge state (H^+), and bonds more strongly to acceptors than it does to donors.[315–333] Figure 74 shows a SIMS depth profile of GaN(Mg) grown on Al_2O_3 by MOCVD—the as-grown material contains $\sim 5.5\times10^{19}$ Mg cm^{-3}, and this remains stable upon annealing at 700 °C. The hole concentration in the material was $\sim 6\times10^{17}\,cm^{-3}$. Note that there is $\sim 10^{18}\,cm^{-3}$ hydrogen in the as-grown sample, more than enough to compensate all the holes. Postgrowth annealing at 700 °C for 60 min reduces the hydrogen concentration to $1-5\times10^{17}\,cm^{-3}$, which is below the hole concentration and hence the *p*-type conductivity returns.[325–327]

An interesting point from Fig. 74 is that a substantial amount of hydrogen remains in the material, probably bound at defects or internal surfaces. This residual hydrogen may give rise to effects such as current gain drift in transistors, or a dependence of apparent material resistivity on the measurement current in Hall measurements because of minority-carrier reactivation of passivated acceptors.

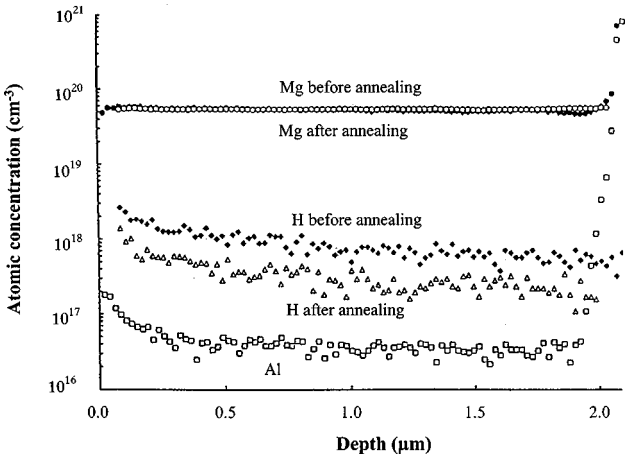

FIG. 74. SIMS depth profile of MOCVD grown GaN(Mg) before and after 700 °C, 60 min anneal in N_2.

Figure 75 shows the hydrogen concentration in undoped, lightly Mg-doped and heavily Mg-doped GaN as a function of annealing time at 700 °C under a N_2 ambient.[328] The hydrogen concentration is reduced with time, but saturates at $\sim 2\times10^{17}\,cm^{-3}$; it is not clear if this represents the background sensitivity of the SIMS apparatus, or is a real concentration. After the anneal, the heavily Mg-doped ($Mg=6\times10^{19}\,cm^{-3}$) sample remained highly resistive. A problem with continuing to increase the Mg concentration is the onset of cracking of the GaN films, and conversion of the conductivity to *n* type. The reasons for this are as yet unclear, and the presence of Mg interstitials acting as shallow donors or formation of Mg-defect complexes with donor nature are just two of the possibilities. As found by Nakamura *et al.* the changes in resistivity are accompanied by strong changes in the PL spectra.[307,308,328] Figure 76 shows 5 K spectra in heavily Mg-doped ($Mg=6\times10^{19}\,cm^{-3}$) GaN before and after different annealing times at 700 °C. The peak at 3.285 eV has been ascribed to a free-to-bound Mg transition, corresponding to a binding energy for Mg of 155 meV,[329] while

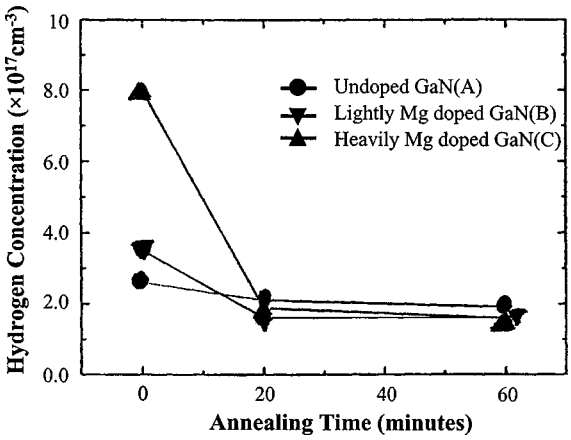

FIG. 75. Hydrogen concentration in undoped or Mg-doped GaN as a function of annealing time at 700 °C in a N_2 ambient (after Ref. 328).

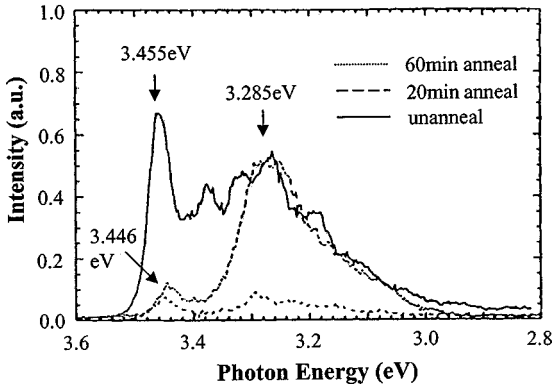

FIG. 76. Low temperature (5 K) PL spectra from heavily Mg-doped ($Mg=6\times10^{19}\,cm^{-3}$) GaN as a function of annealing time at 700 °C in a N_2 ambient (after Ref. 328).

that at 3.445 eV has been identified as a transition involving as exciton bound to Mg.[330] Annealing for 20 min at 700 °C shifts this latter peak to 3.446 eV.[328,331] Li *et al.*[328] attributed the 3.45 eV peak to a transition associated with an exciton bound to the Mg acceptor. For 60 min annealing, observation of a 3.465 eV peak was found in lightly Mg-doped GaN, consistent with a previous assignment of an exciton bound to a nitrogen vacancy.[330] Therefore, loss of N_2 and compensation of the *p*-type doping by introduction of the shallow donor N, states appears to be another reason it is difficult to get strong *p*-type conductivity.

Piner *et al.*[332] found that the hydrogen concentration in MOCVD $In_xGa_{1-x}N$ was a strong function of H_2 and NH_6 flow rates during growth, and also had a strong effect on the background C and O concentrations. Therefore, the overall compensation in the material is affected by the hydrogen flow. Figure 77 shows H, C, and O relative concentrations in InGaN grown at 730 °C, as a function of NH_3 flow rate.

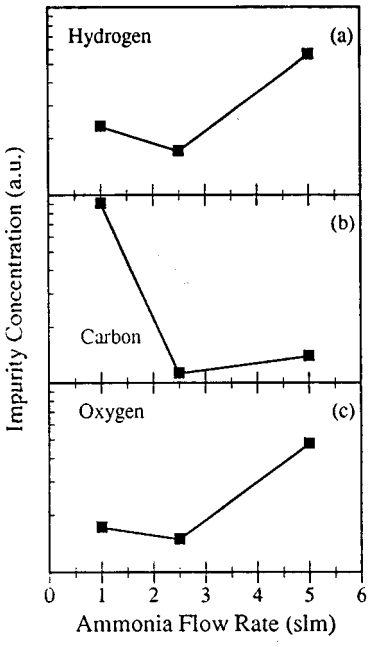

FIG. 77. H, C, and O relative concentrations as a function of NH_3 flow in MOCVD InGaN (after Ref. 372).

While the H clearly originates from the ammonia and the metal organic sources, it appears that the purified NH_3 is the source of oxygen. The reduction in carbon with NH_3 flow probably results from H scavenging reactions.[334]

Johnson *et al.*[335] performed a series of MBE growth experiments in which GaN(Mg) was grown with either pure N_2 plasmas or mixed N_2/H_2 plasmas in order to understand the effect of hydrogen under controlled conditions. However PL examination showed only minor differences in some cases due to Mg compensation. No measurements of H concentrations were reported, and it is likely under the particular growth conditions used there was little H incorporation.

Soto[336] reported that GaN grown by plasma-assisted MOCVD using triethylgallium and N radicals was highly resistive, and attributed to the high density of C and H ($10^{19}-10^{20}\,cm^{-3}$) incorporated into the films. The H signal intensity was linearly related to the C signal, suggesting complexing of the C and H. Annealing at 900 °C did not affect the resistivity.

Lee and Yong[337] grew hydrogenated AlN by rf magnetron sputtering in a $H_2/Ar/N_2$ gas mixture. The addition of H was found to reduce the oxygen background in the material, and the activation energy for the evolution of H_2 gas from the AlN was found to be 0.5 eV/atom as determined by gas chromatography. A variety of N–H IR peaks were found between 2074 and 3532 cm^{-1}—these bonds may hinder formation of N–O bonds.[337] The value of 0.11 eV/atom for hydrogen evolution is consistent with hydrogen bound at N atoms.[338]

1. Dopant passivation

We have recently reported that atomic hydrogen passivates both Mg and Zn, but a number of reports have shown passivation of Ca,[339] C,[340] and Cd.[341] Theoretical considerations initially suggested that Ca might be a shallower acceptor in GaN than Mg.[342] Zolper *et al.*[115] realized *p*-type doping of GaN using implantation of Ca^+ alone, or a coimplantation of Ca^+ and P^+, followed by rapid thermal annealing at $\geqslant$1100 °C. While the activation efficiency of Ca in both implant schemes was ~100%, temperature-dependent Hall measurements showed that the ionization level of Ca was ~168 meV, similar to that of Mg. The Ca atomic profile was thermally stable to temperatures up to 1125 °C. Since Mg has a substantial memory effect in stainless steel epitaxial reactors (or in gas lines leading to quartz chamber systems), Ca may be a useful alternative *p* dopant for epitaxial growth of laser diode or heterojunction bipolar transistor structures in which junction placement, and hence control of dopant profiles, is of critical importance.

In considering Ca-doped GaN for device applications it is also necessary to understand the role of hydrogen, since there is always a ready supply of atomic hydrogen available from NH_3, the metal organic group III source [typically $(CH_3)_3Ga$] or from the gaseous dopant source when using chemical vapor deposition techniques. We have also found that Ca acceptors in GaN are also readily passivated by atomic hydrogen at low temperature (250 °C), but they can be reactivated by thermal annealing at $\leqslant$500 °C for 1 min in lightly doped ($3\times10^{17}\,cm^{-3}$) samples. As the carrier density

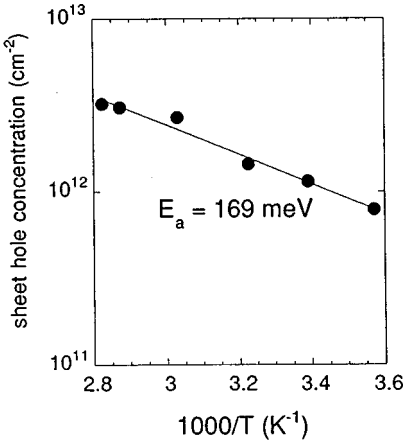

FIG. 78. Annealing plot of sheet hole density in Ca-implanted GaN. The activation energy is 169 ± 12 meV.

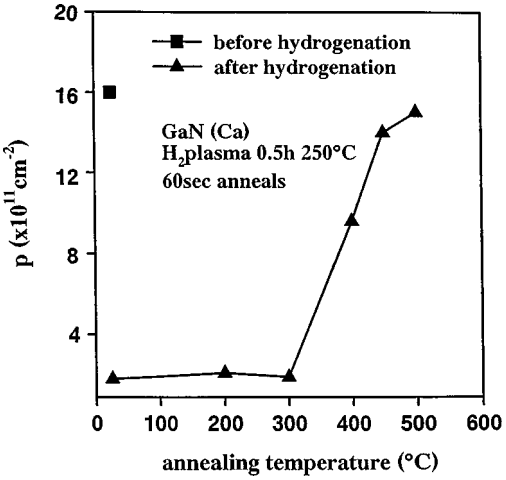

FIG. 79. Sheet hole density at 300 K in hydrogenated GaN(Ca) as a function of subsequent annealing temperature.

is restored by such annealing treatments, there is a true passivation and not just compensation of the Ca acceptors by the hydrogen.

a. Case study: Ca. Nominally undoped ($n < 3 \times 10^{16}\,\mathrm{cm}^{-3}$) GaN was grown on double-side polished c-Al_2O_3 substrates prepared initially by $HCl/HNO_3/H_2O$ cleaning and an *in situ* H_2 bake at 1070 °C. A GaN buffer ≤300 Å thick was grown at ~500 °C and crystallized by ramping the temperature to 1040 °C where trimethylgallium and ammonia are again used to grow the 2-μm-thick epitaxial layer. The materials properties have been discussed in detail earlier,[326,327] but in brief the double x-ray full-width at half-maxima are ~300 arcsec and the total defect density (threading dislocations, stacking faults) apparent in plain view transmission electron microscopy was typically $2-4 \times 10^9\,\mathrm{cm}^{-2}$. The as-grown films are featureless, transparent, and have strong band edge (3.47 eV) luminescence.

^{40}Ca ions were implanted at 180 keV and a dose of $5 \times 10^{14}\,\mathrm{cm}^{-2}$. In some cases, a coimplant of P^+ to the same dose at an energy of 130 keV was performed to try to enhance a substitutional fraction of Ca upon subsequent annealing in analogy to the case of Mg implantation in GaN. For the case of Ca we found there was little additional activation as a result of the coimplant. After rapid annealing at 1150 °C for 15 s under N_2 in a face-to-face geometry we measured sheet carrier densities of $p \sim 1.6 \times 10^{12}\,\mathrm{cm}^{-2}$ with a mobility at 500 K of 6 $\mathrm{cm}^2/\mathrm{V\,s}$. Arrhenius plots of the hole density showed an ionization level of 169 meV for the Ca in GaN (Fig. 78). Samples with alloyed HgIn ohmic contacts were exposed to an electron cyclotron resonance (ECR) H_2 or He plasma with 850 W forward power and a pressure of 10 mTorr. The exposure time was 30 min at 250 °C, and the temperature was lowered to room temperature with the plasma on. The sheet carrier density and hole mobility at 300 K were obtained from Van der Pauw geometry Hall measurements. Posthydrogenation annealing was performed between 100 and 500 °C for 60 s under flowing N_2 with the ohmic contacts already in place.

The initial H_2 plasma exposure caused a reduction in sheet hole density of approximately an order of magnitude, as shown in Fig. 79. No change in electrical properties were observed in the He-plasma treated samples, showing that pure ion bombardment effects are insignificant and the chemical interaction of hydrogen with the Ca acceptors is responsible for the conductivity changes. Posthydrogenation annealing had no effect on the hole density up to 300 °C, while the initial carrier concentration was essentially fully restored at 500 °C. Assuming the passivation mechanism is the formation of neutral Ca–H complexes, then the hole mobility should increase upon hydrogenation. This is indeed the case, as shown in Fig. 80. Note that the mobility decreases to its initial value with posthydrogenation annealing. If the carrier reduction were due to introduction of compensating defects or impurities, then the hole mobility would decrease upon hydrogenation, which is not observed.

In other p-type III–V semiconductors it is generally accepted that atomic hydrogen is predominantly in a positive charge state with the donor level being around midgap. If a similar mechanism exists in GaN then the initial Coulombic attraction between ionized acceptor and hydrogen leads to formation of a neutral close pair, i.e.,

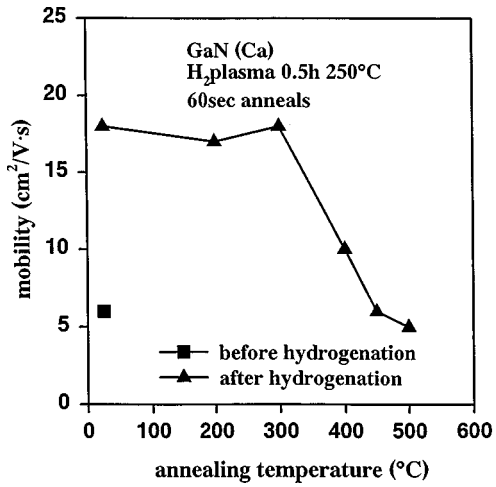

FIG. 80. Hole mobility at 300 K in hydrogenated GaN(Ca) as a function of subsequent annealing temperature.

$$Ca^- + H^+ \leftrightarrow (Ca-H)^0.$$

The existence of the neutral complex should be verified by observation of a vibrational band,[343] but to obtain the sensitivity needed for such a measurement will require a relatively thick epilayer of Ca-doped GaN. Our present implanted samples do not have a sufficient Ca density-times-thickness product to be suitable for infrared spectroscopy.

If the dissociation of the Ca–H species is a first-order process then the reactivation energy from the data in Fig. 79 is ~2.2 eV[343] assuming a typical attempt frequency of $10^{14}\,s^{-1}$ for bond breaking processes. This is similar to the thermal stability of Mg–H complexes in GaN which we prepared in the same manner (implantation) with similar doping levels. In thicker, more heavily doped samples, the apparent thermal stability of hydrogen passivation is much higher because of the increased probability of retrapping of hydrogen at other acceptor sites.[343] This is why for thick, heavily doped ($p > 10^{18}\,cm^{-3}$) GaN(Mg), a postgrowth anneal of at least 700 °C for 60 min is employed to ensure complete dehydrogenation of the Mg. True reactivation energies can only be determined in reserve-biased diode samples where the strong electric fields present sweep the charged hydrogen out of the depletion region and minimize retrapping at the acceptors.[344]

In conclusion we have found that hydrogen passivation of acceptors in GaN occurs for several different dopant impurities and that postgrowth annealing will also be required to achieve full electrical activity in Ca-doped material prepared by gas-phase deposition techniques. The thermal stability of the passivation is similar for Ca–H and Mg–H complexes, with apparent reactivation energies of ~2.2 eV in lightly doped ($\sim 10^{17}\,cm^{-3}$) material.

b. Case study: C, Cd. Abernathy *et al.*[345] reported carbon doping of GaN using CCl_4 in metal organic molecular beam epitaxy, with maximum hole concentrations of $\sim 3 \times 10^{17}\,cm^{-3}$. The total carbon concentration in these films is somewhat higher than this (1–2 orders of magnitude), but the reason for the low doping efficiency is not known at this point.[346] The activation energy of acceptor ionization was reported to be ~26 meV, but this may be due to impurity band conduction.[346]

Exposure of the GaN(C) samples to an electron cyclotron resonance H_2 plasma at 250 °C reduces the hole concentration by approximately a factor of three,[340] with an accompanying increase in hole mobility. Annealing of the hydrogenated material restored the initial hole concentration at ~450 °C. It is well established in other dopant-hydrogen complexes that the apparent thermal stability is a strong function of the doping level and sample thickness because of hydrogen retrapping effects.

There have also been studies on the formation kinetics. Burchard *et al.*[341] studied the formation and properties of Cd–H pairs in GaN using radioactive ^{111}Cd and perturbed $\gamma\gamma$ angular correlation spectroscopy. The H was incorporated by 100 eV implantation, and formation of two different Cd–H complexes (different configurations) with dissociation energies of 1.1 and 1.8 eV, respectively, were found.

Table VII summarizes the information reported to date for hydrogen-acceptor complexes in GaN. To this point there have not been any direct observations of donor dopant passivation in any of the nitrides, although this is fairly typical of what has occurred previously in other semiconductor systems. For example, in Si, acceptor passivation was first reported in 1983,[347] and it was only in 1986 that reports of weak donor passivation were seen.[348] Subsequently in 1988, the first unambiguous observations by IR spectroscopy were made,[349–351] but only after realizing that because of the lower binding energies for donor dopant-hydrogen complexes, the temperature at which the hydrogen was unincorporated should be lowered.[351] Once the plasma injection temperature was reduced (to 120 °C from the usual 200 °C for *p*-type Si), donor passivation efficiencies over 90% were realized.[352] Another feature of dopant passivation by hydrogen is that it depends on the characteristics of the plasma used for injection, i.e., the relative fluxes of H_2, H_2^+, H^0, H^+, and associated excited states, the average ion energy, and the Fermi level at the semiconductor surface.[353] For example, we have seen that increasing the ion energy by ~100 eV in a H_2 plasma increases the incorporation depth of hydrogen in *p*-type GaAs by up to 50%,[334] and somewhat smaller effects have been observed in SiC.[354] This may be due to more efficient transfer of hydrogen across surface potentials.

TABLE VII. *p* dopants found to be passivated by atomic hydrogen in GaN.

Dopant	Comments	Refs.
Mg	residual hydrogen in growth ambient leads to high resistivity in as-grown GaN(Mg)	305–307, 328
Zn	electron injection increases Zn-related emissions in GaN(Zn)	310
C	H_2 plasma exposure decreases hole density by a factor of 3—thermally reversible	339
Ca	H_2 plasma exposure decreases hole density by a factor of 10—thermally reversible	338
Cd	formation of Cd–H complexes seen by PAC—dissociate at <350 °C	338

2. Diffusion and reactivation mechanisms

Typical SIMS profiles of ^2H in *p*-type GaN with [Mg] $\sim 2 \times 10^{19}\,cm^{-3}$ and hole concentration $\sim 1 \times 10^{17}\,cm^{-3}$, and in *n*-type GaN, with Si $\sim 2.5 \times 10^{18}\,cm^{-3}$ and electron concentration $2 \times 10^{19}\,cm^{-3}$, are shown in Figs. 81 and 82, respectively, for samples exposed to a ^2H plasma for 30 min at 250 °C. Note in the *p*-type material the ^2H follows an indiffusion profile where ^2H is trapped at Mg or defects, and there is a very high concentration shallow feature extending to ~0.1 μm from the surface. This is deeper than the usual peak due to nonequilibrium sputtering effects in SIMS, and may result from extended ^2H clusters or platelets. In the *n*-type material there is basically no measurable deuterium, suggesting that ^2H is not readily trapped at donor dopants. However, as pointed out above, this may simply be due to nonoptimized plasma conditions employed thus far.

A number of reports have shown that hydrogen can indeed pair with positively charged native donors in InN,

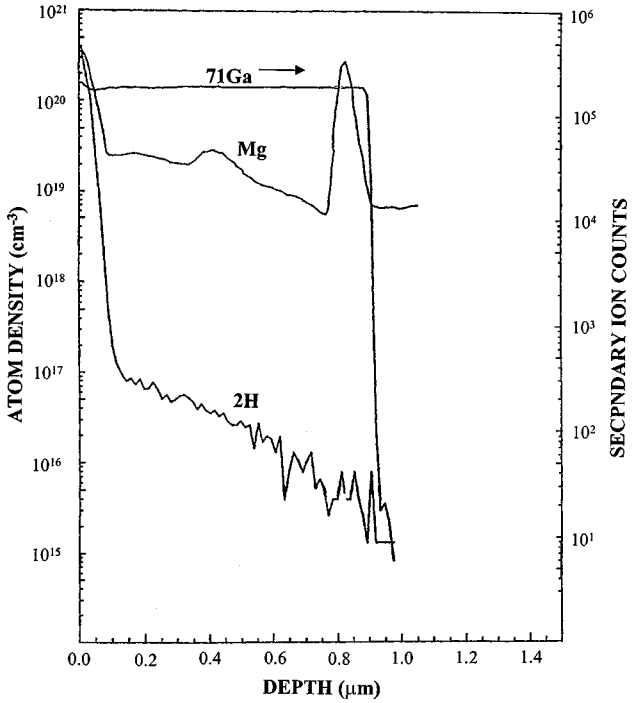

FIG. 81. SIMS profiles of ^{2}H and Mg in GaN(Mg) exposed to a ^{2}H plasma for 30 min at 250 °C.

InGaN, InAlN, and AlGaN.[355–358] Frequently undoped $Al_xGa_{1-x}N$ films with $x<0.4$ show electron concentration in the 10^{18}–$10^{19}\,cm^{-3}$ range and mobilities on the order 10 $cm^2\,V^{-1}\,s^{-1}$.[359–364] In addition, many groups have observed very strong tails at optical absorption near the band edge. High carrier concentrations and strong band tailing in AlGaN make it difficult to use such layers in most applications.

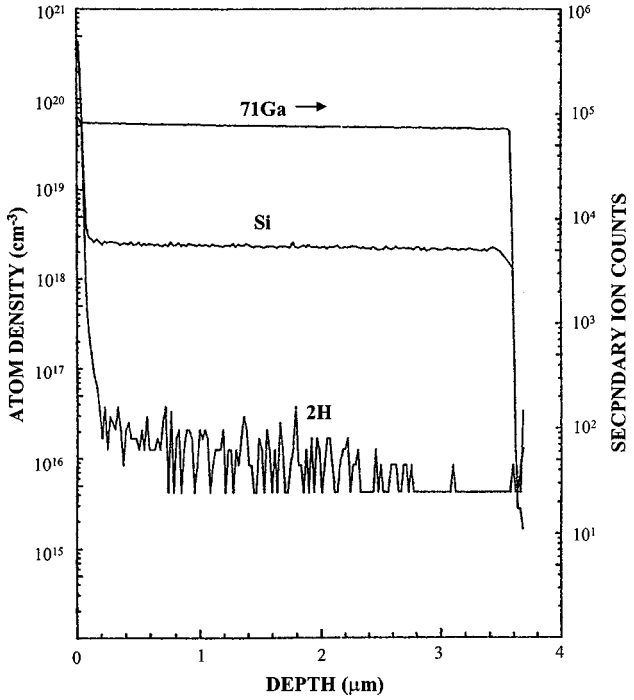

FIG. 82. SIMS profiles of ^{2}H and Si in GaN(Si) exposed to a ^{2}H plasma for 30 min at 250 °C.

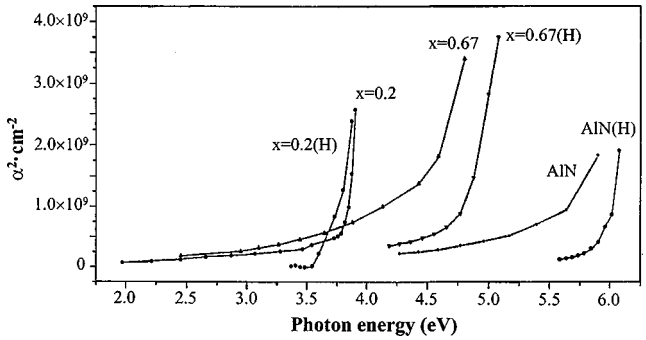

FIG. 83. Dependence of absorption coefficient squared on photon energy before and after hydrogenation of AlGaN samples of various Al contents.

Polyakov *et al.*[358] found that hydrogen plasma exposure at 200 °C for 1 h led to a substantial decrease in carrier concentration accompanied by an increase in electron mobility. The passivation efficiency appears to be higher for AlGaN than for pure GaN, and there was little change in electrical properties for the closely compensated GaN sample with initial carrier concentration of $8\times10^{14}\,cm^{-3}$. By sharp contrast, changes in AlGaN carrier concentration still occur even when the starting concentration is low. Polyakov *et al.*[358] suggested that passivation of native donors in AlGaN proceeds via pairing with negatively charged hydrogen ions,[365] and that the efficiency of passivation drops rapidly as the Fermi level crosses the hydrogen acceptor level. This would place the H^- level in GaN somewhere above $E_c-0.2$ eV and much shallower than that in AlGaN (e.g., in $Al_{0.12}Ga_{0.88}N$ it should be close to $E_c-0.5$ eV). Measurements of the temperature dependence of carrier concentration in high resistivity AlGaN samples after hydrogen treatment yield the same activation energies as before treatment (0.3 eV in $Al_{0.12}Ga_{0.88}N$, 0.22 eV in $Al_{0.67}Ga_{0.33}N$), indicating that no deeper compensating centers have been introduced, and that the decreased carrier concentration is a result of passivation of the existing electrically active centers.

The effect of hydrogen plasma passivation on the absorption spectra near the fundamental absorption edge in AlGaN and AlN samples is shown in Fig. 83. Prior to passivation, the magnitude of the band tailing (manifested in deviation of the squared absorption coefficient versus photon energy from a straight line) is substantial. This band tailing is suppressed by the hydrogen plasma treatment. The origin of the band tails may be related to fluctuations of local electric fields due to fluctuations of the density of charged defects. The hydrogenation treatment reduces the concentration of these defects, reducing the near band edge absorption. For AlN no measurements of electrical properties could be performed because of its high resistivity. The near band edge absorption observed in that case could come from local fields associated with deep levels, and suppression of such absorption could be related to the suppression of electrical activity of these deep centers. PL measurements on these samples showed a decrease in deep level emission and an increase in band edge emission as a result of the hydrogenation.

The thermal stability of native donor-hydrogen complexes was measured by isochronal annealing as shown in

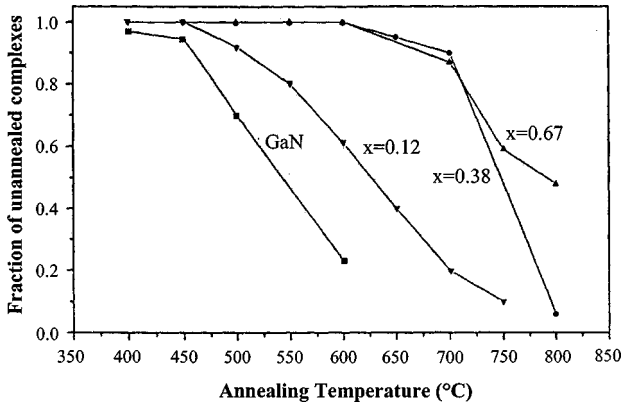

FIG. 84. Dependence of the fraction of unannealed native donor-hydrogen complexes in AlGaN.

Fig. 84. The fraction of unannealed complexes is defined as $N_l - N_T / N_l - N_H$ where N_l is the electron concentration before hydrogenation, N_H the electron concentration after hydrogenation, and N_T is the electron concentration after hydrogenation and subsequent annealing at temperature T. The thermal stability of the donor-hydrogen complexes increases with AlN mole fraction in both MBE and MOCVD material, and this may play a role in the frequently observed decrease in carrier concentration in as-grown AlGaN layers with high Al mole fractions.[366,367]

Lower thermal stabilities were found for In-containing nitrides. Figure 85 shows the fraction of passivated donors remaining in $In_{0.5}Al_{0.5}N$ and $In_{0.25}Al_{0.25}Ga_{0.5}N$ initially hydrogenated at 250 °C for 30 min, as a function of posthydrogenation annealing temperature. Both samples displayed a decrease in carrier concentration of approximately an order of magnitude after hydrogen plasma exposure. The passivated donors begin to reactivate around 400 °C and by 500 °C 78% of the lost carriers were restored in InAlN and 66% in the InAlGaN. The recovery of the donor activity occurred over a broader temperature range than generally observed for other passivated dopants, and is consistent with the presence of a Gaussian distribution of activation energies. This may be due to nitrogen vacancies with different numbers of specific group III neighbors surrounding them (i.e., two In and two Al versus one In and three Al). Assuming a Gaussian distribution of energies, we obtained values of 1.4 eV for the activation energy for donor reactivation, with a full-width at half-maximum of ~0.3 eV.

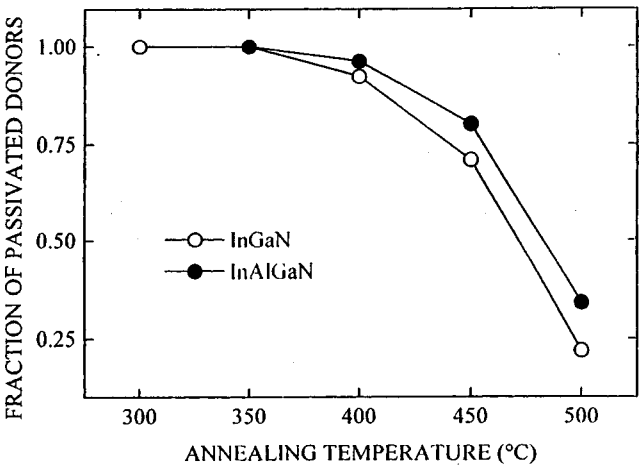

FIG. 85. Fraction of passivated donors remaining in InAlN or InGaN after deuteration at 250 °C and subsequent annealing at different temperatures.

In both Si[368–374] and GaAs[375–378] injection of minority carriers either by forward biasing of a diode structure or illumination with above band gap light produces dissociation of neutral acceptor-hydrogen or donor-hydrogen complexes at temperatures at which they are normally thermally stable. While the details of the reactivation process are not clearly established, it is expected that for an acceptor A the reactions likely can be described by

$$(AH)^0 \leftrightarrow A^- + H^-$$

$$H^+ + e^- \leftrightarrow H^0.$$

The neutral hydrogen most likely forms diatomic or larger clusters with other neutral or charged hydrogen species. The mechanism for acceptor activation during the e-beam irradiation process has not been studied in detail to date. To establish that minority-carrier-enhanced debonding of Mg–H complexes in GaN is responsible for this phenomenon, we examined the effect of forward biasing in hydrogenated p-n junctions. We find that the reactivation of passivated acceptors obeys second-order kinetics and that the dissociation of the Mg–H complex is greatly enhanced under minority-carrier injection conditions. The details are given below.

The sample was grown on c-Al_2O_3 by MOCVD using a rotating disk reactor. After chemical cleaning of the substrate in both acids (H_2SO_4) and solvents (methanol, acetone), it was baked at 1100 °C under H_2. A thin (≤300 Å) GaN buffer was grown at 510 °C, before growth of ~1 μm undoped material. 0.5 μm of GaN(Mg) with a carrier density of $p \sim 1.5 \times 10^{17}\,cm^{-3}$ after 700 °C annealing and 0.3 μm GaN (Si) with a carrier density of $5 \times 10^{18}\,cm^{-3}$. Some of the sample was hydrogenated by annealing under NH_3 for 30 min at 500 °C. This produces passivation of the Mg acceptors (~90%) but has little effect on the Si donors (≤1% passivation).

Mesa p-n junction diodes were processed by patterning 500-μm-diam. TiAl ohmic contacts on the n-GaN by liftoff and then performing a self-aligned dry etch with an electron cyclotron resonance BCl_3/Ar plasma to exposure of the p-type GaN. The e-beam evaporated NiAu was patterned by liftoff to make ohmic contact to the p-type material. The carrier profiles in the p-type layer were obtained from 10 kHz capacitance–voltage measurements at room temperature. Anneals were carried out in the dark at 175 °C under two different types of conditions. In the first, the diode was in the open-circuit configuration, while in the second the junction was forward biased at 9 mA to inject electrons into the p-type GaN. After each of these treatments the samples were returned to 300 K for remeasurement of the net electrically active acceptor profile in this layer.

Figure 86 shows a series of acceptor concentration profiles measured on the same p-n junction sample, after annealing at 175 °C under forward bias conditions. After the

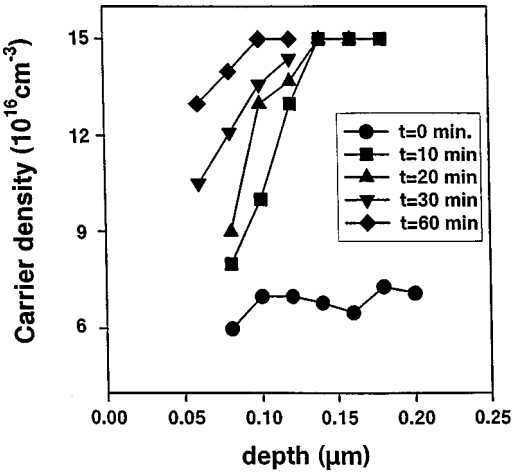

FIG. 86. Carrier concentration profiles in hydrogenated GaN(Mg) after annealing for various times at 175 °C under forward bias conditions.

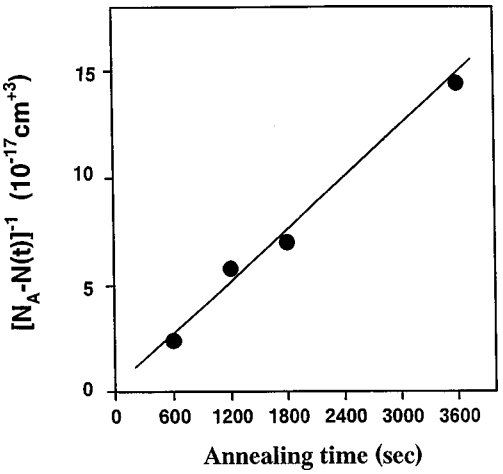

FIG. 87. Plot of inverse net active Mg concentration determined from Fig. 86 at a depth of 0.1 μm from the junction, as a function of forward bias annealing time.

NH_3 hydrogenation treatment the electrically active acceptor density decreased from 1.5×10^{17} to $\sim6-7\times10^{16}\,\mathrm{cm}^{-3}$. If the subsequent annealing was carried in the open-circuit configuration, there was no change in the carrier profile at ~0.1 μm for periods up to 20 h at 175 °C. By sharp contrast Fig. 86 shows that for increasing annealing times under minority-carrier injections conditions there is a progressive reactivation of the Mg acceptors with a corresponding increase in the hole concentration. After 1 h, the majority of these acceptors have been reactivated. Clearly therefore, the injection of electrons has a dramatic influence on the stability of the MgH complexes. The Mg reactivation has a strong dependence on depth into the *p*-type layer, which may result from the diffusion distance of the injected electrons prior to recombination. We rule out heating of the sample during forward biasing as being a factor in the enhanced dissociation of the neutral dopant-hydrogen complexes. The samples were thermally bonded to the stainless-steel stage and the junction temperature rise measured to be minimal ($\leqslant$10 °C). Moreover, from separate experiments we found that reactivation of the Mg did not begin until temperatures above $\sim$450 °C under zero-bias conditions.

Previous experiments on minority-carrier-enhanced reactivation of hydrogen passivated dopants in Si[371] and GaAs[377] have found that for long annealing times the kinetics can be described by a second order equation

$$d[N_A-N(t)]/dt=C[N_A-N(t)]^2,$$

where N_A is the uniform Mg acceptor concentration in the nonhydrogenated sample. $N(t)$ is the acceptor concentration in the hydrogenated GaN after forward bias annealing for time *t*, and *C* is a second-order annealing parameter.

In order to quantitatively analyze the reactivation kinetics of the Mg–H complexes in GaN, we measured the inactive acceptor concentrations $N_A-N(t)$ using the capacitance–voltage measurements at a depth of 0.1 μm in the *p*-GaN layer. Figure 87 shows that there is a linear relationship between $[N_A-N(t)]^{-1}$ and annealing time *t*, confirming that the reactivation process can be described by a second-order equation with $C=4\times10^{-20}\,\mathrm{cm}^3\,\mathrm{s}^{-1}$. This value is consistent with those obtained in Si and GaAs where minority-carrier-enhanced dopant reactivation has also been reported.

The rate of reactivation of passivated acceptors is dependent on the injected minority-carrier density. Moreover, for short annealing times it was found that the dopant reactivation occurred at a faster rate than predicted by the second-order equation for very short annealing times, and that the annealing process was rate limited by the formation of stable, electrically inactive diatomic H species. At this point there have not been enough studies of the various states of hydrogen in GaN as determined by infrared spectroscopy, channeling or secondary-ion-mass spectrometry for us to conclude anything about the ultimate fate of the atomic hydrogen once it has dissociated from the Mg–H complex, but it is likely that it then reacts with other hydrogen atoms to form diatomic or larger clusters. A strong dependence of reactivation rate on injected minority-carrier density would indicate the presence of a charge state for hydrogen and therefore influence the conversion of H^+ into the neutral state and then into the final hydrogen complexes.

The fact that the MgH complexes are unstable against minority-carrier injection has implications for several GaN-based devices. First, in a laser structure the high level of carrier injection would rapidly dissociate any remaining Mg–H complexes and thus would be forgiving of incomplete removal of hydrogen during the postgrowth annealing treatment. In a heterojunction bipolar transistor the lower level of injected minority carriers would also reactivate passivated Mg in the base layer, leading to an apparent time-dependent decrease in gain as the device was operated.

In summary, we have shown that hydrogen-passivated Mg acceptors in GaN may be reactivated at 175 °C by annealing under minority-carrier injection conditions. The reactivation follows a second-order kinetics process in which the $(MgH)^0$ complexes are stable to $\geqslant$450 °C in thin, lightly doped GaN layers. In thicker, more heavily doped layers where retrapping of hydrogen at the Mg acceptors is more prevalent, the apparent thermal stability of the passivation is

higher and annealing temperatures up to 700 °C may be required to achieve full activation of the Mg. Our results suggest the mechanism for Mg activation in e-beam-irradiated GaN is minority-carrier-enhanced debonding of the hydrogen.

The diffusion and trapping behavior of hydrogen in device structures is more complicated than in single-layer structures. For example, light-emitting diodes or laser diodes contain both *n*- and *p*-type GaN cladding layers with one or more InGaN active regions. The first laser reported by Nakamura *et al.*[379] contained 26 InGaN quantum wells. In other III–V semiconductors the diffusivity of atomic hydrogen is a strong function of conductivity type and doping level since trapping by acceptors is usually more thermally stable than trapping of hydrogen by donor impurities.[380–383] Moreover, hydrogen is attracted to any region of strain within multilayer structures and has been shown to pile up at heterointerfaces in the GaAs/Si,[384,385] GaAs/InP,[384,385] and GaAs/AlAs[386] material systems. Therefore it is of interest to investigate the reactivation of acceptors and trapping of hydrogen in double heterostructure GaN/InGaN samples, since these are the basis for optical emitters. We find that the reactivation of passivated Mg acceptors also depends on the annealing ambient, with an apparently higher stability for annealing under H_2 rather than N_2. Hydrogen is found to redistribute to the regions of highest defect density within the structure.

The double heterostructure sample consisted of 300 Å, low-temperature GaN buffer, 3.3 μm of $n^+(\mathrm{Si}=10^{18}\,cm^{-3})GaN$, 0.1 μm undoped InGaN, and 0.5 μm p^+ GaN ($p=3\times10^{17}\,\mathrm{cm}^{-3}$, Mg doped). In the immediate vicinity of the n-GaN/Al_2O_3 interface the defect density was high ($10^{12}\,\mathrm{cm}^{-2}$) but was reduced with increasing film thickness. However after growth of the InGaN active layer the threading dislocation density increased, due to thermal decomposition of the top of the InGaN upon raising the temperature to grow the p-GaN.[387]

XTEM of the DH-LED showed dislocations as dark lines propagating in the direction normal to the substrate. Most of the dislocations appeared to traverse the entire double heterostructure, while some appeared to bend and follow the interface for a short distance before threading out to the surface. The nature of the threading dislocations was studied by conventional XTEM using the $\mathbf{g}\cdot\mathbf{b}=0$ criteria. The dislocation will be invisible when **b** lies in the reflecting plane. Some of the dislocations were invisible both in $\mathbf{g2}=(0002)$ and $\mathbf{g5}=(1\underline{1}01)$ and because **b** was common to both reflections, b was found to be $1/3[11\underline{2}0]$. Assuming that the growth is the same as the translation vector of the dislocation, these defects would be pure edge type in nature. The average threading dislocation density was also found along the plane normal to the growth direction. The dislocation density was found to be $\sim8\times10^{10}\,\mathrm{cm}^2$.

The double-heterostructure sample was exposed to an electron cyclotron resonance H_2 plasma (500 W of microwave power, 10 mTorr pressure) for 30 min at 200 °C. The hole concentration in the p-GaN layer was reduced from 3×10^{17} to $\sim2\times10^{16}\,\mathrm{cm}^{-3}$ by this treatment, as measured by capacitance voltage ($C-V$) at 300 K. Sections from this material were then annealed for 20 min at temperatures from 500 to 900 °C under an ambient of either N_2 of H_2 in a Heatpulse 410T furnace. Figure 88 shows the percentage of passivated Mg remaining after annealing at different temperatures in these two ambients. In the case of N_2 ambients the Mg–H complexes show a lower apparent thermal stability (by ~150 °C) than with H_2 ambients. This has been reported previously for Si donors in InGaP and AlInP, and Be and Zn acceptors in InGaP and AlInP, respectively,[388] and most likely is due to in-diffusion of hydrogen from the H_2 ambients, causing a competition between passivation and reactivation. Therefore, an inert atmosphere is clearly preferred for the postgrowth reactivation anneal of p-GaN to avoid any ambiguity as to when the acceptors are completely active. Previous experimental results by Brandt *et al.*[389] and total energy calculations by Neugebauer and Van de Walle[390] suggest that considerable diffusion of hydrogen in GaN might be expected at $\leqslant$600 °C.

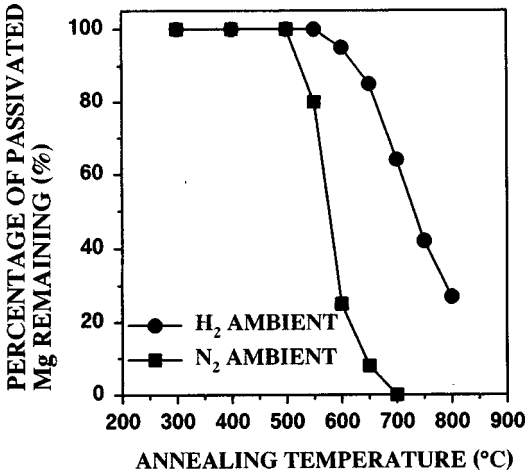

FIG. 88. Fraction of passivated Mg acceptors remaining in hydrogenated p-type GaN after annealing for 20 min at various temperatures in either N_2 or H_2 ambients.

Other sections of the double-heterostructure material were implanted with $^2H^+$ ions (50 keV, $2\times10^{15}\,\mathrm{cm}^{-2}$) through a SiN_x cap in order to place the peak of the implant distribution within the p^+GaN layer. Some of these samples were annealed at 90 °C for 20 min under N_2. As shown in the secondary ion mass spectrometry (SIMS) profiles of Fig. 89, the ^2H diffuses out of the p^+GaN layer and piles up in the defective InGaN layer, which as we saw from the TEM results, suffers from thermal degradation during growth of the p^+GaN. There is a strong attraction of H for crystal defects. Note that there is still sufficient ^2H in the p^+GaN ($\sim10^{19}\,\mathrm{cm}^{-3}$) to passivate all of the acceptors present, but electrical measurements show that the p-doping level was at its maximum value of $\sim3\times10^{17}\,\mathrm{cm}^{-3}$. These results confirm that as in other III–V semiconductors hydrogen can exist in a number of different states, including being bound at dopant atoms or in an electrically inactive form that is quite thermally stable. We expect that after annealing above 700 °C all of the Mg–H complexes have dissociated, and the electrical measurements show that they have not reformed. In other III–Vs the hydrogen in p-type material is in a bond

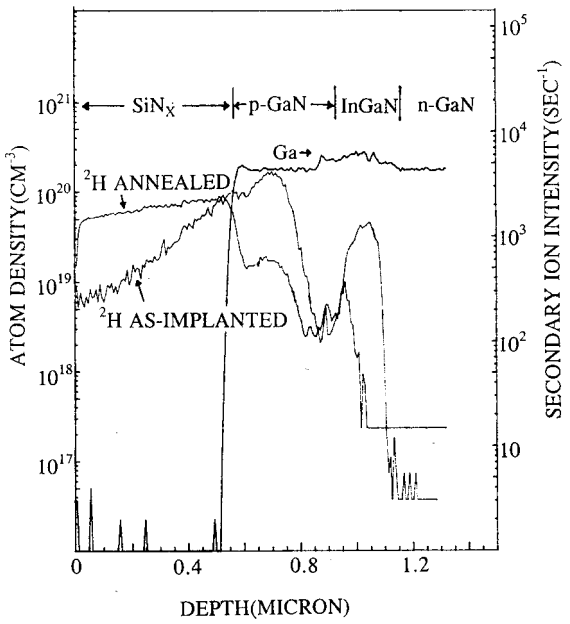

FIG. 89. SIMS profiles of ^2H in an implanted (50 keV, $2\times10^{15}\,cm^{-2}$ through a SiN_x cap) double-heterostructure sample, before and after annealing at 900 °C for 20 min.

centered position forming a strong bond with a nearby N atom, leaving the acceptor threefold coordinated.[390] Annealing breaks this bond and allows the hydrogen to make a short-range diffusion away from the acceptor, where it probably meets up with other hydrogen atoms, forming molecules or larger clusters that are relatively immobile and electrically inactive. This seems like a plausible explanation for the results of Figs. 88 and 89, where the Mg electrical activity is restored by 700 °C, but hydrogen is still present in the layer at 900 °C. In material implanted with hydrogen, there is almost certainly a contribution to the apparently high thermal stability by the hydrogen being trapped at residual implant damage. This is evident by the fact that the ^2H profile retains a Pearson IV type distribution even after 900 °C annealing. The other important point from Fig. 88 is that as in other defective crystal systems, hydrogen is attracted to regions of strain, in this case the InGaN sandwiched between the adjoining GaN layers.

In conclusion, the apparent thermal stability of hydrogen-passivated Mg acceptors in *p* GaN is dependent on the annealing ambient, as it is in other compound semiconductors. While the acceptors are reactivated at $\leqslant$700 °C for annealing under N_2, hydrogen remains in the material until much higher temperatures and can accumulate in defective regions of double-heterostructure samples grown on Al_2O_3. It will be interesting to compare the redistribution and thermal stability of hydrogen in homoepitaxial GaN in order to assess the role of the extended defects present in the currently available heteroepitaxial material.

3. Role of hydrogen during processing

Light-ion implantation is typically used in III–V technology to produce high resistivity material through the introduction of point defects and complexes which are electron

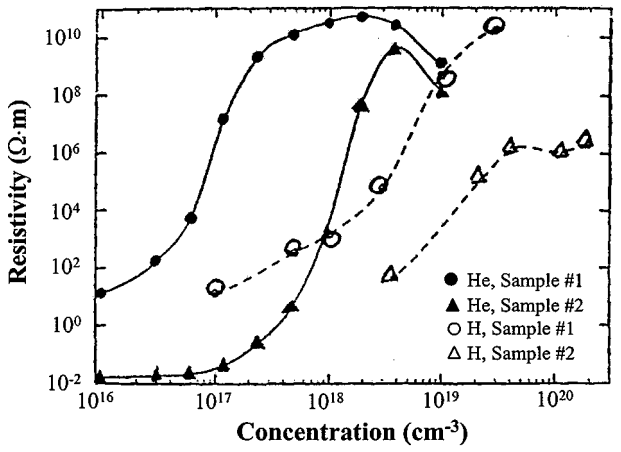

FIG. 90. As-implanted GaN resistivity for He- and H-implanted material, as a function of implant volume concentration (after Ref. 141).

and/or hole traps.[391,392] The thermal stability of this effect is an important consideration for designing the device processing sequence. High resistivity material is produced by implantation of any ion, but annealing at a sufficiently high temperature will remove the trap states, and the resistivity of the material will revert to its original value. If the implanted species has a chemical deep level in the band gap, then the material will remain resistive even at high annealing temperatures.[392]

A number of reports have discussed implant isolation in GaN using H, He, N, or O implantation.[393,394] Binari *et al.*[141] found that higher doses of implanted hydrogen were needed in comparison with He in order to isolate n^+GaN (Fig. 90). This is expected on the basis of the number of stable defects created by the two different species. The H-implanted material maintained high resistivity ($>10^9\,\Omega$ cm) only to $\sim$250 °C, and by 400 °C all samples had resistivity of only $\sim10^3\,\Omega$ cm. In Fig. 91 we compare the thermal stability of proton implant isolation in *n*-GaN and GaAs. The stability is surprisingly higher in GaAs, but higher stabilities for GaN can be obtained with N^+, O^+, or F^+.[394] The maximum incorporation depth of implanted protons in GaN is $\sim2\,\mu$m for

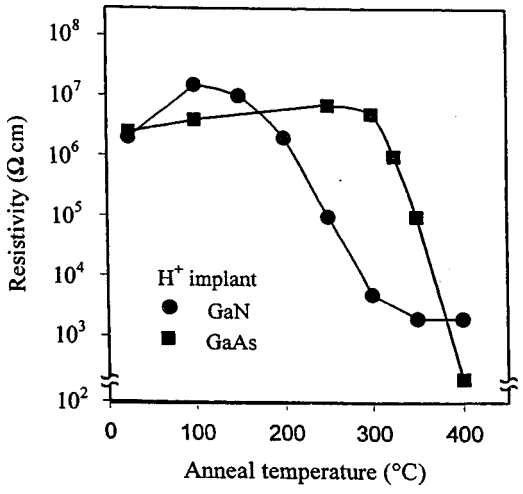

FIG. 91. Thermal stability of proton implant isolation in *n*-GaN or GaAs.

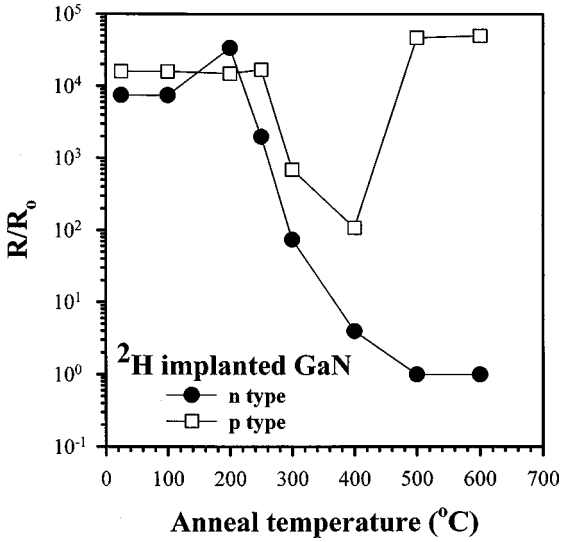

FIG. 92. Ratio of sample sheet resistance after implantation, R, to the control value (R_0) for p-type GaN implanted with multiple-energy $^2H^+$ ions, and subsequently annealed at different temperature.

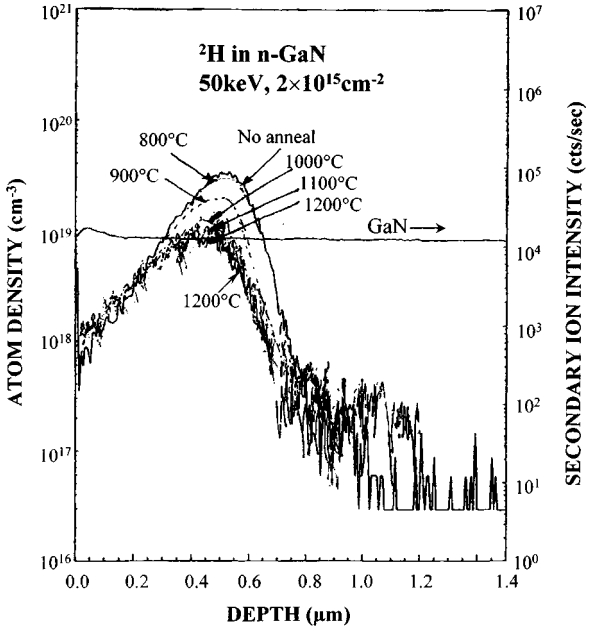

FIG. 93. Profiles of $^2H^+$ implanted n-type GaN, subsequently annealed at different temperatures.

a typical 200 kV implanter. While the deep levels in H-implanted GaN anneal out at $\leqslant$200 °C, temperatures above 800 °C are needed to cause most of the hydrogen to actually leave the material.[395,396]

We find substantial differences in the thermal stability of resistivity changes depending on the initial conductivity type of hydrogen-implanted GaN and a strong Fermi-level dependence of hydrogen diffusivity. In samples implanted with $^2H^+$ ions under two different conditions—for diffusion experiments the samples received a single energy (150 keV) implant at a dose of $2\times10^{15}\,cm^{-2}$, whereas for measurement of the effect on electrical properties of the layers, they were implanted with a multiple-energy (20, 50, 100, and 150 keV for the p-type; 20, 50, 100, 150, 200, 250, and 300 keV for the n-type) scheme, at a dose of $2\times10^{14}\,cm^{-2}$ for each energy. The redistribution of the implanted deuterium for anneals up to 1200 °C (60 s duration) was measured by SIMS using a Cs^+ ion beam. The sheet resistance of the multiply implanted sampled was obtained after different anneals using Van der Pauw geometry Hall measurements. In these samples alloyed HgIn ohmic contacts were fabricated prior to implantation.

Figure 92 shows the ratio of the sheet resistances after implantation and annealing to that before implantation, for both n- and p-type GaN. The as-implanted samples show resistances ~3–4 orders of magnitude higher than unimplanted material. This behavior is typical of ion-damaged compound semiconductors, and arises from the creation of defect states within the GaN band gap that act as traps for both the electrons in n-type material and the holes in p-type material. From separate temperature-dependent conductivity measurements, we find that the Fermi level is at $\sim E_c - 0.8$ eV in the n-type GaN after $^2H^+$ implantation and at $\sim E_v + 0.9$ eV in the implanted p-type GaN. We expect that a variety of different defect levels are created by the nuclear stopping process of the implanted deuterons (which would be measurable by deep level transient spectroscopy or thermally simulated capacitance), but the temperature dependence of conductivity yields only the dominant states. As the implanted samples are annealed, quite different behavior was observed for the two conductivity types. For the n-type GaN, the resistance initially increases with annealing, reaching a maximum at ~200 °C. At higher annealing temperatures the resistance decreases back to the original value. This is the same behavior typically observed in implanted compound semiconductors, and is usually ascribed to an initial reduction of hopping conduction as annealing of some of the implant-induced defect states occurs (leading to an increase in resistance), followed by a decrease in resistance as the trap density falls below the electron concentration and electrons are returned to the conduction band. Similar behavior has been reported previously by Binari *et al.*[141] in $^1H^+$ implanted n-GaN.

The implanted p-GaN shows an initial decrease in resistance up to ~400 °C, but then the resistance again increases and remains high even at 600 °C. This behavior is consistent with an initial annealing for the implant-induced deep level states, followed by the onset of hydrogen passivation of the Mg acceptors. In these bulk (electric-field-free) layers, the acceptor passivation is stable to $\geqslant$700 °C. In structures with strong internal electric fields, such as reverse-biased Schottky diodes, retrapping of the charged H^+ back onto the negatively charged acceptor is minimized, and reactivation of the passivated Mg occurs at lower temperature.

To confirm the above discussion, SIMS measurements were performed to determine the temperatures at which the ^2H is mobile in the implanted GaN. Figure 93 shows the results for the n-type GaN. There is no detectable motion or loss of ^2H until ~800 °C, with the deuterium lost by evolution from the surface at higher temperatures. Note that the remnant ^2H at each temperature decorates the residual implant damage, which persists even at 1200 °C. The peak of

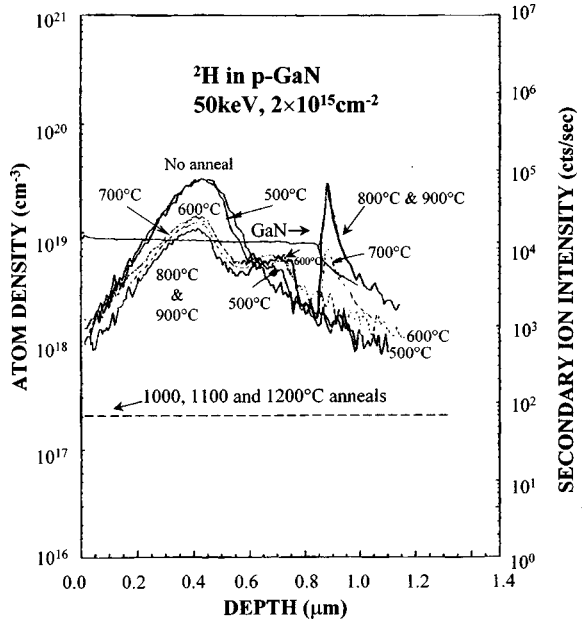

FIG. 94. SIM profiles of $^2H^+$ implanted *p*-type GaN, subsequently annealed at different temperatures.

the distribution shifts from the projected range of the implant to the peak of the damage distribution, which is slightly closer to the surface as confirmed by transport-of-ions-in-matter (TRIM) calculations.[129] Since there is little affinity for hydrogen to passivate donors in GaN, then once the deep level density falls below the electron concentration, the sheet resistance of the material returns to its original value.

The results for the *p*-type GaN are shown in Fig. 94. Diffusion of the hydrogen begins at 500 °C, leading to the creation of a plateau region deeper than the original implanted ^{2}H distribution. This concentration is the same as that of the Mg acceptors (interestingly not the hole density, which is a factor of ~10 lower due to the deep ionization level of the Mg, ~180 meV). The ^{2}H concentration in the original implanted region continues to decrease with higher annealing temperatures, and is completely gone by 1000 °C, a much lower stability than for the *n*-type GaN. By 700 °C there is also a noticeable accumulation of deuterium at the episubstrate interface. This is a region of strain, and it is well established in other semiconductor systems that hydrogen is attracted to, and trapped, at such places. It is clear that at annealing temperatures $\geqslant$500 °C, hydrogen diffuses out of the initial implanted regions and is trapped into Mg–H pairs and the episubstrate interface. This behavior is consistent with the electrical data of Fig. 92, where the presence of acceptor passivation (and the absence of donor passivation) would explain the results. Note also that the SIMS data shows the diffusivity of ^{2}H is much faster in *p*-GaN than in *n*-GaN, consistent with the predictions of Neugebauer and Van de Walle.[390]

In summary, GaN implanted with ^{2}H shows substantially different thermal stability in *n*- and *p*-GaN. In the former there is no apparent chemical effect of the deuterium, with the electrical properties controlled by the implant damage-related deep level states. Upon annealing, deuterium is released from the crystal, with the residual deuterium decorating the remaining implant damage. In *p*-GaN, diffusion of the deuterium starts at lower temperature, leading to the formation of Mg–H complexes that control the sample resistance in the temperature range of 500–700 °C.

In addition to direct implantation of hydrogen, it has been found that it can be unintentionally incorporated during many processing steps, including boiling in water, dry etching, chemical vapor deposition of dielectrics, and annealing in H_2 or NH_3.[397,398] For example, GaN boiled in D_2O at 100 °C for 30 min showed incorporation of ^{2}H up to ~1 μm in the material.[397] It is not known how the columnar nature of the GaN growth affects the hydrogen incorporation but comparisons with bulk crystals or homoepitaxial layers will be enlightening. Boiling in water has previously been shown to be an effective method of introducing hydrogen into Si,[399] and it generally diffuses very rapidly under these conditions because the H flux is low enough to avoid the H–H pairing reactions seen in plasma-exposed material.

KOH-based solutions readily etch AlN selectively over GaN, with etch rates that are temperature and material quality related.[400,401] Exposure of undoped GaN to a solution of KOH/D_2O for 20 min leads to incorporation of ^{2}H at a concentration of $\sim 10^{17}\,cm^{-3}$ to a depth of ~0.5 μm.[397] This shows that even at quite low processing temperatures (25 °C), atomic hydrogen can be readily diffused into GaN.

Another source of hydrogen incorporation is during PECVD of dielectrics such as SiN_x and SiO_2 for masking and surface passivation. It is known from GaAs work that PECVD of these dielectrics using SiN_x can cause extensive hydrogen passivation effects.[402,403] We have previously exported that ECR-CVD of SiN_x onto GaN at a rate of 250 Å min^{-1} at 250 °C produced ^{2}H incorporation depths of ~0.7 μm using SiD_4/N_2.[397] Postdeposition annealing of the SiN_x/GaN structure at 500 °C for 20 min did not produce any further indiffusion of ^{2}H from the SiN_x, indicating that the source of the initial incorporation is the exposure of the GaN surface to the silane discharge. Seaward[402] reported that hydrogen incorporation in GaAs during similar ECR-CVD of silicon nitride could be reduced by employing an initially fast deposition rate to encapsulate the surface as quickly as possible.

There are a variety of dry etch chemistries for GaN and related alloys, including Cl_2, BCl_3, SiC_4, CCl_2F_2, CH_4/H_2, HBr, HI, ICl, and IBr.[404–409] Additives such as Ar, N_2, or H_2 are often included to enhance sputter-assisted desorption of the etch products, or to balance removal of Ga and N etch products. Eddy and Molnar[408] found that ECR $CH_4/H_2/Ar$ discharges caused *n*-GaN to become more insulating and insulating films to become conducting. However these effects may have been due to a combination of ion-induced defects (since the mobility decreased in *n*-GaN) and preferential loss of N from the near-surface (1000 Å). Annealing at 800 °C for 30 s restored most of the original electrical properties.[408] If elevated sample temperatures are employed to enhance desorption of In from In-containing nitrides, then hydrogen indiffusion can be very substantial, with incorporation depths of 0.5–2 μm in 40 s at 170 °C, i.e., diffusivities of 10^{-9}–$6\times10^{-11}\,cm^2\,V^{-1}\,s^{-1}$.[365] Similar results were

found in AlN and GaN in addition to $In_xGa_{1-x}N$.[333] As mentioned before, it is not clear what role the extensive defect density in GaN heteroepitaxial samples plays, but it likely enhances the hydrogen diffusion substantially. The effect of H in dry etching of GaN is therefore two-fold—it may diffuse into the bulk of the sample and passivate dopants or defects, leading to an increased resistivity of the material, or it may produce preferential loss of N right at the surface, leading to a thin n^+ layer ~100 Å thick. In some cases if the loss of N is not too severe, annealing at 400–800 °C may be able to restore the surface stoichiometry, but in In-containing nitrides the vast difference in volatility of In and N of the products usually means that In droplets form and the surface cannot be restored by annealing without first removing the droplets in HCl. Room temperature etching minimizes indiffusion of hydrogen from the plasma.

4. Theory of hydrogen in nitrides

Brandt *et al.*[410] reported a new PL line at 3.35 eV after hydrogenation of *p*-type and unintentionally *n*-type GaN, suggesting the introduction of a hydrogen-related donor level. However these same workers created some confusion by reporting local vibrational modes around 2200 cm^{-1} for Mg–H complexes in GaN.[411] This led to a series of conflicting theoretical work that was guided by incorrect experimental data.

Okamoto *et al.*[412] used local density approximation of the density functional theory to calculate the stable positions of Mg and Mg–H in GaN. Mg was found to occupy a Ga substitutional site, producing a shallow acceptor level. They found the bond-centered (BC) site between Mg–N was the most stable site for hydrogen by ~0.1 eV relative to an antibonding site (AB) near the Mg atom. The N and intervening H were found to form a strong bond with the calculated bond length (1.02 Å) close to that of the NH_3 molecule (1.01 Å), and no bond charge between Mg and H. The distance between Mg and H was 1.96 Å, caused by displacement of the Mg atom from the substitutional site by 0.64 Å in the out-bonding direction (away from the position of the hydrogen). It was to be energetically favorable for the H to form the Mg–H complex, rather than remain an interstitial. The calculated vibrational frequency was ~3490 cm^{-1}, similar to H in NH_3 molecules (3444 cm^{-1}).

Bosin *et al.*[413] used *ab initio* calculations performed within local density functional theory to understand the energetics and geometry of H and its complexes in GaN. They found H to exhibit negative-U behavior, with thermal ionization energies for H_{III}^- and H_V^+ to be $E^{0/-}=0.8\,\text{eV}$ and $E^{+/0}=2.0\,\text{eV}$, respectively. They calculated Be_{Ga} to be a relatively shallow impurity level, while C_N had a deep acceptor level ($E_V+0.40\,\text{eV}$). Mg–H complexes were calculated to have vibrational modes at ~3000 cm^{-1} for antibonding AB_V sites for H, and at 3600–3900 cm^{-1} for BC site hydrogen. It was found that Be_{Ga}, C_N, Ca_{Ga}, and Zn_{Ga} acceptors would all be susceptible to hydrogen passivation.

Estreicher and Maric[414] employed molecular cluster calculations to examine hydrogen in cubic GaN. They considered three possibilities for the effect of hydrogen:

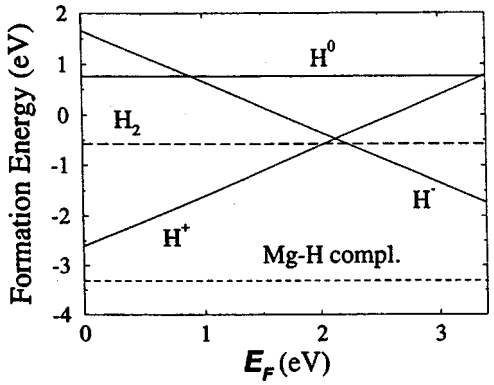

FIG. 95. Formation energy of H^+, H^-, and H^0 as a function of Fermi level position. Results are shown from Mg–H complexes and H_2 molecules (after Ref. 415).

(i) passivation (an electrical level moves from the gap to a band).
(ii) activation (an electrical level moves from a band to the gap).
(iii) level shifting (a level shifts within the gap, e.g., a shallow level becomes deep).

The latter case may be important in wide gap semiconductors because energy levels have to shift a lot to disappear from the gap. They found that H^+ is bound to N in a BC-like position, H^0 is at a BC site with H bound to Ga (and an activation energy for diffusion of <1 eV), while H^- is at the AB_{Ga} site (and an activation energy for diffusion of 1.5 eV). H_2 molecules were found to be stable at the tetrahedral interstitial (T_{Ga}) site.

Neugebauer and Van de Walle[415] performed density functional calculations and found the following:

(i) isolated interstitial hydrogen has a large negative-U energy, 2.5 eV, suggesting H^0 is unstable.
(ii) the hydrogen donor level is near the conduction band ($\sim E_C-0.1\,\text{eV}$) and the acceptor level deep ($E_V+0.9\,\text{eV}$). For $E_F<2\,\text{eV}$, the stable state is H^+, while above that, the stable state is H^-. For $E_F=2\,\text{eV}$, H_2 molecules might form by association of H^+ and H^-.
(iii) H^+ is at the AB_N site, with N–H ~ 1 Å bond length, but the BC configuration is only 0.1 eV higher in energy. The activation energy for diffusion of H^+ is 0.7 eV.
(iv) H^- is at AB_{Ga} site, with an activation energy for diffusion of 3.4 eV.
(v) H–Mg complexes have H at the AB_N site (Mg...N–H), with a N–H stretching frequency of 3360 cm^{-1} and a pair dissociation energy of 1.5 eV.[416] The energetics are summarized in Fig. 95.

Therefore, among theorists there is agreement on the following:[414]

(i) H^- is at the AB_{Ga} site, with a large activation energy for diffusion.
(ii) H^- is within ~1 Å of N.
(iii) H is strongly bound to the N atom in the Mg–H pair.

There is still some disagreement on the following issues:

(i) whether H^0 is at the AB_{Ga}[414–416] or BC sites,[413]
(ii) whether H^+ is at the AB_N site[413,415] or at the BC site,[414]
(iii) whether in the Mg–H complexes the H is at the AB_N side of N[389,391] with a high N–H stretching frequency, or at the BC site with a lower frequency.

Van Vechten *et al.*[417] suggested that hydrogen enables *p*-type doping by suppression of native defects, and suggested the incorporation (and subsequent removal) of hydrogen as a method for improving doping in wide band gap semiconductors. This was expanded upon by Neugebauer and Van de Walle,[418] who suggested that for this method to work, hydrogen would need to be the dominant compensating center, the dissociated hydrogen must have a high diffusion coefficient, and the energy needed to dissociate H-impurity complexes and remove the H would need to be lower than the formation energy of native defects.

Gotz *et al.*[419] corrected their earlier work covering local vibrational modes (LVMs) of Mg–H complexes in GaN, reporting a value of 3125 cm^{-1} for Mg–H and 2321 cm^{-1} for Mg–^{2}H, which were attributed to stretch modes of these complexes. Their previous work,[419] reporting LVMs at ~2200 cm^{-1}, presumably resulted from other defects. As-grown material was highly resistive ($10^{10}\,\Omega$ cm at 400 K), while annealing at 800 °C reduced this to 2 Ω cm. Subsequent hydrogenation at 600 °C increased the resistivity to $10^5\,\Omega$ cm at 400 K, due mainly to the fact this is too high a temperature to prevent substantial dissociation of the Mg–H complexes. There was a relatively poor correlation of IR signal intensity with active Mg concentration.[411] The IR stretch frequency is close to that of H in NH_3(3444 cm^{-1}) and similar to the value of N–H complexes in ZnSe (3195 cm^{-1}).[420,421]

Schematics of the possible configurations of hydrogen-dopant complexes in GaN are shown in Fig. 96. For donor dopants on either the Ga site (e.g., Si) or the N site (e.g., S) the hydrogen is in an antibonding position either attached to the dopant in the case of group IV donors or attached to the Ga neighbor in the case of a group VI donor. At this stage no reports of donor dopant passivation have been made, for the reasons outlined earlier. In acceptor dopants the hydrogen may be at a bond-centered site bonded predominantly either to the acceptor or a N neighbor, respectively, depending on whether the acceptor is from column IV or II of the Periodic Table, or in the antibonding position creating a N–H bond. Current thinking favors the latter for Mg–H, as outlined above, but more work is needed to definitively establish this configuration and to see if the BC site is favored for the other acceptors.

5. Summary

Hydrogen plays a particularly prominent role in *p*-type GaN because of its ability to passivate acceptors, requiring postgrowth annealing of MOCVD material in order to electrically activate the acceptors. Donor passivation is more elusive, but probably occurs under the right conditions. The use of deuterated gases has shown that hydrogen readily enters

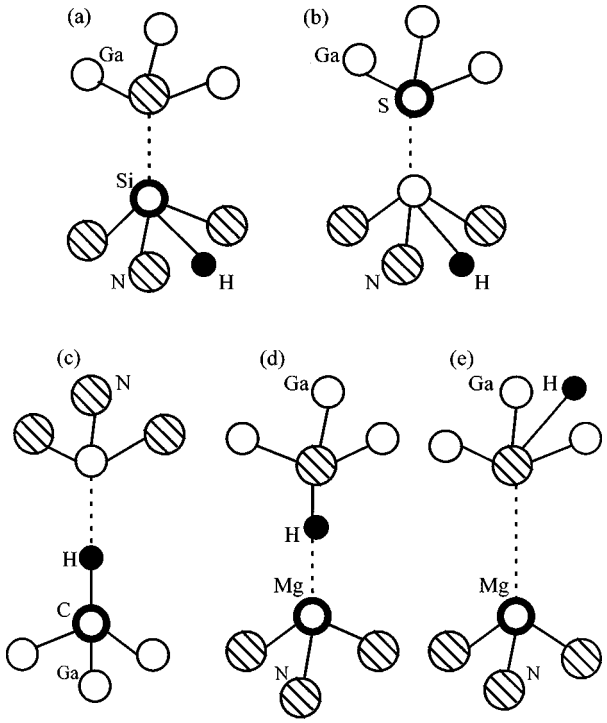

FIG. 96. Schematic representations of H-dopant complexes in GaN. The H occupies either an antibonding (AB) or bond-centered (BC) site.

GaN and related materials during low temperature processes such as CVD of dielectrics, plasma etching, wet etching, boiling in solvents, and contact sintering (metals may act as catalysts for H_2 dissociation). Therefore one faces the situation that hydrogen may be unintentionally incorporated into GaN at many stages of a device fabrication process, particularly when *p*-type layers are uppermost in the structure (i.e., LEDs and lasers). The out-diffusion and hydrogen retrapping behavior is more complex in multilayers (heterostructure) samples. Reactivation of passivated acceptors may be accomplished by thermal annealing or minority carrier injection to dissociate the dopant-hydrogen complexes. It will be very interesting to look at hydrogen incorporation in GaN bulk crystals with controlled doping levels (usually most of these samples are degenerately *n*-type, $n > 10^{19}\,cm^{-3}$) in order to establish the role of grain and column boundaries in heteroepitaxial material in assisting hydrogen diffusion.

B. Oxygen

1. GaN

It has been shown experimentally that the amount of oxygen present during the growth process can have a strong influence on the background *n*-type conductivity,[159,422] indicating that it is a shallow donor in GaN. The source of oxygen is often the NH_3 precursor used in MOCVD growth, the residual water vapor in MBE chambers or oxygen impurities leached from the quartz containment vessel often employed in N_2 plasma sources. Table VIII shows typical concentrations of O (and C, H, and Si, the other major residual impurities in III nitrides) detected by secondary ion mass spectrometry (SIMS) in the binary and ternary nitrides.[423] Under optimized conditions the O background in MOCVD material

TABLE VIII. Impurity densities in III nitrides (cm^{-3}).

Nitride	Growth	H	C	O	Si
GaN	MOCVD	5×17	1×17	1×18	5×16
	(Source A)	4×18	7×16	2×18	2×17
		4×18	3×17	4×18	2×16
		2×19	2×17	5×18	1×16
		2×19	2×17	6×18	3×16
		7×19	2×19	5×19	···
		1.5×18	8×17	1×18	5×17
		1×18	7×17	1×18	7×17
		2×18	4×18	2.5×19	7×17
GaN	MOCVD	3×17	6×15	6×16	1.5×17
	(Source B)	5×17	3×16	2×17	1.5×17
		2×17	3×16	1×17	3×16
		3×18	2.5×17	9×17	5×17
		2×18	5×16	2×17	···
GaN	MOCVD	4×18	1.5×18	2×18	8×17
	(Source C)	2×19	3×17	5×18	2×17
GaN	MOCVD	<1×17	1×15	1×16	5×10^{15}
	(Source D)	2×19	3×17	5×16	···
GaN	MOCVD	1×17	3×15	2×16	2×10^{15}
	(Source E)				
GaN	MOCVD	2×17	3×16	1×17	3×16
	(Source F)	5×17	1×17	1×17	1×17
GaN	MBE	4×19	1.5×18	2×19	3×17
		9×18	1.2×18	2×18	5×17
GaN	LA	1×20	1×21	1×21	1×19
AlN	MOCVD	1–2×18	7×17	2×18	1.5×19
AlN	CVD	3×18	3×15	5×18	3×16
		4×20	1×18	5×19	1×19
AlN	CVD	1×19	5×18	8×18	···
AlN	CVD	4×18	1.5×18	8×18	8×17
AlGaN	MOCVD	2×19	2×18	5×18	3×18
AlGaN	MOCVD	7×18	8×18	2×19	7×17
AlInN	MOMBE	5×18	3×18	2×19	1×20
InN	MOMBE	8×20	7×19	1×21	2×19

can be at the detection limit of SIMS, as shown in Fig. 97. More typical results are shown in Figs. 98 and 99, where the O concentration is $\sim10^{19}\,cm^{-3}$. We find that it is usually the case that high Si concentrations are also present, so that it is difficult to assign residual *n*-type conductivity solely to either impurity. Indeed it is possible that nitrogen vacancies, residual oxygen, and residual silicon all play a role in contributing to the *n*-type conductivity of most epi (and bulk) GaN.

The work of Chung and Gershenzon[159] found a donor state for oxygen in GaN of $E_C-0.078\,eV$, with banding occurring at high concentrations. Zolper *et al.*[134] directly implanted O^+ ions into insulating GaN, and activated by annealing at 1000 °C. The activation efficiency of the implanted oxygen was low, ~4%, but *n*-type material was created and an ionization level of ~29 meV was measured. The diffusivity was $\leqslant2.7\times10^{-13}\,cm^2\,s^{-1}$ at 1125 °C.

Oxygen implantation into initially doped GaN produces damage-related compensation which is thermally stable to ⩽750 °C, and indicates that oxygen does not have a deep acceptor or donor state with high concentration in this material. InGaN which is initially *n* type shows less effective implant isolation characteristics, with a maximum of a 10 fold increase in sheet resistance independent of ion species after a 500 °C anneal.

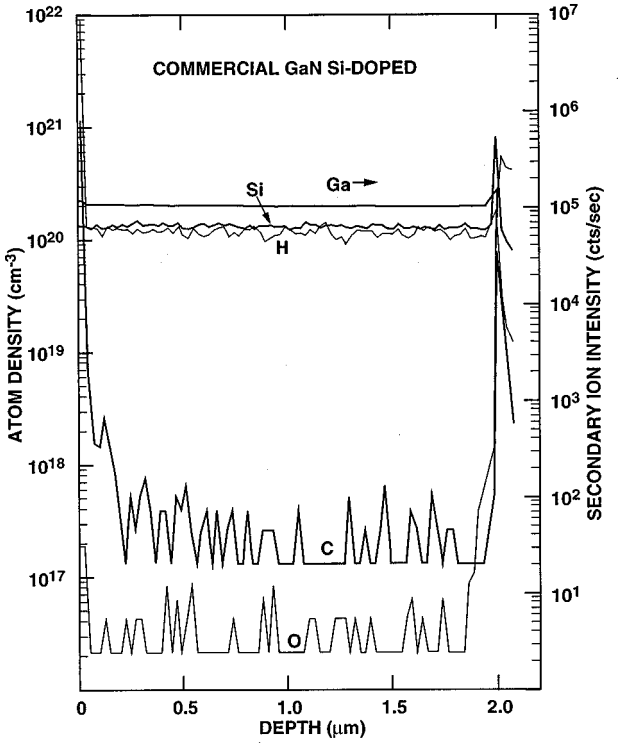

FIG. 97. SIMS profiles of high quality Si-doped MOCVD GaN.

InAlN, in contrast to InGaN, can be highly compensated with N or O implantation with over a 3 order-of-magnitude increase in sheet resistance after a 600–700 °C anneal while F implantation produces only one order-of-magnitude in-

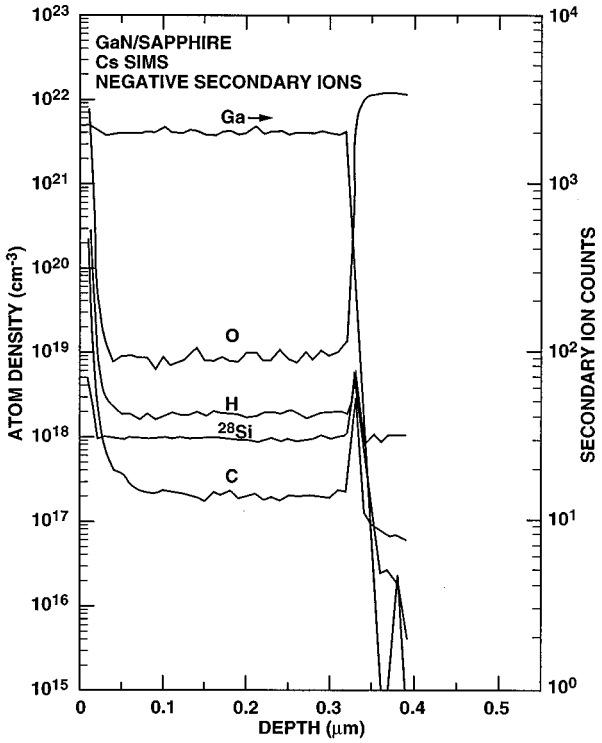

FIG. 98. SIMS profiles of typical undoped MOCVD GaN grown at low pressure.

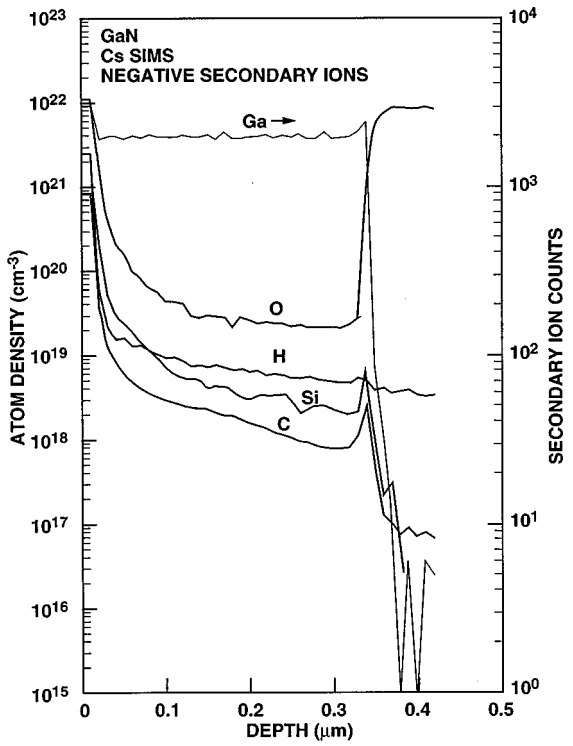

FIG. 99. SIMS profiles of typical undoped MOCVD grown at atmospheric pressure.

crease in sheet resistance. The compensating level in InAlN is also high in the band gap with the deepest level estimated at 580 meV below the conduction band edge in high dose N-isolated material, however it is sufficiently deep to achieve highly compensated material. The enhanced compensation of N and O implantation in InAlN may result from a reduction in N vacancies for N implantation or the formation of an O–Al complex for O implantation. An O–Al complex is thought to also be responsible for thermally stable implant isolation in O-implanted AlGaAs.[275]

Mattila and Nieminen[424] performed an *ab initio* study of oxygen point defects in both GaN and AlN. O_N in GaN was determined to be a shallow donor, for basically all positions of the Fermi level. They found under Ga-rich conditions the formation energy of O_N^+ was much lower than V_N^+ (by about 2 eV) and also O_I. This is consistent with the SIMS data discussed above, which shows large concentrations of oxygen in GaN, and also with other calculations.[425] The fact that O is isoelectronic with N has been suggested as a reason for its surprising affinity for being incorporated into GaN. The formation energies for O_{Ga} were always much larger than O_N and thus these defects should not play an important role.[426]

2. AlN

Concentrations of O up to several percent have been reported in AlN,[427] but high quality epimaterial typically contains levels in the $10^{18}\,cm^{-3}$ range (Table VIII). Theoretical work has suggested that O_N is the favored state, with a relatively low formation energy. The related ionization levels are deep in the gap for both acceptor (O_N^-) and donor (O_N^+) states.[428] Experimentally it is found that AlN is almost always insulating, with a high activation energy (>2 eV).[428] In AlGaN, isolated oxygen is predicted to have a DX-center behavior as the O moves from being a shallow donor in GaN to a deep electron trap in AlN.[424] Little is known about O in InN.

C. Carbon

Carbon can also be a major residual impurity in MOCVD nitrides (Table VIII)—its source is typically the metal organic gallium precursor.[429,430] It is generally assumed that C_N is the dominant species and thus is an acceptor, although some calculations suggest carbon is an amphoteric impurity in both GaN and AlN,[431] with ionization levels of 0.2 and 0.4 eV respectively. It was also predicted that C_N-C_{Ga} pair formation was favorable, leading to self-compensation.[431] It is also expected that carbon can complex with defects such as Ga vacancies.[432,433] Pankove and Hutchby[136,137] reported strong yellow luminescence centered at 2.17 eV for C-implanted GaN, and others have also linked carbon to the yellow luminescence.[434–436] Circumstantial evidence supporting this contention comes from the fact that there is little yellow PL in GaN grown by halide vapor phase epitaxy which employs C-free precursors (Ga, NH_3, and HCl).[437,438] Intentional carbon-doping actually produced n^+GaN ($\sim 4\times 10^{18}\,cm^{-3}$).[439]

The *p*-type GaN obtained by C doping during MOMBE has been reported,[188] with a maximum hole concentration of $\sim 3\times 10^{17}\,cm^{-3}$, and mobility $\sim 100\,cm^2\,V^{-1}\,s^{-1}$. There was little change in hole concentration with postgrowth annealing, suggesting that little hydrogen passivation was present. Parasitic etching by the CCl_4 precursor employed for C doping reduced the growth rate compared to undoped material.

We find that $In_xGa_{1-x}N$ and $In_xAl_{1-x}N$ alloys grown by MOMBE are strongly *n* type for $x \geqslant 0.15$ (InGaN) and for $x \geqslant 0.3$ (InAlN), with steadily decreasing conductivity as the In concentration is decreased. High electron concentrations have also been reported for InN grown by other methods,[440] and are usually ascribed to the presence of N vacancies, although this seems less likely in light of trends observed in InN grown using various III/V ratios.[440] Furthermore, ion channeling and AES do not indicate nitrogen deficiency in these films.

Another possible explanation for the electrical behavior in In-containing nitrides is the presence of unintentionally incorporated carbon. Though carbon has been shown capable of producing *p*-type GaN, the hole concentrations obtained have been limited to low $-10^{17}\,cm^{-3}$ even though carbon levels are measured to be $10^{20}\,cm^{-3}$ or higher. It has been found in other III–V materials that the maximum hole concentration which can be obtained using carbon is related to the difference in bond strength between the group III site and acts as a donor resulting in *n*-type material. Based on this simple model, it is expected that carbon will be a donor in InN and high In concentration alloys (see Fig. 100). Thus at least some of the conduction observed in these ternary films may be due to carbon. Further, as the composition is reduced in In, the tendency for carbon to act as an acceptor rather than a donor increases, thus possibly explaining the reduc-

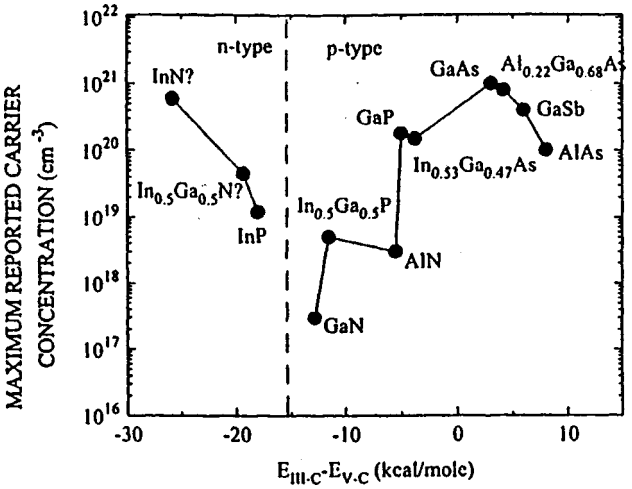

FIG. 100. Maximum reported carrier concentration for materials with various group III carbon and group V carbon bond strengths, as a function of the difference between the two bonds.

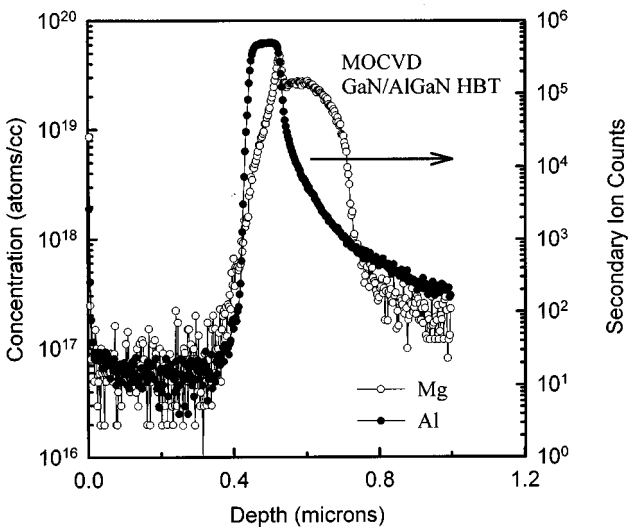

FIG. 102. SIMS profile of Mg in GaN HBT structure.

tion in electron concentration observed with increasing Ga or Al concentration. Clearly more work is needed in this area in order for the role of carbon to be fully understood.

We also implanted C into GaN and annealed at temperatures up to 1100 °C, but did not obtain *p*-type conductivity. Based on the results to date we find that C probably displays amphoteric behavior in the nitrides, with acceptor formation under some conditions (MOMBE-grown GaN) and possible donor action in other cases (implantation in GaN; growth of In-containing alloys).

To give some idea of the effect of impurities on GaN device performance, SIMS measurements were performed on an MOCVD heterojunction bipolar transistor structure (Fig. 101). SIMS profiles of the Mg employed as a base dopant, and the Al marker representing the AlGaN emitter are shown in Fig. 102. Note that residual hydrogen decorates the Mg-doped base region even after annealing of the structure (Fig. 103). This can lead to gain decreases as the device is operated, since the Mg–H complexes will be dissociated by minority carrier injection.

IV. DEVICES

A. AlGaN/GaN electronics

1. Materials requirements

a. Transistors. The potential of the wide band gap, nitride-based, semiconductors (GaN, AlN, and InN) for use in high power, high frequency transistors has been well documented.[441–444] This potential is due to the advantageous materials properties summarized in Table IX along with the existence of the AlGaN/GaN heterostructure.[445–468] The latter allows modulation doping to form a high mobility two dimensional electron gas (2DEG) and, equally important, the formation of piezoelectronically induced sheet carriers. The piezoelectronic effect is at least three times stronger in these materials than GaAs (see values for e_{31} and e_{33} in Table X) and contributes to the realization of high sheet electron densities (sheet electron densities up to $5\times10^{13}\,\mathrm{cm}^{-2}$ are predicted for an AlN/GaN interface) in AlGaN/GaN HEMTs.[446,462]

To realize high performance field effect transistors the following material and doping properties must be repeatably achieved: (1) High resistivity (noncompensated) buffer layers, (2) controllable *n*-type doping between $\sim1\times10^{17}$ (channel doping) and $>1\times10^{19}$ (contact doping), (3) abrupt

500 nm GaN Si-doped (>5x10^{19}cm^{-3})
20 nm AlGaN graded to GaN Si-doped (>10^{19}cm^{-3})
80 nm AlGaN Si-doped (>10^{19}cm^{-3} and Al = 0.2)
20 nm GaN undoped
220 nm GaN Mg-doped (5x10^{17}cm^{-3})
400 nm GaN Si-doped (10^{16}cm^{-3})
500 nm GaN Si-doped (>10^{19}cm^{-3})
GaN Buffer Layer

FIG. 101. Schematic of GaN HBT structure.

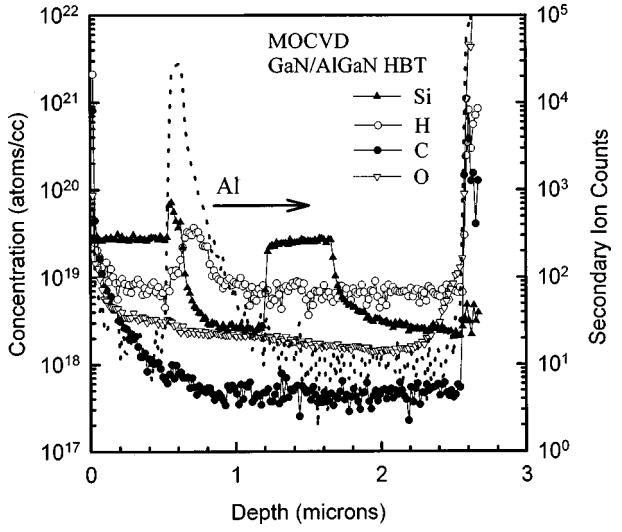

FIG. 103. SIMS profiles of Si, H, C, and O in GaN HBT structure.

TABLE IX. Nitride parameters (after B. E. Foutz; see http://iiiv.tn.cornell.edu/www/foutz/nitride.html).

	Units	GaN	AlN	InN
Crystal structure		Wurtzite	Wurtzite	Wurtzite
Density	g/cm	6.15 (447)	3.23 (447)	6.81 (447)
Transverse constant (C_1)	dyn/cm^2	4.42×10^{11} (447)	4.42×10^{11} (447)	4.42×10^{11} (447)
Longitudinal constant (C_1)	dyn/cm^2	2.65×10^{11} (447)	2.65×10^{11} (447)	2.65×10^{11} (447)
Transverse sound velocity	cm/s	2.68×10^5	3.70×10^5	2.55×10^5
Longitudinal sound velocity	cm/s	6.56×10^5	9.06×10^5	6.24×10^5
Static dielectric constant		8.9 (448)	8.5 (447)	15.3 (448)
High frequency dielectric constant		5.35 (448,461)	4.77 (447)	8.4 (448)
Energy gap (G valley)	eV	3.39 (458)	6.2 (459)	1.89 (460)
Electron effective mass (G valley)	m_e	0.20 (448)	0.48 (447)	0.11 (448)
Deformation potential	eV	8.3 (447)	9.5 (447)	7.1 (447)
Polar optical phonon energy	meV	91.2 (447)	99.2 (447)	89.0 (447)
Piezoelectric constant e_{14}	C/m^2	0.375 (447)	0.92	0.375 (447)
Piezoelectric constant e_{15}	C/m^2	⋯	−0.58 (449)	⋯
Piezoelectric constant e_{31}	C/m^2	⋯	−0/48 (449)	⋯
Piezoelectric constant e_{33}	C/m^2	⋯	1.55 (449)	⋯
Intervalley coupling coefficient	eV	91.2	99.2	89.0
Intervalley deformation potential	eV/cm	1×10^9	1×10^9	1×10^9
Lattice constant, a	Å	3.189 (454)	3.11 (454)	3.54 (454)
Lattice constant, c	Å	5.185 (454)	4.98 (454)	5.70 (454)
Electron mobility	cm^2/V s	1000 bulk 2000 (2D-gas) (455)	135 (456)	3200 Bulk
Hole mobility	cm^2/V s	30 (454)	14 (454)	
Hole lifetime	ns	∼7	⋯	⋯
Hole diffusion length (300 K)	m	$\sim0.8\times10^{-6}$	⋯	⋯
Nonparabolicity constant	(eV)$^{-1}$	0.189	⋯	0.419
Saturation velocity	cm/s	2.5×10^7 (455)	1.4×10^7 (456)	2.5×10^7 (466)
Peak velocity	cm/s	3.1×10^7 (455)	1.7×10^7 (456)	4.3×10^7 (466)
Peak velocity field	kV/cm	150 (455)	450 (456)	67 (466)
Breakdown field	V/cm	$>5\times10^6$ (454)		
Light hole mass	m_e	0.259 (454)	0.471 (454)	
Thermal conductivity	W/cmK	1.5 (454)	2 (454)	
Melting temp	°C	>1700 (454)	3000 (454)	1100 (454)

AlGaN/GaN interfaces, (4) modulation doping of AlGaN, and (5) low trap densities.

In addition for bipolar devices, such as heterojunction bipolar transistors (HBTs), to be produced in the nitride semiconductors improvements in *p*-type doping is needed and issues related to fabricating devices with buried *p*-regions (e.g., how to etch down to the *p*-type layer without creating a *n*-type surface region due to etch damage) need to be addressed.

These points will be addressed in the following sections.

TABLE X. Summary of key material parameters for AlGaAs/GaAs, 4H–SiC, and AlGaN/GaN transistors (after Refs. 444–446).

Metric	AlGaAs/GaAs	4H–SiC	AlGaN/GaN
Maximum sheet electron density (cm^{-2})	$2-3\times10^{12}$	na	$1-5\times10^{13}$
Breakdown field (V/cm) ($\times10^5$)	4	20	33
2 Dimensional electron mobility (cm^2/V s)	8500	na	2000
Saturated electron velocity ($\times10^7$ cm/s)	1.0	2.0	2.2
Thermal conductivity (W/cm K)	0.53	4.9[a]	1.3[b]
Piezoelectric coefficient (C/m$_2$) e_{31}	0.093		−0.36
e_{33}	−0.185	0.2	1.0

[a]This is for undoped SiC. Doped or semi-insulating SiC has a thermal conductivity of 3.3 W/cm K.
[b]This is for highly dislocated GaN. Theory predicts 1.7 W/cm K for low dislocation material [G. A. Slack, J. Phys. Chem. Solid. **34**, 321 (1973)].

b. Detectors. Solid state photodetectors that are sensitive only to radiation with a wavelength less than 400 nm are desirable for detection of photons from high temperature sources without saturation occurring from lower energy photons. This interest stems from the need to monitor furnace flames or to detect missile plumes without the detector being saturated by solar radiation which is characteristically >400 nm. $Al_xGa_{1-x}N$ is an ideal candidate semiconductor for fabrication of such detectors since its spans band gaps from 3.45 to 6.2 eV or wavelengths from 350 to 200 nm.

The first task for realizing $Al_xGa_{1-x}N$-based photodetectors is developing suitable epitaxial processes to realize the requisite compositions. Once this is achieved, and the desirable absorption characteristics are demonstrated, defects and their role on detector leakage and response time become paramount.

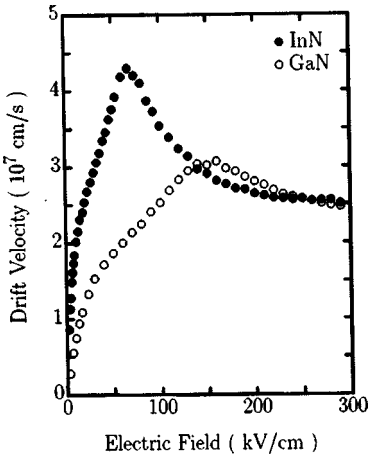

FIG. 104. Velocity curves for InN and GaN (after Ref. 466).

2. Transport properties

The carrier mobility and saturation velocity are the primary determinants of transistor performance. The nature of the electron saturated velocity is reviewed below followed by the electron mobility and its dependence on various scattering mechanisms.

a. Electron saturation velocity. The electron velocity dependence on applied field and low field dependence of electron mobility for GaN was first calculated by Littlejohn *et al.* in 1976.[463] Littlejohn included electron scattering from acoustic phonons, polar optical phonons, ionized impurities, and piezoelectric charge and predicted a peak in the electron drift velocity of 2×10^7 cm/s at a field of 10^5 V/cm. The work of Littlejohn was further expanded by Gelmont *et al.*,[464] to include the effect of upper valleys in the conduction band and account for intervalley scattering using a conduction band valley separation of 1.5 eV. Gelmont predicted a peak electron velocity at 300 K of 2.7×10^7 cm/s for an electron concentration of 10^{17} cm^{-3} and a field of 150 kV/cm.[464] To date, this high electron velocity has not been demonstrated in AlGaN/GaN HEMTs. The best estimate of the saturated electron velocity in present 0.15 μm HEMTs with an f_t for ~65 GHz is $\sim1.5\times10^7$ cm/s.[465] This may be due to scattering at charged dislocations or to ineffective carrier injection in the lateral HEMT structure.

The peak electron velocity of InN has also been calculated by O'Leary *et al.*,[466] as shown in Fig. 104. The calculation predicts an electron peak velocity for InN of 4.3×10^7 cm/s at a field of 60 kV/cm or ~2 times the peak electron velocity of GaN.[466] The saturated velocity of InN, however, was predicted to be equivalent to that of GaN or $\sim2.5\times10^7$ cm/s. Therefore, InN-based transport layers will have increased frequency performance if ballistic transport can be achieved.

When considering the potential for ballistic transport and velocity overshoot effects in transistors it is important to know the distance over which such effects may occur. This has been calculated for InN and GaN for a field twice that for the peak velocity.[467] At these fields significant velocity overshoot is expected to occur with InN calculated to achieve a peak velocity of 8×10^7 cm/s at a distance of ~0.1 μm.

b. Mobility versus impurities/phonons. A very thorough theoretical treatment of the effect of ionized impurity scattering, polar optical scattering, piezoelectric scattering, and acoustic scattering on electron transport in GaN and AlGaN/GaN heterostructures is given by Shur *et al.*[468] Figure 105 shows the results of Shur for the electron mobility in bulk GaN as limited by polar optical, piezoelectric, and acoustic scattering versus temperature. Polar optical scattering is seen to play a dominant role at temperatures greater than 200 K due to the large optical phonon energy of GaN of 91.2 meV, while acoustic, and to lesser extent piezoelectric scattering, dominates at lower temperatures.

Figure 106 shows the calculated dependence of electron mobility versus temperature as limited by ionized impurity scattering for four electron and donor concentrations. It is clear that the mobility increases with electron densities which is due to increase screening of the impurities. This is particularly true for $n>N_T$ which approximates the situation in a 2DEG.

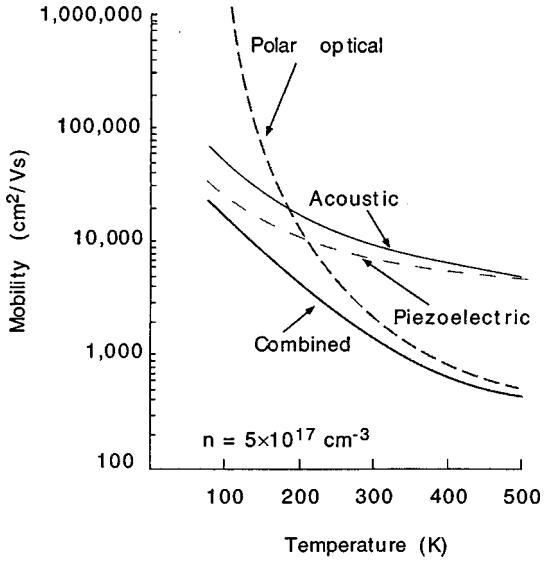

FIG. 105. Contributions to electron mobility in GaN from polar optical, piezoelectric, and acoustic scattering, as a function of temperature (after Ref. 453).

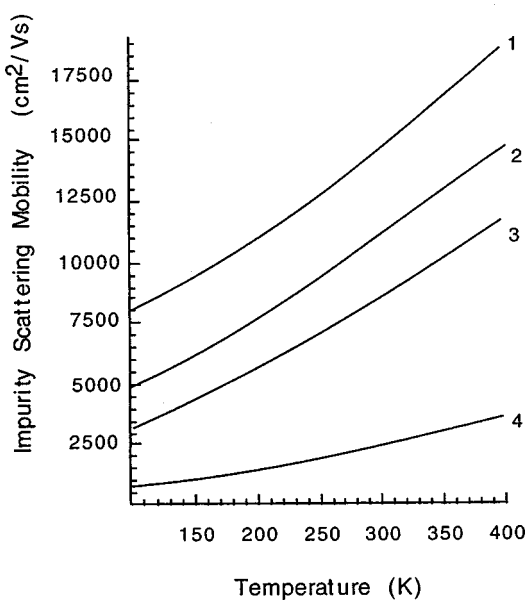

FIG. 106. Effect of ionized impurity scattering on electron mobility in GaN for total ionized impurity concentration of $7.5\times10^{16}\,cm^{-3}$, and carrier densities of (1) 5×10^{17}, (2) 2×10^{17}, (3) 7.5×10^{16}, (4) $2\times10^{16}\,cm^{-3}$ (after Ref. 468).

The combined effect of ionized impurity scattering, where mobility increases with temperature, and polar optical, piezoelectric, and acoustic scattering, where mobility decreases with temperature, has been calculated.[468] Both the bulk case and 2DEG case are included in Fig. 107 for hexagonal and cubic GaN. At 300 K, a 2DEG mobility near 2000 $cm^2/V\,s$ was measured for a AlGaN/GaN structure grown on 6H–SiC with a sheet electron density of $1.3\times10^{13}\,cm^{-2}$.[469] At 10 K the measured mobility increased to 10 250 $cm^2/V\,s$.

c. Mobility versus dislocations. A model addressing the role of dislocations on electron transport perpendicular to the dislocation direction has been developed by Weimann *et al.*[470] This is a critical consideration for GaN material grown on sapphire (a 12% lattice mismatch) or SiC (a 3.5% lattice mismatch) since dislocation densities are typically between 5×10^7 and $1\times10^{10}\,cm^{-2}$. They assumed the GaN grew as hexagonal columns rotated relative to each other by a small angle, (this may not be strictly true for growth on SiC but appears to be true for growth on sapphire) with dislocations propagating vertically between the columns. The dislocations were then treated as charged lines with the dependence of electron mobility calculated and measured experimentally. The increase of mobility with increased free electron concentration with a maximum near $10^{18}\,cm^{-3}$ is due to increased screen of the charged dislocation core. This treatment suggests that transport in vertical devices (e.g., lasers, LEDs, and HBTs) will be unaffected by the dislocations due to the repulsive band bending around the dislocations and the directional dependence of the scattering.[470]

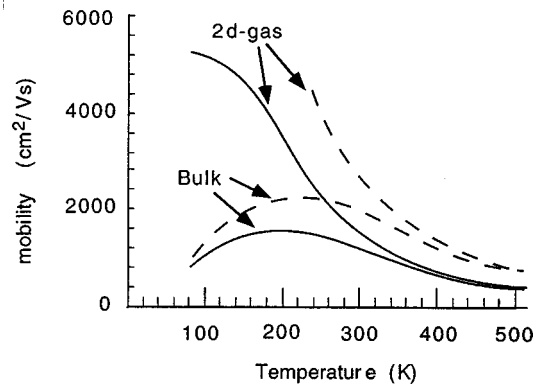

FIG. 107. Electron mobilities in cubic (dashed lines) and hexagonal (solid lines) GaN (after Ref. 468).

d. Negative differential resistance, Gunn effect. Devices based on negative differential resistance (NDR) such as Gunn or IMPATT diodes are attractive for high frequency oscillators. GaN is an attractive material for these devices due to its high breakdown field and high saturated electron velocity. There has been one report of the transferred-electron or NDR effect in GaN by Haung *et al.*[471] The measured current versus applied electric field between interdigitated electrodes on lightly doped ($=10^{14}\,cm^{-3}$) GaN displayed a threshold for NDR at 1.91×10^5 V/cm. This threshold level is much higher than that in GaAs (3×10^3 V/cm) or InP (1.1×10^4 V/cm) which is consistent with the larger band gap and intervalley separation (1.5 eV) in GaN. The threshold value is also close to that predicted theoretically by Littlejohn *et al.*[463] and by Gelmont *et al.*[464]

Practical GaN NDR diodes will also require development of low resistance *n*- and *p*-type ohmic contacts. Presently the *p*-type contact required for the IMPATT diode is limited by marginal *p*-type doping levels due to deep acceptor ionization energies and acceptor solubility limits in GaN. Further work is also needed to characterize the impact ionization rates for both holes and electrons in GaN so proper diode designs can be produced.

3. Piezoelectric effect

The strong piezoelectric coefficients of the III-nitride semiconductors are summarized in Table X. The fact that GaN grown on sapphire and SiC forms in the noncentrosymmetric wurtzite structure, as opposed to the cubic phase, results in large piezoelectric induced charge across III-nitride heterostructures due to strain at the interface.[462] This effect has been known for the (111) orientation of cubic zincblende semiconductors but it is both not as large in magnitude and of opposite sign as in the III-nitride materials.[472–474] The fact that the polarization field is in the opposite direction for the III nitrides as compared to other III–Vs is due to the greater ionicity of the nitrides. This causes the dipole moment arising from the rigid displacement of the atomic core to increase in importance relative to the strain-induced changes in the charge distribution along the bond direction and within the atomic cores.[472,475]

Figure 108 shows the calculated and experimental results for the piezoelectrically induced sheet charge in an AlGaN/GaN heterostructure versus Al composition in the AlGaN.[472] The dashed curve in Fig. 108 assumes a Schottky barrier at the AlGaN surface while the solid curve is for an unpinned Fermi level at the AlGaN surface. While it is clear

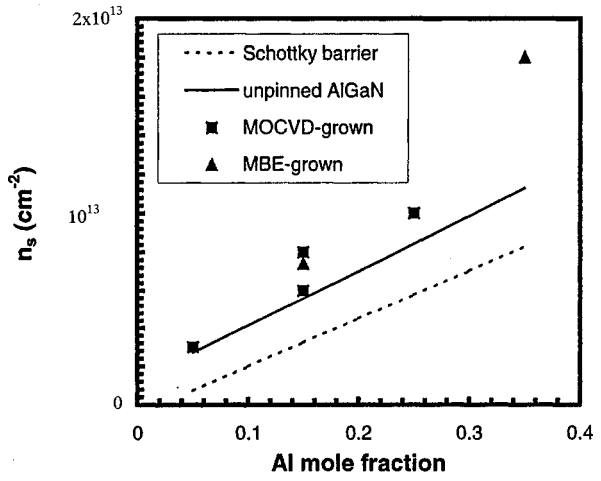

FIG. 108. Sheet electron density vs Al mole fraction in nominally undoped $Al_xGa_{1-x}N$/GaN HFET epitaxial layer. Points are from Hall measurements. The dashed line is the calculated variation assuming a Schottky barrier at the AlGaN surface while the solid curve is calculated assuming an unpinned Fermi level at the AlGaN surface (after Ref. 468).

that the nature of the surface plays an important role in the absolute sheet carrier concentration, the presence of the piezoelectrically induced charge is clear and on the order of 2.5×10^{13} X_{Al} electrons/cm^2.[472]

The piezoelectric effect can also be employed to accumulate free holes when the nature of the strain is compressive as opposed to tensile in the case of AlGaN on GaN.[472,476] This is illustrated in Fig. 109 where a buried AlGaN layer is included below an AlGaN/GaN heterostructure. As seen in the figure, a second buried channel is induced at the first AlGaN/GaN interface and the concentration of induced electrons in the upper channel is reduced to account for the charge balance across the buried AlGaN layer. The reduction in the induced electron concentration at the upper AlGaN/GaN interface was confirmed by $C-V$ profiling for structures with and without the buried AlGaN layer.[476] This same mechanism may be useful to enhance the

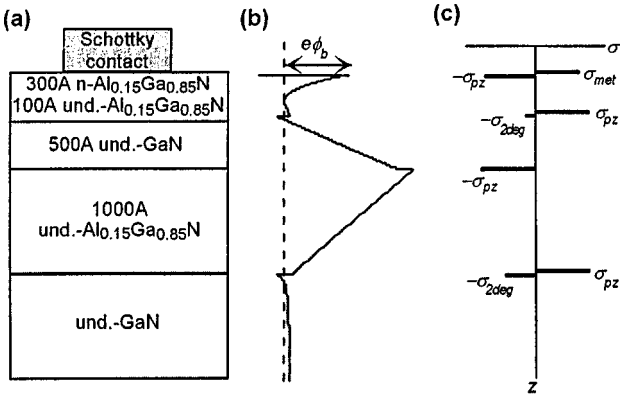

FIG. 109. Illustration of the effect of a buried AlGaN layer on the piezoelectronically induced electron concentration at the upper AlGaN/GaN interface. (a) Schematic diagram of a doped $Al_{0.15}Ga_{0.85}N$/GaN HFET with a buried $Al_{0.15}Ga_{0.85}N$ layer (b) Conduction band energy diagram for the structure in (a) with the dotted line representing the Fermi level. (c) Schematic of piezoelectronically induced charge (σ_{pz}) and free-carrier charge (σ_{2DEG}) (after Ref. 472).

two-dimensional hole gas in the base of HBTs or at *p*-type contacts to increase the effective *p*-type doping level at interfaces of these materials.

4. Properties of AlGaN/GaN transistors

a. dc performance. AlGaN/GaN transistor development has followed the materials improvements driven by photonic devices such as LEDs and laser diodes. Table XI outlines the key historical results for this technology.

As seen in Table XII, the first reports of GaN based transistors were by Khan *et al.* with the demonstration of a GaN MESFET and an AlGaN/GaN HEMT.[506,507] Both transistors had gate lengths of 4 μm with the MESFET having a g_m of 23 mS/mm and I_{DS}(max) of ~180 mA/mm ($@V_{GS}=0$ V, $V_{DS}=20$ V). The AlGaN/GaN HEMT achieved a g_m of 28 mS/mm at 300 K (46 mS/mm at 77 K) and I_{DS}(max) of ~50 mA/mm ($@V_{GS}=0.5$ V, $V_{DS}=25$ V). The HEMT structure had a 2DEG mobility of 563 cm^2/V s at 300 K and 1517 cm^2/V s at 77 K. The first microwave results were published by Binari *et al.*, for a GaN MESFET with a demonstrated f_t of 8 GHz and a f_{max} of 17 GHz for a gate length of 0.7 μm.[54]

Since the early results, significant improvements have been made in material quality and device processing. AlGaN/GaN 2DEG mobilities up to 2019 cm^2/V s have been reported for growth on 6H–SiC substrates and ~1600 cm^2/V s for growth on sapphire substrates.[508] The saturation current has been pushed to 1.6 A/mm and the transconductance has reached 340 mS/mm.[496]

b. Microwave small and large signal performance. Improvements in the small signal microwave performance of AlGaN/GaN HEMTs has tracked the dc improvements. The present state-of-the-art for unity current cut-off frequency (f_t) is 75 GHz; and for the maximum frequency of oscillation (f_{max}) is 140 GHz by Eastman and co-workers at Cornell University.[542] Large signal power results for HEMT on SiC substrates include total power of 4 W (2-mm-wide gate) at 10 GHz with 10 dB of gain with a power density of 6.8 W/mm (4.1 W/mm at 16 GHz) measured on smaller devices.[502] At 18 GHz a power density of 3.1 W/mm has been achieved on a sapphire substrate.[519] Total power results have also been pushed up with 7.6 W achieved at 4 GHz for HEMTs grown on sapphire and flip-chip mounted on AlN carriers.[543] These large signal results, however, are still not up to the level one would predict from the dc characteristics and the small signal performance of up to ~10 W/mm at 10 GHz. In some cases, the performance short fall is evident in current and gain compression at high applied voltages.[544–547] This compression is due to traps in the band gap, possibly at the surface, in the AlGaN barrier, or in the GaN buffer. Presently, the origin of the traps is still being studied, however, a similar phenomena was observed in the early GaAs device work and later overcome. In the GaAs case, the traps were due to surface states but this may not be the same in the AlGaN/GaN system.

c. Elevated temperature performance. The group III-nitride semiconductors have been considered an ideal candidate for high temperature electronic devices due to their large band gap and resulting low thermal carrier generation

TABLE XI. Historical development of GaN-based electronics (adapted from Ref. 13).

Year	Event	Authors	Ref.
1969	GaN by hydride vapor phase epitaxy	Maruska and Tietjen	16
1971	MIS LEDs	Pankove *et al.*	433
	GaN by MOCVD	Manasevit *et al.*	477
1974	GaN by MBE	Akasaki and Hayashi	478
1983	AlN intermediate layer by MBE	Yoshida *et al.*	479
1986	Specular films using AlN buffer	Amano *et al.*	480
1989	*p*-type Mg-doped GaN by LEEBI and	Amano *et al.*	305
	GaN *p-n* junction LED		
1991	GaN buffer layer by MOCVD	Nakamura	481
1992	Mg activation by thermal annealing	Nakamura *et al.*	482
	AlGaN/GaN two-dimensional electron gas	Khan *et al.*	483
1993	GaN MESFET	Khan *et al.*	52
	AlGaN/GaN HEMT	Khan *et al.*	484
	Theoretical prediction of piezoelectric effect in	Bykhovski *et al.*	485
	AlGaN/GaN		
1994	InGaN/AlGaN DH blue LEDs (1 cd)	Nakamura *et al.*	486
	Microwave GaN MESFET	Binari *et al.*	54, 487
	Microwave IIFET, MISFET	Binari *et al.*; Khan *et al.*	487, 488
	GaN/SiC HBT	Pankove *et al.*	489
1995	AlGaN/GaN HEMT by MBE	Ozgur *et al.*	490
1996	Doped channel AlGaN/GaN HEMT	Khan *et al.*	491
	Ion-implanted GaN JFET	Zolper *et al.*	134
	340 V V_{GD} AlGaN/GaN HEMT	Wu *et al.*	492
	1st blue laser diode	Nakamura and Fosal	8
1997	Quantification of piezoelectric effect	Asbeck *et al.*	462
	AlGaN/GaN HEMT on SIC	Binari *et al.*; Ping *et al.*	493, 494
		Gaska *et al.*	495
	1.4 W @ 4 GHz	Thibeault *et al.*	496
	0.85 W @ 10 GHz	Siram *et al.*	497
	3.1 W/mm at 18 GHz	Wu *et al.*	498
1998	3.3 W @ 10 GHz	Sullivan *et al.*	499
	p/*n* junction in LEO GaN	Kozodoy *et al.*	500
	HEMT in LEO GaN	Mishra *et al.*	501
	6.8 W/mm (4 W) @ 10 GHz HEMT on SiC	Sheppard *et al.*	502
	10^{-4} Hooge factor for HEMT on SiC	Levinshtein *et al.*	503
	1st AlGaN/GaN HBT	McCarthy *et al.*	504
		Ren *et al.*	505
	1st GaN MOSFET	Ren *et al.*	505

rate.[548] For this potential to be realized, defect levels in the band gap must be reduced since they will enhance undesirable dark and shunt currents. This can be seen in the temperature dependence of conduction reported by Khan *et al.*,[540] where a AlGaN/GaN HEMT demonstrated a large shunt current apparently resulting from defect assisted conduction in the GaN buffer layer already at 200 °C. Subsequently a GaN MESFET with an improved semi-insulating buffer was shown by Binari *et al.*, to maintain reasonable pinch-off characteristics at 400 °C.[549] When taken to 500 °C, the MESFET gate electrode began to interact with the GaN surface and irreversibly degrade the transistor operation. A AlGaN/GaN HEMT has been further pushed to operate at 750 °C by achieving a 1.0 eV activation energy for conduction in the buffer layer and employing a thermally stable Pt–Au gate contact.[550] More work is needed to optimize such elevated temperature operation and device packaging will also need to be considered.

d. Future direction for GaN electronics. The progress in field effect AlGaN/GaN transistors has been impressive but they may not meet the linearity requirements of some future electromagnetic systems, particularly for the military applications where ultrawide bandwidth and linearity are desired. Therefore, III-nitride based heterostructure bipolar transistors (HBTs) are now being studied since, in GaAs and InP, HBTs have demonstrated improved linearity over the FET counterpart. The first AlGaN/GaN HBTs have been reported, however, the current gain was only 3–10. The initial results were limited by a high base resistance.[504,505] Key issues remain to be resolved for group III-nitride HBTs. First among these is how to overcome the high ionization energy of Mg–*p*GaN that causes a high base resistance. A potential solution includes invoking the piezoelectric field to induce free holes and thereby reduce the base resistance. A second concern is achieving sufficiently long minority carrier lifetimes in the base to realize good current gain.

5. Minority carrier lifetime

Minority carrier lifetime is a critical parameter in the frequency response and detectivity of detectors, the gain of bipolar transistors, and the conductivity modulation of thyristors. Lifetime is also a critical measure of material quality as it relates to traps and recombination centers. Several re-

TABLE XII. AlGaN/GaN HFET device results in reverse chronological order (after B. E. Foutz, http://iiiv.tn.cornell.edu/www/foutz/ganhfet.html and Refs. 506–541).

Gate length	L_{SD}	f_T	f_{max}	L_{sd}	rf power	gm_{ext}	Refs.
micron	micron	GHz	GHz	A/mm	W/mm at GHz	mS/mm	
0.15		65	80	1.300	1.8 at 4	300	Unpublished
3	5			0.800		140	509
0.45		28	114	0.680	6.8 at 0	200	502
0.7	2	15	42	1.100	2.82 at 10	270	499,510
0.4		26	51	0.85			511
1.4	3.6			0.475		220	512,513
0.15		67	140	0.700	1.55 at 3	230	514
0.25	2	28	40	0.750		120	515
0.25	2	53	58	1.430		229	516
0.5	2	33	41	1.400		221	516
1	3	15	24	1.220		205	516
0.7	2	17.5	44	1.050	2.84 at 8 2.57 at 10	220	517
0.9	2	15	35	1.000		255	517
0.25	2		45	1.020	1.71at 8.4	220	518
1.5	5			0.950		142	495
0.25	1.6	52	82	1.130	3.3 at18	240	519
0.2	1.6	50	92	0.806	1.7 at10	240	520
0.12		46.9	103	0.550		120	521
0.25	2–3			1.710		222	522
0.25	2			1.000		130	523
4	6			1.000		130	523
2		6	11	0.260	1.5 at 4	105	524
0.25	2	37	81	1.000		152	525
0.5	2	21	53	0.880			525
0.7	2	14	44	0.850			525
1.0	3	11	31	0.740		122	525
1	3	9.6	27.2	0.700	1.57at 4	160	526
1.5	3			1.100		270	527
0.12		46.9	103	0.560		80	528
0.25	2	37.5	80.4	1.020		220	529
0.25	2	27	80	0.420		120	530
1	5	6	11	0.200		70	493
1.5	4			0.275		142	531
0.15	2	29.8	97.4	0.600	0.27at10	120	532
1	4	6	15	0.340		120	533
1.5	>2.5			0.695		222	534
1.5	3			0.330		130	492
1	3			0.310		140	492
2	4			0.490		186	535
1	5			.0350		120	536
1	5	18.3		0.600		110	491
0.25	>1	21.4	77.5	0.150		40	537
0.25	2	36.1	70.8	0.200		90	538
1	5			0.333		23	539
3	5			0.300		120	490
0.23	1.75	22	70	0.050		24	540
0.25	1.75	11	35	0.060		27	541
4	10			0.500		28	484

ports exist for measurement of recombination lifetimes in GaN with dislocation densities $>1\times10^7\,cm^{-2}$. While the lifetime will depend on sample doping and surface quality (i.e., the surface recombination velocity), there are three reports on the minority hole diffusion length in *n*-type GaN giving values of 0.1–0.3 μm for *n*-type layers in the range of $1-10\times10^{17}\,cm^3$ and dislocation densities in the $\sim10^9\,cm^2$.[547,551,552] This corresponds to a minority hole lifetime on the order of 2–7 ns. These values can be expected to improve as the dislocation density and point defect concentration is reduced.

6. Impact of reduced dislocation via lateral epitaxial overgrowth

To this point the discussion has dealt with GaN material grown on SiC or sapphire that has dislocation densities of

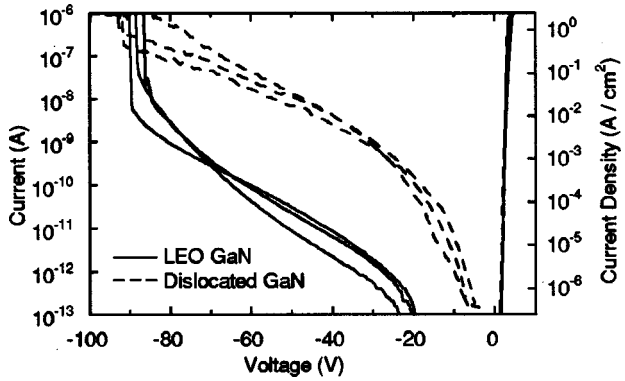

FIG. 110. $I-V$ characteristics from p-n junction on defective or low dislocation GaN (after Ref. 556).

$>1\times10^{7}\,\mathrm{cm}^{-2}$, however the use of lateral epitaxial overgrowth (LEO) had lead to GaN material with threading dislocation densities below the detectable limit of TEM ($<1\times10^{4}\,\mathrm{cm}^{-2}$).[553–555] The effectiveness of the LEO technique to limit threading dislocation propagation into the overgrown regions is clearly seen in TEM micrographs. This approach has been applied to blue laser diodes to extend the room temperature lifetime out to >3000 h of continuous-wave (cw) operation.[8] An explicit understanding of the reason for the laser diode lifetime improvement has not been put forward, but it may be due to a reduction in contact metal spiking down dislocations, reduced optical scattering at dislocations thereby reducing the lasing threshold, or improved doping efficiency (particularly p type) in the absence of dislocation also reducing the lasing threshold. More work is needed to understand the laser operation in the LEO material.

LEO material is also being developed for transistor applications to improve carrier mobility and device reliability. The first electrical data for low dislocation material compared directly to ''conventional'' high dislocation material was reported by Kozodoy *et al.*,[556] for p/n junction diodes. Small area diodes ($2\times20\,\mu\mathrm{m}^2$) were fabricated in adjacent regions of overgrown low dislocation GaN and GaN grown over the mask opening. In this way variations between wafers could be eliminated and the two material regions could be more closely compared. Figure 110 shows the reverse current voltage characteristics of the two diodes with the diode in the LEO material having ~4 orders-of-magnitude less leakage current than the conventional material. Initial results for HEMTs on the LEO material show a large reduction in gate leakage but still have trap induced current compression. Therefore, the defects alone are not the cause of the traps, although they most likely do degrade the electron mobility. Work is underway to characterize the mobility in the LEO material either by growing large overgrowth regions for Hall measurement or implementing a micro-Hall pattern.[557] The reduced leakage should translate to improved transistor breakdown characteristics and mobility enhancement will result lower on resistance and thereby better power performance.

7. Summary of electronics issues

Progress in GaN-based electronics has been remarkably rapid due to several factors. One of these is that the experience gained in GaAs/AlGaAs HEMTs has been quickly applied to the GaN/AlGaN system. At one time it was thought that MBE and related techniques would be the best choice for growth of electronic device structures, and this may still be the case if GaN substrates become available. However for heteroepitaxial growth there is still a need to grow thick buffer or ELO structures, which are best done with MOCVD. The rapid advances in material purity, ohmic contact quality, and gate contact stability have fueled the progress in HFETs in the GaN/AlGaN system. Much work remains to be done on vertical device structures such as thyristors and HBTs, where minority carrier lifetime, interface quality, and doping control are important factors. As with GaAs electronics, much of the impetus for nitride electronics is coming from defense applications and there is as yet no commercialization of these devices.

B. Ultrahigh power switches

There is a strong interest in developing wide band gap power devices for use in the electric power utility industry.[558–561] With the onset of deregulation in the industry, there will be increasing numbers of transactions on the power grid in the US, with different companies buying and selling power. The main applications are in the primary distribution system (100–2000 kVA) and in subsidiary transmission systems (1–50 MVA). A major problem in the current grid is momentary voltage sags, which affect motor drives, computers, and digital controls. Therefore, a system for eliminating power sags and switching transients would dramatically improve power quality. For example it is estimated that a 2 s outage at a large computer center can cost $600 000 or more, and an outage of less than one cycle, or a voltage sag of 25% for two cycles, can cause a microprocessor to malfunction. In particular, computerized technologies have led to strong consumer demands for less expensive electricity, premium quality power, and uninterruptible power.

The basic power electronics hierarchy would include the use of widegap devices such as gate turn-off thyristors (GTOs), MOS-controlled thyristors (MCT), or insulated gate bipolar transistors (IGBTs) combined with appropriate packaging and thermal management techniques to make subsystems (such as switches, rectifiers or adjustable speed devices) which then comprise a system such as flexible ac transmissions (FACTS). A schematic of a typical layout for such a system is shown in Fig. 111. Common power electronics systems, which are inserted between the incoming power and the electrical load include uninterruptible power supplies, advanced motors, adjustable speed drives and motor controls, switching power supplies, solid-state circuit breakers, and power conditioning equipment. About 50% of the electricity in the US is consumed by motors. Motor repairs cost ~$5B each year and could be dramatically reduced by high power electronic devices that permit smoother switching and control. Moreover, control electronics could

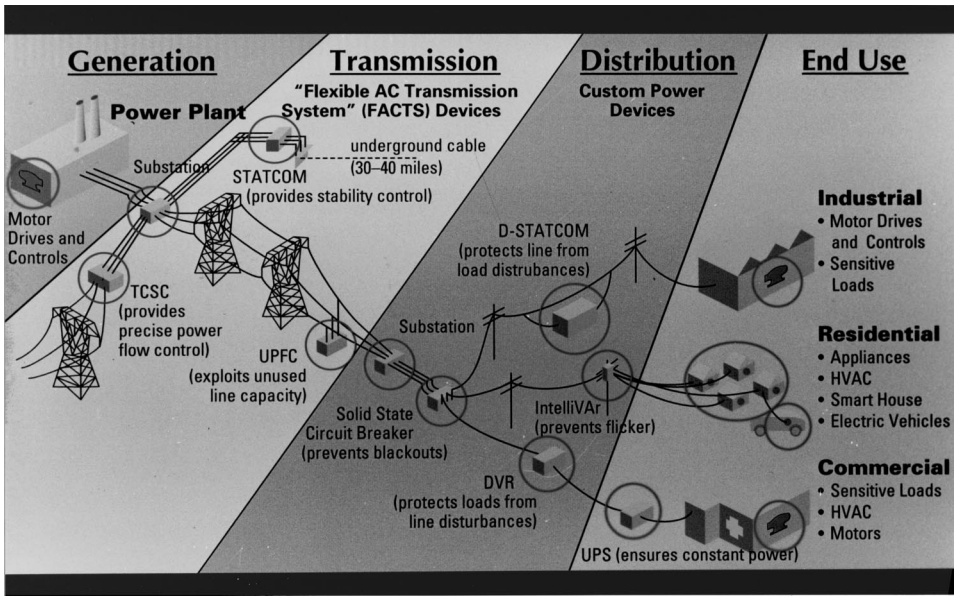

FIG. 111. Schematic of power flow control system utilizing power electronics.

dramatically improve motor efficiency. The other end uses include lighting, computers, heating, and air-conditioning.

The FACTS concept employed in electricity transmission aims for the following:

(1) Precisely regulate power flow on particular lines.
(2) Better system stability by instantly counteracting transients.
(3) Load transmission lines closer to their thermal limits (increase capacity) using:

(a) Thyristor controlled series capacitor (changes line impedance).
(b) Static compensator (STATCOM based on GTO thyristors) provides voltage support on lines by generating or absorbing reactive power without need for large external reactors or capacitor banks and mitigates disturbances.
(c) United power flow controller (comprehensively controls power flow, reduces line impedance, shifts phase angle, provides voltage support).

On the distribution side there is a need to precisely manage power quality and flow for variable loads. The components include the dynamic static compensator (DSTATCOM), which protects the line from a ''dirty'' load (and generally involves Si IGBTs), the dynamic voltage restorer, which protects a sensitive load from line disturbances (and also employs Si IGBTs) and solid-state breaker/transfer switches, which prevent black-outs (and employ semiconductor-controlled rectifiers and GTOs).

Thus the technology drivers for high power semiconductor devices from the utility viewpoint are:

(1) FACTS (flexible ac transmission system) devices that allow power grids to be tuned for maximum performance like low-power integrated circuits, increasing asset utilization.
(2) Distribution system components that enable precise subcycle regulation of voltage and power flow, including solid-state transfer switch (SSTS), solid-state circuit breaker (SSCB), dynamic voltage restorer (DVR), static compensator (DSTATCOM), advanced transformer, fault current limiter.
(3) Power electronics interconnection technologies (ac/dc inverters, frequency changers) that enable wider application of low- and no-emission systems for energy generation and storage including fuel cells, wind power, photovoltaics, batteries and superconducting magnetic energy storage.
(4) Advanced motor speed controllers that reduce or eliminate the significant power disturbances produced by existing adjustable speed drive.
(5) Power management technologies for electric vehicles that reduce pollution and dependence on imported oil.

Other high-power electronics applications include hybrid drivetrain (electric) vehicles, next generation (''all-electric'') battleships and the ''more-electric'' airplane for both military and commercial deployment.

Some desirable attributes of next generation, widegap power electronics include the ability to withstand currents in excess of 5 kA and voltages in excess of 50 kV, provide rapid switching, maintain good thermal stability while operating at temperatures above 250 °C, have small size and light weight, and be able to function without bulky heat-dissipating systems.

The primary limits of Si-based power electronics are:

(i) Maximum voltage ratings <7 kV
- Multiple devices must be placed in series for high-voltage systems.

(ii) Insufficient current-carrying capacity
- Multiple devices must be placed in parallel for typical power grid applications.

(iii) Conductivity in one direction only
- Identical pairs of devices must be installed in anti-parallel for switchable circuits.

(iv) Inadequate thermal management
- Heat damage is a primary cause of failure and expense.

(v) High initial cost
- Applications are limited to the highest-value settings.

(vi) Large and heavy components
- Costs are high for installation and servicing, and equipment is unsuitable for many customers.

For these reasons, there is a strong development effort on widegap power devices, predominantly SiC, with lesser efforts in GaN and diamond, which should have benefits that Si-based or electromechanical power electronics cannot attain. The higher stand-off voltages should eliminate the need for series stacking of devices and the associated packaging difficulties. In addition these widegap devices should have higher switching frequency in pulse-width-modulated rectifiers and inverters.

The current state-of-the-art in Si power devices includes 6 in. diam. light-triggered thyristors rated at 8 kV, 3.5 kA average current,[562,563] GTO thyristors rated at 6 kV and 2 kA in practical applications,[563] and press-pack reverse-conducting IGBTs rated at 2.5 kV and 1 kA.[564] Light triggering is often needed in stacked devices to ensure all of them turn-on at the same time. This might be used to advantage in power grid applications in another way, namely that control signals could be carried on the extensive optical fiber network that accompanies the power grid, and could be used to trigger GaN-based devices. Moreover, Er-doped GaN emitters could be used to send status signals back through the same network.

The absence of Si devices capable of application to 13.8 kV distribution lines (a common primary distribution mode) opens a major opportunity for widegap electronics. However cost will be an issue, with values of \$200–2000 per kV A necessary to have an impact. It is virtually certain that SiC switches will become commercially available within 3–5 years, and begin to be applied to the 13.8 kV lines. MOS turn-off-thyristors involving a SiC GTO and SiC MOSFET are a promising approach.[565] An inverter module can be constructed from an MOS turn-off thyristor (MTO) and a SiC power diode.

Bandic *et al.*[566] predict that a 5 kV stand-off voltage can be supported by a 20 μm $Al_{0.2}Ga_{0.8}N$ layer doped at $\sim 10^{16}\,cm^{-3}$. One of the question marks about the GaN/AlGaN system is whether because they are direct gap materials and have extremely short minority-carrier lifetimes, that thyristors will not be possible due to an inability to build up sufficient charge in thick drift layers. At Al concentrations >0.5, the AlGaN is indirect, but little information is available on lifetimes in the material. As a first step to building these devices, Ren *et al.*[505] recently demonstrated a GaN/AlGaN HBT capable of operation at $\geqslant 300\,°C$.

Packaging and thermal management will be a key part of future power devices. For current Si IGBTs, there are two basic package types—the first is a standard attached die, wire bond package utilizing soft solder, and wire bonds as contacts, while the second is the presspack, which employs dry-pressed contacts for both electrical and thermal paths.[567,568] In the classical package the IGBTs and control diodes are soldered onto ceramic substrates, such as AlN, which provide electrical insulation, and this in turn is mounted to a heat sink (typically Cu). Thick Al wires (500 μm) are used for electrical connections, while silicone gel fills the package.[567] In the newer presspack style, the IGBT and diode are clamped between Cu electrodes, buffered by materials such as molybdenum or composites[568] whose purpose is to account for the thermal expansion coefficient differences between Si and Cu. The package is again filled with gel for electrical insulation and corrosion resistance.

C. Laser diodes

The achievement of continuous wave GaN–InGaN laser diodes has tremendous technological significance. For commercially acceptable laser lifetimes (typically $\geqslant$10 000 h), there is immediate application in the compact disk data storage market. The recording and reading of data on these disks are currently performed with near-infrared ($\sim$780 nm) laser diodes. The switch to the much shorter wavelength ($\sim$400 nm) GaN-based laser diodes will allow higher recording densities [by $\sim(780/400)^2$ or almost a factor of 4]. There is also a large potential market in projection displays, where laser diodes with the three primary colors (red, green, and blue) would replace the existing liquid crystal modulation system. The laser-based system would have advantages in terms of greater design simplicity, lower cost, and broader color coverage. The key development is the need to develop reliable green InGaN laser diodes. The high output power of GaN-based lasers and fast off/on times should also have advantages for improved printer technology, with higher resolution than existing systems based on infrared lasers. In underwater military systems, GaN lasers may have application for covert communications because of a transmission passband in water between 450 and 550 nm.

While a number of groups have now reported room-temperature lasers in the InGaN/GaN/AlGaN heterostructure system under pulsed[569–580] and cw operation,[581–589] the field has been completely dominated by Nakamura *et al.*[569–574,576,577,581–589] The growth is performed by MOCVD, generally at atmospheric pressure. Initial structures were grown on *c*-plane (0001) sapphire, with a low temperature (550 °C) GaN buffer, a thick n^+GaN lower contact region, an n^+InGaN strain-relief layer, an n^+AlGaN cladding layer, a light-guiding region of GaN, then a multi-quantum well region consisting of Si-doped $In_{0.15}Ga_{0.85}N$ wells separated by Si-doped $In_{0.02}Ga_{0.98}N$ barriers. The *p* side of the device consisted of sequential layers of *p*-AlGaN, p^+GaN light-guiding, *p*-$Al_{0.09}Ga_{0.92}N$ cladding and p^+GaN contact. A ridge geometry was fabricated by dry etching in most cases (material removed down to the *p*-$Al_{0.08}Ga_{0.92}N$ layer), followed by dry etching, cleaving or polishing to form a mirror facet. These facets are coated (with TiO_2/SiO_2 in the Nichia case) to reduce laser threshold, while Ni/Au (*p* type) and Ti/Al (*n* type) were employed for ohmic metallization. The typical Nichia structure is shown in Fig. 112.

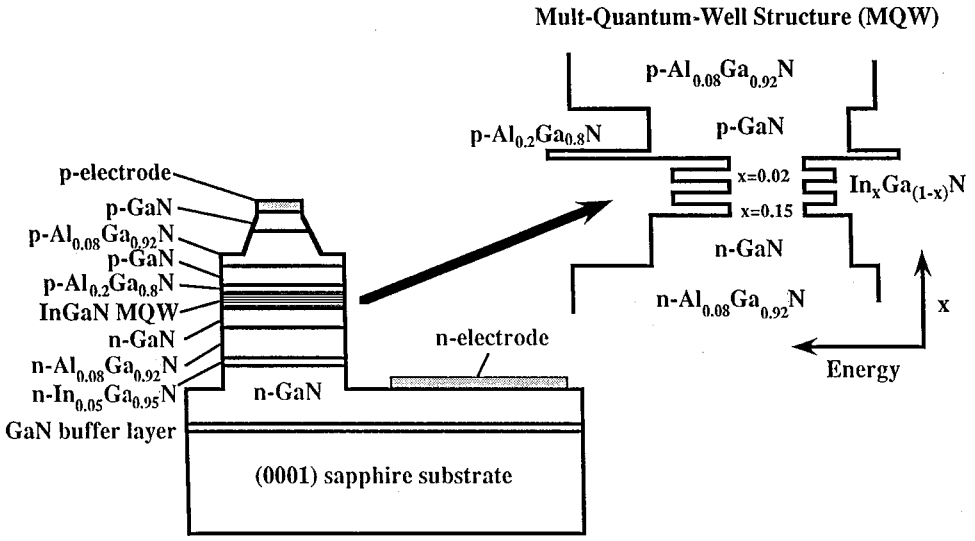

FIG. 112. Schematic of GaN/InGaN/AlGaN laser diodes grown on Al_2O_3 (after Ref. 569).

For this type of structure, threshold current densities are typically $\geqslant 4$ Ka cm^{-2} with an operating voltage of $\geqslant 5$ V at the threshold current. The emission mechanism is still the subject of intense study, but may be related to localization of excitons at compositional fluctuations (leading to potential minima in the band structure) in the InGaN wells.[590–592] These devices display relatively short lifetimes under cw operation, typically tens to hundreds of hours. The failure mechanism is most commonly short circuiting of the *p-n* junction, a result of *p*-contact metallization punch through. It is not that surprising that in this high defect density material that the metal can migrate down threading dislocations or voids under high drive-current conditions. The threshold carrier density of the laser diodes on sapphire are typically $\sim 10^{20}$ cm^{-3}, well above the theoretical values ($\sim 10^{19}$ cm^{-3}).[593–595]

A major breakthrough in laser diode lifetime occurred with two changes to the growth. The first was replacement of the AlGaN cladding layers with AlGaN/GaN strained-layer superlattices, combined with modulation doping. These changes had the effect of reducing formation of cracks that often occurred in the AlGaN, and also to reduce the diode operating voltage.[586] The second was the use of epitaxial lateral overgrowth (ELOG).[553,588,596] In this technique GaN is selectively grown on an SiO_2 masked GaN/Al_2O_3 structure. After ~ 10 μm of GaN is deposited over the SiO_2 stripes, it coalesces to produce a flat surface.[597] For a sufficiently wide stripe width, the dislocation density becomes negligible, compared to $\geqslant 10^9$ cm^{-2} in the window regions. A typical laser diode structure grown by the ELOG method is shown in Fig. 113. The laser itself is fabricated slightly off-center from the mask regions, due to gaps that occur there due to imperfect coalescence of the GaN. These devices have lower threshold current density ($\leqslant 4$ kA cm^{-2}) and operating voltage (4–6 V), and much longer (10 000 h) room-temperature lifetimes.[588,589] The reduction in threading dislocation density dramatically changes the lifetime, since the *p* metal no longer has a direct path for shorting out the junction during operation. The carrier density at threshold is also reduced to $\sim 3\times 10^{19}$ cm^{-3}, not far above the expected values. Output power $>$400 mW, and lifetime $>$160 h at 30 mW constant output power has been reported.[589]

Subsequent work from Nichia has focused on growth of the laser diodes on quasi-GaN substrates.[588,589] The thick (100–200 μm) GaN is grown on ELOG structures by either MOCVD or hydride VPE. The sapphire substrate is then removed by polishing, to leave a free-standing GaN substrate. The mirror facet can then be formed by cleaving. The GaN substrate has better thermal conductivity than sapphire.

The mixed group V nitrides, such as GaAsN, InAsN, AlAsN, GaPN, InPN, AlPN, GaInAsN GaAlAsN, and so on, are of interest for infrared laser and detector applications.[598–606] The addition of N into InGaAs[607] and InAsP[599] improves the temperature characteristics of long wavelength lasers, both quantum well diode structures, and vertical cavity surface-emitting diodes.[608] The use of GaInNAs allows for growth on GaAs substrates,[603] and produces a large conduction bond discontinuity ($\sim$0.5 eV). This leads to better electron confinement at high operation temperatures. Moreover, the large bowing properties of the band gap as nitrogen is added to both GaAs and InP and means that it may be possible to produce a zero band gap at relatively low ($\leqslant$10%) concentrations.[600] These features indicate the possibility of fabricating strain-compensated, quantum-well structures with lasing wavelength $>$1.55 μm. A potential problem

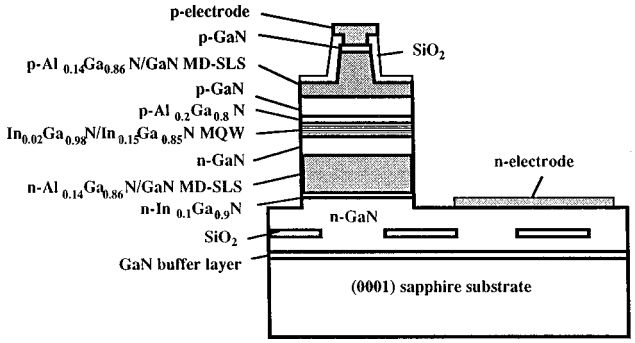

FIG. 113. Schematic of GaN/InGaN/AlGaN laser diodes grown on ELOG substrates (after Ref. 587).

is a shift from type I heterostructure band line-up to type II behavior as the nitrogen concentration increases.[608] There is of course, a large miscibility gap for the arsenides and phosphides with the nitrides, so that continuous alloy compositions over the entire range are not possible.

D. Light-emitting diodes

GaN-based LEDs operating in the green to violet range of the visible spectrum are commercially available. The total market for these devices worldwide is over $200M per year, divided between Nichia, Cree, Toyota Gosei, and Hewlett–Packard. The blue Nichia diodes emitting at 470 nm have luminous intensities of 2 cd with radiant flux 3 mW and spectral half-width 30 nm, while the green diodes emitting at 525 nm have intensity 6 cd, radiant flux 2 mW, and spectral half-width 40 nm. Single quantum well devices emitting in the yellow and even red (and hence requiring large In contents in the InGaN active region) are also soon to be available.

Currently the AlInGaP system is employed for yellow, red, and orange LEDs, with efficiency superior to unfiltered incandescent lamps.[13] Typical visible LEDs now have efficiencies above 10 lumens W^{-1}, extremely good lifetimes (>5 years), rapid response times. This makes them the light source of choice for applications ranging from color outdoor displays and signs, interior automotive lighting, exterior running lights on trucks and traffic lights. The energy savings and cost efficiency of LEDs relative to tungsten-filament incandescent lamps has been the main impetus behind their success.

The availability of the primary colors raises the possibility of white light sources. There are two basic options—the first is color conversion through use of a phosphor or organic dye inside the package to convert the blue light from a GaN LED into white light. The second method would be color mixing through integration of red, blue, and green LEDs in the same package. Nichia produced white light LED products based on combining a blue GaN LED with a yttrium–aluminum–garnet (YAG) fluorescent layer. The efficiency of this approach is less than that of the color-mixing technique since the phosphor efficiency is less than 100%, but it has substantial savings in terms of cost. There is also a program underway to develop this technology for fluorescent tubes for lighting applications, because of the much longer lifetime and reduced energy consumption relative to incandescent and conventional fluorescent lamps. A similar approach is being taken by Siemens.[609]

The GaN-based LEDs evolved from simple *p-n* junction devices comprising only GaN to single quantum well InGaN structures. The GaN *p-n* junction LED emission wavelengths were in the range of 370–390 nm, together with deep level emission at ~550 nm.[610,611,305] By employing InGaN/AlGaN double heterostructures, the output power was increased due to improved carrier confinement and the width of the spectral peak was roughly half that of the homostructure GaN LEDs.[612–615] A limitation of these double heterostructure devices was the limited wavelength range due to rapidly degrading InGaN material quality at high In contents (high misfit dislocation density and thermal mismatch between the InGaN active region and the AlGaN cladding layers). Moreover the InGaN had to be Zn doped to produce efficient blue and green emission. These drawbacks can be overcome by use of a single InGaN quantum well, whose thickness is below the critical value for dislocation introduction. This has been the standard structure for high-brightness LEDs, with colors ranging from blue to red.[616–619]

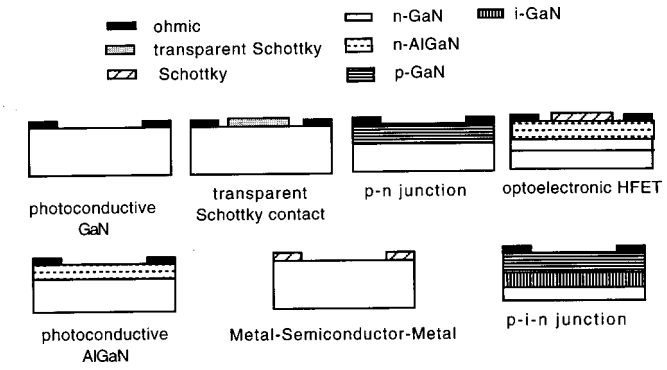

FIG. 114. Schematic of different types of AlGaN photodetectors (after Ref. 629).

Extensive investigations of the emission characteristics of the blue/green InGaN single quantum well have been carried out.[584,620] The electroluminescence is found to originate from carrier recombination at deep localized states, which are equivalent to three-dimensionally confined quantum dots. This explains the blue shift of the emission wavelength with current density in the green LEDs, as these states are filled. The InGaN layers show spatial inhomogeneity of the band gap, due to compositional fluctuations. Phase separation in InGaN has been reported by a number of groups,[621–627] even at relatively low InN mole fractions (<0.2). The potential minima have been examined by monochromatic cathodoluminescence mapping, and found to vary from 60 to 300 nm in lateral size.

E. UV photodetectors

The AlGaN system, spanning band gaps of 3.4–6.2 eV, is ideal for fabrication of solar-blind UV detectors. Smaller gap materials also are sensitive to visible and infrared radiation. The applications for the nitride devices include missile plume detection, flame sensing, ozone monitors, laser detectors, and pollution monitoring. By varying the Al content, the responsivity cut-off wavelength can be varied from 365 to 170 nm. Since the quantum efficiencies are high due to the direct gap of the Ga-rich alloys, there is the ability to form heterojunctions and high temperature operation is possible, $Al_xGa_{1-x}N$ appears to be ideally suited to UV detector fabrication.[628–646] SiC *p-n* junction photodiodes are also operable at high temperatures, but they lack the other advantages of AlGaN devices. However one drawback with AlGaN is the presence of deep states that store charge.

Figure 114 shows a schematic representation of different types of AlGaN photodetectors.[629] *N*-type material is generally used because of its higher carrier mobility. The standard

photoconductor geometries often suffer from high dark currents, dc drift, and slow response time,[641] and faster response can be achieved with *p-n* junction or Schottky diodes, which separate the generated charge more rapidly. The use of heterojunction photodiodes allows one to add an additional short wavelength cut-off.[641,645] Typical *p-n* and *p-i-n* junction UV photodiode responsivities are $\sim 0-1\ \mathrm{A\,W^{-1}}$, which correspond to external quantum efficiencies (i.e., collected *e-h* pairs per incident photon) of roughly 35%.[645] While Schottky photodiodes have better responsivity ($0-18\ \mathrm{A\,W^{-1}}$),[636] there is the disadvantage because of light absorption by the metal contact. It is difficult to realize avalanche photodiodes in GaN due to the high breakdown field needed.

V. SUMMARY

GaN and related alloys are one of the few instances where device applications have appeared before there was a complete understanding of the growth and defect issues. The rapid development and commercialization of blue and green LEDs, and the achievement of long-lifetime laser diodes has been followed by realization of UV photodetectors and numerous different electronic devices. The applications for GaN-based devices include displays and data storage, solar-blind UV detectors, new sensor technologies, wireless communications, solid-state lighting, and high power microwave generation for radar. In our viewpoint several factors have played a key role in realizing these devices, such as better control over the residual oxygen concentration in the MOCVD growth process [especially by use of improved purity precursors, NH_3, and $(CH_3)_3Ga$] and use of optimized buffer layers as a template for active layer growth; the development of low defect density epitaxy, using the ELO or quasi-GaN-substrate approaches; ability to grow high In-content InGaN; better stoichiometry control to avoid high *n*-type doping backgrounds in epitaxial material; improved processing methods in the areas of ohmic and rectifying contacts, dry etching, facet coating, cleaving and implant activation and isolation, and finally in device design. As a better understanding of the defect and impurity issues in these materials evolves, we expect continued rapid development in the areas of LEDs (where a broader range of emission wavelengths will be available through use of higher In content InGaN active layers), laser diodes, microwave and digital electronic devices, UV detectors, and high voltage unipolar and bipolar devices.

ACKNOWLEDGMENTS

The authors are grateful to the many people directly involved in this work through collaboration and discussion, including C. R. Abernathy, J. W. Lee, J. Hong, C. B. Vartuli, H. Cho, J. R. Lothian, X. A. Cao, A. G. Baca, J. Han, R. G. Wilson, J. M. Zavada, H. Shen, R. Singh, J. A. Sekhar, R. Hickman, J. Van Hove, P. P. Chow, M. Hong, S. M. Donovan, B. P. Gila, M. Overberg, T. E. Zipperian, M. Eizenberg, A. Katz, M. Schurmann, P. H. Holloway, T. J. Anderson, C. Constantine, D. Johnson, E. S. Lambers, R. F. Kopf, C. G. Willison, M. M. Bridges, L. Zhang, M. Hagerott-Crawford, R. D. Briggs, C. Tran, K. P. Killeen, L. F. Lester, A. T. Ongstad, L. Griego, A. Sher, S. S. Lau, M. Stavola, M. Weinstein, K. S. Jones, R. M. Biefeld, T. Suski, S. B. Van Deusen, G. Lopez, J. Jun, J. M. Baranowski, D. C. Hays, and S. N. G. Chu. The work at UF is partially supported by a DARPA/EPRI grant, MDA972-98-1-0006 (D. Radack/J. Melcher) and by ONR Grant No. N00014-98-1-6204. Sandia is a multiprogram laboratory operated by Sandia Corporation, a Lockheed-Martin company, for the US Department of Energy under Contract No. DE-AC04-94AC85000.

[1] See, for example, *GaN and Related Materials*, edited by S. J. Pearton (Gordon and Breach, New York, 1997); *GaN*, edited by J. I. Pankove and T. D. Moustakas (Academic, San Diego, 1988), and references therein.
[2] M. G. Craford, presented at IUVSTA Workshop on GaN, Hawaii, August 1997.
[3] S. Nakamura, M. Senoh, S. Nagahama, N. Iwasa, T. Yamada, T. Matsushita, Y. Sugimoto, and H. Kikoyu, Jpn. J. Appl. Phys., Part 2 **36**, L1059 (1997).
[4] S. Nakamura, IEEE J. Sel. Areas Commun. **3**, 435 (1997).
[5] S. Nakamura, presented at 3rd International GaN Conference, Tokushima, Japan, October 1997.
[6] S. Nakamura, IEEE J. Sel. Areas Commun. **4**, 483 (1998).
[7] H. Morkoc, *Wide Band Gap Nitrides and Devices* (Springer, Berlin, 1998).
[8] S. Nakamura and G. Fosol, *The Blue Laser Diode* (Springer, Berlin, 1998).
[9] S. N. Mohammad and H. Morkoc, Prog. Quantum Electron. **20**, 361 (1996).
[10] S. N. Mohammad, A. Salvador, and H. Morkoc, Proc. IEEE **83**, 1306 (1995).
[11] H. Morkoc, S. Strite, G. B. Gao, M. E. Lin, B. Sverdlov, and M. Burns, J. Appl. Phys. **76**, 1368 (1994).
[12] F. A. Ponce, in *Encyclopedia of Applied Physics*, edited by G. L. Trigg (VCH, Weinheim, 1998).
[13] F. A. Ponce and D. P. Bour, Nature (London) **386**, 351 (1997).
[14] I. Akasaki and H. Amano, J. Electrochem. Soc. **141**, 2266 (1994).
[15] Q. Z. Liu and S. S. Lau, Solid-State Electron. **42**, 677 (1998).
[16] A. C. Schmitz, A. T. Ping, M. A. Khan, Q. Chen, J. W. Yang, and I. Adesida, J. Electron. Mater. **27**, 255 (1998).
[17] L. L. Smith and R. F. Davis, in *Properties Of Group III Nitrides*, edited by J. H. Edgar (IEEE, London, 1994).
[18] S. E. Mohney and S. S. Lau, in *GaN and Related Materials II*, edited by S. J. Pearton (Gordon and Breach, New York, 1998).
[19] S. N. Mohammad, Z.-F. Fan, W. Kim, O. Aktas, A. E. Botchkarev, A. Salvador, and H. Morkoc, Electron. Lett. **32**, 598 (1996).
[20] M. R. H. Khan, T. Detchprom, P. Hacke, K. Hiramatsu, and N. Sawaki, J. Phys. D **28**, 1169 (1995).
[21] R. Sporken, C. Silien, F. Malengreau, K. Grigorov, R. Caudano, F. J. Sánchez, E. Calleja, E. Muñoz, B. Beaumont, and Pierre Gibart, MRS Internet J. Nitride Semicond. Res. **2**, 23 (1997).
[22] S. C. Binari, H. B. Dietrich, G. Kelner, L. B. Rowland, K. Doverspike, and D. K. Gaskill, Electron. Lett. **30**, 909 (1994).
[23] J. D. Guo, M. S. Feng, R. J. Guo, F. M. Pan, and C. Y. Chang, Appl. Phys. Lett. **67**, 2657 (1995).
[24] J. D. Guo, F. M. Pan, M. S. Feng, R. J. Guo, P. F. Chou, and C. Y. Chang, J. Appl. Phys. **80**, 1623 (1996).
[25] A. C. Schmitz, A. T. Ping, M. A. Khan, Q. Chen, J. W. Yang, and I. Adesida, Semicond. Sci. Technol. **11**, 1464 (1996).
[26] Q. Z. Liu, L. S. Yu, S. S. Lau, J. M. Redwing, N. R. Perkins, and T. F. Kuech, Appl. Phys. Lett. **70**, 1275 (1997).
[27] T. U. Kampen and W. Mönch, MRS Internet J. Nitride Semicond. Res. **1**, 12 (1997).
[28] Q. Z. Liu, L. S. Yu, K. V. Smith, F. Deng, C. W. Tu, P. M. Asbeck, E. T. Yu, and S. S. Lau, *Proceedings of the ECS Symposium on GaN and Related Materials*, Paris, October 1997, Vol. 97-34 (ECS, Pennington, NJ, 1998).
[29] P. Hacke, T. Detchprom, K. Hiramatsu, and N. Sawaki, Appl. Phys. Lett. **63**, 2676 (1993).
[30] A. T. Ping, A. C. Schmitz, M. A. Khan, and I. Adesida, Electron. Lett. **32**, 68 (1996).

[31] E. V. Kalinina, N. I. Kuznetsov, V. A. Dimitriev, K. G. Irvine, and C. H. Carter, Jr., J. Electron. Mater. **25**, 831 (1996).
[32] L. Wang, M. I. Nathan, T.-H. Lim, M. A. Khan, and Q. Chan, Appl. Phys. Lett. **68**, 1267 (1996).
[33] Z. Fan, S. N. Mohammad, W. Kim, O. Aktas, A. E. Botchkarev, K. Suzue, and H. Morkoc, J. Electron. Mater. **25**, 1703 (1996).
[34] T. U. Kampen and W. Mönch, Appl. Surf. Sci. **117/118**, 388 (1997).
[35] M. A. Khan, J. N. Kuznia, D. T. Olson, and R. Kaplan, J. Appl. Phys. **73**, 3108 (1993).
[36] V. M. Bermudez, J. Appl. Phys. **80**, 1190 (1996).
[37] R. W. Hungt, L. Vanzetti, T. Castro, K. M. Chen, L. Sorba, P. I. Cohen, W. Gladfelter, J. M. Van Hove, J. N. Kuznia, M. A. Khan, and A. Franciosi, Physica B **185**, 415 (1993).
[38] Q. Z. Liu, L. S. Yu, F. Deng, S. S. Lau, Q. Chen, and M. A. Khan, Appl. Phys. Lett. **71**, 1658 (1997).
[39] Q. Z. Liu, S. S. Lau, N. R. Perkins, and T. F. Kuech, Appl. Phys. Lett. **69**, 1722 (1996).
[40] J.-Y. Duboz, F. Binet, N. Laurent, E. Rosencher, F. Scholz, V. Harle, D. Briot, B. Gil, and R. L. Aulombard, Mater. Res. Soc. Symp. Proc. **449**, 1085 (1996).
[41] L. L. Smith, S. W. King, R. J. Nemanich, and R. F. Davis, J. Electron. Mater. **25**, 805 (1996).
[42] S. W. King, L. L. Smith, J. P. Barnak, J.-H. Ku, J. A. Christman, M. C. Benjamin, M. D. Bremser, R. J. Nemanich, and R. F. Davis, Mater. Res. Soc. Symp. Proc. **395**, 739 (1996).
[43] N. V. Edwards, M. D. Bremser, T. W. Weeks, Jr., R. S. Kern, R. F. Davis, and D. E. Aspnes, Appl. Phys. Lett. **69**, 2065 (1996).
[44] A. C. Schmitz, A. J. Ping, M. A. Khan, Q. Chen, J. W. Yang, and I. Adesida, Electron. Lett. **32**, 1832 (1996).
[45] Q. Z. Liu, L.-S. Yu, S. S. Lau, J. M. Redwing, N. R. Perkins, and T. F. Kuech, Appl. Phys. Lett. **70**, 1275 (1997).
[46] J. S. Foresi and T. D. Moustakas, Appl. Phys. Lett. **62**, 2859 (1993).
[47] N. I. Kuznetsov, E. V. Kubinina, V. A. Soloviev, and V. A. Dimitriev, Mater. Res. Soc. Symp. Proc. **395**, 837 (1996).
[48] Z. Fan, S. Mohammad, W. Kim, O. Aktas, A. E. Botchkarev, and H. Morkoc, Appl. Phys. Lett. **68**, 1672 (1996).
[49] M. W. Cole, F. Ren, and S. J. Pearton, J. Electrochem. Soc. **144**, L275 (1997); Appl. Phys. Lett. **71**, 3004 (1997).
[50] J. C. Zolper and R. J. Shul, MRS Bull. **22**, 36 (1997).
[51] M. Murakami, Y. Koide, T. Oku, H. Mori, and C. J. Uchibori, Proc. Electrochem. Soc. **97-21**, (1997).
[52] M. A. Khan, T. N. Kuznia, A. R. Bhattaraia, and D. T. Olson, Appl. Phys. Lett. **62**, 1786 (1993).
[53] S. Nakamura, T. Mukai, and M. Senoh, Jpn. J. Appl. Phys., Part 2 **30**, L198 (1992).
[54] S. C. Binari, L. B. Rowland, W. Kruppa, G. Kelner, K. Doverspike, and D. K. Gaskill, Electron. Lett. **30**, 1248 (1994).
[55] S. Nakamura, M. Senoh, and T. Mukai, Appl. Phys. Lett. **62**, 2390 (1993).
[56] L. L. Smith, R. F. Davis, M. J. Kim, R. W. Carpenter, and Y. Huang, J. Mater. Res. **12**, 2249 (1997).
[57] B. P. Luther, S. E. Mohney, T. N. Jackson, M. A. Khan, Q. Chen, and J. W. Wang, Appl. Phys. Lett. **70**, 57 (1997).
[58] Y. Kribes, I. Harrison, B. Tuck, K. S. Kim, T. S. Cheng, and C. T. Foxon, Semicond. Sci. Technol. **12**, 500 (1997).
[59] M. E. Lin, Z. Ma, F. Y. Huang, ZZ. F. Fan, L. A. Allen, and H. Morkoc, Appl. Phys. Lett. **64**, 1003 (1994).
[60] S. E. Mohney and X. Lin, J. Electron. Mater. **25**, 811 (1996).
[61] L. L. Smith, M. D. Bremser, E. P. Carlson, T. W. Weeks, Jr., Y. Huang, M. J. Kim, R. W. Carpenter, and R. F. Davis, Mater. Res. Soc. Symp. Proc. **395**, 861 (1996).
[62] S. Miller and P. H. Holloway, J. Electron. Mater. **25**, 1709 (1996).
[63] Y. F. Wu, W. N. Jiang, B. P. Keller, D. Kapolneck, S. P. DenBaars, and U. K. Mishra, Solid-State Electron. **41**, 165 (1997).
[64] S. E. Mohney, B. P. Cutler, T. N. Jackson, and M. A. Khan, Mater. Res. Soc. Symp. Proc. **395**, 843 (1996).
[65] S. E. Mohney, J. S. Venugupulan, and B. P. Luther, Proc. Electrochem. Soc. **97-30**, 101 (1997).
[66] S. E. Mohney, D. J. MacMahon, and K. L. Whitmire, Mater. Sci. Eng., B **49**, 152 (1997).
[67] L. F. Lester, J. M. Brown, J. C. Ramer, L. Zhang, S. D. Hersee, and J. C. Zolper, Appl. Phys. Lett. **69**, 2737 (1996).
[68] A. T. Ping, Q. Chan, J. W. Yang, M. A. Khan, and I. Adesida, J. Electron. Mater. **27**, 261 (1998).
[69] A. T. Ping, M. A. Khan, and I. Adesida, J. Electron. Mater. **25**, 819 (1996).
[70] B. P. Luther, J. M. DeLucca, S. E. Mohney, and R. F. Karlicek, Appl. Phys. Lett. **71**, 3859 (1997).
[71] B. P. Luther, S. E. Mohney, J. M. DeLucca, and R. F. Karlicek, J. Electron. Mater. **27**, 196 (1998).
[72] C. T. Lee, M. Y. Yeh, C. D. Tsai, and Y. T. Lyu, J. Electron. Mater. **26**, 262 (1997).
[73] J. Burm, K. Chu, W. A. Davis, W. J. Schaff, L. F. Eastman, and T. J. Eustis, Appl. Phys. Lett. **70**, 464 (1997).
[74] F. Ren, C. R. Abernathy, S. N. G. Chu, J. R. Lothian, and S. J. Pearton, Appl. Phys. Lett. **66**, 1503 (1995).
[75] F. Ren, C. R. Abernathy, S. J. Pearton, and P. W. Wisk, Appl. Phys. Lett. **64**, 1508 (1994).
[76] C. R. Abernathy, J. Vac. Sci. Technol. A **11**, 869 (1993).
[77] C. R. Abernathy, Mater. Sci. Eng., R. **14**, 203 (1995).
[78] R. J. Shul, S. P. Kilcoyne, M. Hagerott-Crawford, J. E. Parmeter, C. B. Vartuli, C. R. Abernathy, and S. J. Pearton, Appl. Phys. Lett. **66**, 1761 (1995).
[79] S. Nakamura, M. Senoh, and T Mukai, Appl. Phys. Lett. **62**, 2390 (1993).
[80] S. Nakamura, T. Mukai, and M. Senoh, Appl. Phys. Lett. **64**, 1687 (1994).
[81] M. Schauler, C. Kirchner, M. Mayer, A. Pelzmann, F. Eberhard, M. Kamp, P. Unger, and K. J. Ebeling, MRS Internet J. Nitride Semicond. Res. **2**, 44 (1997).
[82] H. Ishikawa, S. Kobayashi, Y. Koide, S. Yamasaki, S. Nagai, J. Umezaki, M. Koike, and M. Murakami, J. Appl. Phys. **81**, 1315 (1997).
[83] K. V. Vassilevski, M. G. Rastegaeva, A. I. Babanin, I. P. Nikitina, and V. A. Dmitriev, MRS Internet J. Nitride Semicond. Res. **1**, 38 (1996).
[84] D. J. King, L. Zhang, J. C. Ramer, S. D. Hersee, and L. F. Lester, Mater. Res. Soc. Symp. Proc. **468**, 421 (1997).
[85] L. F. Lester, D. J. King, L. Zhang, J. C. Ramer, S. D. Hersee, and J. C. Zolper, Proc. Electrochem. Soc. **97-1**, 171 (1997).
[86] I. Akasaki, H. Amano, S. Sota, H. Sakai, T. Tanaka, and M. Koike, Jpn. J. Appl. Phys., Part 2 **34**, L1517 (1995).
[87] T. Mori, T. Kozawa, T. Ohwaki, Y. Taga, S. Nagai, S. Yamasaki, S. Asami, N. Shibata, and M. Koike, Appl. Phys. Lett. **69**, 3537 (1996).
[88] T. Kim, J. Kim, S. Chae, and T. Kim, Mater. Res. Soc. Symp. Proc. **468**, 427 (1997).
[89] J. T. Trexler, S. J. Pearton, P. H. Holloway, H. G. Mier, K. R. Evans, and R. F. Karlicek, Mater. Res. Soc. Symp. Proc. **449**, 1091 (1997).
[90] J. T. Trexler, S. J. Miller, P. H. Holloway, and M. A. Khan, Mater. Res. Soc. Symp. Proc. **395**, 819 (1996).
[91] T. Kim, M. C. Yoo, and T. Kim, Mater. Res. Soc. Symp. Proc. **449**, 1061 (1997).
[92] J. M. Van Hove, P. P. Chow, J. J. Klaasen, R. Hickman, A. M. Wowchak, D. R. Croswell, and C. Polley, Mater. Res. Soc. Symp. Proc. **468**, 51 (1997).
[93] J. C. Zolper, R. J. Shul, A. G. Baca, R. G. Wilson, S. J. Pearton, and R. A. Stall, Appl. Phys. Lett. **68**, 2273 (1996).
[94] H. S. Venugopalan, S. E. Mohney, B. P. Luther, J. M. DeLucca, S. D. Wolter, J. M. Redwing, and G. E. Bulman, Mater. Res. Soc. Symp. Proc. **468**, 431 (1997).
[95] V. M. Bermudez, R. Kaplan, M. A. Khan, and J. N. Kuznia, Phys. Rev. B **48**, 2436 (1993).
[96] V. Swaminathan and A. T. Macrander, *Materials Aspects of GaAs and InP Based Structures* (Prentice Hall, Englewood Cliffs, NJ, 1991).
[97] D. E. Davies, Nucl. Instrum. Methods Phys. Res. **7/8**, 387 (1985).
[98] K. G. Stevens, Nucl. Instrum. Methods Phys. Res. **209/210**, 589 (1983).
[99] N. Nishi, T. Inada, and T. Saito, Jpn. J. Appl. Phys. **122**, 401 (1983).
[100] J. D. Oberstar and B. G. Streetman, Thin Solid Films **103**, 17 (1983).
[101] B. Molnar, Appl. Phys. Lett. **36**, 927 (1980).
[102] C. A. Armiento and F. C. Prince, Appl. Phys. Lett. **48**, 1623 (1986).
[103] S. J. Pearton and K. D. Cummings, J. Appl. Phys. **58**, 1500 (1985).
[104] R. T. Blunt, M. S. M. Lamb, and R. Szweda, Appl. Phys. Lett. **47**, 304 (1985).
[105] A. Tamura, R. Uenoyama, K. Nishi, K. Inoue, and T. Onuma, J. Appl. Phys. **62**, 1102 (1987).
[106] T. E. Haynes, W. K. Chu, and S. T. Picraux, Appl. Phys. Lett. **50**, 1071 (1987).
[107] J. M. Woodall, H. Rupprecht, R. J. Chicotka, and G. Wicks, Appl. Phys. Lett. **38**, 639 (1981).
[108] S. Reynolds, D. W. Vook, W. C. Opyd, and J. E. Gibbons, Appl. Phys. Lett. **51**, 916 (1987).
[109] W. H. Haydl, IEEE Electron Device Lett. **5**, 78 (1984).

[110] S. J. Pearton and R. Caruso, J. Appl. Phys. **66**, 663 (1989).
[111] Nitride powders obtained from AESAR.
[112] S. Porowski and I. Grzegory, in *Properties of Group III Nitrides*, edited by J. H. Edgar (INSPEC, Stevenage, UK, 1994).
[113] C. B. Vartuli, S. J. Pearton, C. R. Abernathy, J. D. MacKenzie, E. S. Lambers, and J. C. Zolper, J. Vac. Sci. Technol. B **14**, 2761 (1996).
[114] J. Karpinski, J. Jun, and S. Porowski, J. Cryst. Growth **66**, 1 (1984).
[115] J. C. Zolper, D. J. Rieger, A. G. Baca, S. J. Pearton, J. W. Lee, and R. A. Stall, Appl. Phys. Lett. **69**, 538 (1996).
[116] J. R. Mileham, S. J. Pearton, C. R. Abernathy, J. D. MacKenzie, R. J. Shul, and S. P. Kilcoyne, Appl. Phys. Lett. **67**, 1119 (1995).
[117] H. P. Maruska and J. J. Tietjen, Appl. Phys. Lett. **15**, 327 (1969).
[118] T. Matsuoka, H. Tanaka, T. Susaki, and A. Katsui, Inst. Phys. Conf. Ser. **106**, 141 (1990).
[119] See, for examples, in MRS Bull. **22**, 17–19 (1997).
[120] See, for examples, in MRS Bull. **22**, 22–57 (1997).
[121] J. N. Shenoy, J. A. Cooper, Jr., and M. R. Melloch, IEEE Electron Device Lett. **18**, 93 (1997).
[122] J. C. Zolper, R. J. Shul, A. G. Baca, S. J. Pearton, R. G. Wilson, and R. A. Stall, Appl. Phys. Lett. **68**, 273 (1996).
[123] J. C. Zolper and S. J. Pearton in *Proceedings of the Wide Band Gap Semiconductor Symposium*, edited by J. Dismukes *et al*. (Electrochemical Society, Pennington, NJ, 1997), pp. 268–275.
[124] J. C. Zolper, H. H. Tan, J. S. Williams, J. Zou, D. J. H. Cockayne, S. J. Pearton, M. Hagerott-Crawford, and R. R. Karlicek, Jr., Appl. Phys. Lett. **70**, 2729 (1997).
[125] J. C. Zolper, J. Han, R. M. Biefeld, S. B. Van Deusen, W. R. Wampler, D. J. Reiger, S. J. Pearton, J. S. Williams, H. H. Tan, R. J. Karlicek, Jr., and R. S. Stall, J. Electron. Mater. **27**, 179 (1998).
[126] F. Roozeboom, in *Rapid Thermal Processing: Science and Technology*, edited by R. B. Fair (Academic, New York, 1993), pp. 349–423.
[127] J. A. Sekhar, S. Penumella, and M. Fu, in *Transient Thermal Processing Techniques in Electronic Materials*, edited by N. M. Ravindra and R. K. Singh (TMS, Warrendale, PA, 1996), pp. 171–175.
[128] *MHI Heating Element Handbook*, Version 8 (Cincinnati, OH 1997).
[129] S. J. Pearton, Int. J. Mod. Phys. B **7**, 4687 (1993).
[130] C. B. Vartuli, S. J. Pearton, J. W. Lee, C. R. Abernathy, J. D. Mackenzie, J. C. Zolper, R. J. Shul, and F. Ren, J. Electrochem. Soc. **143**, 3681 (1996).
[131] See for example: M. A. Khan, A. Bhattarai, J. N. Kuznia, and D. T. Olson, Appl. Phys. Lett. **63**, 1214 (1993); S. C. Binari, L. B. Rowland, W. Kruppa, G. Kelner, K. Doverspike, and D. K. Gaskill, Electron. Lett. **30**, 1248 (1994).
[132] Y.-F. Wu, S. Keller, P. Kozodoy, B. P. Keller, S. P. DenBaars, and U. K. Mishra, Conference Proceedings in International Conference of Compound Semiconductors, San Diego, CA September 1997.
[133] J. Burm, W. J. Schaff, G. H. martin, L. F. Eastman, H. Amano, and I. Akasaki, Solid-State Electron. **41**, 247 (1997).
[134] J. C. Zolper, R. J. Shul, A. G. Baca, R. G. Wilson, S. J. Pearton, and R. A. Stall, Appl. Phys. Lett. **68**, 2273 (1996).
[135] J. C. Zolper, *Gallium Nitride and Related Materials*, edited by S. J. Pearton (Gordon and Breach, New York, 1997).
[136] J. I. Pankove and J. A. Hutchby, J. Appl. Phys. **47**, 5387 (1976).
[137] J. I. Pankove and J. A. Hutchby, Appl. Phys. Lett. **24**, 281 (1974).
[138] S. J. Pearton, C. R. Abernathy, C. B. Vartuli, J. C. Zolper, C. Yuan, and R. A. Stall, Appl. Phys. Lett. **67**, 1435 (1995).
[139] J. C. Zolper, R. G. Wilson, S. J. Pearton, and R. A. Stall, Appl. Phys. Lett. **68**, 1945 (1996).
[140] J. C. Zolper, J. Cryst. Growth **178**, 175 (1997).
[141] S. C. Binari, H. B. Dietrich, G. Kelner, L. B. Rowland, K. Doverspike, and K. D. Wickenden, J. Appl. Phys. **78**, 3008 (1995).
[142] O. Ambacher, M. S. Brandt, R. Dimitrov, T. Metzger, M. Stutzmann, R. A. Fischer, A. Miehr, A. Bergmaier, and G. Dollinger, J. Vac. Sci. Technol. B **14**, 3532 (1996).
[143] C. D. Thurmond and R. A. Logan, J. Electrochem. Soc. **119**, 622 (1972).
[144] J. Brown, J. Ramer, K. Zheng, L. F. Lester, S. D. Hersee, and J. C. Zolper, Mater. Res. Soc. Symp. Proc. **395**, 702 (1996).
[145] H. H. Tan, J. S. Williams, C. Yuan, and S. J. Pearton, Mater. Res. Soc. Symp. Proc. **395**, 708 (1996).
[146] H. H. Tan, J. S. Williams, J. Zou, D. J. H. Cockayne, S. J. Pearton, and R. A. Stall, Appl. Phys. Lett. **69**, 2364 (1996).
[147] C. Liu, B. Mecnsching, M. Zeitler, K. Volz, and B. Rauschenbach, Phys. Rev. B **57**, 308 (1997).
[148] C. Ronning, N. Dalmer, M. Deicher, M. Restle, M. D. Bremser, R. F. Davis, and H. Hofsass, Mater. Res. Soc. Symp. Proc. **468**, 407 (1997).
[149] J. C. Zolper, M. H. Crawford, H. H. Tan, J. S. Williams, J. Zhou, D. J. H. Cockayne, S. J. Pearton, and R. F. Karlicek, Jr., Appl. Phys. Lett. **70**, 2729 (1997).
[150] J. C. Zolper, in *GaN and Related Materials II*, edited by S. J. Pearton (Gordon and Breach, New York, 1998).
[151] J. I. Pankove, E. A. Miller, and J. E. Berkeyheiser, *Luminescence of Crystals, Molecules and Solutions*, edited by F. Williams (Plenum, New York, 1973), p. 426.
[152] J. F. Ziegler, J. P. Biersack, and U. Littmark, *The Stopping and Range of Ions in Solids*, Vol. 1 (Pergammon, New York, 1985).
[153] J. C. Zolper, M. Hagerott-Crawford, S. J. Pearton, C. R. Abernathy, C. B. Vartuli, C. Yuan, and R. A. Stall, J. Electron. Mater. **25**, 839 (1996).
[154] H. H. Tan, J. S. Williams, J. Zou, D. J. H. Cockayne, S. J. Pearton, and C. Yuan, J. Electrochem. Soc. **96-11**, 142 (1996).
[155] J. S. Williams (private communication).
[156] J. C. Zolper, J. Han, S. B. Van Deusen, R. Biefeld, M. H. Crawford, J. Jun, T. Suski, J. M. Baranowski, and S. J. Pearton, Mater. Res. Soc. Symp. Proc. **482**, 618 (1998).
[157] J. A. Van Vechten, Phys. Rev. B **7**, 1479 (1973).
[158] J. Karpinski, J. Jun, and S. Porowski, J. Cryst. Growth **66**, 1 (1984).
[159] B-C. Chung and M. Gershenzon, J. Appl. Phys. **72**, 651 (1992).
[160] S. Strite, A. Pelzmann, T. Suski, M. Leszczynski, J. Jun, A. Rocket, M. Kemp, and K. J. Ebeling, MRS Internet J. Nitride Semicond. Res. **2**, (1997).
[161] T. Suski, J. Jun, M. Leszczynski, H. Teisseyre, I. Grzegory, S. Porowski, J. M. Baranowski, A. Rocket, S. Strite, A. Stonert, A. Turos, H. H. Tan, J. S. Williams, and C. Jagadish, Mater. Res. Soc. Symp. Proc. **482**, 703 (1998).
[162] H. Kobayashi and W. M. Gibson, Appl. Phys. Lett. **73**, 1406 (1998).
[163] J. M. Zavada and D. Zhang, Solid-State Electron. **38**, 1285 (1995).
[164] S. Saito, T. Imai, and T. Ito, J. Low Temp. Phys. **9**, 161 (1991).
[165] G. R. Walker, N. G. Walker, R. C. Steele, M. J. Creaner, and M. C. Brain, J. Low Temp. Phys. **9**, 182 (1991).
[166] L. F. Mollenauer, S. G. Evangelides, and H. A. Haus, J. Low Temp. Phys. **9**, 194 (1991).
[167] R. G. Wilson, R. N. Schwartz, C. R. Abernathy, S. J. Pearton, N. Newman, M. Rubin, T. Fu, and J. M. Zavada, Appl. Phys. Lett. **65**, 992 (1994).
[168] C. H. Qiu, M. W. Leksono, J. I. Pankove, J. T. Torvik, R. J. Feuerstein, and F. Namavar, Appl. Phys. Lett. **66**, 562 (1995).
[169] P. N. Favennec, H. L'Haridon, D. Moutonnet, and M. Gauneau, Jpn. J. Appl. Phys., Part 2 **29**, L524 (1990).
[170] J. Michel, J. L. Benton, R. F. Ferrante, D. C. Jacobson, and L. C. Kimmerling, J. Appl. Phys. **70**, 2672 (1991).
[171] J. E. Colon, D. W. Elsaessar, Y. K. Yeo, R. L. Hengehold, and G. S. Pomrenke, Mater. Res. Soc. Symp. Proc. **301**, 169 (1993).
[172] H. H. Tan, C. Jagadish, J. S. Williams, H. Zoa, D. J. H. Cockayne, and A. Sikorski, J. Appl. Phys. **77**, 87 (1995).
[173] A. Y. Polyakov, M. Shin, M. Skowronski, R. G. Wilson, D. W. Greve, and S. J. Pearton, Solid-State Electron. **41**, 703 (1997).
[174] T. S. Zheleva, O-H. Nam, M. D. Bremser, and R. F. Davis, Appl. Phys. Lett. **71**, 2472 (1997).
[175] D. Kapolnek, S. Keller, R. Vetury, R. D. Underwood, P. Kozodoy, S. P. DenBaars, and U. K. Mishra, Appl. Phys. Lett. **71**, 1204 (19917).
[176] S. Nakamura, M. Senoh, S. Nagahama, N. Iwasa, T. Yamada, T. Matsushita, H. Kiyoku, Y. Sugimoto, T. Kozaki, H. Umemoto, M. Sana, and K. Chocho, Appl. Phys. Lett. **72**, 211 (1998).
[177] S. C. Binari, Proc. Electrochem. Soc. **95-21**, 136 (1995).
[178] W. Kruppa, S. C. Binari, and K. Doverspike, Electron. Lett. **31**, 1951 (1995).
[179] M. S. Minsky, M. White, and E. L. Hu, Appl. Phys. Lett. **68**, 1531 (1996).
[180] R. J. Shul, S. R. Kilcoyne, M. H. Crawford, J. E. Parmeter, C. B. Vartuli, C. R. Abernathy, and S. J. Pearton, Appl. Phys. Lett. **66**, 1761 (1995).
[181] S. J. Pearton, C. R. Abernathy, and F. Ren, Appl. Phys. Lett. **64**, 3643 (1994).
[182] M. Passlack, M. Hong, J. P. Mannaerts, R. L. Opila, S. N. G. Chu, N. Moriya, F. Ren, and J. Kwo, IEEE Trans. Electron Devices **44**, 214 (1997).
[183] F. Ren, M. Hong, J. M. Kuo, W. S. Hobson, J. R. Lothian, H. S. Tsai, J. Lin, J. P. Mannaerts, J. Kwo, S. N. G. Chu, Y. K. Chen, and A. Y. Cho, 1997 IEEE GaAs IC Symposium, Anaheim, CA, 12–15 October, 1997.
[184] F. Ren, M. Hong, W. S. Hobson, J. M. Kuo, J. R. Lothian, J. P. Man-

naerts, J. Kwo, S. N. G. Chu, Y. K. Chen, and A. Y. Cho, Solid-State Electron. **41**, 1751 (1997).
[185] F. Ren, J. M. Kuo, M. Hong, W. S. Hobson, J. R. Lothian, J. Lin, H. S. Tsai, J. P. Mannaerts, J. Kwo, S. N. G. Chu, and A. Y. Cho, IEEE Electron Device Lett. **19**, 309 (1998).
[186] D. Y. Noh, Y. Hwu, H. K. Kim, and M. Hong, Phys. Rev. B **51**, 4441 (1995).
[187] L. G. Parratt, Phys. Rev. **95**, 359 (1954).
[188] M. J. Schurman, T. Salagaj, C. Tran, R. Karlicek, Jr., I. Ferguson, R. Stall, and A. Thompson, Mol. Spectrosc. (Chem. Soc., London) **43**, 222 (1997).
[189] C. R. Abernathy, J. D. MacKenzie, S. J. Pearton, and W. S. Hobson, Appl. Phys. Lett. **66**, 1969 (1995).
[190] M. Hong, M. Passlack, J. P. Mannaerts, J. Kwo, S. N. G. Chu, N. Moriya, S. Y. Hou, and V. J. Fratello, J. Vac. Sci. Technol. B **14**, 2297 (1996).
[191] C. B. Vartuli, S. J. Pearton, J. W. Lee, C. R. Abernathy, J. D. MacKenzie, J. C. Zolper, R. J. Shul, and F. Ren, J. Electrochem. Soc. **143**, 3681 (1996).
[192] C. Youtsey, I. Adesida, and G. Bulman, Electron. Lett. **33**, 245 (1997); Appl. Phys. Lett. **71**, 2151 (1997); J. Electron. Mater. **27**, 282 (1998).
[193] B. J. Kim, J. W. Lee, H. S. Park, Y. Park, and T. I. Kim, J. Electron. Mater. **27**, L32 (1998).
[194] D. A. Stocker, E. F. Schubert, and J. M. Redwing, Appl. Phys. Lett. **73**, 2345 (1998).
[195] A. Shintani and S. Minagawa, J. Electrochem. Soc. **123**, 707 (1976).
[196] T. Kozawa, T. Kachi, T. Ohwaki, Y. Taga, and M. Koike, J. Electrochem. Soc. **143**, L17 (1996).
[197] J.-L. Lee, J. K. Kim, J. W. Lee, Y. J. Park, and T. Kim, Solid-State Electron. **43**, 435 (1999).
[198] S. J. Pearton and R. J. Shul, in *Gallium Nitride I*, edited by J. I. Pankove and T. D. Moustakas (Academic, San Diego, 1998).
[199] P. Gillis, D. A. Choutov, P. A. Steiner, J. D. Piper, J. H. Crouch, P. M. Dove, and K. P. Martin, Appl. Phys. Lett. **66**, 2475 (1995).
[200] R. J. Shul, in *Processing of Wide Bandgap Semiconductors*, edited by S. J. Pearton (Noyes, Park Ridge, NJ, 1999).
[201] I. Adesida, A. Mahajan, E. Andideh, M. Asif Khan, D. T. Olsen, and J. N. Kuznia, Appl. Phys. Lett. **63**, 2777 (1993).
[202] I. Adesida, A. T. Ping, C. Youtsey, T. Sow, M. Asif Khan, D. T. Olson, and J. N. Kuznia, Appl. Phys. Lett. **65**, 889 (1994).
[203] O. Aktas, Z. Fan, S. N. Mohammad, A. Botcharev, and H. Morkoc, Appl. Phys. Lett. **69**, 25 (1996).
[204] M. A. Khan, Q. Chen, M. S. Shur, B. T. McDermott, J. A. Higgins, J. Burm, W. Schaff, and L. F. Eastman, Electron. Lett. **32**, 357 (1996).
[205] Y. F. Wu, S. Keller, P. Kozodoy, B. P. Keller, P. Parikh, D. Kapolnek, S. P. DenBaars, and V. K. Mishra, IEEE Electron Device Lett. **18**, 290 (1997).
[206] M. A. Khan, J. N. Kuznia, M. S. Shur, C. Eppens, J. Burm, and W. Schaff, Appl. Phys. Lett. **66**, 1083 (1995).
[207] W. A. Harrison, *Electronic Structure and Properties of Solids* (Freeman, San Francisco, 1980).
[208] S. J. Pearton, C. R. Abernathy, F. Ren, and J. R. Lothian, J. Appl. Phys. **76**, 1210 (1994).
[209] M. E. Lin, Z. F. Zan, Z. Ma, L. H. Allen, and H. Morkoc, Appl. Phys. Lett. **64**, 887 (1994).
[210] A. T. Ping, I. Adesida, M. Asif Khan, and J. N. Kuznia, Electron. Lett. **30**, 1895 (1994).
[211] H. Lee, D. B. Oberman, and J. S. Harris, Jr., Appl. Phys. Lett. **67**, 1754 (1995).
[212] S. J. Pearton, C. R. Abernathy, F. Ren, J. R. Lothian, P. W. Wisk, A. Katz, and C. Constantine, Semicond. Sci. Technol. **8**, 310 (1993).
[213] S. J. Pearton, C. R. Abernathy, and F. Ren, Appl. Phys. Lett. **64**, 2294 (1994).
[214] S. J. Pearton, C. R. Abernathy, and F. Ren, Appl. Phys. Lett. **64**, 3643 (1994).
[215] R. J. Shul, S. P. Kilcoyne, M. Hagerott Crawford, J. E. Parmeter, C. B. Vartuli, C. R. Abernathy, and S. J. Pearton, Appl. Phys. Lett. **66**, 1761 (1995).
[216] C. B. Vartuli, J. D. MacKenzie, J. W. Lee, C. R. Abernathy, S. J. Pearton, and R. J. Shul, J. Appl. Phys. **80**, 3705 (1996).
[217] L. Zhang, J. Ramer, K. Zheng, L. F. Lester, and S. D. Hersee, Mater. Res. Soc. Symp. Proc. **395**, 763 (1996).
[218] L. Zhang, J. Ramer, J. Brown, K. Zheng, L. F. Lester, and S. D. Hersee, Appl. Phys. Lett. **68**, 367 (1996).
[219] B. Humphreys and M. Govett, MRS Internet J. Nitride Semicond. Res. **1**, 6 (1996).
[220] J. W. Lee, J. Hong, J. D. MacKenzie, C. R. Abernathy, S. J. Pearton, F. Ren, and P. F. Sciortino, J. Electron. Mater. **26**, 290 (1997).
[221] C. B. Vartuli, S. J. Pearton, J. W. Lee, J. Hong, J. D. MacKenzie, C. R. Abernathy, and R. J. Shul, Appl. Phys. Lett. **69**, 1426 (1996).
[222] R. J. Shul, A. J. Howard, S. J. Pearton, C. R. Abernathy, C. B. Vartuli, P. A. Barnes, and M. J. Bozack, J. Vac. Sci. Technol. B **13**, 2016 (1995).
[223] C. B. Vartuli, S. J. Pearton, C. R. Abernathy, R. J. Shul, A. J. Howard, S. P. Kilcoyne, J. E. Parmeter, and M. Hagerott Crawford, J. Vac. Sci. Technol. A **14**, 1011 (1996).
[224] R. J. Shul, C. I. H. Ashby, D. J. Rieger, A. J. Howard, S. J. Pearton, C. R. Abernathy, C. B. Vartuli, and P. A. Barnes, Mater. Res. Soc. Symp. Proc. **395**, 751 (1996).
[225] R. J. Shul, in *GaN and Related Materials*, edited by S. J. Pearton (Gordon and Breach, The Netherlands, 1997).
[226] R. J. Shul, G. B. McClellan, S. J. Pearton, C. R. Abernathy, C. Constantine, and C. Barratt, Electron. Lett. **32**, 1408 (1996).
[227] R. J. Shul, G. B. McClellan, S. A. Casalnuovo, D. J. Rieger, S. J. Pearton, C. Constantine, C. Barratt, R. F. Karlicek, Jr., C. Tran, and M. Schurman, Appl. Phys. Lett. **69**, 1119 (1996).
[228] Y. H. Lee, H. S. Kim, G. Y. Yeom, J. W. Lee, M. C. Yoo, and T. I. Kim, J. Vac. Sci. Technol. A **16**, 1478 (1998).
[229] H. S. Kim, Y. H. Lee, G. Y. Yeom, J. W. Lee, and T. I. Kim, Mater. Sci. Eng., B **50**, 82 (1997).
[230] Y. B. Hahn, D. C. Hays, S. M. Donovan, C. R. Abernathy, J. Han, R. J. Shul, H. Cho, K. B. Jung, and S. J. Pearton, J. Vac. Sci. Technol. A (submitted).
[231] H. Cho, C. B. Vartuli, S. M. Donovan, J. D. MacKenzie, C. R. Abernathy, S. J. Pearton, R. J. Shul, and C. Constantine, J. Electron. Mater. **27**, 166 (1998).
[232] H. Cho, C. B. Vartuli, S. M. Donovan, C. R. Abernathy, S. J. Pearton, R. J. Shul, and C. Constantine, J. Vac. Sci. Technol. A **6**, 1631 (1998).
[233] J. W. Lee, H. Cho, D. C. Hays, C. R. Abernathy, S. J. Pearton, R. J. Shul, G. A. Vawter, and J. Han, IEEE J. Sel. Top. Quantum Electron. **4**, 557 (1998).
[234] R. J. Shul, C. G. Willison, M. M. Bridges, J. Han, J. W. Lee, S. J. Pearton, C. R. Abernathy, J. D. MacKenzie, and S. M. Donovan, Solid-State Electron. (submitted).
[235] R. J. Shul, C. I. H. Ashby, C. G. Willison, L. Zhang, J. Han, M. M. Bridges, S. J. Pearton, J. W. Lee, and L. F. Lester, Mater. Res. Soc. Symp. Proc. **512**, 487 (1998).
[236] S. A. Smith, C. A. Wolden, M. D. Bremser, A. D. Hanser, and R. F. Davis, Appl. Phys. Lett. **71**, 3631 (1997).
[237] R. J. Shul, in *GaN and Related Materials II*, edited by S. J. Pearton (Gordon and Breach, New York, 1998).
[238] G. F. McLane, M. Meyyappan, M. W. Cole, and C. Wrenn, J. Appl. Phys. **69**, 695 (1991).
[239] M. Meyyappan, G. F. McLane, H. S. Lee, E. Eckart, M. Namaroff, and J. Sasserath, J. Vac. Sci. Technol. B **10**, 1215 (1992).
[240] G. F. McLane, L. Casas, S. J. Pearton, and C. R. Abernathy, Appl. Phys. Lett. **66**, 3328 (1995).
[241] A. T. Ping, I. Adesida, and M. Asif Khan, Appl. Phys. Lett. **67**, 1250 (1995).
[242] A. T. Ping, A. C. Schmitz, and M. Asif Khan, J. Electron. Mater. **25**, 825 (1996).
[243] A. T. Ping, M. Asif Khan, and I. Adesida, Semicond. Sci. Technol. **12**, 133 (1997).
[244] R. J. Shul, G. A. Vawter, C. G. Willison, M. M. Bridges, J. W. Lee, S. J. Pearton, and C. R. Abernathy, Solid-State Electron. **42**, 2259 (1998).
[245] J. W. Lee, C. Vartuli, C. R. Abernathy, J. MacKenzie, J. R. Mileham, S. J. Pearton, R. J. Shul, J. C. Zolper, M. Crawford, J. Zavada, R. Wilson, and R. Schwartz, J. Vac. Sci. Technol. B **14**, 3637 (1996).
[246] H. P. Gillis, D. A. Choutov, K. P. Martin, and L. Song, Appl. Phys. Lett. **68**, 2255 (1996).
[247] H. P. Gillis, D. A. Choutov, and K. P. Martin, J. Mater **50**, 41 (1996).
[248] H. P. Gillis, D. A. Choutov, K. P. Martin, S. J. Pearton, and C. R. Abernathy, J. Electrochem. Soc. **143**, 251 (1996).
[249] R. T. Leonard and S. M. Bedair, Appl. Phys. Lett. **68**, 794 (1996).
[250] C. B. Vartuli, S. J. Pearton, J. W. Lee, J. D. MacKenzie, C. R. Abernathy, and R. J. Shul, J. Vac. Sci. Technol. A **15**, 638 (1997).
[251] C. B. Vartuli, S. J. Pearton, C. R. Abernathy, R. J. Shul, and F. Ren, Proc. Electrochem. Soc. **97-34**, 39 (1998).
[252] J. W. Lee, J. Hong, and S. J. Pearton, Appl. Phys. Lett. **68**, 847 (1996).

[253] R. J. Shul, C. G. Willison, M. M. Bridges, J. Han, J. W. Lee, S. J. Pearton, C. R. Abernathy, J. D. MacKenzie, and S. M. Donovan, Mater. Res. Soc. Symp. Proc. **482**, 802 (1998).
[254] R. J. Shul, C. G. Willison, M. M. Bridges, J. Han, J. W. Lee, S. J. Pearton, C. R. Abernathy, J. D. MacKenzie, S. M. Donovan, L. Zhang, and L. F. Lester, J. Vac. Sci. Technol. A **16**, 1621 (1998).
[255] C. Constantine, C. Barratt, S. J. Pearton, F. Ren, and J. R. Lothian, Electron. Lett. **28**, 1749 (1992).
[256] C. Constantine, C. Barratt, S. J. Pearton, F. Ren, and J. R. Lothian, Appl. Phys. Lett. **61**, 2899 (1992).
[257] D. G. Lishan and E. L. Hu, Appl. Phys. Lett. **56**, 1667 (1990).
[258] T. R. Hayes, in *Indium Phosphide and Related Materials: Processing, Technology, and Devices*, edited by A. Katz (Artech House, Boston, 1992), Chap. 8, pp. 277–306.
[259] R. J Shul R. D. Briggs, J. Han, S. J. Pearton, J. W. Lee, C. B. Vartuli, K. P. Killeen, and M. J. Ludowise, Mater. Res. Soc. Symp. Proc. **468**, 355 (1997).
[260] F. Ren, J. R. Lothian, J. M. Kuo, W. S. Hobson, J. Lopata, J. A. Caballero, S. J. Pearton, and M. W. Cole, J. Vac. Sci. Technol. B **14**, 1 (1995).
[261] F. Ren, W. S. Hobson, J. R. Lothian, J. Lopata, J. A. Caballero, S. J. Pearton, and M. W. Cole, Appl. Phys. Lett. **67**, 2497 (1995).
[262] R. J. Shul, G. B. McClellan, R. D. Briggs, D. J. Rieger, S. J. Pearton, C. R. Abernathy, J. W. Lee, C. Constantine, and C. Barratt, J. Vac. Sci. Technol. A **15**, 633 (1997).
[263] C. B. Vartuli, S. J. Pearton, J. D. MacKenzie, C. R. Abernathy, and R. J. Shul, J. Electrochem. Soc. **143**, L246 (1996).
[264] C. B. Vartuli, S. J. Pearton, J. W. Lee, J. D. MacKenzie, C. R. Abernathy, and R. J. Shul, J. Vac. Sci. Technol. B **15**, 98 (1997).
[265] Hyun Cho, J. Hong, T. Maeda, S. M. Donovan, J. D. MacKenzie, C. R. Abernathy, S. J. Pearton, R. J. Shul, and J. Han, MRS Internet J. Nitride Semicond. Res. **3**, 5 (1998).
[266] C. B. Vartuli, S. J. Pearton, J. W. Lee, J. D. MacKenzie, C. R. Abernathy, R. J. Shul, C. Constantine, and C. Barratt, J. Electrochem. Soc. **144**, 2844 (1997).
[267] F. Ren, S. J. Pearton, R. J. Shul, and J. Han, J. Electron. Mater. **27**, 175 (1998).
[268] S. J. Pearton, J. W. Lee, J. D. MacKenzie, C. R. Abernathy, and R. J. Shul, Appl. Phys. Lett. **67**, 2329 (1995).
[269] F. Ren, J. R. Lothian, S. J. Pearton, C. R. Abernathy, C. B. Vartuli, J. D. MacKenzie, R. G. Wilson, and R. F. Karlicek, J. Electron. Mater. **26**, 1287 (1997).
[270] T. Ping, A. C. Schmitz, I. Adesida, M. A. Khan, O. Chen, and Y. W. Yang, J. Electron. Mater. **26**, 266 (1997).
[271] R. J. Shul, J. C. Zolper, M. Hagerott Crawford, S. J. Pearton, J. W. Lee, R. F. Karlicek, Jr., C. Tran, M. Schurmann, C. Constantine, and C. Barratt, Proc. Electrochem. Soc. **96–15**, 232 (1996).
[272] S. J. Pearton, Mater. Sci. Rep. **4**, 313 (1990).
[273] M. Orenstein, N. G. Stoffel, A. C. Von Lehmen, J. P. Harbison, and L. T. Florez, Appl. Phys. Lett. **59**, 31 (1991).
[274] K. L. Lear, R. P. Schneider, K. D. Choquette, S. P. Kilcoyne, J. J. Figiel, and J. C. Zolper, IEEE Photonics Technol. Lett. **6**, 1053 (1994).
[275] J. C. Zolper, A. G. Baca, and S. A. Chalmers, Appl. Phys. Lett. **62**, 2536 (1993).
[276] S. J. Pearton, M. P. Iannuzzi, C. L. Reynolds, Jr., and L. Peticolas, Appl. Phys. Lett. **52**, 395 (1988).
[277] J. C. Zolper, M. E. Sherwin, A. G. Baca, and R. P. Schneider, Jr., J. Electron. Mater. **24**, 21 (1995).
[278] S. J. Pearton, C. R. Abernathy, P. W. Wisk, W. S. Hobson, and F. Ren, Appl. Phys. Lett. **63**, 1143 (1993).
[279] J. C. Zolper, S. J. Pearton, C. R. Abernathy, and C. B. Vartuli, Appl. Phys. Lett. **66**, 3042 (1995).
[280] S. J. Pearton, C. R. Abernathy, M. B. Panish, R. A. Hamm, and L. M. Lunardi, J. Appl. Phys. **66**, 656 (1989).
[281] J. C. Zolper, S. J. Pearton, C. R. Abernathy, and C. B. Vartuli, Mater. Res. Soc. Symp. Proc. **378**, 408 (1995).
[282] G. Harrington, Y. Hsin, Q. Z. Liu, P. M. Asbeck, S. S. Lau, M. A. Khan, J. W. Yang, and Q. Chen, Electron. Lett. **34**, 193 (1998).
[283] G. Popovici and H. Morkoc, in *GaN and Related Materials II*, edited by S. J. Pearton (Gordon and Breach, New York, 1998).
[284] T. L. Tansley, E. M. Goldys, M. Godlewski, B. Zhou, and H. Y. Zuo, in *GaN and Related Materials*, edited by S. J. Pearton (Gordon and Breach, New York, 1998).
[285] J. H. Edgar, J. Mater. Res. **7**, 235 (1992).
[286] T. L. Tansley and R. J. Egan, Phys. Rev. B **45**, 10942 (1992).
[287] P. Boguslawski, E. L. Briggs, and J. Bernholc, Phys. Rev. B **51**, 17255 (1995).
[288] D. L. Rode and D. K. Gaskill, Appl. Phys. Lett. **66**, 1972 (1995).
[289] V. L. Chin, T. L. Tansley, and T. Osotchan, J. Appl. Phys. **75**, 7365 (1994).
[290] D. W. Jenkins and J. D. Dow, Phys. Rev. B **39**, 3317 (1989).
[291] P. Perlin, T. Suski, H. Teisseyre, M. Leszczynski, I. Gregory, J. Jun, S. Porowski, P. Boguslawski, J. Berhole, J. C. Chervin, A. Polian, and T. D. Moustakas, Phys. Rev. Lett. **75**, 296 (1995).
[292] S. Strite and H. Morkoc, J. Vac. Sci. Technol. B **10**, 1273 (1992).
[293] B. Goldenberg, J. D. Zook, and J. R. Ulmer, Appl. Phys. Lett. **62**, 381 (1993).
[294] S. J. Pearton, J. W. Corbett, and T. S. Shi, Appl. Phys. A: Solids Surf. **43**, 153 (1987).
[295] S. M. Myers, M. I. Baskes, M. K. Birnbaum, J. W. Corbett, G. G. DeLeo, S. K. Estreicher, E. E. Haller, P. Jena, N. M. Johnson, R. Kircheim, S. J. Pearton, and M. Stavola, Rev. Mod. Phys. **64**, 559 (1992).
[296] *Hydrogen in Semiconductors*, Vol. 34 Semiconductors and Semimetals, edited by J. I. Pankove and N. M. Johnson (Academic Press, San Diego, 1991).
[297] S. J. Pearton, J. W. Corbett, and M. Stavola, *Hydrogen in Crystalline Semiconductors* (Springer, Berlin, 1992).
[298] S. K. Estreicher, Mater. Sci. Eng., R. **15**, 319 (1995).
[299] S. J. Pearton, Mater. Sci. Forum **148/149**, 1247 (1994).
[300] R. J. Street, *Hydrogenated Amorphous Silicon* (Cambridge University Press, New York, 1991).
[301] S. K. Estreicher, Hyperfine Interact. **86**, 625 (1994).
[302] G. Bambakidis and R. C. Bowman, Jr., (eds.) *Hydrogen in Disordered and Amorphous Solids*, NATO ISI Series 136, edited by G. Bambakidis and R. C. Bowman, Jr. (Plenum, New York, 1986).
[303] *Hydrogen in Semiconductors*, edited by M. Stutzmann and J. Chevallier (North Holland, Amsterdam, 1991).
[304] S. J. Pearton, in GaN and Related Materials, Vol. 2 of *Optoelectronic Properties of Semiconductors and Superlattices*, edited by M. O. Manasreh (Gordon and Breach, New York, 1997).
[305] H. Amano, M. Kito, K. Hiramatsu, and I. Akasaki, Jpn. J. Appl. Phys., Part 2 **28**, L2112 (1989).
[306] S. Nakamura, M. Senoh, and T. Mukai, Jpn. J. Appl. Phys., Part 2 **30**, L1708 (1991).
[307] S. Nakamura, T. Mukai, M. Senoh, and T. Mukai, Jpn. J. Appl. Phys., Part 2 **31**, L139 (1992).
[308] S. Nakamura, N. Iwasa, M. Senoh, and T. Mukai, Jpn. J. Appl. Phys., Part 2 **31**, L1258 (1992).
[309] Z. J. Zu, J. H. Edgar, A. V. Ahmed, and A. Rys, J. Electrochem. Soc. **138**, 96 (1991).
[310] H. Amano, I. Akasaki, T. Kozawa, N. Sawaki, K. Ikeda, and Y. Ishii, J. Lumin. **4**, 121 (1988).
[311] Y. Ohba and A. Hatano, Jpn. J. Appl. Phys., Part 2 **33**, L1367 (1994).
[312] W. S. Hobson, Mater. Sci. Forum **148/149**, 27 (1994).
[313] C. R. Abernathy, Mater. Sci. Forum **148/149**, 3 (1994).
[314] T. D. Moustakas, T. Lei, and R. J. Molnar, Mater. Res. Soc. Symp. Proc. **281**, 753 (1993).
[315] D. M. Kozuch, M. Stavola, S. J. Pearton, C. R. Abernathy, and W. S. Hobson, J. Appl. Phys. **73**, 3716 (1993).
[316] M. Stavola, Mater. Sci. Forum **148/149**, 251 (1994).
[317] S. Cole, J. S. Evans, M. J. Harlow, A. W. Nelson, and S. Wong, Electron. Lett. **24**, 929 (1989).
[318] M. Glade, D. Grutzmacher, R. Meyer, E. G. Welk, and P. Balk, Appl. Phys. Lett. **54**, 2411 (1989).
[319] K. Woodhouse, R. C. Newman, T. J. DeLyon, J. M. Woodall, G. J. Scilla, and F. Cardone, Semicond. Sci. Technol. **6**, 330 (1991).
[320] S. A. Stockman, A. W. Hanson, S. L. Jackson, J. E. Baker, and G. E. Stillman, Appl. Phys. Lett. **62**, 1248 (1993).
[321] S. J. Pearton, J. W. Corbett, and M. Stavola, Adv. Magn. Reson. **4**, 332 (1992).
[322] S. K. Estreicher, Mater. Res. Soc. Symp. Proc. **240**, 643 (1992).
[323] S. K. Estreicher, Mater. Sci. Eng., R. **14**, 319 (1995).
[324] J. Chevallier, B. Clerjaud, and B. Pajot, Semicond. Semimet. **34**, 237 (1991).
[325] C. Yuan, T. Salagaj, A. Gurary, A. G. Thompson, W. Kroll, R. A. Stall, C. Y. Hwang, M. Schurmann, Y. Li, W. E. Mayo, Y. Lu, S. Krishnankutty, I. S. Shimagin, R. M. Kolbas, and S. J. Pearton, J. Vac. Sci. Technol. B **13**, 2075 (1995).
[326] C. Yuan, T. Salagaj, A. G. Thompson, R. A. Stall, Y. Li, and S. J.

Pearton, *Proceedings of the Wide Band Gap Semiconductors Symposium* (Electrochemical Society, Pennington, New Jersey, 1995), Vol. 95-21, p. 10.
[327] C. Yuan, T. Salagaj, A. Gurary, P. Zawadzki, C. S. Chen, W. Kroll, R. A. Stall, Y. Li, M. Schurmann, C.-Y. Hwang, W. E. Mayo, Y. Lu, S. J. Pearton, S. Krishnankutty, and R. M. Kolbas, J. Electrochem. Soc. **142**, L163 (1995).
[328] Y. Li, Y. Lu, H. Shen, M. Wraback, C.-Y. Hwang, M. Schurman, W. Mayo, T. Salagaj, and R. A. Stall, Mater. Res. Soc. Symp. Proc. **395**, 369 (1996).
[329] Ilegems, R. Dingle, and R. A. Logan, J. Appl. Phys. **43**, 3797 (1972).
[330] M. Ilegems and R. Dingle, J. Appl. Phys. **44**, 4234 (1973).
[331] N. M. Johnson, W. Gotz, J. Neugebauer, and C. G. Van de Walle, Mater. Res. Soc. Symp. Proc. **395**, 723 (1996).
[332] E. L. Piner, M. K. Behbehani, N. A. El-Masry, J. C. Roberts, F. C. McIntosh, and S. M. Bedair, Appl. Phys. Lett. **65**, 3206 (1997).
[333] Y. Park and D. Pavilidis, J. Electron. Mater. **25**, 1554 (1996).
[334] S. J. Pearton, C. R. Abernathy, R. G. Wilson, F. Ren, and J. M. Zavada, Electron. Lett. **31**, 496 (1995).
[335] M. A. L. Johnson, Z. Yu, C. Boney, W. C. Hughes, J. W. Cook, J. F. Schetzina, H. Zhao, B. J. Skromme, and J. A. Edmond, Mater. Res. Soc. Symp. Proc. **449**, 215 (1997).
[336] M. Soto, Appl. Phys. Lett. **68**, 935 (1996).
[337] J. Y. Lee and Y.-J. Yong, Mater. Res. Soc. Symp. Proc. **449**, 999 (1997).
[338] C. Kittel, *Introduction to Solid State Physics* (Wiley, New York, 1986).
[339] J. W. Lee, S. J. Pearton, J. C. Zolper, and R. A. Stall, Appl. Phys. Lett. **68**, 2102 (1996).
[340] S. J. Pearton, C. R. Abernathy, and F. Ren, Electron. Lett. **30**, 527 (1994).
[341] A. Burchard, M. Deicher, D. Forkel-Wirth, E. E. Haller, R. Magerle, A. Prospero, and R. Stozler, Mater. Res. Soc. Symp. Proc. **449**, 961 (1997).
[342] S. Strite, Jpn. J. Appl. Phys., Part 2 **33**, L699 (1994).
[343] See, for example S. J. Pearton, Mater. Sci. Forum **148/149**, 461 (1994).
[344] T. Zundel and J. Weber, Phys. Rev. B **39**, 13549 (1991).
[345] C. R. Abernathy, J. D. MacKenzie, S. J. Pearton, and W. S. Hobson, Appl. Phys. Lett. **66**, 1969 (1995).
[346] W. Geerts, J. A. MacKenzie, C. R. Abernathy, S. J. Pearton, and T. E. Schmeidel, Solid-State Electron. **39**, 1289 (1996).
[347] J. I. Pankove, D. E. Carlson, J. E. Berkeyheiser, and R. O. Wance, Phys. Rev. Lett. **51**, 2224 (1983).
[348] N. M. Johnson, C. Herring, and D. J. Chadi, Phys. Rev. Lett. **56**, 269 (1986).
[349] K. Bergman, M. Stavola, S. J. Pearton, and J. Lopata, Phys. Rev. B **37**, 2770 (1988).
[350] K. Bergman, M. Stavola, S. J. Pearton, and J. Lopata, Mater. Res. Soc. Symp. Proc. **104**, 281 (1988).
[351] M. Stavola, K. Bergman, S. J. Pearton, and J. Lopata, in *Shallow Impurities in Semiconductors 1988*, edited by B. Monemar (IOP, Bristol, UK, 1989), p. 447.
[352] S. J. Pearton, Mater. Sci. Eng., B **23**, 130 (1994).
[353] W. C. Dautremont-Smith, Mater. Res. Soc. Symp. Proc. **104**, 313 (1988).
[354] F. Ren, J. M. Grow, M. Bhaskaran, R. G. Wilson, and S. J. Pearton, J. Electron. Mater. **26**, 198 (1997).
[355] S. J. Pearton, C. R. Abernathy, P. Wisk, W. S. Hobson, and F. Ren, Appl. Phys. Lett. **63**, 1143 (1993).
[356] S. J. Pearton, C. R. Abernathy, J. D. MacKenzie, R. G. Wilson, F. Ren, and J. M. Zavada, Electron. Lett. **31**, 327 (1995).
[357] S. J. Pearton, C. R. Abernathy, C. B. Vartuli, J. D. MacKenzie, R. J. Shul, R. G. Wilson, and J. M. Zavada, Electron. Lett. **31**, 836 (1995).
[358] A. Y. Polyakov, M. Shin, S. J. Pearton, M. Skowronski, D. W. Greve, and J. A. Freitas, Mater. Res. Soc. Symp. Proc. **423**, 607 (1996).
[359] Y. Koide, N. Itoh, N. Sawaki, and I. Akasaki, J. Electrochem. Soc. **133**, 1956 (1986).
[360] Y. Koide, H. Itoh, M. R. H. Khan, K. Hiramatsu, N. Sawaki, and I. Akasaki, J. Appl. Phys. **61**, 4540 (1987).
[361] Y. Yoshida, S. Mizawa, and S. Gonda, J. Appl. Phys. **53**, 6844 (1982).
[362] M. A. Khan, A. Bhattarai, J. N. Kuznia, and J. T. Olson, Appl. Phys. Lett. **63**, 1214 (1993).
[363] M. A. Khan, J. N. Kuznia, J. M. Van Hove, N. Pan, and J. Carter, Appl. Phys. Lett. **60**, 3027 (1992).
[364] M. A. Khan, Q. Chen, C. J. Sun, J. M. Yang, M. Blasingame, M. S. Shen, and H. Park, Appl. Phys. Lett. **68**, 514 (1996).
[365] A. Y. Polyakov, in *Hydrogen in Compound Semiconductors*, edited by S. J. Pearton (Trans Tech. Publications, Switzerland, 1994), pp. 295–320.
[366] I. Akasaki, H. Amano, Y. Koide, K. Hiramatsu, and N. Sawaki, J. Cryst. Growth **98**, 209 (1989).
[367] X. Zhang, P. Kung, A. Saxler, D. Walker, T. C. Wang, and M. Razeghi, Appl. Phys. Lett. **67**, 1745 (1995).
[368] C. H. Seager and R. A. Anderson, Appl. Phys. Lett. **63**, 1531 (1993).
[369] C. H. Seager and R. A. Anderson, Solid State Commun. **76**, 285 (1990).
[370] A. J. Tavendale, A. A. Williams, D. Alexiev, and S. J. Pearton, Mater. Res. Soc. Symp. Proc. **59**, 469 (1985).
[371] T. Zundel, J. Weber, and L. Tilly, Physica B **170**, 361 (1991).
[372] C. H. Seager and R. A. Anderson, Appl. Phys. Lett. **59**, 585 (1991).
[373] Y. Kamiura, M. Yoneta, Y. Nishiyama, and F. Hashimoto, J. Appl. Phys. **72**, 3394 (1992).
[374] M. Yoneta, Y. Kamiura, and F. Haskimoto, J. Appl. Phys. **70**, 1295 (1991).
[375] I. Szafranek, S. S. Bose, and G. E. Stillman, Appl. Phys. Lett. **55**, 1205 (1989).
[376] I. Szafranek and G. E. Stillman, J. Appl. Phys. **68**, 3354 (1990).
[377] A. J. Tavendale, S. J. Pearton, A. A. Williams, and D. Alexiev, Appl. Phys. Lett. **56**, 1457 (1990).
[378] A. W. R. Leitch, Th. Prescha, and J. Weber, Phys. Rev. B **44**, 5912 (1991).
[379] S. Nakamura, M. Senoh, S. Nagahama, N. Iwasa, T. Yamada, T. Matsushita, H. Kyoku, and Y. Sugimoto, Jpn. J. Appl. Phys., Part 2 **35**, L74 (1996).
[380] N. M. Johnson, C. Doland, F. Ponce, J. Walker, and G. Anderson, Physica B **170**, 3 (1991).
[381] J. Chevallier and M. Aucouturier, Annu. Rev. Mater. Sci. **18**, 219 (1988).
[382] D. Mathiot, Phys. Rev. B **40**, 5869 (1989).
[383] A. Y. Polyakov, M. Stam, A. Z. Li, and A. G. Milnes, Int. Phys. Conf. Ser. **120**, 83 (1992).
[384] S. A. Ringel and B. Chatterjee, in *Proceedings Technology for Semiconductors*, 1997 (RES Signpost, Tivandrum, 1997); B. Chatterjee, S. A. Ringel, R. Sieg, R. Hoffman, and I. Weinberg, Appl. Phys. Lett. **65**, 58 (1994).
[385] U. K. Chakrabarti, S. J. Pearton, W. S. Hobson, J. Lopata, and V. Swaminathan, Appl. Phys. Lett. **57**, 887 (1990).
[386] S. J. Pearton, C. S. Wu, M. Stavola, F. Ren, J. Lopata, and W. C. Dautremont-Smith, Appl. Phys. Lett. **51**, 496 (1987); J. M. Zavada, and R. G. Wilson, Mater. Sci. Forum **148/149**, 189 (1994).
[387] K. Hiramatsu, S. Itoh, H. Amano, I. Akaski, N. Kuwano, T. Shiraishi, and K. Oki, J. Cryst. Growth **115**, 628 (1991).
[388] S. J. Pearton, Int. J. Mod. Phys. B **8**, 1247 (1994).
[389] M. S. Brandt, J. W. Ager, W. Gotz, N. M. Johnson, J. S. Harris, R. J. Molnar, and T. D. Moustakas, Phys. Rev. B **49**, 14 758 (1994).
[390] J. Neugebauer and C. G. Van der Walle, Phys. Rev. Lett. **75**, 4452 (1995).
[391] R. H. Williams, *Modern GaAs Processing Techniques* (Artech House, Norwood, Massachusetts, 1990), pp. 199–208.
[392] S. J. Pearton, Int. J. Mod. Phys. B **8**, 1781 (1994).
[393] M. A. Khan, J. N. Kuznia, A. R. Bhattarai, and D. T. Olson, Appl. Phys. Lett. **62**, 1786 (1993).
[394] C. B. Vartuli, S. J. Pearton, C. R. Abernathy, J. D. MacKenzie, and J. C. Zolper, J. Vac. Sci. Technol. B **13**, 2708 (1995).
[395] J. M. Zavada, R. G. Wilson, C. R. Abernathy, and S. J. Pearton, Appl. Phys. Lett. **64**, 724 (1994).
[396] R. G. Wilson, S. J. Pearton, C. R. Abernathy and J. M. Zavada, J. Vac. Sci. Technol. A **13**, 719 (1995).
[397] S. J. Pearton, R. J. Shul, R. G. Wilson, F. Ren, J. M. Zavada, C. R. Abernathy, C. Vartuli, J. Lee, J. MacKenzie, and J. R. Mileham, J. Electron. Mater. **25**, 845 (1996).
[398] S. J. Pearton, C. R. Abernathy, C. B. Vartuli, J. W. Lee, J. D. MacKenzie, R. G. Wilson, R. J. Shul, F. Ren, and J. M. Zavada, J. Vac. Sci. Technol. A **14**, 831 (1996).
[399] A. J. Tavendale, A. A. Williams, and S. J. Pearton, Appl. Phys. Lett. **48**, 590 (1986).
[400] C. R. Abernathy, S. J. Pearton, J. D. MacKenzie, J. R. Mileham, S. Bharatan, V. Krishnamoorthy, K. S. Jones, R. J. Shul, J. M. Zavada, D. Zheng, and R. M. Kolbas, Solid-State Electron. **39**, 111 (1996).
[401] J. W. Lee, C. Vartuli, C. R. Abernathy, J. D. Mackenzie, J. R. Mileham, S. J. Pearton, R. J. Shul, J. C. Zolper, M. H. Crawford, J. M. Zavada, R. G. Wilson, and R. N. Schwartz, J. Vac. Sci. Technol. B **14**, 3637 (1996).
[402] K. L. Seaward, Appl. Phys. Lett. **61**, 3002 (1992).
[403] J. D. DeSouza, D. Sadana, J. Baratte, and F. Cardone, Appl. Phys. Lett. **57**, 1129 (1990).

[404] S. J. Pearton, C. R. Abernathy, F. Ren, J. R. Lothain, P. Wisk, and A. Katz, J. Vac. Sci. Technol. A **11**, 1772 (1993).
[405] S. J. Pearton, C. R. Abernathy, F. Ren, J. R. Lothain, P. Wisk, A. Katz, and C. Constantine, Semicond. Sci. Technol. **8**, 310 (1993).
[406] S. J. Pearton, F. Ren, C. R. Abernathy, and J. R. Lothain, Semicond. Sci. Technol. **9**, 338 (1994).
[407] R. J. Shul, A. J. Howard, S. J. Pearton, C. R. Abernathy, C. B. Vartuli, and P. A. Barnes, *Proceedings of the Symposium of Wide Band Gap Semiconductors and Devices* (Electrochemical Society, Pennington, New Jersey 1995), pp. 217–230.
[408] C. R. Eddy and B. Molnar, Mater. Res. Soc. Symp. Proc. **395**, 745 (1996).
[409] L. Zhang, J. Ramer, J. Brown, K. Zheng, L. F. Lester, and S. D. Hersee, Mater. Res. Soc. Symp. Proc. **395**, 763 (1996).
[410] M. S. Brandt, N. M. Johnson, R. J. Molnar, R. Singh, and T. D. Moustakas, Appl. Phys. Lett. **64**, 2264 (1994).
[411] M. S. Brandt, J. W. Ager III, W. Gotz, N. M. Johnson, J. S. Harris, R. J. Molnar, and T. D. Moustakas, Phys. Rev. B **49**, 14758 (1994).
[412] Y. Okamoto, M. Saito, and A. Oshiyama, Jpn. J. Appl. Phys., Part 2 **35**, L807 (1996).
[413] A. Bosin, V. Fiorentini, and D. Vanderbilt, Mater. Res. Soc. Symp. Proc. **395**, 503 (1996).
[414] S. K. Estreicher and D. M. Maric, Mater. Res. Soc. Symp. Proc. **423**, 613 (1996).
[415] J. Neugebauer and C. G. Van der Walle, Phys. Rev. Lett. **75**, 4452 (1995).
[416] J. Neugebauer and C. G. Van der Walle, Mater. Res. Soc. Symp. Proc. **378**, 503 (1995); **395**, 645 (1996).
[417] J. Van Vechten, J. D. Zook, R. D. Hornig, and B. Goldenberg, Jpn. J. Appl. Phys. **31**, 362 (1992).
[418] J. Neugebauer and G. C. Van der Walle, Mater. Res. Soc. Symp. Proc. **423**, 619 (1996); Appl. Phys. Lett. **68**, 1829 (1996).
[419] W. Gotz, N. M. Johnson, D. P. Bour, M. D. McCluskey, and E. E. Haller, Appl. Phys. Lett. **69**, 3725 (1996).
[420] A. Kamato, H. Mitsuhashi, and H. Fujita, Appl. Phys. Lett. **63**, 3353 (1993).
[421] J. A. Wolk, J. W. Ager, K. J. Duxstad, E. E. Haller, N. Taskar, D. R. Dorman, and D. J. Olego, Appl. Phys. Lett. **63**, 2756 (1993).
[422] W. Gotz, N. M. Johnson, C. Chen, H. Liu, C. Kuo, and W. Imler, Appl. Phys. Lett. **68**, 3144 (1996).
[423] R. G. Wilson, in *Wide Band Gap Semiconductors*, edited by S. J. Pearton (Noyes, New Jersey, 1998).
[424] T. Mattila and R. M. Nieminen, Phys. Rev. B **54**, 16676 (1996).
[425] J. Neugebauer and C. G. Van de Walle, *Proceedings of the 22nd International Conference Physics of Semiconductors*, edited by D. J. Lockwood (World Scientific, Singapore, 1994), Vol. III, p. 2327.
[426] T. Mattila, A. P. Seitsmen, and R. M. Nieminen, Phys. Rev. B **54**, 1474 (1996); *III–V Nitride Materials and Processes*, edited by T. D. Moustakas, J. P. Dismukes, and S. J. Pearton (Electrochemical Society Pennington, NJ, 1996), p. 205.
[427] R. A. Youngman and J. H. Harris, J. Am. Ceram. Soc. **73**, 3238 (1990).
[428] W. A. Groeau, J. G. van Lierop, and A. Rosen, J. Mater. Sci. Lett. **12**, 1224 (1993).
[429] R. Zhang and T. F. Kuech, Appl. Phys. Lett. **72**, 1611 (1998).
[430] P. de Mierry, O. Ambacher, H. Kratzer, and M. Stutzmann, Phys. Status Solidi A **158**, 587 (1996).
[431] P. Boguslawski, E. L. Briggs, and J. Bernholc, Phys. Rev. B **51**, 17255 (1995).
[432] M. Sato, Appl. Phys. Lett. **68**, 935 (1996).
[433] J. I. Pankove, E. A. Miller, and J. E. Berkeyheiser, RCA Rev. **32**, 383 (1971).
[434] T. Ogino and M. Aoki, Jpn. J. Appl. Phys. **19**, 2395 (1980).
[435] A. Y. Polyakov, M. Shin, J. A. Freitas, M. Skrowronski, D. W. Greve, and R. G. Wilson, J. Appl. Phys. **80**, 6349 (1996).
[436] R. Niebuhr, K. Bachem, K. Dombrowski, M. Maier, W. Pletschen, and U. Kaufman, J. Electron. Mater. **24**, 1531 (1995).
[437] R. J. Molnar, K. B. Nichols, P. Maki, E. R. Brown, and I. Melngailis, Mater. Res. Soc. Symp. Proc. **378**, 479 (1995).
[438] N. R. Perkins, M. N. Horton, Z. Z. Bandic, T. C. McGill, and T. F. Kuech, Mater. Res. Soc. Symp. Proc. **395**, 243 (1996).
[439] T. A. Tansley and C. P. Foley, Electron. Lett. **20**, 1066 (1984).
[440] C. R. Abernathy, P. Wisk, F. Ren, and S. J. Pearton, J. Vac. Sci. Technol. B **11**, 179 (1993).
[441] B. J. Baliga, IEEE Electron Device Lett. **10**, 455 (1989).
[442] T. P. Chow and R. Tyagi, IEEE Trans. Electron Devices **41**, 1481 (1994).
[443] R. J. Trew, M. W. Shin, and V. Gatto, Solid-State Electron. **41**, 1561 (1997).
[444] M. N. Yoder, IEEE Trans. Electron Devices **43**, 1633 (1996).
[445] T. P. Chow, N. Ramungul, and M. Ghezzo, Mater. Res. Soc. Symp. Proc. **483**, 89 (1998).
[446] A. D. Bykhovski, B. L. Gelmont, and M. S. Shur, J. Appl. Phys. **81**, 6332 (1997).
[447] V. W. L. Chin, T. L. Tansley, and T. Osotchan, J. Appl. Phys. **75**, 7365 (1994).
[448] S. N. Mohammad and H. Morkoc, Prog. Quantum Electron. **20**, 361 (1996).
[449] J. G. Gaultieri, J. A. Kosinski, and A. Ballato, IEEE Trans. Syst. Sci. Cybern. **41**, 53 (1994).
[450] M. A. Littlejohn, J. R. Hauser, and T. H. Glisson, J. Appl. Phys. **48**, 4587 (1997).
[451] W. R. L. Lambrecht and B. Segall, in *Properties of Group III Nitrides, No. 11 EMIS Datareviews Series*, edited by J. H. Edgar (Inspec, London, 1994), Chap. 4.
[452] T. Lei, T. D. Moustakas, R. J. Graham, Y. He, and S. J. Berkowitz, J. Appl. Phys. **71**, 4933 (1992).
[453] M. Fanciulli, T. Lei, and T. D. Moustakas, Phys. Rev. B **48**, 15144 (1993).
[454] M. S. Shur and M. Asif Khan, Mater. Res. Bull. **22**, 44 (1997).
[455] U. V. Bhapkar and M. S. Shur, J. Appl. Phys. **82**, 1649 (1997).
[456] S. K. O'Leary, B. E. Foutz, M. S. Shur, U. V. Bhapkar, and L. F. Eastman, Solid State Commun. **105**, 621 (1998).
[457] J. Kolnik, I. H. Oguzman, K. F. Brennan, R. Wang, P. P. Ruden, and Y. Wang, J. Appl. Phys. **78**, 1033 (1995).
[458] H. P. Maruska and J. J. Tietjen, Appl. Phys. Lett. **15**, 327 (1969).
[459] W. M. Yim, E. J. Stofko, P. J. Zanzucchi, J. I. Pankove, M. Ettenburg, and S. L. Gilbert, J. Appl. Phys. **44**, 292 (1973).
[460] T. L. Tansley and C. P. Foley, J. Appl. Phys. **59**, 3241 (1986).
[461] A. S. Barker, Jr. and M. Ilegems, Phys. Rev. B **7**, 743 (1973).
[462] P. M. Asbeck, E. T. Yu, S. S. Lau, G. J. Sullivan, J. Van Hove, and J. Redwing, Electron. Lett. **33**, 1230 (1997).
[463] M. A. Littlejohn, J. R. Hauser, and T. H. Glisson, Appl. Phys. Lett. **26**, 625 (1976).
[464] B. Gelmont, K. Kim, and M. Shur, J. Appl. Phys. **74**, 1818 (1993).
[465] L. F. Eastman (private communication).
[466] S. K. O'Leary, B. E. Foutz, M. S. Shur, U. Bhaphkar, and L. F. Eastman, J. Appl. Phys. **83**, 826 (1998).
[467] B. E. Foutz, S. K. O'Leary, M. S. Shur, L. F. Eastman, and U. V. Bhaphkar, Materials Research Society Spring, 1998.
[468] M. Shur, B. Gelmont, and M. A. Khan, J. Electron. Mater. **25**, 777 (1996).
[469] R. Gaska, J. W. Wang, A. Osinsky, Q. Chen, M. A. Khan, A. O. Orlov, G. L. Snider, and M. S. Shur, Appl. Phys. Lett. **72**, 707 (1998).
[470] N. G. Weimann, L. F. Eastman, D. Doppalapudi, H. M. Ng, and T. D. Moustakas, J. Appl. Phys. **83**, 3656 (1998).
[471] Z. C. Huang, R. Goldberg, J. C. Chen, Y. Zheng, D. B. Mott, and P. Shu, Appl. Phys. Lett. **67**, 2825 (1995).
[472] E. T. Yu, P. M. Asbeck, S. S. Lau, and G. J. Sullivan, Planet. Space Sci. **98-2**, 468 (1998).
[473] D. L. Smith, Solid State Commun. **57**, 919 (1986).
[474] T. F. Kuech, R. T. Collins, D. L. Smith, and C. Mailhoit, J. Appl. Phys. **67**, 2650 (1990).
[475] R. M. Martin, Phys. Rev. B **5**, 1607 (1992).
[476] E. T. Yu, G. J. Sullivan, P. M. Asbeck, C. D. Wang, D. Qiao, and S. S. Lau, Appl. Phys. Lett. **71**, 2794 (1997).
[477] H. M. Manasevit, F. M. Erdmann, and W. I. Simpson, J. Electrochem. Soc. **118**, 1864 (1971).
[478] I. Akasaki and I. Hayashi, Ind. Sci. Technol. **17**, 48 (1976) (in Japanese).
[479] S. Yoshida, S. Misawa, and S. Gonda, Appl. Phys. Lett. **42**, 427 (1983).
[480] H. Amano, N. Sawaki, I. Akasaki, and Y. Toyoda, Appl. Phys. Lett. **48**, 353 (1986).
[481] S. Nakamura, Jpn. J. Appl. Phys., Part 2 **30**, L1705 (1991).
[482] S. Nakamura, T. Mukai, M. Senoh, and N. Iwasa, Jpn. J. Appl. Phys., Part 2 **31**, L139 (1992).
[483] M. A. Khan, J. N. Kuznia, J. M. Van Hove, N. Pan, and J. Carter, Appl. Phys. Lett. **60**, 3027 (1992).
[484] M. A. Khan, A. R. Bhattarai, J. N. Kuznia, and D. T. Olsen, Appl. Phys. Lett. **63**, 1214 (1993).
[485] A. Bykhovski, B. Gelmont, and M. Shur, J. Appl. Phys. **74**, 6734 (1993).

[486] S. Nakamura, T. Mukai, and M. Senoh, Appl. Phys. Lett. **64**, 1687 (1994).
[487] S. C. Binari, L. B. Rowland, G. Kelner, W. Kruppa, H. B. Dietrich, K. Doverspike, and D. K. Gaskill, in *Compound Semiconductors 1994*, edited by H. Goronkin and U. Mishra (IOP, Bristol, 1995) p. 459.
[488] M. A. Khan, J. N. Kuznia, D. T. Olsen, W. Schaff, J. Burm, and M. S. Shur, Appl. Phys. Lett. **65**, 1121 (1994).
[489] J. Pankove, S. S. Chang, H. C. Lee, R. J. Molnar, T. D. Moustakas, and B. Van Zeghbroeck, IEEE IEDM, San Francisco, CA, 11–14 December 1994 (unpublished), p. 389.
[490] A. Ozgur, W. Kim, Z. Fan, A. Botchkarev, A. Salvador, S. N. Mohammad, B. Sverdlov, and H. Morkoc, Electron. Lett. **31**, 1389 (1995).
[491] M. A. Khan, Q. Chen, M. S. Shur, B. T. McDermott, J. A. Higgins, J. Burm, W. Schaff, and L. F. Eastman, Electron. Lett. **32**, 357 (1996).
[492] Y. F. Wu, B. P. Keller, S. Keller, D. Kapolnek, P. Kozodoy, S. P. DenBaars, and U. K. Mishra, Appl. Phys. Lett. **69**, 1438 (1996).
[493] S. C. Binari, J. M. Redwing, G. Kelner, and W. Kruppa, Electron. Lett. **33**, 242 (1997).
[494] A. T. Ping, Q. Chen, J. W. Yang, M. A. Khan, and I. Adesida, IEEE IEDM Washington, DC, 7–10 December 1997 (unpublished), p. 561.
[495] R. Gaska, Q. Chen, J. Yang, A. Osinksy, M. A. Khan, and M. S. Shur, IEEE Electron Device Lett. **18**, 492 (1997).
[496] B. J. Thibeault, B. P. Keller, Y.-F. Wu, P. Fina, U. K. Mishra, C. Nguyen, N. X. Nguyen, and M. Le, IEEE IEDM Washington, DC, 7–10 December 1997 (unpublished), p. 569.
[497] S. Siram, R. L. Messham, T. J. Smith, R. J. Bojko, M. D. Bremser, R. F. Davis, L. T. Kehias, and T. J. Jenkins, Mater. Res. Soc. Symp. Proc. **482**, 271 (1998).
[498] Y.-F. Wu, B. P. Keller, P. Fim, J. Pusl, M. Le, N. X. Nguyen, C. Nguyen, D. Widman, S. Keller, S. P. DenBaars, and U. K. Mishra, Electron. Lett. **33**, 1743 (1997).
[499] G. J. Sullivan, M. Y. Chen, J. A. Higgins, J. W. Yang, Q. Chen, R. L. Pierson, and B. T. McDermott, IEEE Electron Device Lett. **19**, 198 (1998).
[500] P. Kozodoy, J. P. Ibbetson, H. Marchand, R. T. Fini, S. Keller, J. S. Speck, S. P. DenBaars, and U. K. Mishra, Appl. Phys. Lett. **73**, 975 (1998).
[501] U. Mishra, S. DenBaars, S. Keller, R. J. Fini, J. S. Speck, and P. Kozodoy, WOSEMMAD, Monterey, CA, February 1998.
[502] S. T. Sheppard, K. Doverspike, W. L. Pribble, S. T. Allen, and J. W. Palmour, 56th Device Research Conference, Charlottesville, VA, 22–24 June 1998 (unpublished), paper V.B.-5.
[503] M. E. Levinshtein, S. L. Rumyantsev, R. Gaska, J. W. Yang, and M. S. Shur, Appl. Phys. Lett. **73**, 1089 (1998).
[504] L. S. McCarthy, P. Kozodoy, S. P. DenBaars, M. Rodwell, and U. K. Mishra, 25th Inter. Symp. on Compound Semiconductors, 12–16 October 1998 (unpublished), Nara, Japan, paper We2A-1.
[505] F. Ren, C. R. Abernathy, J. Van Hove, P. P. Chow, R. Hickman, K. B. Jung, H. Cho, T. LaRoche, R. J. Shul, J. Han, and S. J. Pearton, MRS Internet J. Nitride Semicond. Res. **3**, 41 (1998); F. Ren, M. Hong, S. N. G. Chu, M. A. Marcus, M. J. Schurman, A. G. Baca, S. J. Pearton, and C. R. Abernathy, Appl. Phys. Lett. **73**, 3893 (1998).
[506] M. A. Khan, J. N. Kuznia, A. R. Bhattarai, and D. T. Olsen, Appl. Phys. Lett. **62**, 1786 (1993).
[507] M. A. Khan, A. R. Bhattarai, J. N. Kuznia, and D. T. Olsen, Appl. Phys. Lett. **63**, 1214 (1993).
[508] R. Gaska, J. W. Yang, A. Osinsky, Q. Chen, M. A. Khan, A. O. Orlov, G. L. Snider, and M. S. Shur, Appl. Phys. Lett. **72**, 707 (1998).
[509] D. V. Kuksenkov, H. Temkin, R. Gaska, and J. W. Yang, IEEE Electron Device Lett. **19**, 222 (1998).
[510] G. J. Sullivan, J. A. Higgins, M. Y. Chen, J. W. Yang, Q. Chen, R. L. Pierson, and B. T. McDermott, Electron. Lett. **34**, 922 (1998).
[511] N. X. Nguyen, C. Nguyen, and D. E. Grider, Electron. Lett. **34**, 811 (1998).
[512] H. Kawai, M. Hara, F. Nakamura, and S. Imanaga, Electron. Lett. **34**, 592 (1998).
[513] R. Gaska, A. Osinsky, J. W. Yang, and M. S. Shur, IEEE Electron Device Lett. **19**, 89 (1998).
[514] K. Chu, L. F. Eastman, I. Smart, and J. R. Shealy, WOCSEMMAD, Monterey, CA, February 1998.
[515] C. Nguyen, N. X. Nguyen, M. Le, and D. E. Grider, Electron. Lett. **34**, 309 (1998).
[516] A. T. Ping, Q. Chen, J. W. Yang, M. Asif Khan, and I. Adesida, IEEE Electron Device Lett. **19**, 54 (1998).
[517] Y.-F. Wu, B. P. Keller, P. Fini, S. Keller, R. J. Jenkins, L. T. Kehias, S. P. DenBaars, and U. K. Mishra, IEEE Electron Device Lett. **19**, 50 (1998).
[518] Q. Chen, J. W. Yang, R. Gaska, M. Asif Khan, M. S. Shur, G. J. Sullivan, A. L. Sailor, J. A. Higgins, A. T. Ping, and I. Adesida, IEEE Electron Device Lett. **19**, 44 (1998).
[519] Y.-F. Wu, B. P. Keller, P. Fini, J. Pusl, M. Le, N. X. Nguyen, D. Widman, S. Keller, S. P. DenBaars, and U. K. Mishra, Electron. Lett. **33**, 1742 (1997).
[520] Y.-F. Wu, B. P. Keller, S. Keller, N. X. Nguyen, M. Le, C. Nguyen, T. J. Jenkins, L. T. Kehias, S. P. DenBaars, and U. K. Mishra, IEEE Electron Device Lett. **18**, 438 (1997).
[521] L. Eastman, K. Chu, W. Schaff, M. Murphy, N. G. Weimann, T. Eustis, MRS Internet J. Nitride Semicond. Res. **2**, 17 (1997).
[522] Q. Chen, J. W. Yang, M. A. Khan, A. T. Ping, and I. Adesida, Electron. Lett. **33**, 1413 (1997).
[523] R. Gaska, Q. Chen, J. Yang, M. Asif Khan, M. S. Shur, A. Ping, and I. Adesida, Electron. Lett. **33**, 1255 (1997).
[524] O. Aktas, Z. F. Fan, A. Botchkarev, S. N. Mohammad, M. Roth, T. Jenkins, L. Kehias, and H. Morkoc, IEEE Electron Device Lett. **18**, 293 (1997).
[525] A. T. Ping, M. Asif Khan, Q. Chen, J. W. Yang, and I. Adesida, Electron. Lett. **33**, 1081 (1997).
[526] Y.-F. Wu, S. Keller, P. Kozodoy, B. P. Keller, P. Parikh, D. Kapolnek, S. P. DenBaars, and U. K. Mishra, IEEE Electron Device Lett. **18**, 290 (1997).
[527] Z. Fan, C. Lu, A. E. Botchkarev, H. Tang, A. Salvador, O. Aktas, W. Kim, and H. Morkoc, Electron. Lett. **33**, 814 (1997).
[528] J. Burm, K. Chu, W. J. Schaff, L. F. Eastman, M. Asif Khan, Q. Chen, J. W. Yang, and M. S. Shur, IEEE Electron Device Lett. **18**, 141 (1997).
[529] Q. Chen, R. Gaska, M. Asif Khan, M. S. Shur, A. Ping, I. Adesida, J. Burm, W. J. Schaff, and L. F. Eastman, Electron. Lett. **33**, 637 (1997).
[530] N. X. Nguyen, B. P. Keller, S. Keller, Y.-F. Wu, M. Le, C. Nguyen, S. P. DenBaars, U. K. Mishra, and D. Grider, Electron. Lett. **33**, 334 (1997).
[531] O. Aktas, Z. F. Fan, S. N. Mohammad, A. E. Botchkarev, and H. Morkoc, Appl. Phys. Lett. **69**, 3872 (1996).
[532] M. Asif Khan, W. Che, M. S. Shur, B. T. Dermott, J. A. Higgins, J. Burm, W. J. Schaff, and L. F. Eastman, IEEE Electron Device Lett. **17**, 584 (1996).
[533] Y.-F. Wu, B. P. Keller, S. Keller, D. Kapolnek, S. P. DenBaars, and U. K. Mishra, IEEE Electron Device Lett. **17**, 455 (1996).
[534] S. N. Mohammad, Z.-F. Fan, A. Salvador, O. Aktas, A. E. Botcharev, W. Kim, and Hadis Morkoc, Appl. Phys. Lett. **69**, 1420 (1996).
[535] Z. Fan, S. N. Mohammad, O. Aktas, A. E. Botcharev, A. Salvador, and Hadis Morkoc, Appl. Phys. Lett. **69**, 1229 (1996).
[536] Q. Chen, M. Asif Khan, J. W. Yang, C. J. Sun, M. S. Shur, and H. Park, Appl. Phys. Lett. **69**, 794 (1996).
[537] J. Burm, W. J. Schaff, L. F. Eastman, H. Amano, and I. Akasaki, Appl. Phys. Lett. **68**, 2849 (1996).
[538] M. A. Khan, Q. Chen, M. S. Shur, B. T. Dermott, J. A. Higgins, J. Burm, W. Schaff, and L. F. Eastman, Electron. Lett. **32**, 357 (1996).
[539] M. Asif Khan, Q. Chen, C. J. Sun, J. W. Yang, M. Blasingame, M. S. Shur, and H. Park, Appl. Phys. Lett. **68**, 514 (116).
[540] M. Asif Khan, M. S. Shur, J. N. Kuznia, Q. Chen, J. Burm, and W. Schaff, Appl. Phys. Lett. **66**, 1083 (1995).
[541] M. Asif Khan, J. N. Kuznia, D. T. Olson, W. J. Schaff, J. W. Burm, and M. S. Shur, Appl. Phys. Lett. **65**, 1121 (1994).
[542] L. F. Eastman, K. G. Chu, J. Smart, and J. R. Shealy, Mater. Res. Soc. Symp. Proc. **512**, 3 (1998).
[543] Y.-F. Wu, B. J. Thibeault, B. P. Keller, S. Keller, S. P. DenBaars, and U. K. Mishra, Topic Workshop on Heterostructure Microelectronics, Kanagawa, Japan, August 31–September 2, 1998, paper S4-5.
[544] W. Kruppa, S. C. Binari, and K. Doverspike, Electron. Lett. **31**, 1951 (1995).
[545] S. C. Binari, W. Kruppa, H. B. Dietrich, G. Kelner, A. E. Wickenden, and J. A. Freitas, Sr., Solid-State Electron. **41**, 1549 (1997).
[546] U. Mishra (private communication).
[547] X. Zhang, P. King, D. Walker, J. Piotrowski, A. Rogalski, and A. Saxler, Appl. Phys. Lett. **67**, 2028 (1995).
[548] See, for example, M. W. Shin and R. J. Trew, Electron. Lett. **31**, 498 (1995).
[549] S. C. Binari, Proc. Electrochem. Soc. **95–21**, 112 (1995).
[550] L. Daumiller, C. Kirchner, M. Kamp, K. J. Ebeling, L. Pond, C. E.

Weitzel, and E. Kohn, 56th Device Research Conference, Charlottesville, VA, 22–24 June, 1998 (unpublished), paper V.B-5.
[551] S. J. Rosner, E. C. Carr, M. J. Ludowise, G. Girolami, and H. I. Erikson, Appl. Phys. Lett. **70**, 420 (1997).
[552] Z. Z. Bandic, P. M. Bridger, E. C. Piquette, and T. C. McGill, Appl. Phys. Lett. **72**, 3166 (1998).
[553] A. Usai, H. Sunakawa, A. Sakai, and A. Yamaguchi, Jpn. J. Appl. Phys., Part 2 **36**, L899 (1997).
[554] D. Kapolnek, S. Keller, R. Vetury, R. D. Underwood, P. Kozodoy, S. P. DenBaars, and U. K. Mishra, Appl. Phys. Lett. **71**, 1204 (1997).
[555] T. S. Zheleva, O.-H. Nam, M. D. Bremser, and R. F. Davis, Appl. Phys. Lett. **71**, 2472 (1997).
[556] P. Kozodoy, J. P. Ibbetson, H. Marchand, D. T. Fini, S. Keller, J. S. Speck, S. P. DenBaars, and U. K. Mishra, Appl. Phys. Lett. **73**, 975 (1998).
[557] R. Shealy and U. Mishra (private communication).
[558] H. Akagi, IEEE Trans. Power Electron. **13**, 345 (1998).
[559] G. T. Heydt and B. J. Skromme, Mater. Res. Soc. Symp. Proc. **483**, 3 (1998).
[560] E. R. Brown, Solid-State Electron. **43**, 1918 (1998).
[561] *Power Semiconductor Devices*, edited by S. J. Baliga (PWS, Boston, 1996).
[562] T. Hasegawa, K. Yamaji, H. Itokawa, H. Shirahama, C. Tanaka, and K. Akabane, IEEE Trans. Power Deliv. **11**, 1783 (1996).
[563] A. Nakagawa and Y. Seki, Proc. 1996 IEE Japan Ann. Convention, paper 5-15-1 (in Japanese).
[564] Y. Takahashi, K. Yoshikawa, M. Soutome, T. Fujii, M. Ichijyou, and Y. Seki, Proc. 8th Int. Symp. Power Semiconductor Devices and IC's, Hawaii, Sept. 1996 (unpublished), pp. 299–302.
[565] J. B. Casady, A. K. Agarwal, L. B. Rowland, S. Seshadri, R. R. Siergiej, S. S. Mani, D. C. Sheridan, P. A. Sanger, and C. D. Brandt, Mater. Res. Soc. Symp. Proc. **483**, 27 (1998).
[566] Z. Z. Bandic, E. C. Piquette, P. M. Bridger, T. F. Kuech, and T. C. McGill, Mater. Res. Soc. Symp. Proc. **483**, 399 (1998).
[567] R. Zehringer, A. Stack, and T. Lang, Mater. Res. Soc. Symp. Proc. **483**, 369 (1998).
[568] See, for example J. Mater. **50**, 46 (1998).
[569] S. Nakamura, M. Senoh, S. Nagahama, N. Iwasa, T. Yamada, T. Matsushita, H. Kiyoku, and Y. Sugimoto, Jpn. J. Appl. Phys., Part 2 **35**, L74 (1996).
[570] S. Nakamura, M. Senoh, S. Nagahama, N. Iwasa, T. Yamada, T. Matsushita, H. Kiyoku, and Y. Sugimoto, Jpn. J. Appl. Phys., Part 2 **35**, L217 (1996).
[571] S. Nakamura, M. Senoh, S. Nagahama, N. Iwasa, T. Yamada, T. Matsushita, H. Kiyoku, and Y. Sugimoto, Appl. Phys. Lett. **68**, 2105 (1996).
[572] S. Nakamura, M. Senoh, S. Nagahama, N. Iwasa, T. Yamada, T. Matsushita, H. Kiyoku, and Y. Sugimoto, Appl. Phys. Lett. **68**, 3269 (1996).
[573] S. Nakamura, M. Senoh, S. Nagahama, N. Iwasa, T. Yamada, T. Matsushita, Y. Sugimoto, and H. Kiyoku, Appl. Phys. Lett. **69**, 1477 (1996).
[574] S. Nakamura, M. Senoh, S. Nagahama, N. Iwasa, T. Yamada, T. Matsushita, Y. Sugimoto, and H. Kiyoku, Appl. Phys. Lett. **69**, 1568 (1996).
[575] K. Itaya, M. Onomura, J. Nishino, L. Sugiura, S. Saito, M. Suzuki, J. Rennie, S. Nunoue, M. Yamamoto, H. Fujimoto, Y. Kokubun, Y. Ohba, G. Hatakoshi, and M. Ishikawa, Jpn. J. Appl. Phys., Part 2 **35**, L1315 (1996).
[576] S. Nakamura, M. Senoh, S. Nagahama, N. Iwasa, T. Yamada, T. Matsushita, Y. Sugimoto, and H. Kiyoku, Appl. Phys. Lett. **69**, 3034 (1996).
[577] S. Nakamura, M. Senoh, S. Nagahama, N. Iwasa, T. Yamada, T. Matsushita, Y. Sugimoto, and H. Kiyoku, Appl. Phys. Lett. **70**, 616 (1997).
[578] G. E. Bulman, K. Doverspike, S. T. Sheppard, T. W. Weeks, H. S. Kong, H. M. Dieringer, J. A. Edmond, J. D. Brown, J. T. Swindell, and J. F. Schetzina, Electron. Lett. **33**, 1556 (1997).
[579] M. P. Mack, A. Abare, M. Aizcorbe, P. Kozodoy, S. Keller, U. K. Mishra, L. Coldren, and S. DenBaars, MRS Internet J. Nitride Semicond. Res. **2**, 41 (1997). (Available from http://nsr.mij.mrs.org/2/5/).
[580] A. Kuramata, K. Domen, R. Soejima, K. Horino, S. Kubota, and T. Tanahashi, Jpn. J. Appl. Phys., Part 2 **36**, L1130 (1997); T. Kobayashi, F. Nakamura, K. Naganuma, T. Toyjo, H. Nakajima, T. Asatsuma, H. Kawai, and M. Ikeda, Electron. Lett. **34**, 1494 (1998).
[581] S. Nakamura, M. Senoh, S. Nagahama, N. Iwasa, T. Yamada, T. Matsushita, Y. Sugimoto, and H. Kiyoku, Appl. Phys. Lett. **69**, 4056 (1996).
[582] S. Nakamura, M. Senoh, S. Nagahama, N. Iwasa, T. Yamada, T. Matsushita, Y. Sugimoto, and H. Kiyoku, Appl. Phys. Lett. **70**, 1417 (1997).
[583] S. Nakamura, M. Senoh, S. Nagahama, N. Iwasa, T. Yamada, T. Matsushita, Y. Sugimoto, and H. Kiyoku, Appl. Phys. Lett. **70**, 2753 (1997).
[584] S. Nakamura, IEEE J. Sel. Top. Quantum Electron. **3**, 435 (1997).
[585] S. Nakamura, M. Senoh, S. Nagahama, N. Iwasa, T. Yamada, T. Matsushita, Y. Sugimoto, and H. Kiyoku, Jpn. J. Appl. Phys., Part 2 **36**, L1059 (1997).
[586] S. Nakamura, 24th International Symposium on Compound Semiconductors, San Diego, CA, Plen-1, 8–11 September 1997 (unpublished).
[587] S. Nakamura, M. Senoh, S. Nagahama, N. Iwasa, T. Yamada, T. Matsushita, H. Kiyoku, Yasunobu Sugimoto, T. Kozaki, H. Umemoto, M. Sano, and K. Chocho, Jpn. J. Appl. Phys., Part 2 **36**, L1568 (1997).
[588] S. Nakamura, M. Senoh, S. Nagahama, N. Iwasa, T. Yamada, T. Matsushita, H. Kiyoku, Y. Sugimoto, T. Kozacki, H. Umemoto, M. Sano, and K. Chocho, Appl. Phys. Lett. **72**, 2014 (1998); Jpn. J. Appl. Phys., Part 2 **37**, L309 (1998).
[589] S. Nakamura, M. Senoh, S. Nagahama, N. Iwasa, T. Yamada, T. Matsushita, H. Kiyoku, Y. Sugimoto, T. Kozacki, H. Umemoto, M. Sano, and K. Chocho, Appl. Phys. Lett. **73**, 832 (1998); Jpn. J. Appl. Phys., Part 2 **37**, L627 (1998).
[590] S. Chichibu, T. Azuhata, T. Sota, and S. Nakamura, Appl. Phys. Lett. **69**, 4188 (1996).
[591] Y. Narukawa, Y. Kawakami, S. Fujita, and S. Nakamura, Phys. Rev. B **55**, 1938R (1997).
[592] Y. Narukawa, Y. Kawakami, M. Funato, S. Fujita, S. Fujita, and S. Nakamura, Appl. Phys. Lett. **70**, 981 (1997).
[593] M. Suzuki and T. Uenoyama, Jpn. J. Appl. Phys., Part 1 **35**, 1420 (1996).
[594] M. Suzuki and T. Uenoyama, Appl. Phys. Lett. **69**, 3378 (9916).
[595] W. W. Chow, A. F. Wright, and J. S. Nelson, Appl. Phys. Lett. **68**, 296 (1996).
[596] O. H. Nam, M. D. Bremser, T. Zheleva, and R. F. Davis, Appl. Phys. Lett. **71**, 2638 (1997).
[597] Y. Kato, S. Kitamura, K. Hiramatsu, and N. Sawaki, J. Cryst. Growth **144**, 133 (1994).
[598] J. Salzman and H. Temkin, Mater. Sci. Eng., B **50**, 148 (1997).
[599] W. G. Bi, Y. Ma, J. P. Zhang, L. W. Yang, S. T. Ho, and C. W. Tu, IEEE Photonics Technol. Lett. **9**, 1072 (1997).
[600] M. Kondow, K. Uomi, A. Niwa, T. Kitami, S. Watahiki, and Y. Yazawa, Jpn. J. Appl. Phys., Part 1 **35**, 1273 (1996).
[601] W. G. Bi and C. W. Tu, J. Appl. Phys. **80**, 1934 (1996).
[602] T. Miyamoto, K. Takeuchi, F. Koyama, and K. Iga, IEEE Photoniics Technol. Lett. **9**, 1448 (1997).
[603] K. Nakahara, K. Kondow, T. Kitatani, Y. Yazawa, and K. Uomi, Electron. Lett. **32**, 1585 (1996).
[604] M. C. Larson, M. Kondow, T. Kitatani, K. Nakahara, K. Tamura, H. Inoue, and K. Uomi, IEEE Photonics Technol. Lett. **10**, 188 (1998).
[605] M. C. Larson, M. Kondow, T. Kitatani, K. Tamura, Y. Yazawa, and M. Okai, IEEE Photonics Technol. Lett. **9**, 1549 (1997).
[606] M. Kondow, S. Nakatsuka, T. Kitatani, Y. Yazawa, and M. Okai, Electron. Lett. **32**, 2244 (1996).
[607] T. Kitatani, M. Kondow, S. Nakatsuka, Y. Yazawa, and M. Okai, IEEE J. Sel. Top. Quantum Electron. **3**, 206 (1997).
[608] M. Kondow, T. Kitatani, S. Nakatsuka, M. C. Larson, K. Nakahara, Y. Yazawa, M. Okai, and K. Uomi, IEEE J. Sel. Top. Quantum Electron. **3**, 719 (1997).
[609] Compound Semiconductor July/August 1997 (unpublished), p. 24.
[610] S. Nakamura, in *GaN and Related Materials, Vol. 2*, edited by S. J. Pearton (Gordon and Breach, New York, 1997).
[611] S. Nakamura, T. Mukai, and M. Senoh, Jpn. J. Appl. Phys., Part 2 **30**, L1998 (1991).
[612] S. Nakamura, M. Senoh, and T. Mukai, Jpn. J. Appl. Phys., Part 2 **31**, L8 (1993).
[613] S. Nakamura, J. Cryst. Growth **145**, 911 (1994).
[614] S. Nakamura, J. Vac. Sci. Technol. A **13**, 705 (1995).
[615] S. Nakamura, T. Mukai, and M. Senoh, J. Appl. Phys. **76**, 8189 (1994).
[616] S. Nakamura, T. Mukai, M. Senoh, S. Nagahama, and N. Iwasa, J. Appl. Phys. **74**, 3911 (1993).
[617] S. Nakamura, M. Senoh, N. Iwasa, and S. Nagahama, Jpn. J. Appl. Phys., Part 1 **34**, 1797 (1995).
[618] S. Nakamura, M. Senoh, N. Iwasa, and S. Nagahama, Appl. Phys. Lett. **67**, 1868 (1995).
[619] S. Nakamura, M. Senoh, N. Iwasa, S. Nagahama, T. Yamada, and T. Mukai, Jpn. J. Appl. Phys., Part 2 **34**, L1332 (1995).
[620] S. Chichibu, T. Sota, K. Wada, and S. Nakamura, J. Vac. Sci. Technol. B **16**, 2204 (1998).
[621] K. Osamura, S. Naka, and Y. Murakami, J. Appl. Phys. **46**, 3432 (1975).

[622] R. Singh, D. Doppalapudi, T. D. Moustakas, and L. T. Romano, Appl. Phys. Lett. **70**, 1089 (1997).
[623] T. Matsuoka, Appl. Phys. Lett. **71**, 105 (1997).
[624] M. Shimizu, Y. Kawaguchi, K. Hiramatsu, and N. Sawaki, Solid-State Electron. **41**, 145 (1997).
[625] A. Wakahara, T. Tokuda, X. Dang, S. Noda, and A. Susaki, Appl. Phys. Lett. **71**, 906 (1997).
[626] S. Chichibu, M. Arita, H. Nakanishi, J. Nishio, L. Sugiura, Y. Kokubun, and K. Itaya, J. Appl. Phys. **83**, 489 (1998).
[627] F. Scholz, V. Harle, F. Steuber, A. Sohmer, H. Bolay, V. Sygahow, A. Doernen, J. Im, A. Hangleiter, J. Y. Duboz, P. Galtier, E. Rosencher, O. Ambacher, D. Brunner, and H. Lakner, Mater. Res. Soc. Symp. Proc. **449**, 3 (1997).
[628] M. Razeghi and A. Rogalski, J. Appl. Phys. **79**, 7433 (1996).
[629] M. S. Shur and M. A. Khan, MRS Bull. **22**, 44 (1997).
[630] K. S. Stevens, M. Kinniburgh, and R. Beresford, Appl. Phys. Lett. **66**, 3518 (1995).
[631] P. Kung, X. Zhang, D. Walker, A. Saxler, J. Piotrowski, A. Rogulski, and M. Razeghi, Appl. Phys. Lett. **67**, 3792 (1995).
[632] E. Monroy, J. A. Garrido, E. Muñoz, I. Izpura, F. J. Sanchez, M. A. Sanchez-Garcia, E. Calleja, B. Beaumont, and P. Gibart, MRS Internet J. Nitride Semicond. Res. **2**, 12 (1997).
[633] D. Walker, X. L. Zhang, P. Kung, A. Saxler, S. Javadpour, J. Xu, and M. Razeghi, Appl. Phys. Lett. **68**, 2100 (1996).
[634] B. W. Lim, Q. Chen, M. A. Khan, C. J. Sun, and J. Yang, Appl. Phys. Lett. **68**, 3761 (1996).
[635] M. A. Khan, J. N. Kuznia, D. T. Olson, M. Blasingame, and A. R. Bhattarai, Appl. Phys. Lett. **63**, 2455 (1993).
[636] Q. Chen, J. W. Yang, A. Osinsky, S. Gangopadhyay, B. Lim, M. Z. Anwar, D. Kuksenkov, and H. Temkin, Appl. Phys. Lett. **70**, 2277 (1997).
[637] M. A. Khan, M. S. Shur, Q. Chen, J. N. Kuznia, and C. J. Sun, Electron. Lett. **31**, 398 (1995).
[638] J. C. Carrano, T. Li, P. A. Gradowski, C. J. Eiting, R. D. Dupuis, and J. C. Campbell, Appl. Phys. Lett. **72**, 542 (1998).
[639] A. Osinsky, S. Gangopadhyay, J. W. Yang, R. Gaska, D. Kuksenkov, H. Temkin, I. K. Shmagin, Y. C. Chung, J. F. Muth, and R. M. Kolbas, Appl. Phys. Lett. **72**, 551 (1998).
[640] A. Osinsky, S. Gangopadhyay, R. Gaska, B. Williams, M. A. Khan, D. Kuksenkov, and H. Temkin, Appl. Phys. Lett. **71**, 2334 (1997).
[641] S. Krishnankutty, W. Yang, T. Nohava, and P. P. Ruden, MRS Internet J. Nitride Semicond. Res. **3**, 7 (1998).
[642] W. Yang, T. Nohava, S. Krishnankutty, R. Torreano, S. McPherson, and H. Marsh, Appl. Phys. Lett. **73**, 978 (1998).
[643] G. Y. Xu, A. Salvador, W. Kim, Z. Fan, C. Lu, H. Tang, H. Morkoc, G. Smith, M. Estes, B. Goldenberg, W. Yang, and S. Krishnankutty, Appl. Phys. Lett. **71**, 2154 (1997).
[644] J. C. Carrano, P. A. Grudowski, C. J. Eiting, R. D. Dupuis, and J. C. Campbell, Appl. Phys. Lett. **70**, 1992 (1997).
[645] W. Yang, T. Nohava, S. Krishnankutty, R. Torreano, S. McPherson, and H. Marsh, Appl. Phys. Lett. **73**, 1086 (1998).
[646] J. M. Van Hove, R. Hickman, J. J. Klaasen, P. P. Chow, and P. P. Ruden, Appl. Phys. Lett. **70**, 2282 (1997).